# Discrete-time modelling of brass and reed woodwind instruments with application to musical sound synthesis

**Thesis** · January 2002

CITATIONS
32

READS
416

**1 author:**

Maarten Van Walstijn
Queen's University Belfast
**96** PUBLICATIONS **1,260** CITATIONS

SEE PROFILE

# Discrete-Time Modelling of Brass and Reed Woodwind Instruments with Application to Musical Sound Synthesis

Maarten van Walstijn


PhD
University of Edinburgh
2002

# Abstract

This work deals with simulation of brass and reed woodwind instruments. The principal objective is to develop discrete-time models that are suitable for application in a musical sound synthesis environment.

The main bulk of the thesis describes methods for linear modelling of the instrument air column. Using a travelling-wave based approach, the air column is modelled as a series of modules, each representing a part of the bore. New methods for digital modelling of brass and woodwind mouthpieces, woodwind toneholes, and brass bells are presented. The study also includes new methods for discrete-time modelling of conical bore sections.

In addition, the mechanical behaviour of a clarinet reed is studied by means of a distributed model that is formulated numerically using the finite-difference approach. Precise measurements of the reed shape and the mouthpiece lay geometry have been carried out in order to accurately simulate the bending of the reed against the lay during oscillation. An equivalent lumped oscillator model is formulated, and its properties are analysed in application to a reed-driven pipe simulation.

In general, the discrete-time models described in this work are validated via comparison with either measurements or established acoustic theories. The modular approach taken in the derivation of these models allow for dynamic and intuitive control of the musically important simulation parameters.

# Declaration

I declare that this thesis is composed by myself, and that the work therein is my own.

(Maarten van Walstijn)

# Acknowledgements

My great and sincere thanks go to Murray Campbell and Peter Nelson, my supervisors, who provided continuous support and guidance during the course of this research project.

I am also greatly indebted to a number of researchers who have helped me significantly in developing the methods and ideas that are presented in this work. Vesa Välimäki and Julius Smith made useful comments and suggestions about digital modelling of acoustical horns. I was very fortunate to have the opportunity to learn from their expertise in the fields of digital signal processing and discrete-time modelling of acoustic systems through numerous discussions by email.

Previous work on pulse reflectometry measurements and bore reconstruction algorithms by Noam Amir and David Sharp convinced me that such techniques could be useful in the context of my thesis, and I am very grateful for their patience and enthusiasm in explaining and discussing this subject.

Gary Scavone provided guidance on the subject of tonehole modelling, and the work on modelling the single reed excitation mechanism was greatly helped by the comments and suggestions by Federico Avanzini. It was a pleasure to collaborate with them.

The matlab implementations of the multi-modal method are due to Jonathan Kemp. Discussions with Jonathan also helped me to understand various issues related to the principles and influences of higher modes in wave propagation in acoustic horns.

Furthermore, I would like to thank Davide Rocchesso, Joël Gilbert, Riccardo Di Federici, John Cullen, Howard Wright, Orlando Richards and Josep Comajuncosas for many stimulating and interesting discussions on subjects in the fields of musical acoustics and computer modelling of musical instruments, and Vince Devine, Frank Morris and Andrew Downie for technical support.

This study would not have been possible without the financial support provided by the University of Edinburgh.

Finally, I would like to express gratitude to my wife Juliana and my parents for their constant moral support.

# Contents

# List of Symbols

| | |
|---|---|
| $t$ | time |
| $f$ | frequency |
| $\omega$ | angular frequency |
| $f_s$ | sampling frequency |
| $\Delta t$ | sampling period |
| $\Delta x$ | spatial sampling interval |
| $j$ | imaginary unit ($j = \sqrt{-1}$) |
| $s$ | Laplace variable |
| $z$ | $z$-transform variable ($z = e^{sT}$) |
| $\Gamma$ | propagation constant |
| $H(\omega)$ | analogue filter transfer function |
| $H(z)$ | digital filter transfer function |
| $p, P$ | pressure and its Fourier transform |
| $u, U$ | volume velocity and its Fourier transform |
| $p^+, P^+$ | forward-propagating pressure wave and its Fourier transform |
| $p^-, P^-$ | backward-propagating pressure wave and its Fourier transform |
| $g(t), Z(\omega)$ | Green's function and its Fourier transform, impedance |
| $r(t), R(\omega)$ | reflection function and its Fourier transform, reflectance |
| $Z_0$ | characteristic impedance |
| $Y_0$ | characteristic admittance |
| $\delta(t)$ | Dirac delta function |
| $\epsilon(t)$ | Heaviside function |
| $c$ | wave velocity |
| $\rho$ | air density |
| $\eta$ | viscosity coefficient |
| $\mathcal{T}$ | temperature |

# List of Abbreviations

| | |
|---|---|
| DWG | digital waveguide |
| FD | fractional delay |
| FIR | finite impulse response |
| FFT | fast Fourier transform |
| IFFT | inverse fast Fourier transform |
| IIR | infinite impulse response |
| TIIR | truncated infinite impulse response |
| WD | wave digital |
| WDF | wave digital filter |
| WGF | waveguide filter |

# List of Figures

# List of Tables

# Chapter 1

# Introduction

This work describes methods for time-domain simulation of acoustic wind instruments. The objective is to develop models that can be used for sound synthesis of brass and reed woodwind instruments.

## 1.1 General Introduction to Discrete-Time Modelling of Musical Instruments

Discrete-time modelling is a relatively new approach to studying musical instruments. Until a few decades ago, most studies in the field of musical acoustics were based around purely analytical calculations, usually carried out in the frequency-domain. A more recent trend is to study the oscillations taking place inside and outside the instrument by means of *time-domain simulation*. The main reason for taking this approach is that the sound production in most musical instruments involves complex non-linear phenomena, and this generally tends to make it extremely difficult to give an accurate description of the oscillatory behaviour by analytical means.

Although some attempts at time-domain simulation of musical instruments have been made by means of analogue computer systems (see for example, [29]), the predominant hardware tool that is used for implementation of such *physical models* is the digital computer. An important consequence of the use of a digital system is that models have to be formulated in numerical form, which requires the combination of acoustical modelling methods with signal processing and numerical modelling techniques. The main drawback of the time-domain modelling approach is that precise simulations typically require large amounts of computational power. A common approach is therefore to use an efficient model that simplifies the acoustic behaviour of the instrument but still captures its main operational features. Because computing power has been rapidly increasing for the past few decades and will continue to do so in the immediate future, it may be expected that

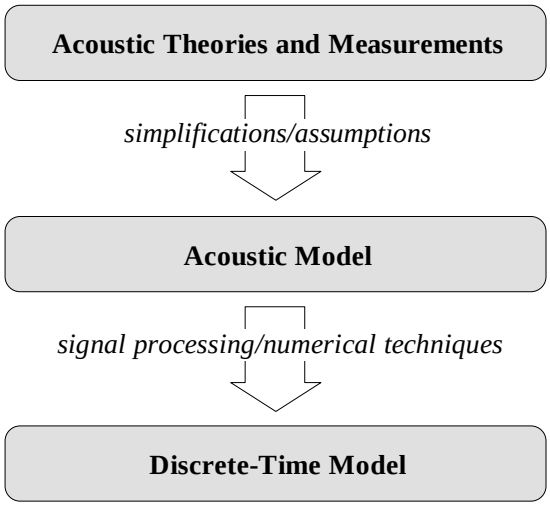


Figure 1.1: General procedure for derivation of a discrete-time model of an acoustic system.

the computational burden will form less of an obstacle in future applications. However, as will be explained later in this section, computational efficiency is likely to remain an important modelling criterion, especially in music-oriented applications.

To derive a discrete-time model of an acoustic system, one usually proceeds in two steps (see figure 1.1). The first step consists of formulating a set of mathematical formulae that together describe the acoustic behaviour of the system. This acoustic model is then put into numerical form in the second step, which is commonly referred to as *discretisation*.

Although the present study is mainly motivated by the desire for high quality sound synthesis, the objective for developing discrete-time models is generally twofold. Initially, the objective was largely confined to gaining insight into the sound production mechanisms of musical instruments. The area of expertise that is most likely to benefit from this research is that of the design and production of real acoustic instruments. Applications might for example take the form of providing useful advice to instrument manufacturers about the improvement and repair of traditional instruments. More recently, a second objective has emerged in the form of musical sound synthesis. For example, physical modelling techniques have already been implemented in various commercial synthesizers, and it is widely expected that this development will eventually lead to realistic reproduction of the sounds of real instruments. There is no reason to confine the area of application to pure *imitation* efforts though: the modelling framework that is used for simulation of real instruments can also be employed for the creation of new, "virtual acoustic" instruments. Developments in this direction form a particularly promising prospect for use in compositions and performances of electronic and electro-acoustic music.

The reason that physical modelling has become a popular sound synthesis method

is that it offers distinct advantages over previously developed techniques such as additive synthesis, frequency modulation and sampling. Because these methods are typically aimed at reproduction of *waveforms*, they usually fail to capture the transient features of the acoustically produced sound. By simulating the *behaviour* of the acoustical system, the physical properties of the acoustical system are embedded within the model, and as a result the transient characteristics are naturally reproduced with it. This is of primary importance because the transient features of acoustic signals such as speech and music appear to be of fundamental importance from the point of view of perception. The method also allows, to some extent, the restoration of the traditional relation between player and instrument. That is, a physical model can be controlled through parameters that correspond to the "real-life" parameters of a musician. For example, a violin model can be formulated such that the excitation of the strings is controlled though variation of bowing pressure and velocity. The intuitive nature of such control has been a natural part of musical skills for centuries, but has to some extent been lost with the introduction of electronic instruments. The lack of intuitive control has certainly been one of the major drawbacks of many previous sound synthesis methods [68].

In the literature, one can often make a distinction between studies that are mainly aimed at either the first objective (understanding) or the second objective (sound synthesis). However, in practice these are not completely independent objectives. That is, in order to formulate a realistic sound synthesis model, one needs to first gain a very good understanding of the acoustic system. On the other hand, the ultimate test for assessing the quality of an acoustic model is perhaps by judging its sound output. Given this coherence between the two objectives, the main difference that remains is that there tends to be a much sharper trade-off between efficiency and accuracy in the derivation of physical models with sound synthesis purposes. This is mainly because the musical potential of sound synthesis applications is most effectively explored in a *real-time* environment. This requires a very high modelling efficiency, especially if the processing power has to be shared with a controller interface.

## 1.2 Wind Instrument Modelling

The first wind instrument time-domain simulation to appear in the literature is the clarinet model by Schumacher [124]. In this model, the response of the instrument air column is computed by means of a convolution with its impulse response. The convolution is part of a non-linear feedback loop that forms the basic structure of the model, where the non-linear part corresponds to the reed excitation mechanism. This type of formulation was later generalised for simulation of a wide variety of self-sustaining musical oscillators by McIntyre, Schumacher and Woodhouse [95], and has since been adopted and developed

further by a large number of researchers. Although remarkably realistic sound output can be obtained within this approach, the convolution method is not particularly suitable for application to musical sound synthesis due to the fact that a different impulse response is required for each configuration of the instrument bore. For example, in order to simulate the functioning of the valves of a trumpet, the model would have to switch or interpolate between a large set of impulse responses. In order to enable precise control of those parts of the instrument that are used for pitch adjustment (i.e., toneholes, valves or slides) without having to resort to methods which require large amounts of computational power and storage space, a *modular* approach is required. That is, if the instrument is modelled as a series of interacting modules, these modules can be controlled independently, which tends to allow for a much more direct, simpler and meaningful form of parameterisation. For example, a modular clarinet model could consist of a series of cylindrical bore sections and tonehole units, and in a way analogous to a real clarinet player, the pitch of the instrument could then be adjusted by opening and closing of the holes.

Various modular approaches to modelling wind instrument bores can be found in the literature. The first attempts in this direction were made by Smith [129] in the form of a *digital waveguide model* of the clarinet. Although this model is based on strong simplifications concerning the reed excitation mechanism and the acoustical function of the toneholes, it must be considered as an essential step forward, since it establishes the basic principles of modelling the air column vibrations by explicitly simulating the transmission and reflection of waves inside the bore. The ideas behind the digital waveguide modelling approach were initially developed in application to string instruments, and were partly inspired by earlier work on sound synthesis of strings by Karplus and Strong [71] and Jaffe and Smith [69]. The digital waveguide approach was later developed further in a number of different studies, for example for simulation of woodwinds [38, 63, 148, 119] and brass instruments [27], and have been widely adopted (for example, in [4, 45, 99]). At around the same time as Smith initiated the digital waveguide approach, Martínez et al. [94] developed a method that is extremely similar to digital waveguide modelling. That is, their *multi convolution algorithm* is based on the same principle of simulation by explicitly modelling the propagating waves in the bore. Another approach for modular simulation was developed by Adrien in form of *modal synthesis* [3]. This method is based on a representation of a vibrating structure as a set of normal modes, where each mode has its own frequency, damping coefficient and modal shape coordinate. The modal synthesis method tends to be rather inefficient when applied to modelling woodwind instrument bores, because a set of modes has to be defined for each individual tonehole and bore section.

Given these basic methods for linear modelling of the instrument bore, it is worthwhile pointing out a number of recent developments and possible improvements. In a study

on trombone simulation, Msallam et al. [100] have presented methods for including the non-linear effects that typically occur at high amplitude oscillations in the bore. These non-linear features form an essential part of the sound of most brass instruments, and a much improved sound quality can be obtained by including them in the simulation. Vergez [160], starting from earlier work on this subject by Msallam [99], has presented an improved algorithm for discrete-time modelling of non-linear effects, and incorporated this algorithm in a trumpet simulation. In terms of modelling the lip excitation mechanism, various models can be found in the literature, usually in the form of one-mass or two-mass models [45, 141, 49, 142, 1, 2, 44, 99, 100, 160, 161]. It is often assumed that for the purpose of sound synthesis, a one-mass model is sufficient [58]. It appears that the one-mass models presented by Msallam et al. [100] and by Rodet and Vergez [161] are particularly suitable for sound synthesis, as they have taken care to avoid the generation of artificial high-frequency components during the lip closure.

With respect to modelling of reed woodwinds, Hirschberg et al. [64] have pointed out several aero-acoustic features that can be incorporated in a basic acoustic model in order to obtain a more realistic sound output. However, while diverse improvements in this direction have been made for flue instruments [159] as well as for brass instruments [99, 160], physical models of reed woodwinds in which such phenomena are carefully taken into account have yet to appear in the literature.

Another issue that has not yet been addressed properly is the mechanical behaviour of the reed. In most discrete-time models that have been developed so far, the reed is represented as a lumped oscillator (see for example, [124, 77, 115, 54, 43]). These models are based on the assumption that the reed has one (constant) mechanical degree of freedom. Unfortunately, this assumption only holds for oscillations at very small amplitudes. Moreover, reed beating is usually included in a highly simplified manner, which results in the artificial generation of higher harmonics. As pointed out in [140] and [137], the reed/mouthpiece interaction can be simulated in a more realistic way by means of a *distributed model*. The large computional burden of such a model renders it unsuitable for sound synthesis purposes though. Ducasse [48] and Gazengel [55] have formulated lumped models in which the effects of the reed curling up to the mouthpiece lay is included by formulating the lumped parameters as a function of the reed deflection. However, both these studies are very theoretical, and the derivation of the lumped parameters is not based on careful measurements of the reed and the mouthpiece geometries.

There are also numerous improvements possible with respect to discrete-modelling of the instrument air column. One aspect that appears to be well covered at this stage is the possibility of adjusting the length of an acoustical bore. Välimäki and colleagues [152, 148] have carried out an extensive study on this subject in the context of digital waveguide modelling, and Barjau et al. [19] have recently removed the limitations concerning the

bore lengths in the multi convolution algorithm.

The first woodwind tonehole model that could be employed within the context of digital waveguide modelling was presented by Välimäki et al. [151]. This rather simplified model, which can not be used for simulation of closed toneholes, was later greatly improved by Scavone and Cook [121]. However, the applicability of their *three-port tonehole model* is limited because (1) it requires a minimum tonehole length of at least half the spatial sample interval [120] and (2) it has not been formulated for modelling toneholes in conical bores.

Surprisingly little work has been done on discrete-time modelling of woodwind mouthpieces. The only available model appears to be the lumped two-port representation proposed by Scavone [119]. This model requires four filters of relatively high order (Scavone employed 13th-order IIR filters), and can therefore not be regarded as particularly efficient. The "brute force" solution by means of lumped filters was deemed necessary by Scavone because a more straight-forward implementation of his model was assumed to be unstable because it involved the implementation of an air column junction of decreasing taper rate.

The problem of potential instability encountered by Scavone is in fact related to a wider discussion about simulation of conical bore systems. It is interesting to note that there seems to be no consensus about this in the literature. On the one hand, Välimäki [148] claims that digital models are bound to be stable because they simulate passive physical systems. This line of reasoning appears to be supported by the fact that Martínez et al. [94], employing techniques that are very similar to those used by Välimäki , are able to compute the impulse response of conical bore systems directly in discrete-time without running into numerical problems. On the other hand, Scavone [119] has reported that finite-precision simulations of conical bore models are problematic because unstable growth tends to occur if the model is computed over long time durations. This subject clearly deserves some more investigation.

Berners [27] has used so-called "Sturm-Liouville (S-L)" modelling techniques for modelling acoustic bores; with this approach, passively terminated bore systems can always be simulated in a stable manner. The main disadvantage of the S-L model is that it is less suited to efficient time-domain implementation of musical instrument bores, especially in cases where any of the flared sections of an instrument contain toneholes that are controlled dynamically [28].

Further possible improvements are possible with respect to modelling brass air columns. As in the case of woodwinds, discrete-time modelling of the brass mouthpiece appears to be a rather poorly covered subject. Dietz [45] employs a trumpet mouthpiece model that is based on a lumped element model described by Backus [18], whereas Msallam [99] has employed a digital waveguide implementation of a simple model consisting of

two cylindrical sections for modelling a trombone mouthpiece. However, neither of these models has been properly assessed in terms of accuracy so far.

With respect to modelling the flaring brass bell, Berners [27] has carried out extensive research on how to determine analytically a brass bell reflectance, although perhaps a more systematic approach to this problem can be found in the studies on multi-modal decomposition by Pagneux et al. [105] and Amir et al. [8]. It appears that the only two methods for *digital approximation* of such a bell reflectance available in the literature are the waveguide filter method employed by Dietz [45] and the convolution method used by Msallam [99]. Unfortunately, both these methods are computationally rather expensive, which leaves the development of a cheaper method still very much desirable.

## 1.3 Thesis Outline

The aims of this work are:

(1) to develop a woodwind tonehole model that can represent toneholes of a wide variety of physically and musically feasible dimensions, and that is applicable to discrete-time modelling of cylindrical bore as well as conical bore woodwind instruments. Furthermore, this model should allow dynamic control of its state.

(2) to develop techniques for discrete-time modelling of brass and woodwind mouthpieces.

(3) to improve on the existing techniques for digital approximation of brass bell reflectances.

(4) to establish under which conditions a travelling-wave based digital simulation of a conical bore system remains stable.

(5) to develop a single reed excitation model that incorporates the interaction between the reed and the mouthpiece lay in a precise way.

In pursuing these aims, we consider it as important that the following criteria are taken into account:

($\mathcal{A}$) In the derivation of discrete-time models, the central criterion is to obtain a good trade-off between efficiency, accuracy and perceptual relevance.

($\mathcal{B}$) The methodology should result in stable models of brass and woodwind air columns.

($\mathcal{C}$) The modelling approach should always be modular for simulation of those parts of the instrument that require dynamic control of one or more of their parameters

(i.e. the length of the bore of a brass instrument, the states of the toneholes of a woodwind instrument).

($\mathcal{D}$) The resulting discrete-time models should always be compared to their continuous-time counterparts, and the causes of any discrepancies should be clarified.

($\mathcal{E}$) Where possible, model parameters should be derived from measurements on real instruments.

Aero-acoustical aspects, such as those outlined in [64], are not included in the aims. We take the view that the first step in developing musically useful physical models is to formulate basic models in a modular way. With respect to modelling the excitation mechanism, we consider the mechanical interaction between the reed and the mouthpiece as the most urgent aspect to be investigated.

The thesis is organised as follows. Chapter 2 reviews the basic theories and principles of modelling tubular acoustic systems such as pipes, cavities and horns. Acoustic bores of varying cross-section are studied by means of piecewise modelling techniques, and results are compared with those obtained using multi-modal decomposition methods.

Methods for modelling acoustic systems in discrete-time are discussed in chapter 3. Two well-known modelling approaches, namely *convolution methods* and *digital waveguide modelling*, are reviewed. In addition, we introduce the application of *wave digital filter* techniques, and give an outline of how to combine these with digital waveguide techniques. The resulting modelling approach, which is referred to as *wave digital modelling*, forms the basis for various techniques and applications described in subsequent chapters.

Chapter 4 discusses digital waveguide modelling of non-flaring bores in detail. New ways of formulating taper junctions are described, and modelling errors related to the inclusion of viscothermal losses are analysed. An important part of this chapter is the investigation into the stability of conical bore simulations.

In chapter 5 we describe a new method for simulation of woodwind toneholes, using wave digital modelling techniques. The methodology is based on and verified with established tonehole theories.

Chapter 6 discusses techniques for simulation of the main bore of a woodwind instrument. A different method for modelling taper and diameter discontinuities, which enables the derivation of realisable discrete-time formulations of conical bore systems containing lumped elements, is presented. Example applications of the wave digital modelling approach are discussed, and a detailed comparison with the multi convolution approach is given.

Chapter 7 deals with digital approximation of the bell of a brass instrument. Application of conventional IIR filter design methods to a typical brass bell reflectance is

investigated. A new method that makes use of one-pole TIIR filter elements is introduced. These are digital filters of a type that have only been developed very recently [162], and have properties that allow for an efficient approximation. We also present a second method, that uses a FIR filter instead of TIIR elements. Both methods are applied to an experimentally determined trumpet bell reflectance.

Chapter 8 discusses discrete-time modelling of the mouthpiece of a brass or reed woodwind instrument. Basic frequency-domain models are presented and verified with measurements on a trumpet and a clarinet. Discretisation of these models is accomplished with the use of wave digital modelling techniques.

In chapter 9, the elements discussed in chapters 3 to 8 are combined in the simulations of the complete air column of a trumpet and of a clarinet.

Finally, in chapter 10, we describe techniques for discrete-time modelling of the single reed excitation mechanism. The emphasis in this chapter is mainly on modelling the mechanical behaviour of the reed. A distributed model of the reed/mouthpiece system is presented, in which the interaction of the reed with the mouthpiece lay is carefully taken into account. Furthermore, it is shown that an equivalent lumped oscillator model can be derived, and the properties of this model are analysed in a simulation of a reed-driven pipe.

# Chapter 2

# Linear Models of Tubular Acoustic Systems

The air column of a wind instrument is a tubular system filled with air, which is driven into oscillation when the instrument is played. For oscillations at small amplitudes, such as occur when playing a brass or reed woodwind instrument at low or medium dynamic levels, we may assume linear vibrational behaviour. For oscillation at high amplitudes - for example, when playing a brass instrument at *forte* levels - the assumption of linearity no longer holds.

In this chapter, *linear* models of tubular acoustic systems are discussed. The chapter provides a foundation for the discrete-time modelling techniques described in the subsequent chapters. Most of the material presented here forms a review of acoustics theory as given in standard acoustic textbooks (for example, [139, 103, 84, 98, 52]). In addition, a few novel modelling techniques and analysis methods are presented.

The chapter is organised as follows. Section 2.1 describes the basic fluid dynamical properties and principles of acoustical wave motion. Then in section 2.2, wave propagation in non-flaring bores (cylindrical and conical) is discussed. Finally in section 2.3, we discuss how more complex bore shapes can be modelled by means of piecewise modelling techniques.

## 2.1 Acoustic Wave Motion

Sound waves are pressure disturbances that propagate through air, resulting in increases and decreases of local pressure. The pressure variations correspond to a continuous transfer between potential and kinetic energy, which is possible because air has both mass and elasticity. This section presents the basic laws and properties that govern acoustic wave motion.

### 2.1.1 Basic Fluid Dynamical Properties

An essential characteristic of the fluid air is that it is compressible. Analogous to storing potential energy in a mechanical spring by displacing it from its equilibrium position, potential energy can be stored in a volume of air by compressing or decompressing it. Consider a volume of air, having a volume $V_0$ and pressure $\mathcal{P}_0$ at equilibrium. With small pressure fluctuations, the elastic behaviour is approximately linear, and the relation between changing pressure ($\mathcal{P}$) and volume ($V$) of a fixed mass of gas may be expressed as [52]:

$$\mathcal{P} - \mathcal{P}_0 = B\left(\frac{V_0 - V}{V}\right), \tag{2.1}$$

where $B$ is called the *bulk modulus* [52, 84]. The pressure variation or excess pressure ($\mathcal{P} - \mathcal{P}_0$) is usually referred to as the *acoustic pressure* ($p$). Apart from *volume elasticity*, air has *mass density* (mass/volume). During compression or decompression of the volume, its total mass $M$ stays unaltered, in other words the product of density ($\rho$) and volume is constant:

$$\rho V = \rho_0 V_0 = M. \tag{2.2}$$

Combining (2.2) and (2.1) yields the relationship between density and pressure:

$$\rho = \rho_0\left(\frac{p}{B} + 1\right). \tag{2.3}$$

For small pressure fluctuations ($p/B \ll 1$), the density may be considered constant ($\rho \approx \rho_0$). In general, volume compression will also influence the air temperature ($\mathcal{T}$), and the bulk modulus depends on the way this variable is related to the pressure and volume. The general equation of state for a perfect gas is [84]:

$$\mathcal{P}V = \mathcal{R}\mathcal{T}, \tag{2.4}$$

where $\mathcal{R}$ is a constant dependent on the type of gas. Equation (2.4) can be further specified by determining the level of thermal energy transfer within the gas. It has been experimentally found that in acoustic processes no appreciable heat conduction takes place [84, 52]. This type of thermodynamic behaviour is called *adiabatic* and its corresponding equation of state for a perfect gas is [84]:

$$\frac{\mathcal{P}}{\mathcal{P}_0} = \left(\frac{\rho}{\rho_0}\right)^{\gamma}, \tag{2.5}$$

where $\gamma = C_p/C_v$ is the *ratio of specific heats* at constant temperature and constant volume, respectively [1]. In the case of small pressure fluctuations, the bulk modulus may

[1] See appendix A for thermodynamic constants.

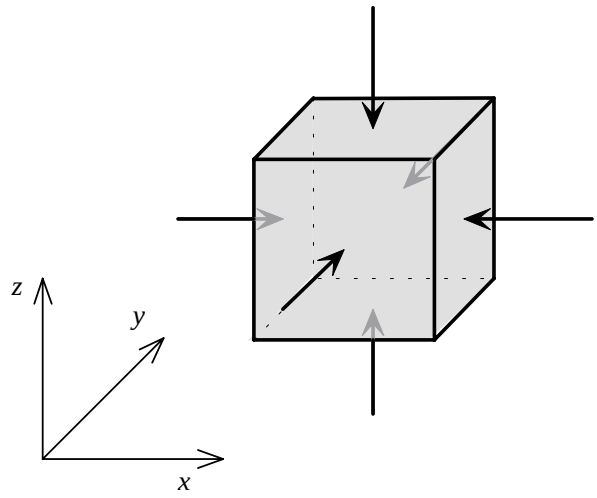


Figure 2.1: A spatially fixed volume of air experiencing pressure forces in three dimensions.

be expressed in terms of the first coefficient of the Taylor-expansion of an experimentally derived equation of state [84]:

$$B = \rho_0 \left( \frac{\partial \mathcal{P}}{\partial \rho} \right)_{\rho_0} . \tag{2.6}$$

Now differentiating (2.5) with respect to $\rho$, and substituting (2.6) gives the value for the *adiabatic bulk modulus*:

$$B = \gamma \, \mathcal{P}_0. \tag{2.7}$$

### 2.1.2 The Linearised Wave Equation

In the absence of viscothermal losses[2], all energy involved in acoustic wave motion is mechanical, and all forces involved are determined by the mechanical properties such as defined in section 2.1.1. Consider the volume depicted in figure 2.1. This spatially fixed volume has mass flux and experiences pressure forces in three dimensions $(x, y, z)$. In order to obtain a differential equation for describing the acoustic wave motion in this volume, two fundamental equations are required. The first one is the *equation of continuity*:

$$\begin{aligned} \frac{\partial \rho}{\partial t} \cdot V_0 &= -\left[ \frac{\partial (\rho v_x)}{\partial x} + \frac{\partial (\rho v_y)}{\partial y} + \frac{\partial (\rho v_z)}{\partial z} \right] \cdot V_0 \\ &\textit{or} \\ \frac{\partial \rho}{\partial t} &= -\nabla \cdot (\rho \vec{v}) \, , \end{aligned} \tag{2.8}$$

[2] Viscothermal losses occur due to heat conduction and viscous drag.

where $\vec{v}$ denotes the particle velocity vector. This equation states that the net influx of mass must be equal to the total mass increase rate of the volume. Substituting (2.3) into (2.8) and assuming small pressure fluctuations ($p/B \ll 1$) leads to the linear equation of continuity:

$$\frac{1}{B}\frac{\partial p}{\partial t} + \nabla \cdot \vec{v} = 0. \tag{2.9}$$

The second equation is the application of Newton's second law to the mass of volume $V_0$:

$$\begin{aligned} -\left[\frac{\partial \mathcal{P}}{\partial x} + \frac{\partial \mathcal{P}}{\partial y} + \frac{\partial \mathcal{P}}{\partial z}\right] V_0 &= (\rho V_0)\frac{\partial^2 \vec{\zeta}}{\partial t^2} \\ & \textit{or} \\ -\nabla \mathcal{P} &= \rho\left(\frac{\partial^2 \vec{\zeta}}{\partial t^2}\right), \end{aligned} \tag{2.10}$$

which states that the total force applied in each direction should equal the mass times acceleration, where $\vec{\zeta}$ is the local fluid particle displacement vector. Defining the particle velocity $\vec{v} = \partial\vec{\zeta}/\partial t$, and taking into account that the fluid moves $\vec{v}\,dt$ in time $dt$, allows us to write the local acceleration as [84]:

$$\frac{d^2\vec{\zeta}}{dt^2} = \frac{\partial \vec{v}}{\partial t} + v_x\frac{\partial \vec{v}}{\partial x} + v_y\frac{\partial \vec{v}}{\partial y} + v_z\frac{\partial \vec{v}}{\partial z}. \tag{2.11}$$

The higher order terms on the right side of (2.11) cause the force equation to be non-linear. Fortunately, at small pressure fluctuations these terms are very small, so the expression for acceleration may be simplified $\left[\partial^2\vec{\zeta}/\partial t^2 = \partial\vec{v}/\partial t\right]$. Now again assuming a constant density $\rho \approx \rho_0$ and using the fact that $\nabla\mathcal{P} = \nabla p$, we can reduce (2.10) to the linear force equation:

$$\rho_0\frac{\partial \vec{v}}{\partial t} = -\nabla p. \tag{2.12}$$

Taking the divergence of (2.12) and differentiating (2.9) with respect to $t$ allows the elimination of $\vec{v}$ and results in the linearised lossless wave equation:

$$\nabla^2 p = \frac{1}{c^2}\frac{\partial^2 p}{\partial t^2}. \tag{2.13}$$

where $\nabla^2$ is the Laplacian operator for Cartesian coordinates[3], and $c = \sqrt{B/\rho_0}$ is the acoustic *wave velocity*[4].

[3] See appendix B for the definition of various coordinate systems.

[4] In the remaining part of the thesis, the suffix "0" in $\rho_0$ is suppressed, thus from here on $\rho$ indicates a constant density value.

### 2.1.3 Distributed Models and Lumped Elements

For propagation of plane waves in one dimension only, the wave equation reduces to:

$$\frac{\partial^2 p}{\partial x^2} = \frac{1}{c^2}\frac{\partial^2 p}{\partial t^2}. \tag{2.14}$$

The solution of (2.14) for frequency $\omega$ takes the form of a superposition of forward- and backward-travelling waves:

$$\begin{aligned} p(x,t) &= p^+(x,t) + p^-(x,t) \\ &= Ae^{j(\omega t - kx)} + Be^{j(\omega t + kx)}, \end{aligned} \tag{2.15}$$

where $A$ and $B$ represent the amplitudes of the forward and backward travelling waves, and $k = \omega/c$ is the *wave number*. The acoustic wave length of the longitudinal plane wave for frequency $\omega$ is $\lambda = 2\pi c/\omega$. Suppose now that this wave propagates in an enclosed air volume $V$. If the length of $V$ in the $x$-direction is large in comparison with the wavelength $\lambda$, (2.15) describes planar wave motion for frequency $\omega$ at all points $x$ along the axis. Such a model of wave propagation is referred to as a *distributed acoustic model*. On the other hand, if the wavelength is not small in comparison with the dimensions of $V$, the time-varying behaviour of the acoustic variables is almost independent of distance over the dimensions of the device [84]. Modelling wave motion is strongly simplified in this case, since spatial coordinates may be ignored. Acoustical devices in this *long-wavelength limit* or *low-frequency limit* are usually termed *lumped acoustic elements*.

A simple example of an acoustic system that can be described with lumped acoustic elements is the *Helmholz resonator*. This system consists of a small acoustic cavity that communicates with the outside through a short neck (see figure 2.2). The acoustic mass of the air in the neck is:

$$M = \rho S l. \tag{2.16}$$

Suppose that an external force $F_1$ is applied to mass $M$. Newton's second law states that the force equals mass times acceleration:

$$F_1 = M\frac{d^2 x}{dt^2}, \tag{2.17}$$

where $x$ represents the displacement of the air mass in the neck. This force will cause the neck air mass to move, which will trigger a restoring force from the acoustic volume (see figure 2.2). Assuming linear elastic behaviour (equation (2.1)), the restoring force due to

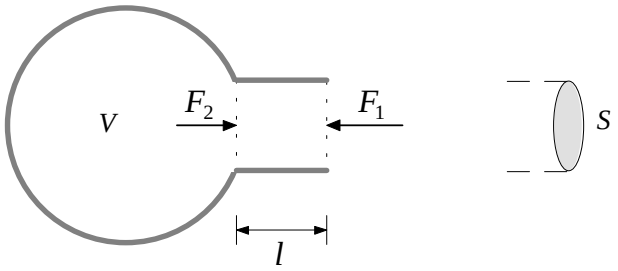


Figure 2.2: Schematic representation of an acoustic Helmholz resonator. The driving-force $F_1$ causes a displacement of the air in the neck and triggers a restoring force $F_2$ due to compression of the volume $V$.

a volume compression $dV$ is:

$$F_2 = -p\,S = -B\,S\,\frac{dV}{V}. \tag{2.18}$$

The volume compression in the cavity due to a neck air displacement $x$ is:

$$dV = S \cdot x. \tag{2.19}$$

If we assume that the opening at the end of the neck presents a mechanical resistive force $F_3 = R_{mech} \cdot (dx/dt)$, it follows that the net force applied on $M$ is:

$$F = F_1 - F_2 + F_3. \tag{2.20}$$

Combining (2.20), (2.19) and (2.18) gives the differential equation describing the neck air mass motion:

$$M\frac{d^2x}{dt^2} + R_{mech}\frac{dx}{dt} + Kx = F. \tag{2.21}$$

where $K = \rho c^2 S^2/V$ is the *acoustic stiffness* of the volume $V$. Equation (2.21) describes a *driven harmonic oscillator*[5]. When referring to acoustic systems, it is custom to express the behaviour of a lumped acoustic element in terms of its acoustic impedance, which is not the same as the mechanical impedance. For frequency $\omega$, the acoustic impedance expresses the frequency-dependent ratio $(Z(\omega) = p(\omega)/u(\omega))$, where $u = S \cdot v$ is the *volume velocity*. The *mechanical* impedance of the Helmholz resonator is:

$$Z_{mech}(\omega) = \frac{F(\omega)}{v(\omega)} = j\omega M + R_{mech} + \frac{K}{j\omega}, \tag{2.22}$$

[5] see appendix F for the mathematics of the driven harmonic oscillator.

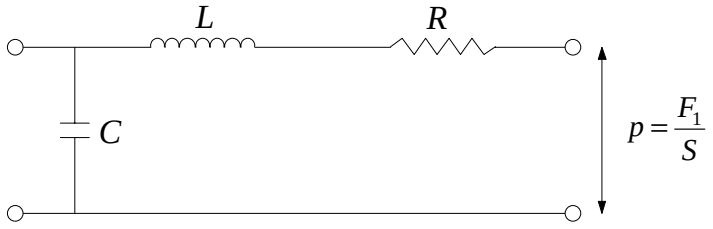


Figure 2.3: Equivalent network of the acoustic Helmholz resonator.

where $v = \partial x/\partial t$ is the velocity of the neck air mass. The *acoustic* impedance is

$$Z(\omega) = \frac{p(\omega)}{u(\omega)} = \frac{F(\omega)\, S^{-1}}{v\, S} = \frac{Z_{mech}(\omega)}{S^2}. \tag{2.23}$$

Often it is convenient to use the analogy between electrical circuits and acoustic systems. In the case of the Helmholz resonator, we can derive an equivalent network (see figure 2.3), and write the acoustic impedance in terms of the components of this network:

$$Z(\omega) = j\omega L + R + \frac{1}{j\omega C}, \tag{2.24}$$

where $L = \rho l/S$ is the *acoustic inertance*, $R = R_{mech}/S^2$ is the *acoustic resistance*. and $C = V/(\rho c^2)$ is the *acoustic compliance*.

In application to modelling wind instrument bores, both the distributed modelling and the lumped element approach are useful. The dimensions of wind instrument air columns are usually such that the main bore is well represented by a distributed model, whereas small acoustical devices such as toneholes and mouthpieces may be modelled as lumped elements.

## 2.2 Wave Propagation in Non-Flaring Bores

There are two elemental bore shapes that appear in musical wind instruments: cylindrical bores and conical bores. For such "non-flaring" bore shapes, the solution of the wave equation can be split up into different modes of propagation. For cylindrical bores, the wave equation can be solved analytically in a cylindrical coordinate system. A one-dimensional solution exists in the form of longitudal propagation of plane wavefronts, and is usually referred to as the *plane wave mode*. Because the higher modes in cylindrical pipes are evanescent at low frequencies, the plane wave mode is the "primary" mode of the system. For conical bores, such a one-dimensional solution also exists, in the form of propagation of spherical wavefronts. For both elemental bore shapes, the "primary mode" represents

wave propagation in which all the gas particles in the wavefront move with the same speed and phase, and with the wavefront perpendicular to the walls of the bore. More complex motion in cylindrical and conical ducts involves some form of transverse flow, and requires contributions from higher propagation modes.

The analytical solution of wave motion in bores with varying cross-section is generally much more complicated. The main reason for this is that in the cylindrical and spherical coordinate system, the wave equation can be solved in separated coordinates. This means that the different modes remain distinct at all times, i.e., there is no *conversion* of acoustical energy between the modes. Such a coordinate system does not usually exist in horns with varying cross-section. Non-separability of the horn wave equation means that mode-conversion is inevitable, i.e. all acoustic wave motion is composed of a mixture of higher modes [25].

A one-dimensional formulation of wave propagation in *flaring* horns exists in the form of *Webster's equation* [164]. For wave propagation governed by this equation, the propagation constant depends on a parameter called the *horn function*. We may formulate a certain class of flaring horns for which the horn function is constant. Such horns are similar to cylindrical and conical bores in the sense that they have uniform propagation characteristics. In other words, they act as waveguides in which the waves smoothly propagate from one end to the other without back-scattering. If we assume that the wavefronts that propagate inside the horn are planar, then the profile of such a horn can be described with a simple mathematical formula, and the family of horns of this type is sometimes referred as *Salmon horns*, after [117, 118]. Unfortunately, the assumption of plane waves in a flaring horn is not very convincing from a physical point of view, since the wavefront tends to "bulge" as it travels through the horn. Assuming spherical waves is more realistic, but in that case the condition of uniform propagation characteristics does not lead to a simple mathematical formulation of the horn radius as a function of axial distance [25]. More important to the scope of the present study is that, even in the case of uniform propagation characteristics, Webster's equation does not allow for a simple time-domain implementation, mainly because propagation in a flared horn is strongly frequency-dependent, and would require powerful and computationally expensive digital approximation techniques. The present study is mainly concerned with efficient discrete-time modelling, therefore we limit ourselves in this section to modelling non-flaring bore sections. However, we may approximate the acoustic behaviour of moderately flaring bores with the use of piecewise modelling techniques.

### 2.2.1 Cylindrical Bores

First the hypothetical case of wave motion in an infinitely long cylindrical pipe is discussed. This means no reflections appear in the $x$-direction, and the solutions are conveniently somewhat simplified. The wave motion in a cylindrical bore can be divided into *axial* motion ($x$), *transverse radial* motion ($a$), and *transverse concentric* motion ($\phi$). In these cylindrical polar coordinates $(a, \phi, x)$, the wave equation is [52]:

$$\frac{1}{a}\frac{\partial}{\partial a}\left(a\frac{\partial p}{\partial a}\right) + \frac{1}{a^2}\frac{\partial^2 p}{\partial \phi^2} + \frac{\partial^2 p}{\partial x^2} = \frac{1}{c^2}\frac{\partial^2 p}{\partial t^2}. \tag{2.25}$$

Assuming that the tube walls are perfectly rigid, the radial pressure gradient should vanish at the wall ($a = a_0$):

$$\left(\frac{\partial p}{\partial a}\right)_{a=a_0} = 0. \tag{2.26}$$

Equation (2.25) can be separated into three differential equations corresponding to the motion along each coordinate-axis, and has solutions of the form [52, 119]:

$$p_{mn}(a, \phi, x) = p_0\, e^{(-jm\phi)} \cdot J_m\left(\frac{\alpha_{mn} a}{a_0}\right) \cdot e^{j(-k_{mn}x + \omega t)}, \tag{2.27}$$

where $J_m$ is a Bessel function and $\alpha_{mn}$ is defined by the boundary condition (2.26) such that the derivative $J_m'(\alpha_{mn})$ is zero. Equation (2.27) expresses pressure wave solutions for each mode $(m, n)$, having $m$ nodal diameter lines and $n$ nodal circular lines, so the first mode $(0, 0)$ is the plane wave mode. For each mode $(m, n)$, the axial motion at frequency $\omega$ takes the form:

$$p(x, t) = Ce^{-j(k_{mn}x + \omega t)}, \tag{2.28}$$

where $C$ is a constant defined by the first two terms of the product in (2.27), and the cylindrical wave number $k_{mn}$ is defined by:

$$k_{mn} = \sqrt{k^2 - \left(\frac{\alpha_{mn}}{a_0}\right)^2}, \tag{2.29}$$

where $k = \omega/c$ is the free space wave number. In order for a mode to propagate at a certain frequency, its wave number should be real. It can be seen from (2.29) that this is only the case if the term $\left[k^2 - (\alpha_{mn}/a_0)^2\right]$ is positive. For the plane wave mode $(0, 0)$ this is true at all frequencies, so this mode propagates unconditionally. For each secondary mode, a certain critical frequency $\omega_c$ exists above which the wave number becomes imaginary. Frequencies below this *cut-off* frequency decay over distance, in other words the mode is *evanescent* for $\omega < \omega_c$. As can be seen from (2.29), the cut-off frequency for mode $(m, n)$

is defined as:

$$\omega_c = \frac{\alpha_{mn} c}{a_0}. \tag{2.30}$$

The cut-off frequencies of the first two transversal modes $(1,0)$ and $(2,0)$ are $\omega_c = 1.84c/a_0$ and $\omega_c = 3.05c/a_0$, and for the first non-planar axial mode $(0,1)$ we have $\omega_c = 3.83c/a_0$. The radius of a cylindrical bore typically found in musical instruments roughly varies between 3mm and 10mm. For example, the cylindrical part of a clarinet bore typically has a radius of about 7.5mm. Assuming a wave velocity $c = 343.0m/s$, the cut-off frequencies of the $(1,0)$, $(2,0)$ and $(0,1)$ mode of the clarinet bore are 13.5kHz, 22.2kHz and 27.9Hz, respectively. Although propagation of these higher modes is in principle possible at frequencies above their cut-off values, there is usually no appreciable excitation of the higher modes in musical instrument bores. This is due to the fact that high frequencies are usually strongly damped. Most wind instrument bores are either terminated by an open end or a bell with an open end, both functioning as a lowpass reflection filter for the waves that propagate towards the bell. Further lowpass filtering occurs due to viscothermal losses. Therefore there is no significant build-up of standing waves at frequencies above the cut-off frequencies of the higher modes. Taking into account this simplification, we may disregard the influence of the higher modes, and reduce the wave equation (2.25) to:

$$\frac{\partial^2 p}{\partial x^2} = \frac{1}{c^2}\frac{\partial^2 p}{\partial t^2}. \tag{2.31}$$

The pressure wave solution for frequency $\omega$, written as a function of place $x$ and time $t$ is:

$$\begin{aligned} p(x,t) &= p^+(x,t) + p^-(x,t) \\ &= Ae^{j(\omega t - kx)} + Be^{j(\omega t + kx)}, \end{aligned} \tag{2.32}$$

where $A$ and $B$ represent the amplitudes of the forward- and backward-travelling pressure waves, respectively, at the bore entry ($x = 0$) at time $t = 0$. The particle velocity solution can be found using the linear force equation (2.12). For tubular acoustic wave motion, it is usually more convenient to compute in terms of *volume velocity* $u = S \cdot v$ rather than particle velocity $v$, where $S = \pi a_0^2$ represents the pipe area. The solution for volume velocity waves is:

$$\begin{aligned} u(x,t) &= u^+(x,t) + u^-(x,t) \\ &= A\left(\frac{S}{\rho c}\right)e^{j(\omega t - kx)} - B\left(\frac{S}{\rho c}\right)e^{j(\omega t + kx)}. \end{aligned} \tag{2.33}$$

In the case of wave propagation in forward-direction only (i.e., $p^-(x,t) = 0$), the acoustic impedance at any point $x$ in the pipe is:

$$Z_0 = \frac{p^+(x,t)}{u^+(x,t)} = \frac{\rho c}{S}. \tag{2.34}$$

This "one-way" acoustic impedance $Z_0$ in a bore is usually referred to as the *characteristic impedance*. Note that for propagation in backward-direction, we have:

$$Z_0 = -\frac{p^-(x,t)}{u^-(x,t)}. \tag{2.35}$$

So far, the discussion has been limited to pipes of infinite length. More insight can be established by assuming a pipe-length $L$ and a termination load $Z_L(\omega)$. The termination load defines the relation between pressure and volume velocity at the far end ($x = L$):

$$Z_L(\omega) = \frac{p(L,t)}{u(L,t)} = Z_0 \left[\frac{p^+(L,t) + p^-(L,t)}{p^+(L,t) - p^-(L,t)}\right]. \tag{2.36}$$

The termination load is directly related to the reflectance of forward-travelling waves at the end of the cylindrical bore. A reflectance is expressed as the fraction of the incident wave that is reflected. Given a termination load $Z_L(\omega)$ and a characteristic impedance $Z_0$, the end-reflectance is formulated:

$$R_L(\omega) = \frac{p^-(L,t)}{p^+(L,t)} = \frac{Z_L(\omega) - Z_0}{Z_L(\omega) + Z_0}. \tag{2.37}$$

In general it is also very useful to know the ratio of pressure waves at the bore entry ($x = 0$). Evaluating (2.32) at the bore entry and bore end gives:

$$p^+(0,t) = \left[e^{+jkL}\right] p^+(L,t), \tag{2.38a}$$

$$p^-(0,t) = \left[e^{-jkL}\right] p^-(L,t). \tag{2.38b}$$

Using (2.37), the reflectance at the entry yields:

$$R_f(\omega) = \frac{p^-(0,t)}{p^+(0,t)} = e^{-2jkL} \cdot R_L(\omega). \tag{2.39}$$

The exponential term in (2.39) simply represents the round-trip of the pressure wave through the pipe. The impedance at the bore entry is usually referred to as the *input impedance*, and is found by combining (2.32), (2.33), (2.34) and (2.39):

$$Z_{in}(\omega) = \frac{p(0,t)}{u(0,t)} = Z_0 \left[\frac{1 + R_f(\omega)}{1 - R_f(\omega)}\right]. \tag{2.40}$$

### 2.2.2 Conical Bores

In spherical coordinates $(\phi, \vartheta, r)$, the wave equation is [98, 119]:

$$\frac{1}{r^2}\frac{\partial}{\partial r}\left(r^2\frac{\partial p}{\partial r}\right) + \frac{1}{x^2 sin\vartheta}\frac{\partial}{\partial \vartheta}\left(sin\vartheta\,\frac{\partial p}{\partial \vartheta}\right) + \frac{1}{r^2 sin^2\vartheta}\frac{\partial^2 p}{\partial \phi^2} = \frac{1}{c^2}\frac{\partial^2 p}{\partial t^2}. \tag{2.41}$$

The boundary condition at the wall ($\vartheta = \vartheta_0$) is that the pressure gradient vanishes:

$$\left(\frac{\partial p}{\partial \vartheta}\right)_{\vartheta=\vartheta_0} = 0. \tag{2.42}$$

The Helmholtz-version of equation (2.41) can be separated into three differential equations corresponding to the motion along each coordinate, and has solutions of the form [119]:

$$p_{mn}(r, \vartheta, \phi) = p_0\, e^{-jm\phi} \cdot \Theta_n^m(cos\vartheta) \cdot \left(\frac{\alpha_{mn} r}{a}\right) \cdot \frac{J_{n+\frac{1}{2}}(kx)}{(kx)^{\frac{1}{2}}}, \tag{2.43}$$

where $\Theta_n^m(cos\vartheta)$ is a Legendre function and $J_{n+\frac{1}{2}}(kx)$ is a Bessel function. The computation of the possible modes and their cut-off frequencies is much more complicated than in the case of cylindrical coordinates. For conical bore segments of dimensions that appear in musical instruments, the cut-off frequencies will generally be lower than for cylindrical segments [119]. However, as was explained earlier for cylindrical bores, excitation of these higher modes will not happen at a significant level in musical instruments. Taking into account only the primary mode, the wave equation (2.25) reduces to:

$$\frac{\partial^2 p}{\partial r^2} + \frac{2}{r}\frac{\partial p}{\partial r} = \frac{1}{c^2}\frac{\partial^2 p}{\partial t^2}, \tag{2.44}$$

with the pressure wave solutions:

$$\begin{aligned} p(r,t) &= p^+(r,t) + p^-(r,t) \\ &= \frac{A}{r}e^{j(\omega t - kr)} + \frac{B}{r}e^{j(\omega t + kr)}, \end{aligned} \tag{2.45}$$

where $A$ and $B$ represent the forward- and backward-travelling pressure waves, respectively, at the bore entry ($x = 0$) at time $t = 0$. The volume velocity waves are found by rewriting (2.12) for spherical coordinates:

$$\frac{\rho}{S}\frac{\partial u}{\partial t} = -\frac{\partial p}{\partial r}. \tag{2.46}$$

Now substituting (2.45) and integrating with respect to $t$ yields the volume velocity wave solution:

$$\begin{aligned} u(r,t) &= u^+(r,t) + u^-(r,t) \\ &= \left[1 + \frac{1}{jkr}\right] \frac{A}{r}\left(\frac{S}{\rho c}\right) e^{j(\omega t - kr)} - \left[1 - \frac{1}{jkr}\right] \frac{B}{r}\left(\frac{S}{\rho c}\right) e^{j(\omega t + kr)}. \end{aligned} \quad (2.47)$$

The characteristic impedance in a conical bore depends on frequency, location and travelling direction:

$$Z_0^+(r,\omega) = \frac{p^+(r,t)}{u^+(r,t)} = \left(\frac{\rho c}{S^*}\right)\left(\frac{jkr}{jkr+1}\right), \quad (2.48a)$$

$$Z_0^-(r,\omega) = -\frac{p^-(r,t)}{u^-(r,t)} = \left(\frac{\rho c}{S^*}\right)\left(\frac{jkr}{jkr-1}\right), \quad (2.48b)$$

where $S^*$ is the (spherical) local wave surface and $r$ is the local cone apex distance. For a cone truncated at $r = r_0$, the length taken is that along the cone wall:

$$L^* = r_L - r_0. \quad (2.49)$$

Given a termination load

$$Z_L(\omega) = \frac{p(L^*,t)}{u(L^*,t)} = \frac{p^+(L^*,t) + p^-(L^*,t)}{\frac{p^+(L^*,t)}{Z_0^+(\omega)} - \frac{p^-(L^*,t)}{Z_0^-(\omega)}}, \quad (2.50)$$

the end-reflectance of this truncated cone is:

$$R_L^*(\omega) = \frac{p^-(L^*,t)}{p^+(L^*,t)} = \frac{Z_L(\omega) - Z_0^+(\omega)}{Z_L(\omega) + Z_0^-(\omega)}. \quad (2.51)$$

Evaluation of (2.45) at the bore entry and bore end gives:

$$p^+(r_0,t) = \frac{r_L}{r_0}\left[e^{+jkL^*}\right] p^+(L^*,t), \quad (2.52a)$$

$$p^-(r_0,t) = \frac{r_L}{r_0}\left[e^{-jkL^*}\right] p^-(L^*,t), \quad (2.52b)$$

thus the reflectance at the cone entry is:

$$R_f^*(\omega) = \frac{p^-(r_0,t)}{p^+(r_0,t)} = e^{-2jkL^*} \cdot R_L^*(\omega). \quad (2.53)$$

The exponential term represents the round-trip time of the pressure wave through the cone. The input impedance at the bore entry is found by combining (2.45), (2.47), (2.48)

and (2.53):

$$Z_{in}(\omega) = \frac{p(r_0,t)}{u(r_0,t)} = \left[ \frac{1 + R_f^*(\omega)}{\frac{1}{Z_0^+(r_0,\omega)} - \frac{R_f^*(\omega)}{Z_0^-(r_0,\omega)}} \right]. \tag{2.54}$$

Note that the reflectances $R_L^*(\omega)$ and $R_f^*(\omega)$ have been computed according to spherical coordinates here. In other words, they are *spherical wave* reflectances, which are not equivalent to plane wave reflectances. How to compute the plane wave reflectance of a conical section is discussed in section 2.3.

### 2.2.3 Viscothermal Losses

In the previous sections, it was assumed that all wave propagation is lossless. In reality, wave energy is absorbed from the main mechanical process due to wall vibrations and viscothermal losses near the wall. In musical instruments, the wall vibrations are usually small enough to be neglected [52]. Thermal losses (heat conduction) and viscous drag occur at the boundary layer of a bore, and have a significant damping effect on the propagating waves. The magnitude of these effects depends strongly on the relative thickness of the boundary layers in which they occur. Given a bore radius ($a$), the ratio of the tube radius to the viscous boundary layer is [75]:

$$a_v(\omega) = \left(\frac{\omega\rho}{\eta}\right)^{\frac{1}{2}} a, \tag{2.55}$$

where $\eta$ is the shear viscosity coefficient. A similar ratio can be found for the thermal energy exchange between the wall and the air [75]:

$$a_t(\omega) = \left(\frac{\omega\rho C_p}{\kappa}\right)^{\frac{1}{2}} a, \tag{2.56}$$

with the specific heat constant $C_p$ and thermal conductivity $\kappa$. The next step is to find out how these parameters are related to the exact influence of viscothermal effects on the transmittance of waves. This can be done by rewriting the characteristic impedance $Z_0$ in a complex, frequency-dependent form, and writing the product $jk$ in the term $e^{-jkx}$ as a lossy, complex propagation constant $\Gamma$. Expressions for $Z_0$ and $\Gamma$ for lossy cylindrical ducts were found by Benade [21] and later improved by Keefe [75] in the form of truncated expansions. These expansions are derived in terms of both $a_v$ and $a_t$, but

may be conveniently formulated as a function only $a_v$:

$$Z_0(\omega) = \frac{\rho c}{S}\left[\left(1 + d_1 a_v^{-1} - d_3 a_v^{-3}\right) + j\left(d_1 a_v^{-1} + d_2 a_v^{-2} + d_3 a_v^{-3}\right)\right], \tag{2.57a}$$

$$\Gamma(\omega) = \alpha(\omega) + j\left(\frac{\omega}{v(\omega)}\right) = \left(\frac{\omega}{c}\right)\left[\left(e_1 a_v^{-1} + e_2 a_v^{-2} + e_3 a_v^{-3}\right) + j\left(1 + e_1 a_v^{-1} - e_3 a_v^{-3}\right)\right], \tag{2.57b}$$

where the coefficients $(d_i, e_i)$ depend on the thermodynamic constants[6] $\nu$, $c$, and $\gamma$, where $\nu = a_t/a_v$.

No upper limit is given for the value of $a_v$ by Keefe in [75], but comparisons by Amir et al. [11] between theory and experimental results on acoustic bores of dimensions of the same order as musical instruments have indicated that equations (2.57) are valid for upto at least 6kHz. There are in fact indications that these equations are valid for a larger bandwidth; Sharp [126] has carried out bore reconstructions from experimentally determined impulse response data, in which losses were taken into account using equations (2.57). Using a bandwidth of 25kHz, bore profile reconstructions in which losses were taken into account were shown to be accurate within 0.05 millimeter, whereas reconstructions in which losses were neglected exhibited significant deviations from the direcly measured profile.

Cylindrical Bores

The effect of including viscothermal losses in cylindrical and conical bore models is well observed in the bore transmittance (the filter transfer function for waves travelling from one end to the other). For a cylindrical duct of length $L$, the transmittance is:

$$H_t(\omega) = e^{-\Gamma L}, \tag{2.58}$$

where the product $G = \Gamma L$ fully characterises the transmission losses. In the lossless case $H_t(\omega)$ is the frequency-domain equivalent of a pure delay $t = L/c$. Figure 2.4 shows the magnitude (a) and phase delay[7] (b) of the lossy transmittance for a duct with length $L = 0.4m$ and radius $a = 0.5cm$. The attenuation is relatively small at low frequencies, and increases slowly with frequency. The small dispersion due to viscothermal effects is mainly concentrated in the low-frequency area.

The real and imaginary part of the normalised lossy characteristic impedance $Z_0(\omega) \cdot S/(\rho c)$ of the duct is depicted figure 2.4c and figure 2.4d, respectively. The imaginary component is relatively small in comparison with the real component, and the deviation

[6] See appendix A for the definition of the coefficients $d_i$ and $e_i$.

[7] The phase delay of a response $H(\omega)$ is defined as $-(\angle H(\omega)/\omega)$.

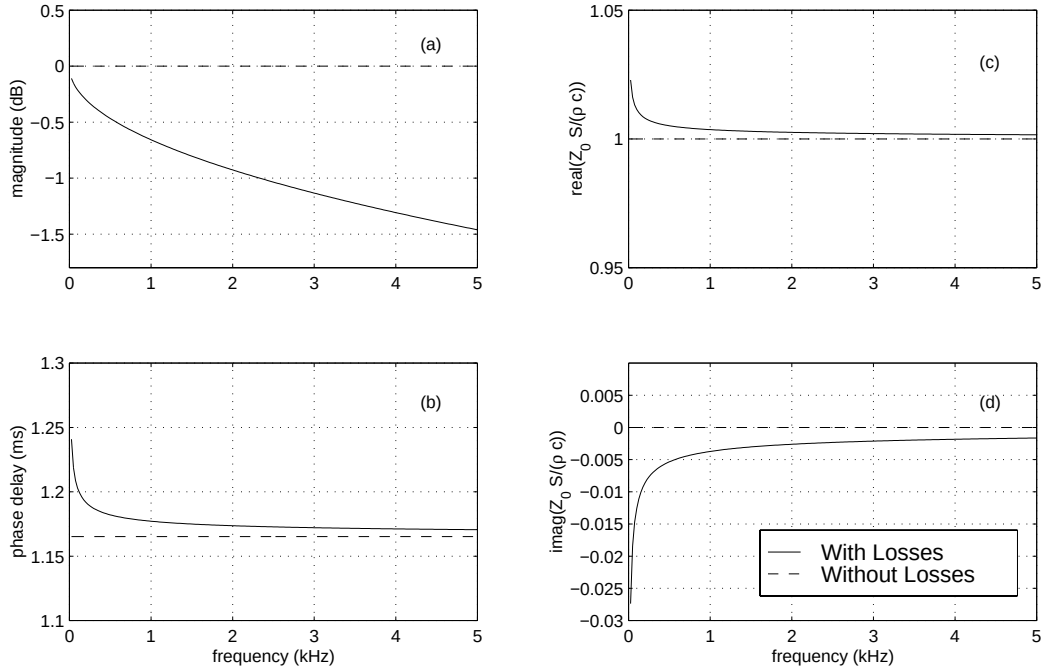


Figure 2.4: Effects of taking into account viscothermal losses in modelling a cylindrical pipe. Left: pipe transmittance magnitude (a) and phase delay (b). Right: real part (c) and imaginary part (d) of the pipe characteristic impedance. The pipe length is $L = 0.4m$ and the radius is $a = 0.5cm$.

of the real component from the lossless impedance $Z_0 = \rho c/S$ is also very small. Hence the frequency-dependence can usually be neglected, and we may simply use $Z_0 = \rho c/S$.

Conical Bores

It can be seen from (2.55) that the main variable in the formulation of viscothermal losses in cylindrical bores is proportional to its radius. For conical bores, the radius varies with the distance, so the calculation of the transmittance is somewhat more complicated. In order to determine analytically the losses in a cone it is convenient to first write the viscous boundary layer ratio $a_v$ as a linear function of the local apex distance $r$:

$$\begin{aligned} a_v(r) &= sin(\theta) \cdot \left[ \frac{2\,(1 - cos\theta)}{sin^2\theta} \cdot \left( \frac{\omega\rho}{\eta} \right) \right]^{\frac{1}{2}} \cdot r \\ &= \left[ 2 \left( \frac{\omega\rho}{\eta} \right) \left( 1 - \frac{L}{L^*} \right) \right]^{\frac{1}{2}} \cdot r. \end{aligned} \tag{2.59}$$

Here $a_v$ is the viscous boundary layer ratio that relates to the effective radius $a^*$ that corresponds to the surface $S = \pi(a^*)^2$ of a spherical wavefront, and $L^*$ is the length along the cone wall (see figure 2.5). The term $2(1-cos\theta)/sin^2\theta$ represents the ratio between the surface area of a spherical wavefront and that of a plane wavefront at equal cross-section

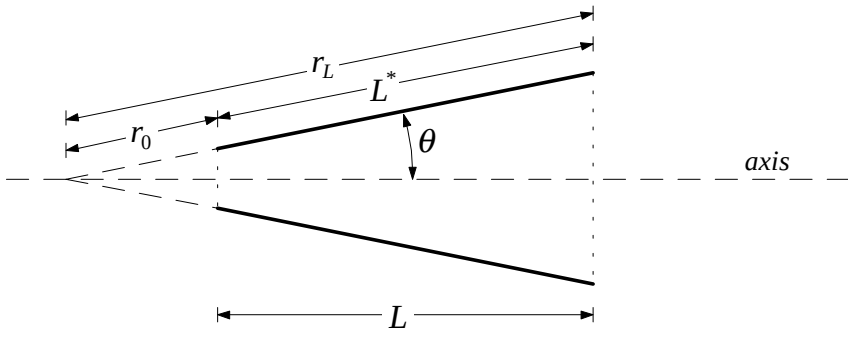


Figure 2.5: A truncated conical bore and its geometrical parameters.

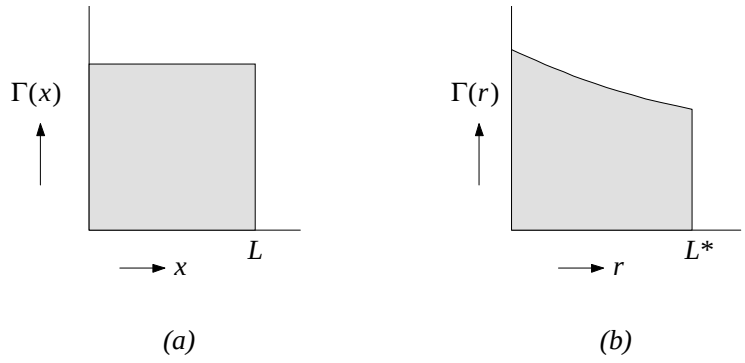


Figure 2.6: Graphical representation of the transmission exponent $G$, for a cylindrical bore section (a) and a conical bore section (b). Given $\Gamma$ as a function of propagation distance, $G$ equals the area under this function between bore entry and bore end. The curve in (b) is purely symbolical.

(See appendix B). For a cylindrical section, the transmission exponent $G$ is computed as the product $\Gamma L$ (see (2.58)). Graphically, $G$ may be interpreted as the area under the function $\Gamma(x)$ in between the values $x = 0$ and $x = L$ (see figure 2.6a). For a conical section, this area (see figure 2.6b) is not simple product, but must be computed as an integrand:

$$G = \int_{r=r_0}^{r_L} \Gamma(r)dr = \left(\frac{\omega}{c}\right) \cdot [I_a + j\,I_p], \tag{2.60}$$

where $I_a$ is the *attenuation integral* and $I_p$ the *phase integral*, for which analytic expressions can be found after substitution of (2.57). The attenuation integral is:

$$\begin{aligned} I_a &= \left(\frac{c}{\omega}\right) \int_{r=r_0}^{r_L} \alpha(r)dr \\ &= \left(\frac{e_1}{c_a}\right) log(r_L/r_0) + \left(\frac{e_2}{c_a^2}\right)(r_0^{-1} - r_L^{-1}) + \left(\frac{e_3}{2c_a^3}\right)(r_0^{-2} - r_L^{-2}), \end{aligned} \tag{2.61}$$

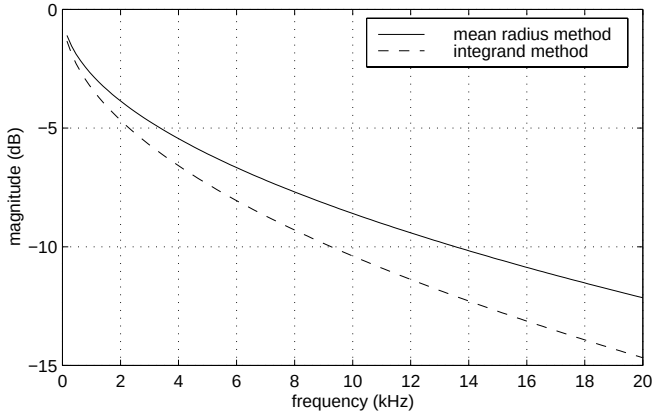


Figure 2.7: Transmission losses in a divergent conical bore section of length $L^* = 2$m, with a bore radius varying from $r_0 = 2$mm to $r_L = 10$mm, computed using the mean-radius method and the integrand method.

and the phase integral is:

$$\begin{aligned} I_p &= c \int_{r=r_0}^{r_L} v^{-1}(r)dr \\ &= (r_0 - r_L) + \left(\frac{e_1}{c_a}\right) log(r_L/r_0) - \left(\frac{e_3}{2c_a^3}\right)(r_0^{-2} - r_L^{-2}), \end{aligned} \tag{2.62}$$

where $log(x)$ denotes the natural logarithhm of $x$. In the field of musical acoustics, the fact that the radius varies with axial distance in a cone is often considered negligible, and usually the losses in a conical section are calculated as for a cylindrical section with identical length and with a radius that equals the mean radius of the cone [52, 25]. For bores of short length and with small conical angle the discrepancy due to this simplification is extremely small, but for longer conical sections, the accuracy is significantly improved when using the integrand method. Figure 2.7 shows the magnitude response of the transmittance of a divergent cone of length $L^* = 2$m. The radii at the small and the large end were taken to be $r_0 = 2$mm and $r_L = 10$mm, respectively. The difference between the "mean-radius method" and the "integrand method" is most apparent at the higher frequencies.

We can also model the long conical section as a piecewise series of short conical sections, using the mean radius method for each section. It was found that if one keeps increasing the number of sections, the solution converges towards the result obtained using the integrand formulation. This verifies the correctness of the integrand method.

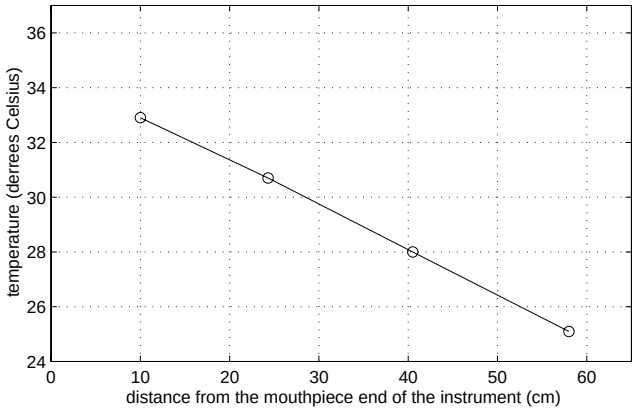


Figure 2.8: Temperature profile measured in a cornetto under playing conditions.

### 2.2.4 Thermal Gradients

Viscothermal effects in wave propagation are dependent on temperature. So far it has been assumed that the temperature is constant throughout a tubular system. However, under playing conditions the higher temperature of the player's mouth and heat conduction in the boundary layers result in a temperature profile along the length of the air column. To investigate the effect of such a *thermal gradient* on the acoustics of a brass instruments, van Walstijn et al. [155] measured the spatial variation of temperature inside a cornetto under playing conditions, using thermocouples. It was found that the temperature inside the air column of the cornetto varies linearly with distance from the mouthpiece end of the instrument (see figure 2.8). This temperature profile was then reproduced during input impedance measurements[8] by applying voltages to heating tapes wrapped around the instrument. For comparison, measurements were also carried out on a "cold" instrument and on an instrument uniformly heated to the mean value of the temperature profile. In figure 2.9a the measured impedance curve for an unheated cornetto filled with air at room temperature (16$^o$C) is compared with the measured impedance curve for the same cornetto with temperature gradient. The amplitudes of all resonances differ substantially here, as well as the positions of the higher frequency resonance peaks. On the other hand, the input impedance curve of the uniformly heated (29$^o$C) hardly differs from the curve of the cornetto with thermal gradient (see figure 2.9b). These results imply that the cornetto air column with a thermal gradient is accurately represented by a model with uniform temperature equal to the average of the temperature profile. In other words, it may be assumed that the presence of a thermal gradient has no significant influence on the acoustics of the instrument. In the scope of this study, this assumption will be considered to hold for all brass and woodwind instruments.

[8] See appendix J for a short description of the acoustic measurement techniques used in this study.

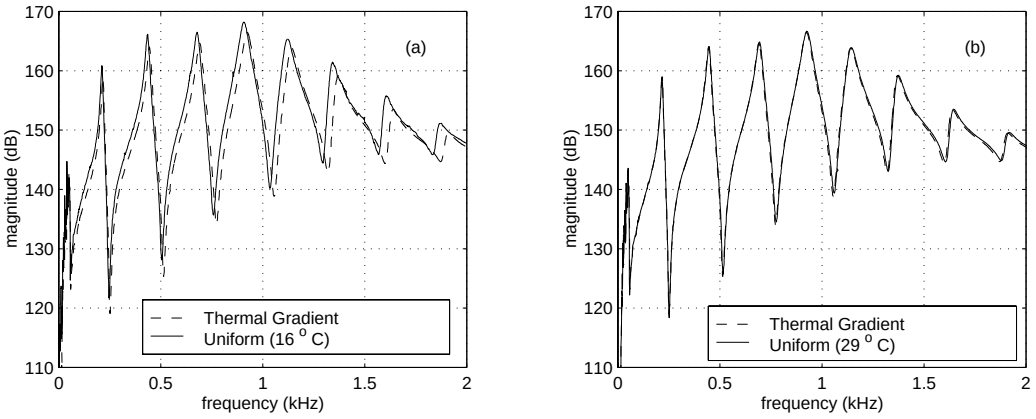


Figure 2.9: Influence of a thermal gradient. Left: measured input impedance of a cornetto with uniform temperature (16°C) and with thermal gradient (25°C to 33°C). Right: measured input impedance of a cornetto with uniform mean temperature (29°C) and with thermal gradient (25°C to 33°C).

### 2.2.5 Open-End Reflectance

Most brass and reed woodwind instrument air columns are open-ended. The transition from inside the air column to free space corresponds to a change in characteristic impedance for the travelling waves. At high frequencies, the acoustic wavelength is small compared to the bore diameter, which means that the radiation impedance is approximately equal to the characteristic impedance. At these frequencies, the waves travel easily through the "acoustic barrier" imposed by the small change of impedance. At lower frequencies, the change from small tubular dimensions to free space is more significant, since the acoustic wavelength is relatively large in comparison with the bore diameter. This results in a radiation resistance ($\mathcal{R}$) and radiation reactance ($\mathcal{X}$), which represent dissipation and dispersion of the travelling waves, respectively. Kinsler et al. [84] give a low-frequency approximation of the radiation impedance of an unflanged cylindrical pipe:

$$\begin{aligned} Z_L &= \mathcal{R} + j\mathcal{X} \\ &= Z_0 \left[ \frac{1}{4} (ka)^2 + j0.6ka \right], \end{aligned} \tag{2.63}$$

where $k$ is the free-space wave number and $a$ the pipe radius. Levine and Schwinger [88] developed a more accurate approximation of the radiation impedance for unflanged ends, in which mode-coupling at the open-end discontinuity is taken into account. Due to the high mathematical complexity of this formulation, a curve fitting procedure is often applied to their results in order to obtain a more manageable representation. Caussé et al. applied such a procedure in [35] at frequencies corresponding to $ka < 3.5$. Later, Scavone [119] applied similar methods to obtain an open-end reflectance approximation

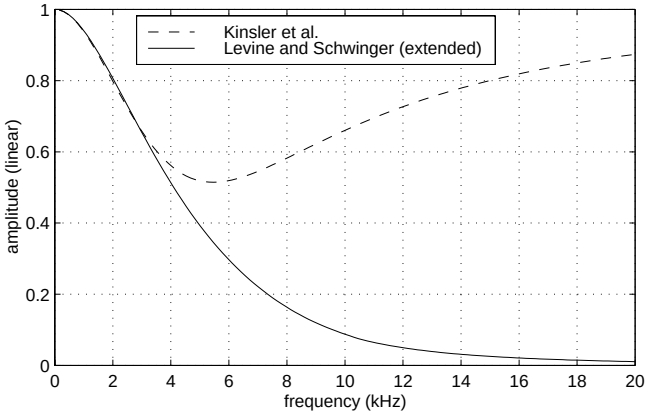


Figure 2.10: Open end reflectance magnitude response of a cylindrical pipe with radius $a = 2cm$.

for a much wider frequency range ($ka < 20$). This method enables application to high sampling-frequency sound synthesis. In figure 2.10 the low-frequency approximation via equation (2.63) is compared to Scavone's extension of Levine and Schwinger's results.

The open-end radiation models described above were computed for open-ended cylindrical ducts. Computing the radiation impedance of open-ended acoustic cones is even more complex. An accurate impedance load can be obtained by considering the effects of mode-coupling at the open-end discontinuity. This approach has been taken by Zorumski [169], who formulated the radiation load for each individual mode in the case of an open-ended waveguide with infinite flange. If mode-coupling effects are small, then the radiation load of an open-ended cone approximates to that of an open-ended cylinder. Causse et al. [35] suggest that the transmission equations are similar for cones and cylinders and that therefore the main difference lies in the larger wavefront surface for spherical coordinates. Scaling the cylindrical open-end model by the spherical/plane wavefront surface ratio then gives an expression for the conical open-end radiation impedance $Z_L^*$:

$$Z_L^*(\omega) = Z_L(\omega)\frac{S}{S^*}, \tag{2.64}$$

where $Z_L(\omega)$ is the cylindrical open-end radiation impedance, and $S$ and $S^*$ represent the plane and spherical wavefront areas at the open-end discontinuity, respectively.

## 2.3 Piecewise Modelling

As indicated in the introduction of section 2.2, no exact analytic solutions can be found for the general case of bores with varying cross-section. However, approximate solutions can be found via spatial discretisation of the horn into a piecewise series of short elemental sections. A general name for this approach is *piecewise modelling*. This approach has

previously been applied using cylindrical sections [107, 76, 10], conical sections [35, 76, 27, 10], and exponential sections [9, 27], where in all cases a single propagation mode was modelled. Berners [27] has recently carried out an extensive study on one-dimensional scattering methods, including those methods that are based on Webster's equation. As far as the author knows, methods based on spatial discretisation which take into account the higher order modes have only been applied using cylindrical sections (see, e.g., [7, 105, 8]). It can be argued that it is unnecessary to consider more complex shaped sections, because bending and bulging of the wavefront can already be represented within the (multi-modal) piecewise cylindrical model. Although the influence of higher modes is of interest in the scope of the present study, the computational methodologies involved in multi-modal decomposition are beyond it. Hence we will limit ourselves to using the results obtained with the multi-modal approach as a reference with which we can compare the results obtained with the one-dimensional formulations.

### 2.3.1 Transmission-Line Models

A common objective in the field of wind instrument acoustics is to predict the input impedance at the mouthpiece end of the air column. The classical method of piecewise modelling is to start with a known radiation impedance $Z_L(\omega)$ at the open end, and approximate the tubular profile with a series of cylindrical sections, that are considered to function as lossy *transmission-lines* [107]. The input impedance at the mouthpiece end is then obtained by successively computing the impedance relations between the individual sections using the formula:

$$Z_{in,n} = Z_{0,n} \frac{Z_{out,n} + Z_{0,n}\, tanh\,(\Gamma L_n)}{Z_{0,n} + Z_{out,n}\, tanh\,(\Gamma L_n)}, \tag{2.65}$$

where $Z_{in,n}$, $Z_{out,n}$, $Z_{0,n}$ and $L_n$ are the input impedance, output impedance, characteristic impedance and length of the $n$th section, respectively.

Keefe [76] gives a transfer-matrix formulation of the transmission-line model using piecewise cylindrical and conical sections. For frequency $\omega$, the transmission-line matrix relates the output pressure $p_2$ and volume flow $u_2$ to the input pressure $p_1$ and volume flow $u_1$:

$$\begin{bmatrix} p_1 \\ u_1 \end{bmatrix} = \begin{bmatrix} A & B \\ C & D \end{bmatrix} \begin{bmatrix} p_2 \\ u_2 \end{bmatrix}, \tag{2.66}$$

where $A$, $B$, $C$ and $D$ are complex-valued. The values of these transmission-line matrix elements for an individual cylindrical or conical section are given in section 2.3.2. Let $\mathbf{S_n}$ denote such an $ABCD$-matrix for the $n$th section, then the $ABCD$-matrix that describes

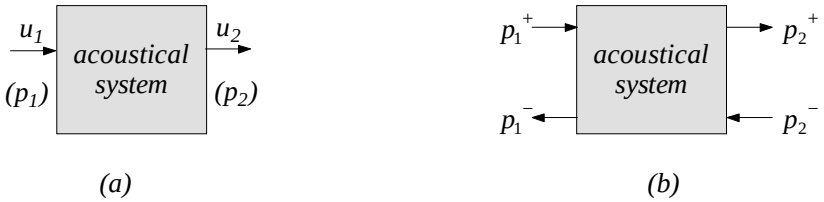


Figure 2.11: Two-port representations of an acoustic system, for acoustic pressure and volume velocity (a), and propagating pressure waves (b).

the total piecewise model is computed as the cascade of the individual sections:

$$\begin{bmatrix} A & B \\ C & D \end{bmatrix} = \mathbf{S_1} \cdot \mathbf{S_2} \cdot \ldots \cdot \mathbf{S_n} \cdot \ldots \cdot \mathbf{S_{N-1}} \cdot \mathbf{S_N}. \tag{2.67}$$

The input impedance is computed as follows: given a load impedance $Z_L(\omega) = p_2/u_2$, the input impedance $Z_{in}(\omega) = p_1/u_1$, according to the matrix relation in (2.66) is:

$$Z_{in}(\omega) = \frac{AZ_L(\omega) + B}{CZ_L(\omega) + D}. \tag{2.68}$$

Let $Z_0 = \rho c/S_0$ be the characteristic impedance at the entry of the first section, then the plane wave reflectance is obtained via (2.40):

$$R_f(\omega) = \frac{Z_{in}(\omega) - Z_0}{Z_{in}(\omega) + Z_0}. \tag{2.69}$$

### 2.3.2 Scattering Models

The $ABCD$-matrix is a two-port representation of an acoustical system, and is formulated in terms of pressure and volume flow (see figure 2.11a). Alternatively, the same system may be described in terms of travelling waves, in this case pressure waves (see figure 2.11b). Such a model is often referred to as a *scattering model*. The relation between the pressure waves on the left and the pressure waves on the right of the system can be expressed by the following matrix equation:

$$\begin{bmatrix} p_1^+ \\ p_1^- \end{bmatrix} = \begin{bmatrix} E & F \\ G & H \end{bmatrix} \begin{bmatrix} p_2^+ \\ p_2^- \end{bmatrix}, \tag{2.70}$$

where $E$, $F$, $G$ and $H$ are complex-valued and frequency-dependent. Matrices of this type appear to have been applied originally in the field of micro-wave technology, where they are sometimes referred to as *wave-amplitude transmission matrices* (see, e.g., [37]). In

acoustic applications, they have been referred to as *chain-scattering matrices* [130] and *waveguide matrices* [156, 119]. In this study we will use the latter term, or alternatively use the term "*EFGH*-matrices". As in the case with *ABCD*-matrices, *EFGH*-matrices can be cascaded, although some restrictions have to be made concerning the choice of coordinate system. For example, the wave equation for conical bores is based on a spherical coordinate system, and the characteristic impedance is defined in a different way than for the cylindrical coordinate system. This results in different definitions of the acoustic variables $(p^+, p^-)$, so that multiplying the corresponding *EFGH*-matrices is in this case not straight-forward. In order to obtain uniformity of waveguide matrices, they are defined here *according to cylindrical coordinates*. Non-cylindrical bore sections are then defined such that the input-variables $(p_1^+, p_1^-)$ and output-variables $(p_2^+, p_2^-)$ are defined according to cylindrical coordinates:

$$p = p^+ + p^-, \tag{2.71a}$$

$$u = \frac{p^+ - p^-}{Z_0}, \tag{2.71b}$$

where $Z_0 = \rho c/S$ is the characteristic impedance associated with the local cross-section $S$. Furthermore, we note that in order to compute a cascade of two waveguide matrices via matrix multiplication:

$$\begin{bmatrix} E & F \\ G & H \end{bmatrix} = \begin{bmatrix} E_1 & F_1 \\ G_1 & H_1 \end{bmatrix} \cdot \begin{bmatrix} E_2 & F_2 \\ G_2 & H_2 \end{bmatrix}, \tag{2.72}$$

the characteristic impedance $Z_1$ at the output-end of the acoustic system represented by the first matrix must be equal to the characteristic impedance $Z_2$ at the input-end of the acoustic system represented by the second matrix. If this condition is not fulfilled, then an additional "impedance matching matrix" is required:

$$\begin{bmatrix} E & F \\ G & H \end{bmatrix} = \begin{bmatrix} E_1 & F_1 \\ G_1 & H_1 \end{bmatrix} \cdot \begin{bmatrix} E_{im} & F_{im} \\ G_{im} & H_{im} \end{bmatrix} \cdot \begin{bmatrix} E_2 & F_2 \\ G_2 & H_2 \end{bmatrix}, \tag{2.73}$$

with

$$\begin{bmatrix} E_{im} & F_{im} \\ G_{im} & H_{im} \end{bmatrix} = \begin{bmatrix} 1 + Z_1/Z_2 & 1 - Z_1/Z_2 \\ 1 - Z_1/Z_2 & 1 + Z_1/Z_2 \end{bmatrix}. \tag{2.74}$$

*EFGH*-matrices are directly related to *ABCD*-matrices: suppose that the *ABCD*-matrix for a certain acoustic system is known, then the corresponding *EFGH*-matrix can be found by applying a simple matrix transformation. The formulae for this transformation and the inverse transformation are given in appendix D. As in the case of *ABCD*-matrices, *EFGH*-matrices can be used to compute the input impedance or reflectance of an acousti-

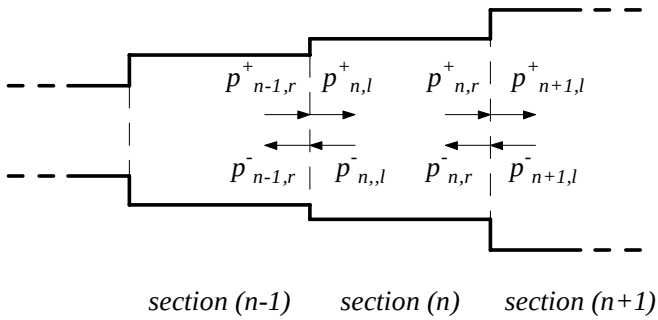


Figure 2.12: Piecewise cylindrical section model. The subscript $l$ or $r$ indicates a wave on the left or right side of the bore section.

cal system. Given a load impedance $Z_L(\omega)$, the end reflectance $R_L(\omega)$ is computed using (2.37). The plane wave reflectance is found by substituting the end reflectance equation $p_2^- = R_L(\omega) \cdot p_2^+$ into (2.70), and solving for $p_1^-/p_1^+$:

$$R_f(\omega) = \frac{p_1^-}{p_1^+} = \frac{G + HR_L(\omega)}{E + FR_L(\omega)}. \tag{2.75}$$

The input impedance can then be computed using (2.40).

### 2.3.3 Cylindrical Sections

Consider the piecewise cylindrical system in figure 2.12. As seen in section 2.2.1, the propagation of waves in section $n$ of length $L_n$ may be formulated as:

$$p_{n,l}^+ = \left[e^{+\Gamma L_n}\right] p_{n,r}^+, \tag{2.76a}$$

$$p_{n,l}^- = \left[e^{-\Gamma L_n}\right] p_{n,r}^-. \tag{2.76b}$$

In matrix formulation, (2.76) becomes:

$$\begin{bmatrix} p_{n,l}^+ \\ p_{n,l}^- \end{bmatrix} = \begin{bmatrix} e^{+\Gamma L_n} & 0 \\ 0 & e^{-\Gamma L_n} \end{bmatrix} \begin{bmatrix} p_{n,r}^+ \\ p_{n,r}^- \end{bmatrix} = \mathbf{P_n} \cdot \begin{bmatrix} p_{n,r}^+ \\ p_{n,r}^- \end{bmatrix}. \tag{2.77}$$

where $\mathbf{P}_n$ is the *propagation matrix* of the $n$th section. The conditions at the boundary of the junction between sections $n$ and $n-1$ are that the pressure is continuous and that the net flow is zero:

$$p_{n-1,r} = p_{n,l}, \tag{2.78a}$$

$$u_{n-1,r} = u_{n,l}. \tag{2.78b}$$

Substituting the travelling-wave decomposition (2.71) gives:

$$p^+_{n-1,r} + p^-_{n-1,r} = p^+_{n,l} + p^-_{n,l}, \tag{2.79a}$$

$$\frac{p^+_{n-1,r} - p^-_{n-1,r}}{Z_{0,n-1}} = \frac{p^+_{n,l} - p^-_{n,l}}{Z_{0,n}}. \tag{2.79b}$$

Solving for $p^+_{n-1,r}$ and $p^-_{n-1,r}$ yields the matrix equation:

$$\begin{bmatrix} p^+_{n-1,r} \\ p^-_{n-1,r} \end{bmatrix} = \frac{1}{2} \begin{bmatrix} 1 + \frac{Z_{0,n-1}}{Z_{0,n}} & 1 - \frac{Z_{0,n-1}}{Z_{0,n}} \\ 1 - \frac{Z_{0,n-1}}{Z_{0,n}} & 1 + \frac{Z_{0,n-1}}{Z_{0,n}} \end{bmatrix} \begin{bmatrix} p^+_{n,l} \\ p^-_{n,l} \end{bmatrix} = \mathbf{J_{n-1,n}} \begin{bmatrix} p^+_{n,l} \\ p^-_{n,l} \end{bmatrix}. \tag{2.80}$$

The final *EFGH*-matrix that describes the total piecewise model using is computed as the following cascade:

$$\begin{bmatrix} E & F \\ G & H \end{bmatrix} = \mathbf{P}_1 \cdot \mathbf{J}_{1,2} \cdot \mathbf{P}_2 \ldots \cdot \mathbf{J}_{n-1,n} \cdot \mathbf{P}_n \ldots \cdot \mathbf{J}_{N-2,N-1} \cdot \mathbf{P}_{N-1} \cdot \mathbf{J}_{N-1,N} \cdot \mathbf{P}_N. \tag{2.81}$$

The elements of the *ABCD*-matrix for a single cylindrical section of length $L$ and characteristic impedance $Z_0$ can be found by applying the *EFGH* to *ABCD* matrix transformation formulae (appendix D) to (2.77):

$$A = \frac{1}{2}\left[e^{+\Gamma L} + e^{-\Gamma L}\right] = cosh\left(\Gamma L\right), \tag{2.82a}$$

$$B = \frac{Z_0}{2}\left[e^{+\Gamma L} - e^{-\Gamma L}\right] = Z_0 sinh\left(\Gamma L\right), \tag{2.82b}$$

$$C = \frac{1}{2Z_0}\left[e^{+\Gamma L} - e^{-\Gamma L}\right] = \frac{1}{Z_0} sinh\left(\Gamma L\right), \tag{2.82c}$$

$$D = \frac{Z_0}{2Z_0}\left[e^{+\Gamma L} + e^{-\Gamma L}\right] = cosh\left(\Gamma L\right). \tag{2.82d}$$

This result is equivalent to the general *ABCD*-matrix for cylindrical sections found in the literature [76, 24, 119].

### 2.3.4 Conical Sections

For conical sections, the derivation of the propagation and junction scattering equations is somewhat more complicated, since the associated wave equation is derived assuming a spherical coordinate system. The difference in coordinate system results in two problems. Firstly, in the case of coupling two conical sections of different aperture angle (see figure 2.13), wave propagation in these sections is formulated within two different (spherical) coordinate systems. When a wavefront travels through such a conical junction, it has to make a sudden "jump" in order to fit into the coordinate system of the next conical

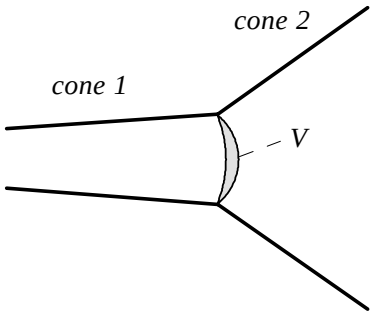


Figure 2.13: Junction of two conical sections.

section, which is physically not possible. This problem is clearly related to the fact that the bulging of the wavefront in bores with varying cross-section requires contributions of higher transversal modes, which are not present in the one-dimensional wave equation. Amir et al. [10] address this problem by assuming pressure and volume velocity continuity in the "missing volume" $V$ (see figure 2.13), and by taking into account the difference in wavefront area across the volume. In the present study, we follow this approach. However, we note that Berners [27] has offered a variety of alternative ways of addressing the "missing volume" problem, as well as addressing the related "doubly defined volume" problem that accurs when modelling a junction in which the taper decreases.

The second problem is how to compute the plane wave reflectance from a piecewise conical model. Consider the arbitrary acoustical system depicted in figure 2.14. Suppose that this system can be represented with an *EFGH*-matrix, which, by definition, relates plane input-waves to plane output-waves. The key observation is that if we want to compute the plane wave reflectance using (2.75), then the variables on *both* sides of the system should be defined according to the "cylindrical" travelling wave decomposition (2.71). In other words, an *EFGH*-matrix may be formulated for a non-cylindrical system, by ensuring that the input- and output-waves are plane waves. Figure 2.15 illustrates this concept for a single conical section. The cone input/output relations can be defined

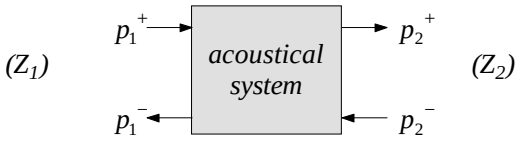


Figure 2.14: Two-port acoustical system, with travelling wave variables defined according to cylindrical coordinates. $Z_1$ and $Z_2$ represent the characteristic impedances on the left and right side of the system.

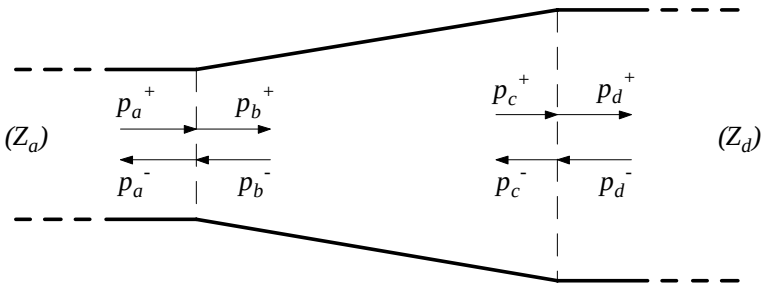


Figure 2.15: A single conical section, connected on both ends with cylindrical tubing of matching cross-section.

in a cylindrical coordinate system if the cone is coupled on both sides to a cylindrical section. The *EFGH*-matrix for a single conical section can be formulated by deriving the cone propagation equations and the scattering equations for both cylindrical-conical junctions. The propagation equations for conical bores are given by equations (2.45). The propagation equation for the cone in figure 2.15 is expressed:

$$\begin{bmatrix} p_b^+ \\ p_b^- \end{bmatrix} = \begin{bmatrix} \frac{r_c}{r_b} e^{+\Gamma L^*} & 0 \\ 0 & \frac{r_c}{r_b} e^{-\Gamma L^*} \end{bmatrix} \begin{bmatrix} p_c^+ \\ p_c^- \end{bmatrix} = \mathbf{P} \cdot \begin{bmatrix} p_c^+ \\ p_c^- \end{bmatrix}. \tag{2.83}$$

The conditions at the left junction boundary in figure 2.15 are:

$$p_a^+ + p_a^- = p_b^+ + p_b^-, \tag{2.84a}$$

$$\frac{p_a^+ - p_a^-}{Z_a} = \frac{p_b^+}{Z_b^+} - \frac{p_b^-}{Z_b^-}, \tag{2.84b}$$

where $Z_a$ is the characteristic impedance of the cylindrical bore and $Z_b^+$ and $Z_b^-$ are the characteristic impedances at the left end of the cone in positive and negative travelling direction, respectively. Solving for $p_a^+$ and $p_a^-$ gives:

$$\begin{bmatrix} p_a^+ \\ p_a^- \end{bmatrix} = \frac{1}{2} \begin{bmatrix} 1 + \frac{Z_a}{Z_b^+} & 1 - \frac{Z_a}{Z_b^-} \\ 1 - \frac{Z_a}{Z_b^+} & 1 + \frac{Z_a}{Z_b^-} \end{bmatrix} \begin{bmatrix} p_b^+ \\ p_b^- \end{bmatrix} = \mathbf{J}_l \cdot \begin{bmatrix} p_b^+ \\ p_b^- \end{bmatrix}. \tag{2.85}$$

The equations for the cylindrical-conical junction on the right side can be derived in a similar way, which yields:

$$\begin{bmatrix} p_c^+ \\ p_c^- \end{bmatrix} = \begin{bmatrix} \frac{Z_d + Z_c^-}{Z_c^+ + Z_c^-} \frac{Z_c^+}{Z_d} & \frac{Z_d - Z_c^-}{Z_c^+ + Z_c^-} \frac{Z_c^+}{Z_d} \\ \frac{Z_d - Z_c^+}{Z_c^- + Z_c^+} \frac{Z_c^-}{Z_d} & \frac{Z_d + Z_c^+}{Z_c^- + Z_c^+} \frac{Z_c^-}{Z_d} \end{bmatrix} \begin{bmatrix} p_d^+ \\ p_d^- \end{bmatrix} = \mathbf{J}_r \cdot \begin{bmatrix} p_d^+ \\ p_d^- \end{bmatrix}. \tag{2.86}$$

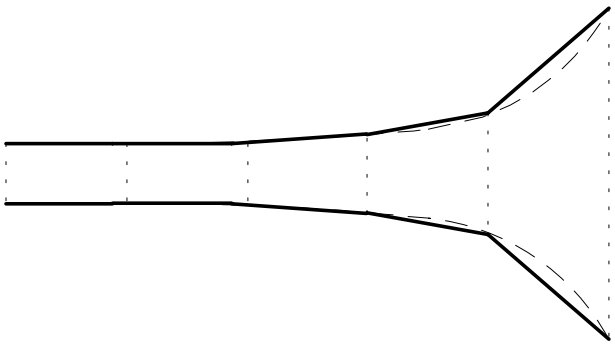

Figure 2.16: Piecewise conical model of a smoothly varying cross-section. The profile of the piecewise approximation exhibits no diameter discontinuities, only taper discontinuities.

The *EFGH*-matrix for a single conical section is then computed as the product:

$$\begin{bmatrix} E & F \\ G & H \end{bmatrix} = \mathbf{S} = \mathbf{J}_l \cdot \mathbf{P} \cdot \mathbf{J}_r. \tag{2.87}$$

In piecewise conical modelling of horns with smoothly varying cross-section, the section geometries are usually chosen such that only taper discontinuities result [10] (see figure 2.16). Within this approach, the wavefront area discontinuities at the conical junctions are neglected, so that no impedance matching junctions between individual sections are required. In that case the complete piecewise conical model is computed by a straightforward cascade of the section matrices:

$$\begin{bmatrix} E & B \\ C & D \end{bmatrix} = \mathbf{S}_1 \cdot \mathbf{S}_2 \ldots \cdot \mathbf{S}_n \ldots \cdot \mathbf{S}_{N-1} \cdot \mathbf{S}_N, \tag{2.88}$$

where $\mathbf{S}_n$ represents the $n$th the conical section. The *EFGH*-matrix (2.87) has input/output variables defined according to cylindrical coordinates, so the formulae for transformation to an *ABCD*-matrix as given in appendix D may be used. This is most easily done by treating each section-matrix in the decomposed form. In fact, the propagation-matrix $\mathbf{P}$ may be further decomposed into:

$$\mathbf{P} = \begin{bmatrix} e^{+\Gamma L} & 0 \\ 0 & e^{-\Gamma L} \end{bmatrix} \begin{bmatrix} \frac{r_c}{r_b} & 0 \\ 0 & \frac{r_c}{r_b} \end{bmatrix}. \tag{2.89}$$

The junction matrices are somewhat simplified if we neglect the difference between spherical and planar wavefront areas[9] (i.e., $Z_a = Z_b$ and $Z_c = Z_d$), so that the *EFGH*-matrix

[9] Figure B.4 in appendix B shows that this difference is very small for small conical angles.

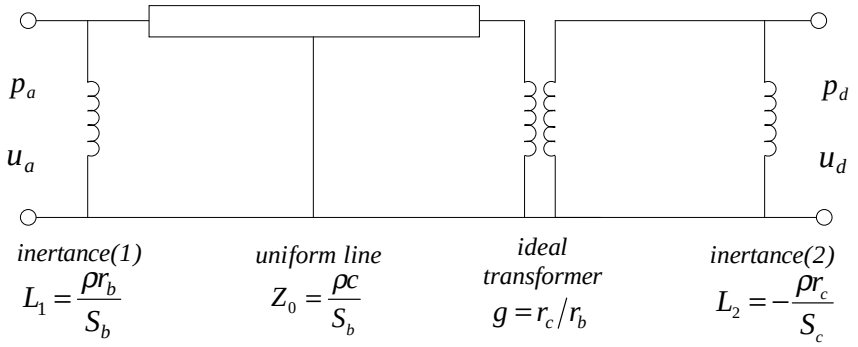


Figure 2.17: Equivalent circuit of a conical bore section (after Benade [24]).

product for a single conical section can be written:

$$\begin{bmatrix} E & F \\ G & H \end{bmatrix} = \begin{bmatrix} 1+\frac{1}{2\Gamma r_b} & \frac{1}{2\Gamma r_b} \\ -\frac{1}{2\Gamma r_b} & 1-\frac{1}{2\Gamma r_b} \end{bmatrix} \begin{bmatrix} e^{+\Gamma L} & 0 \\ 0 & e^{-\Gamma L} \end{bmatrix} \begin{bmatrix} \frac{r_c}{r_b} & 0 \\ 0 & \frac{r_c}{r_b} \end{bmatrix} \begin{bmatrix} 1-\frac{1}{2\Gamma r_c} & -\frac{1}{2\Gamma r_c} \\ \frac{1}{2\Gamma r_c} & 1+\frac{1}{2\Gamma r_c} \end{bmatrix}. \tag{2.90}$$

Applying the transformation to transmission-line matrices to each separate matrix in (2.90) yields:

$$\begin{bmatrix} A & B \\ C & D \end{bmatrix} = \begin{bmatrix} 1 & 0 \\ \frac{1}{Z_a \Gamma r_b} & 1 \end{bmatrix} \begin{bmatrix} cosh\,(\Gamma L) & Z_b sinh\,(\Gamma L) \\ Z_b^{-1} sinh\,(\Gamma L) & cosh\,(\Gamma L) \end{bmatrix} \begin{bmatrix} \frac{r_c}{r_b} & 0 \\ 0 & \frac{r_b}{r_c} \end{bmatrix} \begin{bmatrix} 1 & 0 \\ \frac{1}{-Z_d \Gamma r_c} & 1 \end{bmatrix}. \tag{2.91}$$

This formulation as a product of four individual matrix elements corresponds to the equivalent circuit of a conical waveguide [24], as depicted in figure 2.17. The impedances of the "conicity inertances" $L_1$ and $L_2$ associated with the left and right junctions are:

$$Z_1 = j\omega L_1 = Z_a \Gamma r_b, \tag{2.92a}$$

$$Z_2 = j\omega L_2 = -Z_d \Gamma r_c. \tag{2.92b}$$

These impedances correspond to the $ABCD$-matrices that represent the conicity inertances in (2.91). Computing the product in (2.91) yields the elements of the $ABCD$-matrix:

$$A = \left(\frac{r_c}{r_b}\right) cosh\,(\Gamma L) - \left(\frac{1}{\Gamma r_b}\right) sinh\,(\Gamma L)\,, \tag{2.93a}$$

$$B = \left(\frac{r_b}{r_c}\right) Z_0\, sinh\,(\Gamma L)\,, \tag{2.93b}$$

$$C = \left(\frac{1}{Z_0}\right) \left\{ \left[\frac{r_c}{r_b} - \left(\frac{1}{\Gamma r_b}\right)^2\right] sinh\,(\Gamma L) + \frac{L}{\Gamma r_b^2} cosh\,(\Gamma L) \right\}, \tag{2.93c}$$

$$D = \left(\frac{r_b}{r_c}\right) \left[cosh\,(\Gamma L) + \left(\frac{1}{\Gamma r_b}\right) sinh\,(\Gamma L)\right], \tag{2.93d}$$

where $Z_0 = Z_a = Z_b$ is the characteristic impedance at the bore entry. The expressions for the $ABCD$-elements in (2.93) are in agreement with the values found in the literature [24, 76]. The $ABCD$-matrix product computed without the assumption ($Z_a = Z_b$ and $Z_c = Z_d$), is given in [119].

The fact that a single conical section can be represented by a simple equivalent network has an interesting consequence. Namely, each of the four parts of the network may be re-interpreted as a two-port network, for which the travelling wave decomposition may be carried out as if the waves on either side of the two-port are plane waves. Hence we may consider the cone as a cylindrical waveguide with three additional lumped elements. Benade already indicated this property in [24]:

> *"the conical waveguide may be represented by a combination of impedance elements that belong to the cylindrical guide and its derived lumped-constant circuit elements."*

Thus, although the waves inside the conical sections must from a physical point of view be regarded as spherical waves, they may be treated as plane waves within a mathematically equivalent model.

### 2.3.5 Piecewise Model Comparison

In order to study the accuracy and convergence of piecewise modelling methods, the plane wave power reflectances of two types of horns were computed, and the results were compared with the results obtained via multi-modal decomposition, as described in [105, 8, 80]. The multi-modal method used in the present study employs a piecewise cylindrical framework (this method is referred to as the "Discrete Segment (DS) method" in [105]), taking into account a finite set of non-planar axial modes. Results predicted with multi-modal decomposition generally compare well with results obtained using the more general but computationally considerably more expensive finite difference model [105]. One of the main conclusions in [8] is that adding only a few modes can be very effective in improving the accuracy.

In the DS model, propagation and scattering are modelled with equations that are simlar to those for the one-dimensional piecewise cylindrical model, but where each acoustic variable is represented with a vector. For example, pressure is denoted with the vector $\mathbf{P}$, where the element $\mathbf{P}_n$ is the pressure component of the $n$th axially symmetric mode; $n = 0$ indicates the plane-wave mode. Within this notation, the acoustic impedance (which relates pressure to volume velocity) takes on a matrix-form, thus we may write:

$$\mathbf{P} = \mathbf{Z}\mathbf{U}, \tag{2.94}$$

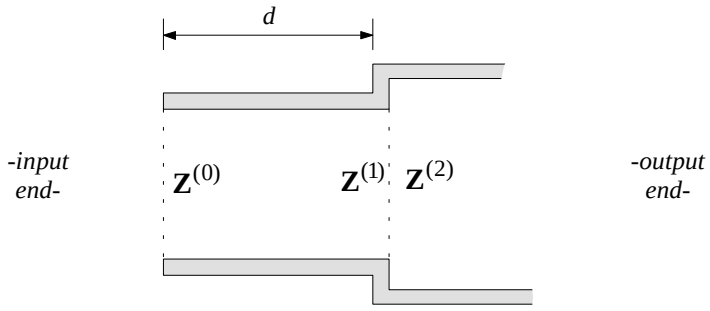


Figure 2.18: Cylindrical junction with associated multi-modal impedance matrices.

where $\mathbf{U}$ is the volume velocity vector and $\mathbf{Z}$ is the impedance matrix. Note that the corner-element $\mathbf{Z}_{00}$ represents the "plane-wave impedance". We may also derive a reflectance matrix:

$$\mathbf{R} = (\mathbf{Z}_c^{-1}\mathbf{Z} - \mathbf{I})^{-1} \cdot (\mathbf{Z}_c^{-1}\mathbf{Z} + \mathbf{I}), \tag{2.95}$$

where $\mathbf{Z}_c$ is the characteristic impedance, which is a diagonal matrix. Again, the corner-element $\mathbf{R}_{00}$ represents the plane-wave component, and this component is used for comparison with the one-dimensional scattering methods. Instead of following the exact DS method outlined in [105], we will present the propagation and scattering equations in the form as presented in [79, 80]. Let $\mathbf{Z}^{(0)}$ denote the impedance at the input-end of a cylindrical section, and $\mathbf{Z}^{(1)}$ the impedance at the output-end (see figure 2.18), then the propagation through the cylindrical section is formulated:

$$\mathbf{Z}^{(0)} = (\mathbf{Z}^{(1)} - j\mathbf{D}_3\mathbf{Z}_c)(j\mathbf{D}_3\mathbf{Z}_c^{-1}\mathbf{Z}^{(1)} + \mathbf{I})^{-1}, \tag{2.96}$$

where $\mathbf{I}$ is the identity matrix and $\mathbf{D}_3$ is a diagonal matrix for which the $n$th diagonal is given by $tan(k_n d)$, where $k_n$ is the wave number of the $n$th mode, and $d$ is the length of the cylindrical section. As explained in section 2.2.1, the $n$th mode only propagates at frequencies for which $k_n$ is real. Scattering at a junction of two cylindrical sections is implemented with

$$\mathbf{Z}^{(1)} = \mathbf{F}\mathbf{Z}^{(2)}\mathbf{F}^t, \tag{2.97}$$

where $\mathbf{Z}^{(1)}$ is the impedance at the input-end of the junction, $\mathbf{Z}^{(2)}$ is the impedance at the output-end of the junction, and $\mathbf{F}$ is a non-diagonal matrix that is derived using the condition of continuous pressure and volume velocity at the junction boundary. We refer to references [105, 79, 80] for the derivation of these equations. In our computations with the DS method[10], we included 11 modes (i.e., the plane wave mode plus the first ten

[10] A *MATLAB*© implementation of the DS model by Jonathan Kemp was used for computing the reference power reflectance.

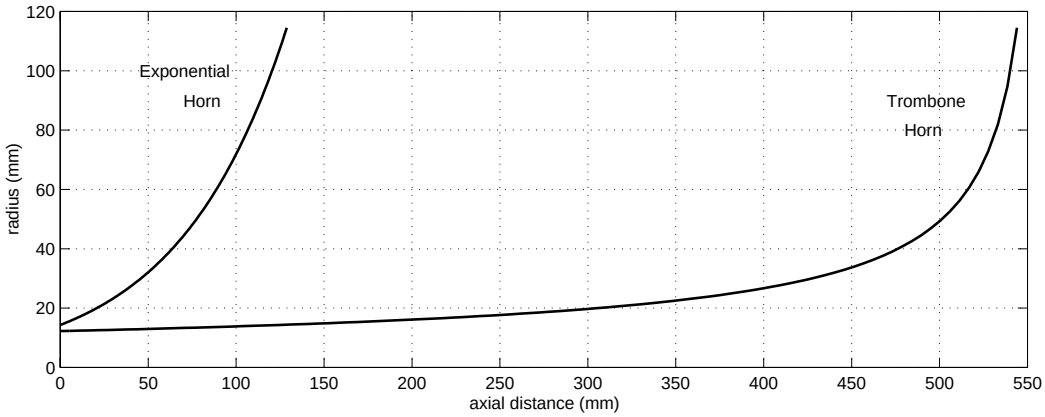


Figure 2.19: The radius as a function of axial distance of the exponential horn and the trombone bell horn.

non-planar axial modes).

The power reflectance is calculated for the dimensions of the two horns depicted in figure 2.19. In both examples, we assume that the horn is terminated by an anechoic duct of matching cross-section. Given a plane wave reflectance $R_f(\omega)$, the power reflectance is

$$R_p(\omega) = |R_f(\omega)|^2 \,. \tag{2.98}$$

Conveniently, the power reflectance represents an entire class of horns of the same proportions if plotted against normalised frequency $f/f_c$, where $f_c = (3.84c)/(2\pi a)$ is the cut-off frequency of the first non-planar axial mode. Since we assume plane wave excitation of the horn, transverse modes are not excited, thus $f_c$ is the lowest cut-off of the system, and any deviation from plane wave propagation for frequencies below $f_c$ must be due to mode coupling. In both examples, the radius of the terminating duct is 114.5mm, which corresponds to a cut-off frequency $f_c = 1831$Hz.

Naturally, the accuracy of the computation depends on the spatial resolution (i.e., the number of piecewise sections $N$). In order to get insight into how quickly the piecewise cylindrical and piecewise conical models converge, the computations were carried out a number of times, each time using an increased number of sections. For each computed power reflectance $R_p(\omega)$, an "error" was determined as the average of the summed absolute differences with the power reflectance $R_p^{'}(\omega)$ obtained using the multi-modal method with 100 sections:

$$\varepsilon = \frac{1}{M} \sum_{m=1}^{M} \left| R_p^{'}(m\Delta\omega) - R_p(m\Delta\omega) \right| , \tag{2.99}$$

where each power reflectance is evaluated for a set of $M$ equally spaced frequencies ($\Delta\omega$ is the frequency step).

The Exponential Horn

The flare of the exponential horn is not very strong, so we may expect that one-dimensional piecewise models perform reasonable well in this case. Figure 2.20a illustrates the convergence of the one-dimensional piecewise models. The piecewise cylindrical model converges quite rapidly, though clearly not towards a zero error. As could be expected, using conical sections results in a smaller error. Perhaps somewhat surprising though is that increasing the number of sections does not appear to reduce the error in this case: the minimum error is in fact found for $N = 6$. Figure 2.20b shows the power reflectances obtained when $N = 100$. Apparently, the piecewise conical model forms a reasonable approximation for this particular horn, whereas the piecewise cylindrical model clearly overestimates the effective cut-off of the horn.

The Trombone Bell

The same piecewise modelling and multi-modal decomposition computations were carried out for the trombone horn. The profile of this horn was measured at a number of positions along the horn axis[11] by Amir et al. [8]. Following their approach, we computed intermediate points using third-order polynomial interpolation. The piecewise modelling convergence for this horn is depicted in figure 2.21a. As with the exponential horn, the error does not converge to a minimum when using the piecewise conical model. Furthermore, it appears that using conical sections in this case does not give a significantly improved result in comparison with using cylindrical sections. (see Figure 2.21b). Apparently, the trombone bell is not modelled particularly accurately with either of the one-dimensional piecewise models. Because the trombone bell is characterised by a rapid flare at the end, a high level of mode coupling occurs at this point, which explains why the piecewise cylindrical model performs poorly in this case. On the other hand, the piecewise conical model should to some extent approximate the effect of mode coupling, because each conical junction models the frequency-dependent scattering that occurs when the wavefront "bulges" as the angle of conicity increases. However, the model is based on the assumption that the wavefront takes on a spherical shape at all points along the horn: this assumption typically breaks down at points where the horn exhibits a rapid flare. Another problem occurs whenever the gradient of the horn profile is steep at the boundary, such as with the trombone horn. Due to the large angle of conicity at this point, there is a big "mismatch" in predicted wavefronts, which results in a large "doubly defined volume" (see figure 2.22). As in the case of the "missing volume" discussed in section 2.3.4, we address this problem by assuming that the pressure and volume velocity are equal at the boundaries. This "mismatched volume problem" also explains why increasing the number of sections does

[11] The radius versus axial distance data is given in table I in [8].

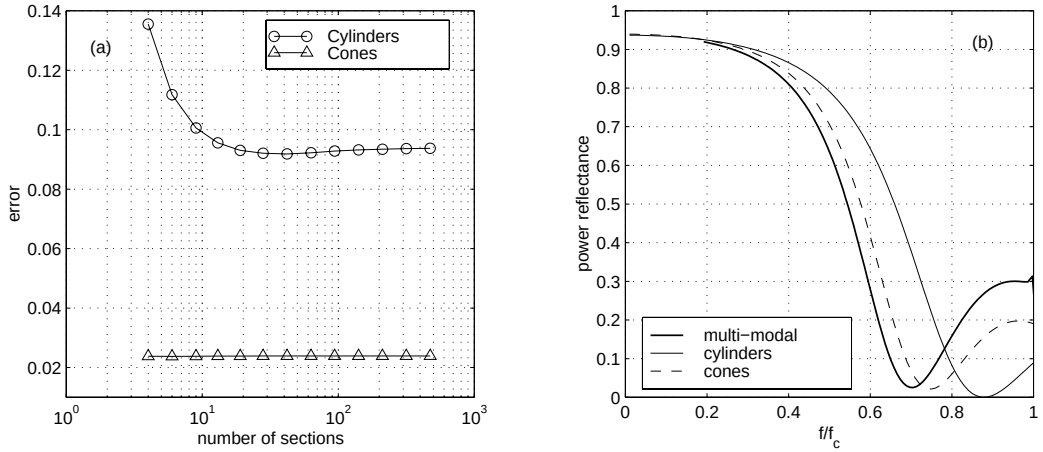


Figure 2.20: Piecewise modelling of the exponential horn. Left: piecewise modelling error as a function of the number of sections. Right: reflected power.

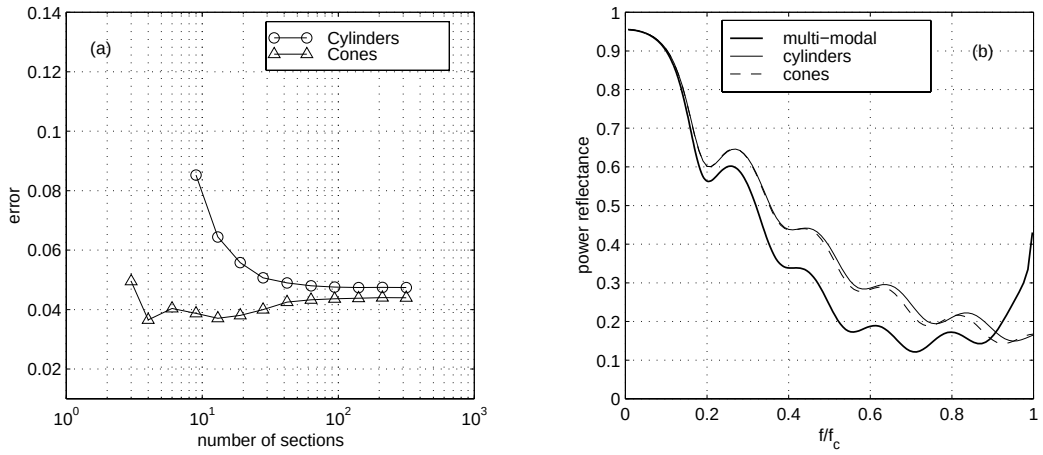


Figure 2.21: Piecewise modelling of the trombone bell. Left: piecewise modelling error as a function of number of sections. Right: reflected power.

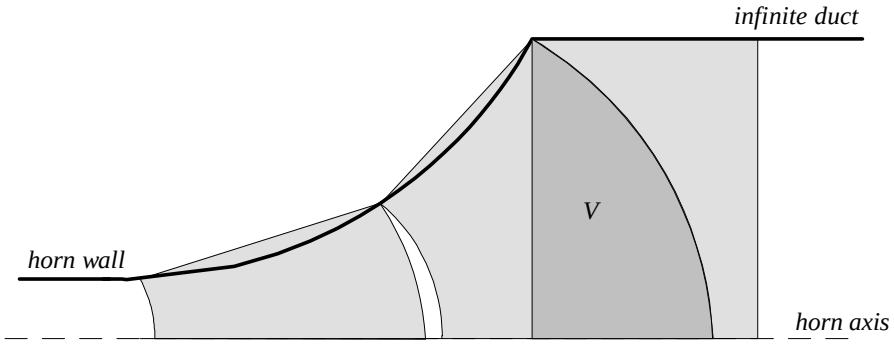


Figure 2.22: Piecewise conical modelling of a horn that is terminated by an infinite duct. The volume $V$ is doubly defined.

not improve the accuracy of the piecewise conical model: shortening the section at the end corresponds to increasing the mismatch at the junction with the infinite duct. One might be able to reduce the error due to the volume mismatch problem (that in fact occurs at each junction) by defining a "scattering region" in which the wavefront shape smoothly evolves from one spherical shape to another when travelling through the junction. This approach was taken by Berners [27], who has shown that the scattering region may be modelled with a short flaring section in which wave propagation is governed by Webster's equation, which is equivalent to the Schrödinger equation for one-dimensional scattering, as used in quantum mechanics; within the analogy between acoustics and quantum mechanics, a parabolic flare may in fact corresponds to a "square acoustic potential barrier". However, given the relatively high computational load of a time-domain implementation of such a junction model, this approach is not further investigated in the present study.

## 2.4 Conclusions

In this chapter we have discussed linearised models of tubular resonators. In section 2.1, the basic principles of acoustic wave motion were briefly reviewed. Of particular interest to the present study are (1) the concept of the linearised wave equation (on which we will base efficient discrete-time formulations of wave propagation in elemental bore shapes) and (2) the concept of lumped acoustic elements (on which we will base efficient discrete-time models of small acoustic units). In section 2.2, one-dimensional formulations of wave propagation in cylindrical and conical bore sections were reviewed. In addition, we have discussed how these formulations can be adapted when boundary effects (such as viscothermal losses and open-end radiation) are taken into account. Finally in section 2.3, one-dimensional modelling of acoustical waveguides with varying cross-section by means of piecewise modelling techniques was discussed. Piecewise modelling with cylindrical

and conical sections has been investigated by means of waveguide matrices, which are closely related to the more conventional transmission-line matrices. We have seen that in the case of modelling a horn with moderate flare, the piecewise conical model forms a reasonable approximation to the multi-modal solution. For the case of the strongly flared trombone bell, increasing the number of conical sections does not improve the accuracy, which is mainly due to the large wavefront area mismatch at the boundary. The piecewise cylindrical model performs poorly for both cases.

# Chapter 3

# Discrete-Time Modelling

A physical model of a wind instrument simulates sustained excitation of the resonances of the instrument air column. Hence a physical model generally consists of a *driving mechanism* (that represents the reed or lip excitation) and a *resonator* (that represents the air column vibrations), and simulates the interaction between them (see figure 3.1). Due to the non-linear character of the driving mechanism, physical models are usually computed in the time-domain. For time-domain simulation on a digital computer system, *discrete-time* modelling techniques are required. Discrete-time modelling of the driving mechanism is usually done by numerically solving a set of non-linear equations that relate pressure to flow at the mouthpiece end of the air column.

In this chapter, techniques for discrete-time modelling of the resonator are discussed. As in chapter 2, we assume linear behaviour, which facilitates the computations in two ways. Firstly, we may move freely between frequency-domain and time-domain, and secondly, the resonator is fully characterised by its time-domain response.

The most elementary approach for modelling the resonator is by means of convolution with the air column impulse response, which is discussed in section 3.1. The next two sections are introductions to the two major discrete-time modelling techniques employed in this study. In section 3.2, the basic concepts of *digital waveguide modelling techniques* are explained, and in section 3.3, *wave digital filter techniques* are discussed. These are closely related techniques, which can easily be applied in combination. The combined

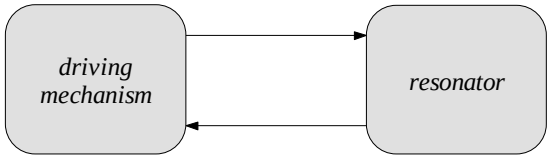


Figure 3.1: Modelling the interaction between the driving mechanism and the resonator.

| **Impulse Response** | **Description** | **Fourier Transform** |
|---|---|---|
| Green's function $g(t)$ | *pressure* response to a *volume flow* input impulse, with *echoic* input-end. | impedance $Z(\omega) = P/U$ |
| reflection function $r(t)$ | *pressure wave* response to a *pressure wave* input impulse, with *anechoic* input-end. | reflectance $R(\omega) = P^-/P^+$ |

Table 3.1: Definition of impulse response types.

approach (referred to here as "wave digital modelling") is outlined in section 3.4, and forms the fundamental modelling framework for various subsequent chapters.

A general feature of discrete-time modelling is that the model variables are computed only at discrete-time instants $t = nT$, where $n$ is integer, $T = 1/f_s$ is the *sample period* and $f_s$ is the *sample rate*. For example, the variable $x(t)$ is represented in the discrete time-domain as:

$$x(t) \equiv x(nT) \tag{3.1}$$

For convenience, the sample period $T$ is usually suppressed in the notation, thus $x(n)$ denotes the variable $x$ at time $t = nT$.

## 3.1 Convolution Methods

In this section, modelling of the resonator using *convolution* is discussed. Convolution means computation of the system response to a certain input signal by means of filtering with the system *impulse response*. The impulse response of an acoustic system can be defined in more than one way. The two main types of impulse responses and their Fourier transforms are defined in table 3.1. Green's function is computed using an echoic input-end, which means that a wave travelling towards the entry is fully reflected at the entry (without change of sign), i.e. the reflectance at the entry is 1 at all frequencies. On the other hand, the reflection function is computed using an anechoic input-end, i.e. the reflectance at the entry is zero at all frequencies. The reflectance $R(\omega)$ is sometimes called the "reflection coefficient". This naming is based on the idea that in the frequency-domain, filtering corresponds to multiplication. However, the use of the term "coefficient" suggests that $R(\omega)$ is a constant, whereas it really is a function of frequency. Therefore we simply refer to $R(\omega)$ as the "reflectance". In this study, the input impedance at the entry is denoted with $Z_{in}(\omega)$, and the reflectance at the entry is denoted with $R_f(\omega)$. The inverse Fourier transforms are denoted with $g_{in}(t)$ and $r_f(t)$, respectively[1].

[1] In the present study, variables are generally denoted with lower case in the time-domain and the corresponding upper case in the frequency-domain. However, in the case of impedance, the lower case $z$ is

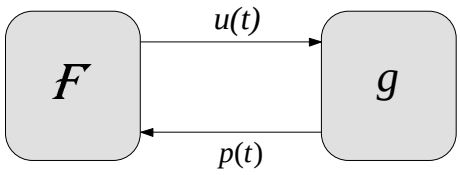


Figure 3.2: Feedback structure of a physical model using Green's function.

### 3.1.1 Using Green's Function

Assuming linear wave propagation in the bore, the resonator is fully characterised by its input impedance $Z_{in}(\omega)$ [22, 52]:

$$P(\omega) = Z_{in}(\omega) \cdot U(\omega). \tag{3.2}$$

Multiplication in the frequency-domain corresponds to convolution in the time-domain, so the time-domain equation is written:

$$p(t) = \int_{-\infty}^{+\infty} g_{in}(\tau) \cdot u(t-\tau) d\tau = g_{in}(t) * u(t), \tag{3.3}$$

where $p(t)$ and $u(t)$ are the inverse Fourier transforms of $P(\omega)$ and $U(\omega)$, respectively, and where the operator "$*$" denotes convolution. Green's function is by definition a causal response ($g_{in}(t)$ is zero for $t < 0$), thus (3.3) can be simplified to:

$$p(t) = \int_{0}^{\infty} g_{in}(\tau) \cdot u(t-\tau) d\tau = g_{in}(t) * u(t). \tag{3.4}$$

For simplicity, we define the other part of the physical model (the driving mechanism) as a non-linear mapping[2] $\mathcal{F}$:

$$u(t) = \mathcal{F}\{p(t)\}. \tag{3.5}$$

Equations (3.4) and (3.5) form the most basic possible feedback structure for physical modelling of a wind instrument. From inspection of the signal flow graph (figure 3.2) it becomes obvious that this structure forms an *incomputable loop*: $p$ has to be known at time $t$ in order to compute $u$ at time $t$ via (3.5), and similarly, $u$ has to be known at time

already reserved for denoting the $z$-transform variable. Hence we denote the inverse Fourier transform of $Z(\omega)$ with $g(t)$.

[2] In wind instrument modelling, the driving mechanism is usually not represented with such a simple instantaneous mapping (see, for example, chapter 10). However, this is not relevant to the discussion on how to model the resonator: the methods for modelling the resonator are also applicable when the excitation model is more complex.

$t$ to compute $p(t)$ through (3.4). Schumacher [124] addresses this problem by rewriting Green's function as:

$$g_{in}(t) = Z_0\,\delta(t) + \hat{g}_{in}(t), \tag{3.6}$$

where $Z_0$ is the characteristic impedance at the bore entry, $\delta(t)$ is the Dirac delta-function and $\hat{g}_{in}(t)$ is the "residual" or "remainder" Green's function:

$$\hat{g}_{in}(t) = \begin{cases} 0, & t = 0 \\ g_{in}(t), & t > 0 \end{cases}. \tag{3.7}$$

The equation for modelling the resonator (3.4) can now be written:

$$p(t) = Z_0 u(t) + \int_0^\infty \hat{g}_{in}(\tau) \cdot u(t-\tau)d\tau = Z_0 u(t) + \hat{g}_{in}(t) * u(t). \tag{3.8}$$

The discrete-time version of (3.8) is obtained by sampling $\hat{g}_{in}(t)$, $p(t)$ and $u(t)$ at time instants $t = nT$ for $n = 1, 2, 3 \ldots$, and replacing convolution with *discrete* convolution:

$$p(n) = Z_0 u(n) + \sum_{m=0}^{N} (\hat{g}_{in}(m) \cdot u(n-m)) = Z_0 u(n) + \hat{g}_{in}(n) * u(n). \tag{3.9}$$

In this discrete representation, the convolution length $N$ is finite, and the remainder Green's function $\hat{g}_{in}(n)$ is effectively truncated at $n = N$. Therefore $N$ should be taken such that $\hat{g}_{in}(n)$ has decayed towards zero before $t = NT$. Since it is known that $\hat{g}_{in}(0) = 0$ and that $\hat{g}_{in}((N+1)T)$ is effectively zero, (3.9) can be rewritten:

$$\begin{aligned} p(n) &= Z_0 u(n) + \sum_{m=1}^{N+1} [\hat{g}_{in}(m) \cdot u(n-m)] \\ &= Z_0 u(n) + \sum_{m=0}^{N} [\hat{g}_{in}(m+1) \cdot u(n-m-1)] \\ &= Z_0 u(n) + \breve{g}_{in}(n-1) * u(n-1), \end{aligned} \tag{3.10}$$

where $\breve{g}_{in}(m) \equiv \hat{g}_{in}(m+1)$ is the remainder Green's function *shifted by one delay*. The convolution term in (3.10) now only depends on the *history* of $u$, and not on the current value $u(n)$. In other words, the convolution term represents the *pressure history* of the system:

$$p_{hist}(n) = \breve{g}_{in}(n-1) * u(n-1). \tag{3.11}$$

After combining (3.5) with (3.10) and (3.11), the feedback structure can be expressed:

$$u(n) = \mathcal{F}\left\{(Z_0 \cdot u(n) + p_{hist}(n))\right\}. \tag{3.12}$$

This non-linear equation can be solved numerically for $u(n)$, and the corresponding pressure $p(n)$ can then be obtained through (3.10). Next, the volume velocity at the following time instant $u(n+1)$ can be computed, and so on. Thus the feedback loop is made computable in this way.

### 3.1.2 Using the Reflection Function

In general, the reflection function decays quicker than Green's function. This is because the reflection function is defined under the assumption that the input-end of the air column is *anechoic*, whereas Green's function is defined under the assumption that the input-end is *echoic*. Thus Green's function exhibits a much higher level of multiple reflections than the reflection function. Hence a time-domain simulation of the resonator is generally implemented more efficiently using the reflection function. Rewriting the resonator model in terms of propagating waves gives:

$$p^+(t) = Z_0 u(t) + p^-(t), \tag{3.13a}$$

$$p^-(t) = r_f(t) * p^+(t), \tag{3.13b}$$

$$p(t) = p^+(t) + p^-(t). \tag{3.13c}$$

This is the classic reflection function convolution model as originally described in [95]. Figure 3.3a shows the corresponding signal flow graph. In many applications, the reflection function model is formulated in a slightly different way, by using $p_{hist}(t)$ as a variable:

$$p(t) = Z_0 u(t) + p_{hist}(t), \tag{3.14}$$

where the pressure history is computed in terms of propagating waves [54] (signal flow graph is depicted in figure 3.3b):

$$p_{hist}(t) = 2p^-(t) = r_f(t) * 2p^+(t), \tag{3.15}$$

or in terms of pressure and volume velocity [124, 77] (signal flow graph depicted in figure 3.3c)

$$p_{hist}(t) = r_f(t) * [Z_0 u(t) + p(t)]. \tag{3.16}$$

These are variations of the same (reflection function) model. For brevity, we will only consider the reflection function model formulated with equation (3.14), using the pressure

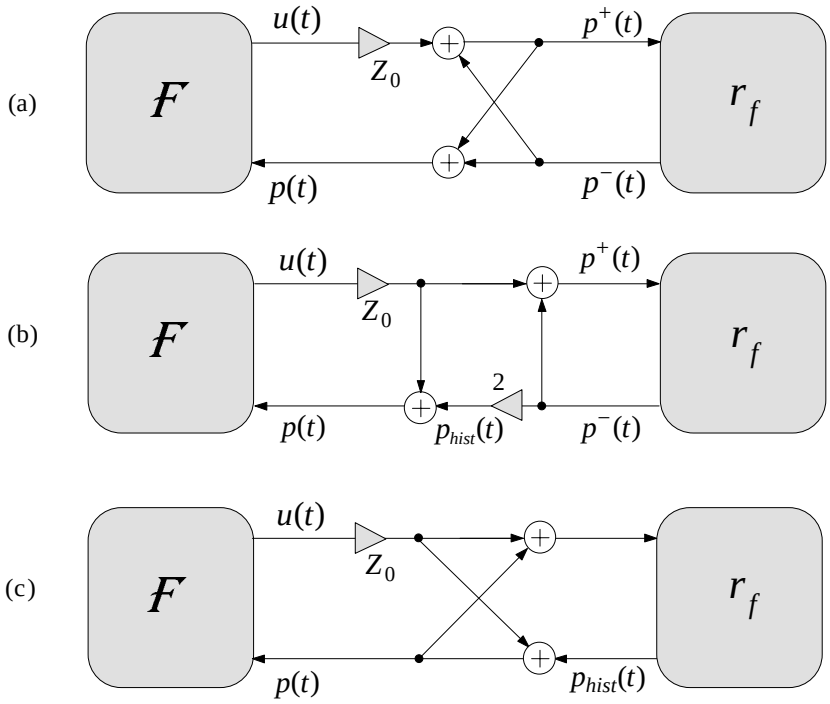


Figure 3.3: Feedback structure of a physical model using the reflection function. Three ways of interfacing the resonator to the excitation are possible: (a) without using the pressure history, (b) using the pressure history formulation with propagating waves, and (c) using the pressure history formulation for pressure and volume velocity.

history formulated with equation (3.16).

The feedback structure corresponding to using Green's function (figure 3.2) is made computable by assuming that Green's function may be written as the scaled delta-function $Z_0\delta(t)$ plus the "remainder" Green's function $\hat{g}_{in}(t)$. This implies that $g_{in}(0) = Z_0$. It can be easily shown that this is equivalent to assuming a reflection function $r_f(t)$ for which $r_f(0) = 0$. As seen in section 2.2, the relation between the input impedance and the reflectance is:

$$Z_{in}(\omega) = Z_0 \left( \frac{1 + R_f(\omega)}{1 - R_f(\omega)} \right). \tag{3.17}$$

The corresponding time-domain relation between Green's function and the reflection function is:

$$g_{in}(t) = Z_0 \cdot [\delta(t) + r_f(t)] *^{-1} [\delta(t) - r_f(t)], \tag{3.18}$$

where the operator $*^{-1}$ denotes *deconvolution*. From inspection of (3.18) it becomes clear that $g_{in}(0) = Z_0$ only if $r_f(0) = 0$. By taking this assumption into account in the reflection

function method, the pressure history can be computed in discrete-time as:

$$\begin{aligned} p_{hist}(n) &= \sum_{m=0}^{N+1} r_f(m)\ [Z_0 u(n-m) + p(n-m)] \\ &= \sum_{m=1}^{N+1} r_f(m)[Z_0 u(n-m) + p(n-m)] \\ &= \sum_{m=0}^{N} r_f(m+1)[Z_0 u(n-m-1) + p(n-m-1)] \\ &= \breve{r}_f(n-1) * [Z_0 u(n-1) + p(n-1)], \end{aligned} \tag{3.19}$$

where $\breve{r}_f(m) \equiv r_f(m+1)$ is the time-shifted version of the reflection function. The model can then be numerically solved for $u(n)$ by combining (3.19) with the discrete-time versions of (3.5) and (3.14).

Note that both the Green's function method and the reflection function method (the last one being the currently most widely used method in the context of wind instrument modelling) are based on the assumption that $r_f(0) = 0$. Translated into physical terms, this assumption means that the instrument bore has a perfectly cylindrical entry at the mouthpiece end. Unfortunately, this is not always the case for real wind instruments. For example, the mouthpiece of a brass instrument usually has a mouthcup with a curved profile. Such an "angled" start of the air column profile causes an immediate reflection at $t = 0$ back to the reed or lips. In many cases, the angle of conicity is rather small, thus the "instantaneous reflection" at $t = 0$ can be expected to be small. Nevertheless it would be more accurate to use the full reflection function that includes the instantaneous reflection. A method in which the full reflection function is applied is presented in the next section.

### 3.1.3 The Full Reflection Function Method

The full reflection function method is based on the principle of separating out all contributions at $t = nT$. The resulting equation can then be rewritten such that $p(n)$ becomes explicit, and the complete system can be solved for $u(n)$. In discrete-time, the reflection function model is expressed:

$$p(n) = Z_0 u(n) + \sum_{m=0}^{N} r_f(m)\,[Z_0 u(n-m) + p(n-m)]\,. \tag{3.20}$$

Separating the contributions at $t = nT$ from the convolution term (i.e., extracting all terms with $m = 0$) gives:

$$\begin{aligned} p(n) &= Z_0 u(n) + r_f(0) \cdot [Z_0 u(n) + p(n)] + \sum_{m=1}^{N} r_f(m)\ [Z_0 u(n-m) + p(n-m)] \\ &= Z_0 u(n) + r_f(0) \cdot [Z_0 u(n) + p(n)] + \breve{r}_f(n-1) * [Z_0 u(n-1) + p(n-1)] \\ &= Z_0 u(n) + r_f(0) \cdot [Z_0 u(n) + p(n)] + p_{hist}(n). \end{aligned} \tag{3.21}$$

Solving for $p(n)$ gives:

$$p(n) = \frac{[1 + r_f(0)]\, Z_0 u(n) + p_{hist}(n)}{1 - r_f(0)}. \tag{3.22}$$

Combining (3.5) with (3.22) gives the final equation from which $u(n)$ can be solved:

$$u(n) = \mathcal{F}\left\{\alpha_1 u(n) + \alpha_2\right\}, \tag{3.23}$$

where

$$\alpha_1 = Z_0 \left[\frac{1 + r_f(0)}{1 - r_f(0)}\right], \tag{3.24a}$$

$$\alpha_2 = \frac{p_{hist}(n)}{1 - r_f(0)}. \tag{3.24b}$$

The convolution approach provides a rigorous method for modelling the resonator, but as discussed in section 1.2, it has various limitations when applied to musical sound synthesis. In the next two sections of this chapter, we discuss two types of discrete-time modelling techniques that are based on treating the air column as a series of modules.

## 3.2 Digital Waveguide Modelling Techniques

A digital waveguide (DWG) model is a discrete-time model of a distributed acoustic system [132], based on the travelling-wave solution of the wave equation. The main difference when compared with more conventional numerical simulation techniques, such as finite element methods and modal analysis, is that a DWG model explicitly simulates travelling waves rather than localised physical quantities. Because DWG modelling techniques are based on a modular approach and allow for efficient computer implementations, they are particularly suitable in the context of musical sound synthesis. The development of DWG techniques was initiated more than a decade ago at CCRMA[3] by Prof. Julius Smith [129, 130, 131]. Since then, DWG modelling techniques have been further developed

[3] The Stanford University Center for Computer Research in Music and Acoustics, California (USA).

for application to various musical instruments, for example, string instruments [70, 149, 154, 145], wind instruments [63, 38, 151, 148, 119, 27], vocal tract models [39, 147] and percussive instruments [153, 53]. DWG modelling techniques have also been employed for simulation of room acoustics [128, 134, 114, 113, 146]. For elaborate overviews of physical modelling using DWG techniques we refer to [131, 132]. This section contains a summary of the basic concepts of DWG modelling plus a short review of some specific issues that are related to DWG modelling of tubular acoustic systems.

### 3.2.1 Modelling One-dimensional Wave Propagation

The general one-dimensional wave equation that describes lossless wave motion in uniform resonators (such as ideal strings and pipes) is:

$$\frac{\partial^2 y}{\partial x^2} = \frac{1}{c^2}\frac{\partial^2 y}{\partial t^2}, \tag{3.25}$$

where $y$ is an acoustical variable (e.g., string displacement or acoustic pressure), $t$ is time, and $x$ is the position along the resonator in the modelling dimension (e.g., position along string or pipe). The general time-domain solution of (3.25) was published by d'Alembert in 1747 [42]:

$$y(x,t) = f_1(t - x/c) + f_2(t + x/c), \tag{3.26}$$

where $f_1$ and $f_2$ are arbitrary waveforms that travel in positive and negative $x$-direction, respectively, with wave speed $c$. The wave equation solution is a simple superposition of travelling waves, and physical systems that are governed by the wave equation are therefore usually referred to as *waveguides*. In order to simulate a waveguide in the discrete-time domain, it is necessary to sample the travelling waves. Given a sample rate $f_s$ and a sample period $T = 1/f_s$, the sampling is formally carried out by the change of variables [130]:

$$x \to x_m = m\Delta x, \tag{3.27a}$$

$$t \to t_n = nT, \tag{3.27b}$$

where $\Delta x = cT$ is the *spatial sampling interval*. For lossless sound propagation in air, the wave speed is about 343m/s. Using an audio sampling rate $f_s = 44.1$kHz, the sampling interval then becomes about 7.8 mm. Substituting the change of variables into the travelling-wave solution gives:

$$y(t_n, x_m) = f_1\left[(n-m)T\right] + f_2\left[(n+m)T\right]. \tag{3.28}$$

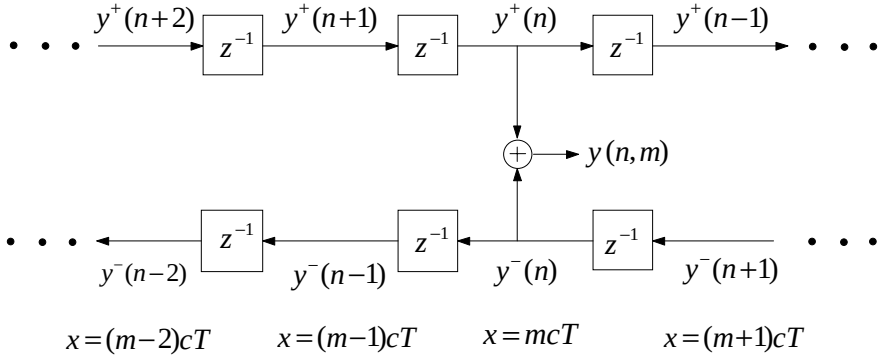


Figure 3.4: Digital simulation of a lossless waveguide using a bi-directional delay-line. The $z^{-1}$ blocks indicate a single delay. The acoustic variable at time $n$ and position $m$ is obtained by summing the two components $y^+(n,m)$ and $y^-(n,m)$.

This expression can be simplified by suppressing $T$ and defining:

$$y^+(n,m) = f_1\left[(n-m)T\right], \tag{3.29a}$$

$$y^-(n,m) = f_2\left[(n+m)T\right], \tag{3.29b}$$

where the superscripts $+$ and $-$ indicate wave travel in positive and negative direction, respectively. The final expression that describes the *digital waveguide* is:

$$y(n,m) = y^+(n,m) + y^-(n,m). \tag{3.30}$$

The basic structure of the digital waveguide is depicted in figure 3.4. The upper delay-line simulates the forward-travelling wave $y^+$, and the lower delay-line simulates the backward-travelling wave $y^-$. The values of $y^+$ and $y^-$ at consecutive time instants are stored in the upper and lower rail of the bi-directional delay-line structure, respectively.

### 3.2.2 Basic Properties of DWG Models

The basic properties of DWG models have been extensively studied and described in prior work [130, 131, 132, 135]. The DWG model features that are relevant to this study are summarised below.

Propagation Losses

In a one-dimensional resonator, the propagation losses are distributed over the length of the resonator. In other words, the amount of energy dissipation of a wave depends on the distance it has travelled. Such losses may be lumped, and the resulting expression can be approximated with a digital filter (i.e., a *loss-filter*). In a DWG model, wave

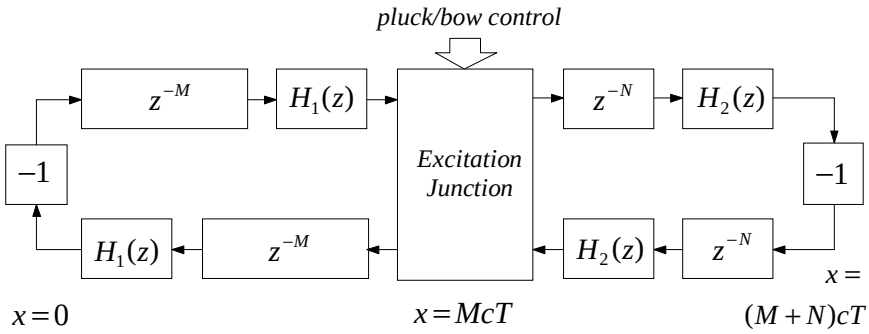


Figure 3.5: Digital waveguide implementation of a string, taking into account the propagation losses. Each "−1" block indicates a rigid termination. A $z^{-M}$ unit represents a delay-line of $M$ samples. The filters $H_1(z)$ and $H_2(z)$ model the lumped propagation losses along the string lengths $L_1 = Mct$ and $L_2 = Nct$, respectively. The string excitation (plucking or bowing) is modelled with a special excitation-junction at a position $x = Mct$.

propagation is represented by interconnected digital waveguide sections. The propagation losses can thus be taken into account by filtering the propagating wave at points in the DWG structure where it exits a digital waveguide section. This idea is demonstrated in the DWG implementation of a lossy string as depicted in figure 3.5. The string is rigidly terminated at both ends, and plucked or bowed at position $x = M\,c\,T$.

Linearity and Commutativity

In general, the modelling units of a DWG model are *linear* and *commutative*. These properties allow us to re-arrange the DWG string model into a more efficient structure. For example, all the units in the delay-loop on the right side of the excitation junction in figure 3.5 are linear and commutative. Hence the reflectance of this delay-loop, as seen from the excitation junction, may be re-formulated as follows:

$$\begin{aligned} R_{dl}(z) &= z^{-N} \cdot H_2(z) \cdot (-1) \cdot z^{-N} \cdot H_2(z) \\ &= (-1) \cdot z^{-2N} \cdot [H_2(z)]^2 \,. \end{aligned} \tag{3.31}$$

The delay-loop on the left side of the excitation junction can be re-arranged in the same manner. In other words, we may change the *order* of the linear elements of the DWG structure. We will refer to this as the *commutativity principle*. Assuming that the excitation-junction in figure 3.5 models non-linear interaction with the string, the structure can not be re-arranged such that the elements on the right side are combined with the elements on the left side. Hence the re-arranged DWG model now exhibits two delay loops that each contain a single delay-line of twice the original length and loss-filters with squared transfer-function (see figure 3.6).

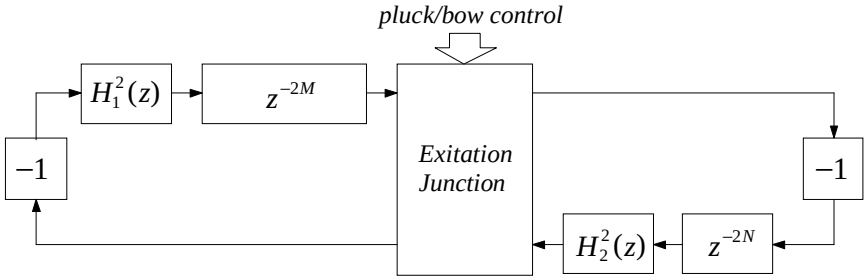


Figure 3.6: Digital waveguide implementation of a string with commuted losses and delays. Each "−1" block indicates a rigid termination. A $z^{-2M}$ unit represents a delay-line of $2M$ samples. The filter-blocks $(H_1(z))^2$ and $(H_2(z))^2$ model the lumped propagation losses along the string lengths $2L_1 = 2Mct$ and $2L_2 = 2Nct$, respectively.

Fractional Delays

The length of the string in figure 3.6 is restricted to be a multiple of the spatial sample length $cT$. In order to enable continuous adjustment of the string length and excitation point, *fractional delay filters* are applied [131, 148]. Fractional delay (FD) filters simulate the propagation of waves over a fraction of the spatial sampling length, and can be placed within the delay loops of a DWG model.

Band-Limited Signals

In a digital waveguide model, the travelling waves are sampled in space and time, therefore the input signals must be *band-limited* according to the sampling theorem [131]. Hence signal variables that contain frequencies higher than half the sample rate suffer from the effects of *spectral aliasing*.

Passivity

DWG models simulate passive physical systems. One condition for a DWG model to be stable and passive is that the gains of its delay-loops must not exceed unity. A possible strategy for upholding this condition is to design the digital filters that are to be included in a DWG model such that their magnitude response is equal to or less than unity at all frequencies [148].

Computational Efficiency

In a DWG model, delay-lines are used to implement lossless wave propagation. A single delay-line only requires one fetch, store and pointer update per sampling period, independent of its delay length $N$. Therefore, in the case of modelling an $N$th order lossless

waveguide, the DWG modelling approach is extremely economic in comparison with other discrete-time modelling approaches (such as finite-difference, finite-element, or modal analysis methods), which require a number of the order $N$ of such computations [132]. Losses, dispersion or fractional delays can generally be represented with a few lower-order digital filters, so that the total computational cost of a DWG model can be kept very low.

### 3.2.3 Modelling Tubular Acoustic Systems

This section summarises how DWG techniques can be applied to the simulation of wave propagation in elemental bore shapes, such as cylindrical and conical sections.

Cylindrical Bores

In section 2.2.1 we have seen that linear wave propagation in a cylindrical bore can be described by the one-dimensional wave equation in cylindrical co-ordinates (equation (2.31)). As explained in section 3.2.1, wave propagation that is governed by this equation can be implemented using a simple bi-directional delay-line structure. Viscothermal losses and fractional delays can be simulated as described in the last section. A detailed discussion of the exact design of the digital loss-filters and fractional delay filters applicable to modelling acoustic bores is given in chapter 4.

Conical Bores

Wave propagation in conical bores was described in section 2.2.2. Just as for the cylindrical case, wave propagation in conical bores may be described with a one-dimensional wave equation, though in this case in spherical co-ordinates (equation (2.44)). According to this wave equation, waves propagate smoothly (without back-scattering) from one end to the other, therefore wave propagation in conical bores can also be implemented using a digital waveguide. However, there are some extra features to be taken into account, such as the spreading of the wavefront as it travels away from the cone apex. These issues are discussed in chapter 4.

Tubular Junctions

As seen in section 2.3, wave scattering occurs at a junction of tubular sections of different diameter or different taper. In a DWG model, wave scattering at a tubular interconnection can be modelled using a *scattering junction*, which is a unit that computes the reflectance and transmittance of incident waves. For example, if we connect two cylindrical bore sections of different diameter (see figure 3.7a) or different diameter and different taper (see figure 3.7b), we need to work out how much of the incident wave energy is reflected

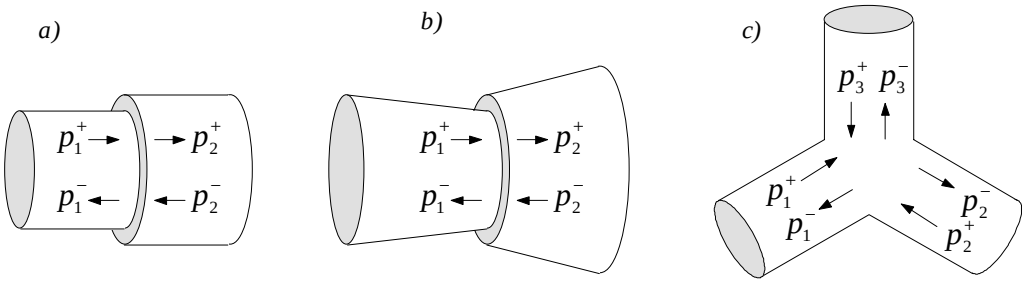


Figure 3.7: Tubular junctions. Junction of two cylindrical bore sections (a), of two conical bore sections (b), and of three cylindrical bore sections (c).

backward, and how much is transmitted into the other tube. Modelling the wave scattering at junctions of two tubular sections is further discussed in detail in chapter 4 and chapter 6.

In some cases, a wind instrument bore contains an interconnection of three tubular sections (see figure 3.7c). For example, a woodwind tonehole may be considered as a short tubular section that is interconnected with two other tubes, namely the part of the main bore before and after the tonehole. A *three-port scattering junction* is required to model the wave scattering at such a junction. This subject is further discussed in chapter 5 and appendix E.

### 3.2.4 Relation to Conventional Ladder and Lattice Filters

DWG models were designed to simulate acoustical systems. However, DWG models may be also interpreted as digital filter structures, and are closely related to several existing signal processing techniques. It is worthwhile establishing this relation, since it allows us to apply a variety of techniques developed in the field of signal processing to a discrete-time acoustical model.

Waveguide Filters

The digital filter structure that results from modelling a lossless, distributed acoustic model as a network of intersecting *uniform waveguide sections* is referred to as a *waveguide digital filter* or *waveguide filter* (WGF) [130]. Uniform waveguide sections are sections with constant characteristic impedance. For example, when modelling an acoustic bore, this means the bore is divided into cylindrical sections, and implemented in the discrete time-domain using a chain of bi-directional delay-lines connected via cylindrical scattering junctions. Hence a DWG model of the piecewise cylindrical system discussed in chapter 2 (see figure 2.12)) can be regarded as a WGF.

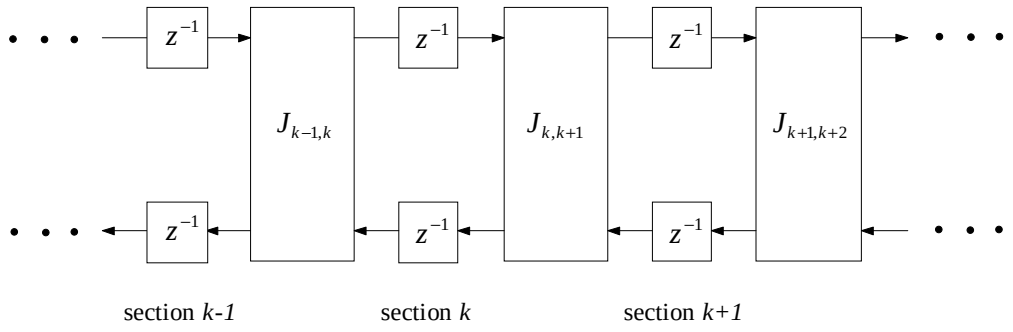


Figure 3.8: Structure of the waveguide filter with optimal spatial resolution. Each cylindrical section has a round-trip $2cT$. The scattering at the junction between section $k$ and section $k+1$ is modelled with the cylindrical scattering junction $J_{k,k+1}$.

When modelling an acoustic bore using a WGF, the optimal spatial resolution is obtained by using a section-length that corresponds to a round-trip time (which is the total time for propagating forward and backward through a cylindrical section) of $2cT$. Figure 3.8 depicts the structure of a WGF with optimal spatial resolution.

Kelly-Lochbaum Model

Cylindrical scattering junctions are equivalent to the *Kelly-Lochbaum scattering junctions* that are used for modelling the vocal tract in speech synthesis applications [78]. The Kelly-Lochbaum (KL) filter model (see figure 3.9), is very similar to the WGF model with optimal spatial resolution, where the main difference is that the KL structure only contains delays at its "lower rail". In [130] it is shown that the KL structure is a "reduced equivalent form" of a WGF structure that uses a sample rate that is twice is high. In other words, the spatial resolution of a KL model computed at sample rate $f_s$ is twice as high as the spatial resolution of a WGF model computed at the same sample rate. Furthermore, the Kelly-Lochbaum model is mathematically equivalent to various other ladder and lattice filter structures [92, 130].

### 3.2.5 Relation to Inverse Scattering Techniques

One of the lattice filter structures that is mathematically equivalent to the Kelly-Lochbaum model is the linear predictive coding (LPC) model, as used in speech synthesis applications [92]. From a digital signal processing point of view, this is a particularly interesting feature, since the filter coefficients for this structure can be directly derived from an acoustic signal, using LPC analysis. This raises the possibility of using LPC analysis techniques for derivation of the parameters of the Kelly-Lochbaum Model. The Kelly-Lochbaum model may be interpreted as an acoustical bore model, thus we may consider

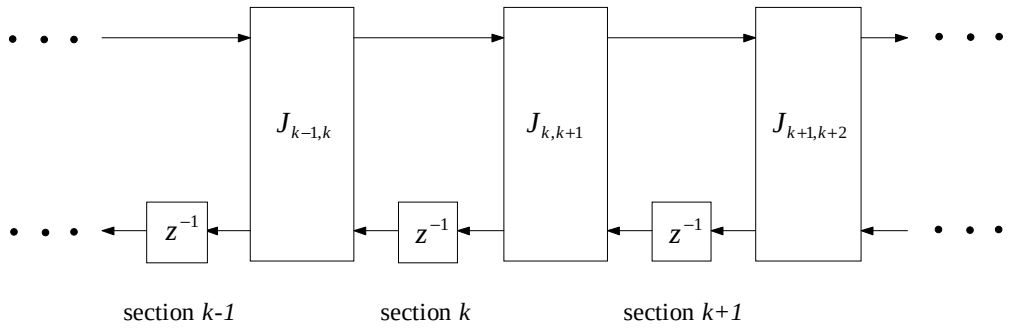


Figure 3.9: Structure of the Kelly-Lochbaum model. Each cylindrical section has a round-trip $cT$. The scattering at the junction between section $k$ and section $k+1$ is modelled with the cylindrical scattering junction $J_{k,k+1}$.

this application as a form of *bore reconstruction*. Such an *inverse-modelling* approach has previously been applied in speech synthesis, with the aim of reconstructing the shape of the vocal tract [92]. Interestingly, a similar approach has been applied in the context of musical wind instrument modelling. By first measuring the impulse response (reflection function) of a certain tubular object, and then applying an inverse-modelling algorithm, the internal bore profile of the instrument can be reconstructed. Various techniques for bore reconstruction have been developed, usually based on the piecewise cylindrical model (see, e.g., [163, 10]). The piecewise cylindrical model is often referred to as a"scattering model", hence the inverse method is usually referred to as "inverse-scattering". Such an inverse-scattering technique is applied in chapter 7, in order to empirically derive the reflectance of a flared horn. For a detailed description of inverse-scattering techniques and the experimental techniques for obtaining the bore impulse response, we refer to Sharp [126].

## 3.3 Wave Digital Filter Techniques

Wave digital filter (WDF) techniques are used for digital simulation of analogue networks [51, 87]. The resulting digital networks are called *wave digital filters*. Many theoretical acoustic models are developed using the strong analogy between electric and acoustic systems, and can be expressed in terms of electric components, such as inductance ($L$), capacitance ($C$) and resistance ($R$). A good example is the equivalent network of the Helmholtz resonator, as discussed in section 2.1.3. Hence WDF techniques can be applied to discretise such lumped elements in an acoustic model. WDFs are similar to DWG models in the sense that they both simulate continuous-time models in the discrete-time

domain using wave variables[4]. As a consequence, the two modelling approaches easily combine. This section starts with a short review of aspects of WDF theory that are relevant to this study. Next, the application to acoustical systems is discussed.

### 3.3.1 Wave Digital Filter Theory

Detailed explanations of WDF theory can be found in [51, 87]. The basic procedure for derivation of a WDF consists of two steps:

(1) transformation from electrical circuit variables (voltage, current) to wave variables (voltage waves or current waves).

(2) discretisation of frequency-dependent network components via the bilinear transform.

There are two basic approaches for WDF derivation. In the *one-port* approach, each network component is discretised individually, and multi-port systems are connected with each other via *adaptors*. In the *two-port* approach, the network is divided into two-port (and one-port) units, which are then discretised individually (see figure 3.10). Here we will review WDF theory mainly along the lines of the two-port modelling approach as described in [87].

A two-port analogue network can be expressed in terms of its $ABCD$-matrix. For example, the parallel inductance network in figure 3.11 is described by the matrix equation:

$$\begin{bmatrix} V_1 \\ I_1 \end{bmatrix} = \begin{bmatrix} 1 & sL \\ 0 & 1 \end{bmatrix} \begin{bmatrix} V_2 \\ I_2 \end{bmatrix}, \tag{3.32}$$

where $s = j\omega$ is the Laplace variable. The first step in the derivation of the WDF model is to transform the instantaneous variables (voltage and current) into wave variables. This is accomplished here by the decomposition into the *voltage waves*:

$$V = \frac{V^+ + V^-}{2}, \tag{3.33a}$$

$$I = \frac{V^+ - V^-}{2R}, \tag{3.33b}$$

where $V^+$ and $V^-$ are voltage waves, and $R$ is a constant with the dimensions of resistance and is called the *port-resistance* [87]. In principle, the port-resistance at any point in the

[4] We note that WDF techniques are primarily used for simulation of lumped element systems, in which case the wave variables do not correspond to actual *travelling* waves. That is, in the case of modelling a distributed system the decomposition of the acoustical variables into wave variables has a clear physical meaning, whereas in the case of modelling a lumped system it is merely a matter of mathematical representation.

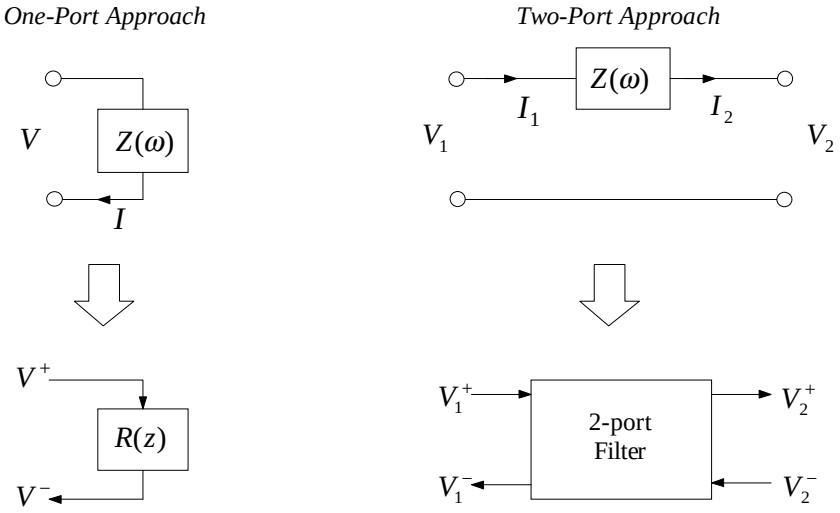


Figure 3.10: One-port and two-port approach for derivation of wave digital filters.

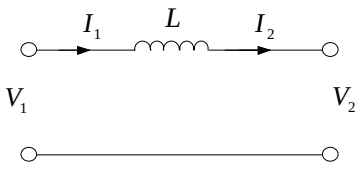


Figure 3.11: A two-port series inductance network.

network may be chosen freely. Let us note however that one of the main features of WDF modelling is that this freedom has to be used to avoid delay-free loops in the final digital filter structure. If we apply the wave decomposition in figure 3.33 to the acoustic variables on both sides of the relationship in equation (3.32), we get

$$\begin{bmatrix} V_1^+ + V_1^- \\ V_1^+ - V_1^- \end{bmatrix} = \begin{bmatrix} 1 & \frac{sL}{R_2} \\ 0 & \frac{R_1}{R_2} \end{bmatrix} \begin{bmatrix} V_2^+ + V_2^+ \\ V_2^+ - V_2^- \end{bmatrix}, \tag{3.34}$$

where $R_1$ and $R_2$ are the left-hand side and the right-hand side port-resistance, respectively. These equations may be re-arranged such that the relationships between the scattering waves at either side of the system are obtained:

$$\begin{bmatrix} V_1^+ \\ V_1^- \end{bmatrix} = \begin{bmatrix} 1 + \frac{sL}{R_2} + \frac{R_1}{R_2} & 1 - \frac{sL}{R_2} - \frac{R_1}{R_2} \\ 1 + \frac{sL}{R_2} - \frac{R_1}{R_2} & 1 - \frac{sL}{R_2} + \frac{R_1}{R_2} \end{bmatrix} \begin{bmatrix} V_2^+ \\ V_2^- \end{bmatrix}. \tag{3.35}$$

The scattering matrix[5], that relates the incident waves $V_1^+, V_2^-$ to the reflected waves $V_2^+, V_1^-$, is expressed:

$$\begin{bmatrix} V_2^+ \\ V_1^- \end{bmatrix} = \begin{bmatrix} T^+(s) & R^+(s) \\ R^-(s) & T^-(s) \end{bmatrix} \begin{bmatrix} V_1^+ \\ V_2^- \end{bmatrix}, \tag{3.36}$$

with the transmittances and reflectances:

$$T^+(s) = \frac{2R_2}{R_2 + sL + R_1}, \tag{3.37a}$$

$$R^+(s) = \frac{-R_2 + sL + R_1}{R_2 + sL + R_1}, \tag{3.37b}$$

$$R^-(s) = \frac{R_2 + sL - R_1}{R_2 + sL + R_1}, \tag{3.37c}$$

$$T^-(s) = \frac{2R_1}{R_2 + sL + R_1}. \tag{3.37d}$$

Since we have

$$T^+(s) = 1 - R^+(s), \tag{3.38a}$$

$$T^-(s) = 1 - R^-(s), \tag{3.38b}$$

the scattering relations can be written conveniently as:

$$V_2^+ = V_1^+ + R^+(s)\left[V_2^- - V_1^+\right], \tag{3.39a}$$

$$V_1^- = V_2^- - R^-(s)\left[V_2^- - V_1^+\right]. \tag{3.39b}$$

What remains is to formulate the reflectances $R^+(s)$ and $R^-(s)$ in digital form. Discretisation of frequency-dependent units in WDF modelling is done via the *bilinear transform* (BT) [51, 87]. The BT is carried out by means of a mapping of the Laplace variable $s$ to the $z$-transform variable $z$:

$$s = \beta \frac{1 - z^{-1}}{1 + z^{-1}}, \tag{3.40}$$

with the bilinear operator $\beta = 2/T$. Applying the BT to the reflection coefficients gives the first-order IIR filters:

$$R^+(z) = \frac{\alpha_1 + \alpha_2 z^{-1}}{1 + \alpha_3 z^{-1}}, \tag{3.41a}$$

$$R^-(z) = -\frac{\alpha_2 + \alpha_1 z^{-1}}{1 + \alpha_3 z^{-1}}, \tag{3.41b}$$

[5] In [87], the scattering matrix is defined differently. Nevertheless this results in an equivalent WDF structure.

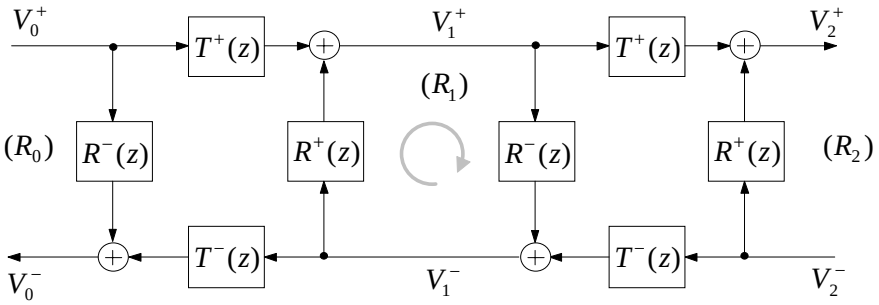


Figure 3.12: Signal flow structure of a WDF simulation of two two-port networks of the same type connected to each other. The structure is only computable if the loop (indicated with the grey arrow) is not delay-free. This means that either $R^+(z)$ or $R^-(z)$ has to be non-immediate.

where

$$\alpha_1 = \frac{R_1 - R_2 + \beta L}{R_1 + R_2 + \beta L}, \tag{3.42a}$$

$$\alpha_2 = \frac{R_1 - R_2 - \beta L}{R_1 + R_2 + \beta L}, \tag{3.42b}$$

$$\alpha_3 = \frac{R_1 + R_2 - \beta L}{R_1 + R_2 + \beta L}. \tag{3.42c}$$

One of the key aspects of WDF techniques is to ensure *realisability*. In principle, the WDF model of the series inductance network can be implemented as an isolated system, using equations (3.39) and (3.41). However, if more components are added to the system, special care must be taken to ensure that no delay-free loops result. For example, if the network is connected to another two-port series inductance network (see figure 3.12), the resulting WDF model of the total network exhibits a loop that is only computable if it contains at least one delay. This means that at least one of the reflectances $R^+(z), R^-(z)$ must be *non-immediate*. By non-immediacy of a reflectance $R(\omega)$ we mean that its inverse Fourier transform $r(t)$ has a zero instantaneous reflection (i.e., $r(0) = 0$)). In order to achieve this, either $\alpha_1$ or $\alpha_2$ must be set to zero, which corresponds to imposing non-immediacy on respectively the *left* and the *right* side of an individual two-port WDF unit. This choice (left or right non-immediacy) is a general feature of a two-port WDF derivation [87]. However, note that in order to be able to connect a series of two-port WDF units freely, they must all be designed according to the same choice for non-immediacy. In this example, we choose to have non-immediacy on the *left* side[6]. In the case of the series inductance network, this means that $\alpha_2$ has to be set to zero. The port-resistance on the

[6] Units with "left-side non-immediacy" will be indicated with WD-*l*, whereas units with "right-side non-immediacy" are indicated with WD-*r*.

left side then has to be:

$$R_1 = R_2 + \beta L. \tag{3.43}$$

After substitution of (3.43) into (3.41), the reflectances $R^+(z), R^-(z)$ of the WD-$l$ series inductance can be written:

$$R^+(z) = \frac{\alpha_1}{1 + \alpha_3 z^{-1}}, \tag{3.44a}$$

$$R^-(z) = \frac{-\alpha_1 z^{-1}}{1 + \alpha_3 z^{-1}} = -z^{-1} R^+(z), \tag{3.44b}$$

with the coefficients

$$\alpha_3 = \frac{R_2}{R_2 + \beta L}, \tag{3.45a}$$

$$\alpha_1 = \frac{\beta L}{R_2 + \beta L} = 1 - \alpha_3. \tag{3.45b}$$

If we define the intermediate signal variables

$$W_1 = \left[V_2^+ - V_1^-\right], \tag{3.46a}$$

$$W_2 = \left[\frac{1 - \alpha_3}{1 + \alpha_3 z^{-1}}\right] W_1, \tag{3.46b}$$

the final WDF formulae are found by combining (3.39), (3.44), (3.45) and (3.46):

$$W_1 = \left[V_2^- - V_1^+\right], \tag{3.47a}$$

$$W_2 = W_1 - \alpha_3 \left[W_1 + W_2 z^{-1}\right], \tag{3.47b}$$

$$V_2^+ = V_1^+ + W_2, \tag{3.47c}$$

$$V_1^- = V_2^- + W_2. \tag{3.47d}$$

The signal flow of the two-port WD-$l$ is depicted in figure 3.13. Note that just one delay and one multiplication is required in order to simulate the series inductance network.

### 3.3.2 Application to Acoustical Systems

In the analogy between electrical and acoustical systems, voltage is considered analogous to pressure, and current is considerd analogous to volume velocity [84, 52]. Hence we can apply WDF techniques to lumped acoustical systems by simply replacing the electrical variables with their corresponding acoustical variables. In the case of a distributed acoustic element, the wave variables correspond to pressure waves travelling in a certain medium. In that case the port-resistance equals the reference impedance ($\rho c/S$) that characterises the medium (as in DWG modelling). In the lumped case however, the wave variables

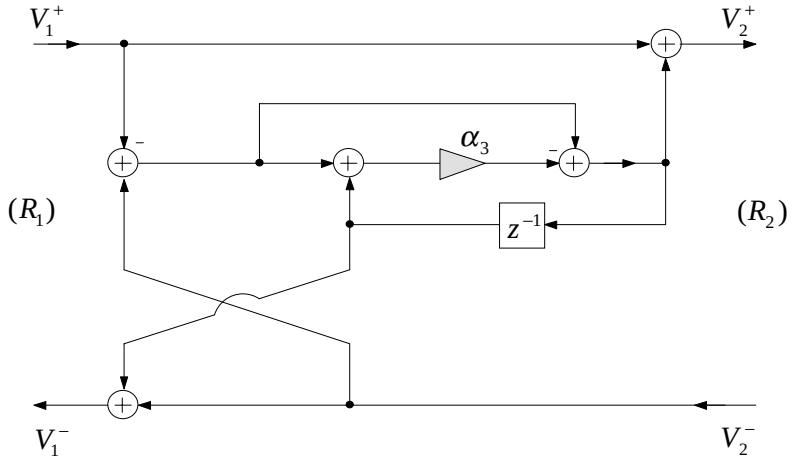


Figure 3.13: Wave digital filter simulation of a series inductance network, derived using the two-port approach, with non-immediacy on the left side. $R_1$ and $R_2$ are the port-resistances.

may only be understood to be travelling *instantaneously*. In other words, the waves do not in fact travel over any distance, and the travelling wave formulation is purely a matter of mathematical representation. The port-resistance may therefore, at least from an acoustical point of view, be considered as arbitrary. As seen in section 3.3.1, this freedom can be used to avoid delay-free loops in the final discrete-time modelling structure.

Suppose that we want to model a cylindrical pipe with a local volume expansion (see figure 3.14a). The equivalent network of this system consists of a uniform transmission-line shunted by a parallel capacitor [84] (see figure 3.14b). The acoustic *compliance* (the acoustical analogue of capacitance) of the volume $V$ is:

$$C = \frac{V}{\rho c^2}. \tag{3.48}$$

In discrete-time, the cylindrical pipe (the uniform line) is modelled with a bi-directional delay-line (see figure 3.14c), as described in section 3.2. The task is now to discretise the volume section by deriving the WDF structure for simulation of the equivalent two-port capacitor network. Since the two-port parallel capacitor is connected directly with a uniform line (modelled as a DWG unit) on both sides, the port-resistances at these connections should be set equal to the characteristic impedance $Z_0$ of the pipe. The digital waveguide sections have no immediate reflection, so that no delay-free loops will arise. In principle we can derive a WDF simulation of the volume expansion using the two-port approach, in the same way as with the series inductance network in the last section. However, in application to a *parallel* network, the one-port approach is more

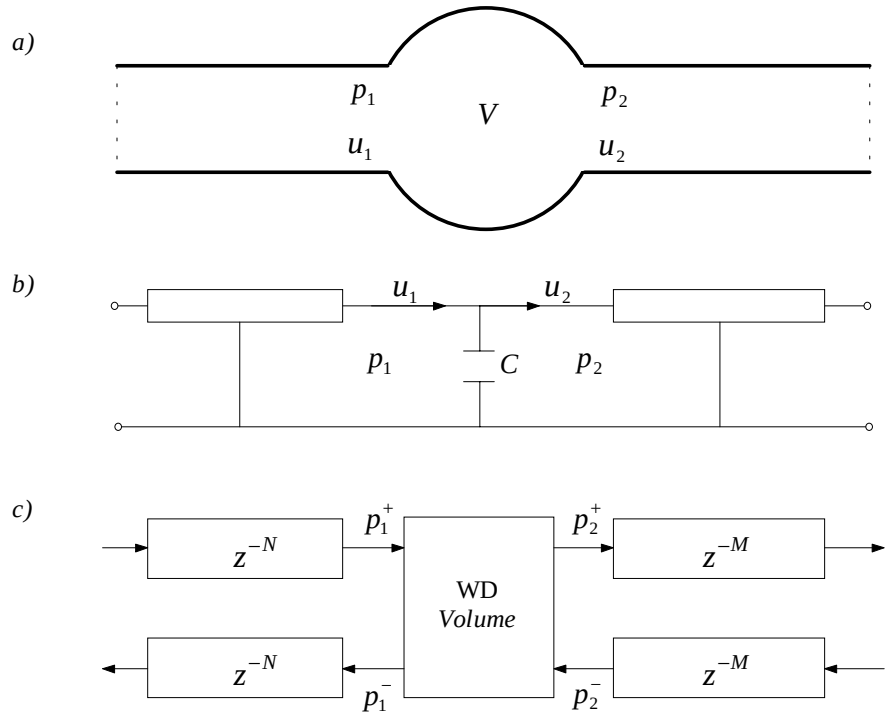


Figure 3.14: Two pipes connected via an acoustic volume (a), the equivalent electrical circuit (b), and the discrete-time model (c).

practical. The derivation of this "wave digital volume" is done as follows. The connection between the parallel capacitor and the rest of the network in figure 3.14b is as a *parallel three-port*. By drawing this part of the network in a slightly different way (see figure 3.15), this notion becomes more clear. Kirchoff's laws apply to the three-port:

$$P_1 = P_2 = P_3, \tag{3.49a}$$

$$U_1 = U_2 + U_3. \tag{3.49b}$$

The first step in the WDF derivation is the transformation from localised acoustic variables to wave variables. In order to ensure compatibility with DWG modelling, the travelling wave decomposition[7] is chosen as:

$$P_k = P_k^+ + P_k^-, \tag{3.50a}$$

$$U_k = \frac{P_k^+ - P_k^-}{R}, \tag{3.50b}$$

for $k = 1, 2, 3$. The direction of the waves is as depicted in figure 3.16. The scattering of

[7] This wave decomposition differs by a factor 2 from the decomposition in (3.33), but this factor does not affect the WDF derivation.

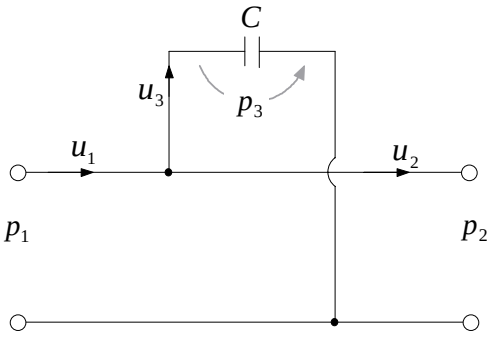


Figure 3.15: A three-port interconnection with a compliant load at one of its ports.

the wave variables at the three-port junction can be expressed through the matrix equation (see appendix E):

$$\begin{bmatrix} P_1^- \\ P_2^+ \\ P_3^+ \end{bmatrix} = \begin{bmatrix} \frac{G_1-G_2-G_3}{G_1+G_2+G_3} & \frac{2G_2}{G_1+G_2+G_3} & \frac{2G_3}{G_1+G_2+G_3} \\ \frac{2G_1}{G_1+G_2+G_3} & \frac{-G_1+G_2-G_c}{G_1+G_2+G_3} & 2G_3 \\ \frac{2G_1}{G_1+G_2+G_3} & \frac{2G_2}{G_1+G_2+G_3} & \frac{-G_1-G_2+G_3}{G_1+G_2+G_3} \end{bmatrix} \begin{bmatrix} P_1^+ \\ P_2^- \\ P_3^- \end{bmatrix}, \tag{3.51}$$

where $G_k = 1/R_k$ is the local *port-admittance*. The port-admittance $G_3$ of the compliance may be freely chosen, and the other port-admittances $G_1$ and $G_2$ equal the characteristic admittance $Y_0 = 1/Z_0$ of the pipe:

$$G_1 = G_2 = Y_0. \tag{3.52}$$

The second step in the WDF derivation is the discretisation of the frequency-dependent component (the volume compliance). The impedance load of the compliance is $Z_{com}(\omega) = 1/j\omega C$. The corresponding wave reflectance $R_{com}(\omega)$ is:

$$R_{com}(\omega) = \frac{P_3^-}{P_3^+} = \frac{Z_{com}(\omega) - R_3}{Z_{com}(\omega) + R_3} = \frac{G_3 - j\omega C}{G_3 + j\omega C}. \tag{3.53}$$

Discretisation of (3.53) via the bilinear transform gives:

$$R_{com}(z) = \frac{G_3 - \beta C\left(\frac{1-z^{-1}}{1+z^{-1}}\right)}{G_3 + \beta C\left(\frac{1-z^{-1}}{1+z^{-1}}\right)}, \tag{3.54a}$$

$$= \frac{\alpha + z^{-1}}{1 + \alpha z^{-1}}. \tag{3.54b}$$

with the filter coefficient

$$\alpha = \frac{G_3 - \beta C}{G_3 + \beta C}. \tag{3.55}$$

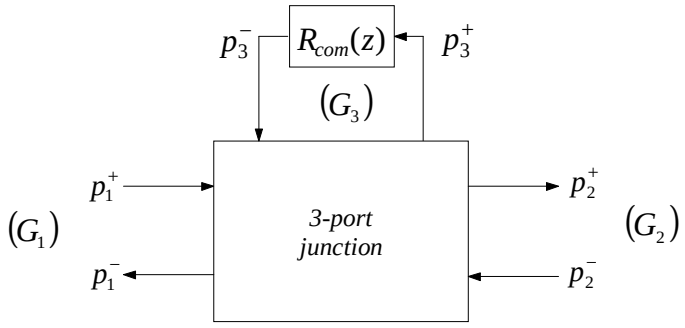


Figure 3.16: Basic WDF structure for simulation of a three-port interconnection with a compliance load at one of its ports. The interconnection is modelled as a three-port junction, and the compliance is represented by its wave reflectance $R_{com}(z)$. The structure is only computable if $G_3$ is chosen such that the capacitor loop is not delay-free.

Now in order to ensure that the compliance-loop in the WDF structure (see figure 3.16) is delay-free, we need to choose $G_3$ such that the reflectance $R_{com}(z)$ is non-immediate. In other words, $\alpha$ has to be to zero, which is achieved by setting:

$$G_3 = \beta C. \tag{3.56}$$

The wave digital reflectance then becomes:

$$R_{com}(z) = \frac{0 + z^{-1}}{1 + 0} = z^{-1}. \tag{3.57}$$

We note that the compliance-loop is thus modelled very efficiently with a single delay. The final equations of the wave digital volume are found by substituting the values for the port-admittances (equations (3.52) and (3.56)) into the scattering matrix equation (3.51), and combining with (3.57):

$$\begin{aligned} P_3^- &= P_3^+ z^{-1}, \\ W &= k_j \left[ P_1^+ + P_2^- - 2P_3^- \right], \\ P_1^- &= P_2^- + W, \\ P_2^+ &= P_1^+ + W, \\ P_3^+ &= P_1^+ + P_2^- - P_3^- + W, \end{aligned} \tag{3.58}$$

with the three-port junction coefficient:

$$k_j = \frac{-\beta C}{\beta C + 2Y_0}. \tag{3.59}$$

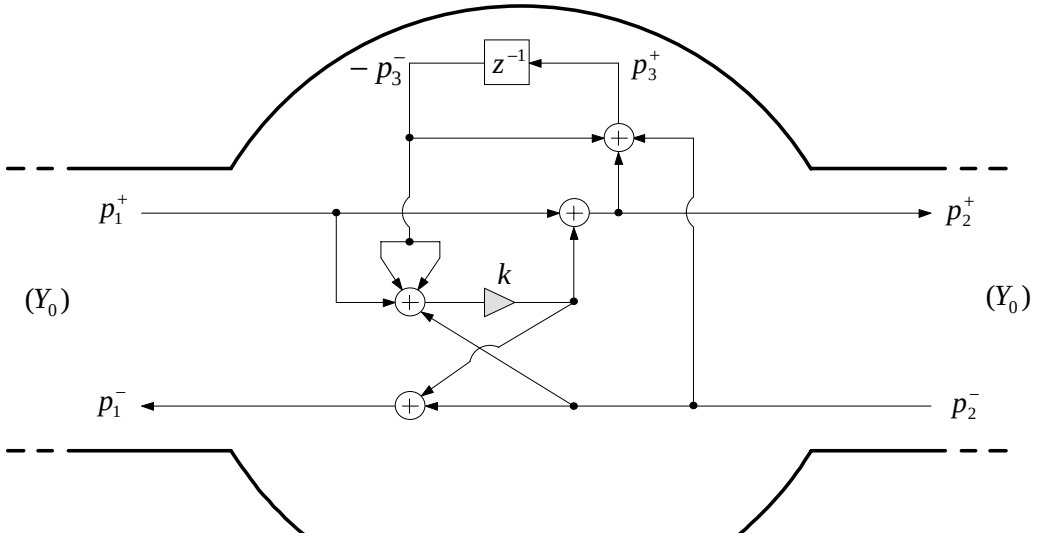


Figure 3.17: Wave digital simulation structure of a volume expansion in a cylindrical pipe, derived using the one-port approach.

The signal flow of the "wave digital volume" is depicted in figure 3.17. Note that also in this case only one multiplication is required.

## 3.4 The Combined Approach

The previous two sections of this chapter describe two different techniques for discrete-time modelling of acoustic systems. These two techniques both use wave variables, and can therefore easily be combined in a discrete-time model. For example, van Duyne et al. [153] take such a combined approach for digital simulation of force interaction between hammer and string in a piano. In this section, a comparison between the two techniques is made, starting from a comparison between waveguide filters (WGFs) and wave digital filters (WDFs). The results of this comparison are then used to work towards a more specified definition of the techniques such that they are compatible when applied to acoustical systems.

### 3.4.1 A Comparison between WDFs and WGFs

The theory of WGFs is described in detail in [130], and an overview of WDF theory can be found in [51, 87]. The main similarities between WGFs and WDFs are:

- Both WGFs and WDFs are derived from physical systems using wave variables.
- Both WGFs and WDFs implement $N$-dimensional networks, where $N$ can theoretically vary from 1 to any positive integer.

- $N$-port interconnections are modelled with $N$-port junctions[8].
- Both WGFs and WDFs are scattering-type filters, for which finite-precision artefacts such as overflow oscillations and limit cycles can be suppressed, and sensitivity to quantisation errors can be minimised.

The main differences between WGFs and WDFs are:

- WGFs are derived from uniform *transmission-lines*, which in the analogy between electrical networks and acoustical systems correspond to *distributed* model elements. WDFs are derived from *lumped circuit elements*, which in the analogy between electrical networks and acoustical systems correspond to *lumped* model elements.
- In the time-domain, the correspondence between a WGF and the lossless, distributed physical model it implements is *exact*. The correspondence between a WDF and the physical system it implements is *not exact*, because frequency-dependent units are discretised using the bilinear transform [9].
- WGFs are formulated using the wave decomposition $P = (P^+ + P^-), U = (P^+ - P^-)/Z$, and WDFs are formulated using the wave decomposition $P = (P^+ + P^-)/2, U = (P^+ - P^-)/2R$.

### 3.4.2 A Re-definition of DWG Techniques and WDF Techniques

In this section we work towards a definition of DWG techniques and WDF techniques such that they are compatible in application to acoustical systems. Two issues need to be clarified beforehand:

- The definition of DWG models is wider than that of WGFs. While WGF sections model uniform cylindrical sections, DWG models may include sections that implement conical tubes (e.g., in [148, 119]). DWG models may also include any type of other digital filter to represent a lumped reflectance (e.g., a bell reflectance) or transmittance phenomenon (e.g., lumped propagation losses).
- Several overlaps between WDF techniques and DWG techniques can be found in the literature. For example, in [119], the bilinear transform (that is normally associated with WDF techniques) is applied in a DWG modelling context. Furthermore, *unit elements*, which are equivalent to short transmission-line sections, have been modelled in WDF theory such that the resulting digital structure is equivalent to a short bi-directional delay-line [51].

[8] In WDF theory, $N$-port junctions are called $N$-port *adaptors*.
[9] The bilinear transform causes frequency-warping effects [109].

Given the above, we "re-define" DWG techniques and WDF techniques such that there remain two fundamental differences:

- DWG models are based on distributed models (which are spatially discretised at a fixed spatial resolution), and WDFs are based on lumped elements (which are discretised in a way that is independent of their spatial dimensions).
- In DWG modelling, the port-resistance is always equal to the characteristic impedance, and as a consequence, the wave variables are always components of physical quantities[10]. In the WDF approach, the port-resistance does not necessarily equal the characteristic impedance, and therefore the wave variables are not necessarily physical quantities.

In classical WDF theory, the wave variables are voltage waves, and DWG models are usually formulated using pressure waves. In order to ensure compatibility between the two techniques, we define that the decomposition into travelling waves is always carried out by:

$$P = P^+ + P^-, \tag{3.60a}$$

$$U = \frac{P^+ - P^-}{R}. \tag{3.60b}$$

where $R$ is the port-resistance.

The choice between using DWG techniques and WDF techniques is mainly dependent on the dimensions of the acoustical element that is to be simulated. This can be illustrated with the following example. Consider the pipe with local volume expansion in figure 3.18. The volume expansion can be modelled as a DWG model, based on a piecewise cylindrical bore approximation of the volume shape. Alternatively we can model it using WDF techniques as described in section 3.3.2. Let's assume a desired model bandwidth of $BW =$ 10kHz, a sample rate $f_s = 44.1$kHz, and a free wave velocity $c = 343$m/s. The smallest acoustic wavelength is then $\lambda = c/BW = 34.3$mm, and the spatial sampling interval of the DWG model with highest possible spatial resolution (i.e., the Kelly-Lochbaum model) is $\Delta x = cT/2 = 3.89$mm. If the length of the volume expansion is of the same order as the spatial sampling interval, then the volume is not well simulated with a DWG model, because the spatial resolution is too low for a good approximation of the volume shape (see figure 3.18). Assuming that all dimensions of $V$ are of the same order as the sampling interval, it follows that they are small in comparison with the acoustic wavelength. Thus, the acoustical behaviour of the volume is well described by a lumped element model and as a consequence, a WDF model will provide good results in this case. On the other

[10] By "physical quantaties" we mean quantaties that *in principle* can be directly physically measured.

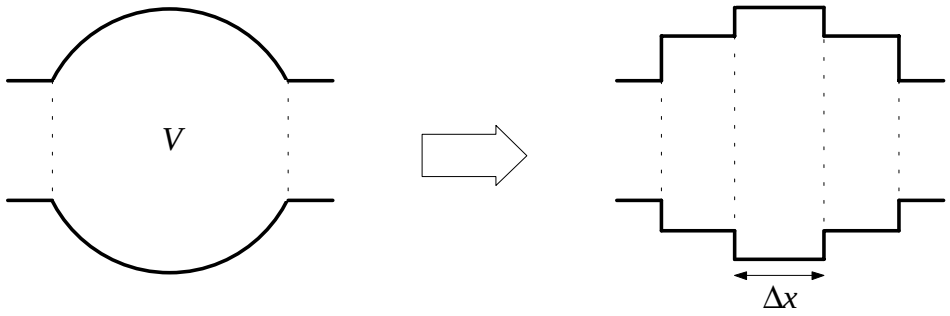


Figure 3.18: Piecewise cylindrical bore approximation of a small volume shape. The section length $\Delta x = cT/2$ is the smallest possible section length in a DWG model. Because the length of the volume is relatively small in comparison with $\Delta x$, the piecewise approximation is not very accurate.

hand, if the dimensions of $V$ are large in comparison with the acoustic wavelength, a lumped element model is inaccurate at the higher frequencies, thus a WDF model would not form an accurate simulation. Since $\lambda > \Delta x$, it follows that in this case the length of the volume expansion is large in comparison with the spatial sampling interval, thus a more accurate piecewise bore model approximation is possible. Provided that *only* the length of the volume expansion is large in comparison with the acoustic wavelength, the acoustical behaviour of the volume is then be accurately simulated with a one-dimensional DWG model.

### 3.4.3 Wave Digital Modelling

A suitable name for the combined approach is "wave digital modelling" (WD modelling), since both DWG techniques and WDF techniques use *wave* variables in the *digital* domain. It is advantageous to use this combined approach because, as seen in the last section, DWG and WDF techniques are complementary in the sense that the DWG approach works well for simulation of long acoustic systems (that may be treated as distributed acoustic elements), and the WDF approach works well for small acoustic systems (that may be treated as lumped acoustic elements).

We note that an extensive study has recently been carried out by Bilbao [30] on strongly related techniques for discrete-time modelling of vibrating systems. Bilbao's work addresses the more general problem of numerically solving partial differential equations (PDEs) by means of methods that use wave variables. While the methods used in the present study are limited to simulation of one-dimensional waveguides, Bilbao discusses multidimensional (MD) systems. However, the process of deriving a discrete-time simulation consists of the same steps: given a set of PDEs that describes a certain physical system, the first step is to derive an equivalent network of this system, and the second

step is to introduce wave variables and apply some form of discretisation. As shown by Bilbao, WDF and DWG modelling techniques can in fact be unified as alternative cases of a more general class of finite difference schemes for numerical integration of PDEs. This larger class is referred to by Bilbao as "wave" or "scattering" methods. The wave digital modelling approach developed in the present study can be considered as a specific subset of this larger class of methods.

### 3.4.4 Frequency Warping

A possible disadvantage of mixing WDF techniques with DWG modelling techniques is that the frequency-axis is different for the elements derived with these methods; elements derived with WDF techniques have a frequency axis that is warped by the BT [109], while no such frequency warping occurs for elements derived with DWG modelling techniques. However, distortion of the frequency axis can occur with using DWG modelling techniques due to aliasing effects. If we assume that the signal variables of a wave digital model are band-limited, so that aliasing effects are negligible, the two approaches are only exactly compatible at frequency $\omega = 0$ (DC); away from DC they diverge. Via variation of the value of the bilinear operator (the coefficient $\beta$ in equation (3.40)), the BT allows one more WDF frequency to be matched to a DWG frequency. Hence in principle it is possible to match the resonance frequency of a WDF element compatibly to the DWG frequency axis. For example, this approach is potentially useful for accurate modelling of the resonance of a brass mouthpiece.

However, one may also argue that if the sampling frequency of the wave digital model is chosen sufficiently high, the warping effects due to the BT will always be very small in the frequency range that is important with respect to modelling the vibrations inside the bore of the instrument. That is, the frequencies below the cut-off of the bore (which for wind instruments is usually between 1 and 3 kHz) are far more important with respect to the sound generation mechanism than the frequencies above cut-off. Hence one may construct a discrete-time model of a wind instrument in which the bore is modelled accurately only at low frequencies; the "engine" for generating vibrations inside the bore can be simulated this way, and the generated vibrations will be accurate at low frequencies. The high frequency components are not modelled accurately, but this only affects the sound that is radiated from the instrument, and can be compensated by applying an appropriate filter. An additional reason for taking such a "low-frequency engine" approach is that many of the acoustic theories from which efficient discrete-time models can be derived are valid only for a limited bandwidth. For example, the woodwind tonehole model discussed in chapter 5 has been shown to agree with experimental results only up to 5kHz.

Within the "low-frequency engine" approach, the main thing to consider with respect

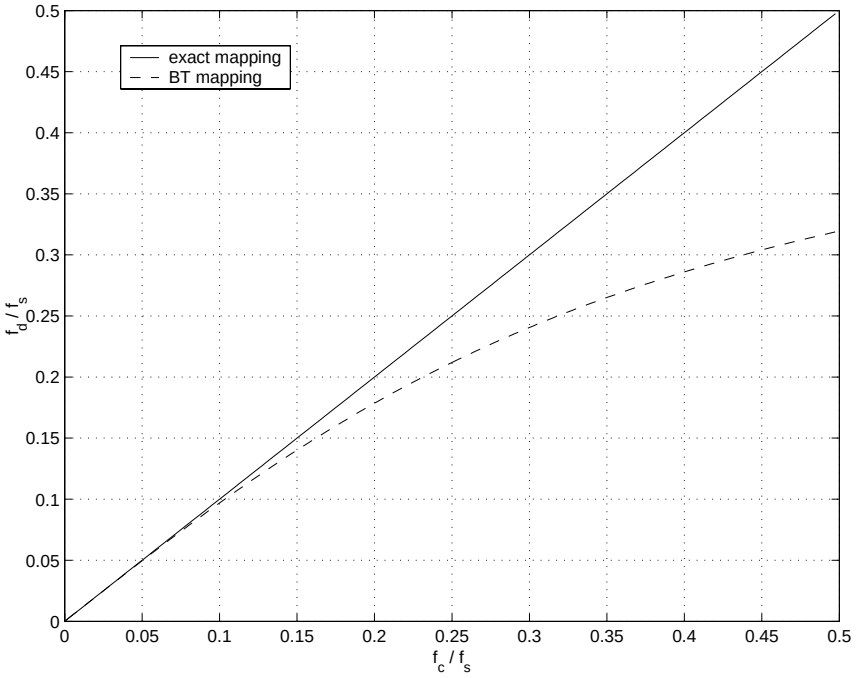


Figure 3.19: Mapping between the normalised continuous-time and discrete-time frequencies resulting from the bilinear transform.

to frequency warping effects is the level of warping at the highest relevant frequency. When using the customary value $\beta = 2f_s$, the warping introduced with the BT can be expressed with the relationship [109]:

$$\Omega_d = \frac{1}{\pi} tan^{-1}(\pi\Omega_c), \tag{3.61}$$

where $\Omega_c$ is the continuous-time frequency $f_c$ divided by the sample rate $f_s$ and $\Omega_d$ is resulting discrete-time frequency $f_d$, also divided by $f_s$. The plot of this relationship in figure 3.19 demonstrates that the warping increases with frequency. From equation (3.61) one may derive that the difference between $f_c$ and $f_d$ is smaller than 1 percent at frequencies below $0.05f_s$. For instance, the warping effect is smaller than 1 percent at frequencies below 2.4kHz when using a standard audio sample rate $f_s = 44100$. We note that wave digital models do generally not exhibit the exact BT-warping; this is because only parts of the model are discretised using the BT. Nevertheless, the mapping relation plotted figure 3.19 provides useful information when deciding on wave digital simulation parameters such as the sample rate.

## 3.5 Conclusions

In this chapter we have discussed various techniques for discrete-time modelling of linear acoustic tubular systems. In section 3.1 we have seen that the basic feedback structure

for modelling a musical wind instrument can be numerically solved using the reflection function method without making the traditional assumption of a zero instantaneous reflection. We did not discuss how the reflection function can be derived from an acoustical measurement. For a detailed discussion of this subject, we refer to Gazengel et al. [54]. Convolution methods, such as the full reflection method, are not particularly suitable for application in a musical sound synthesis context. However, they provide a means for verification of and comparison with the other techniques employed in this study.

In section 3.2, the basic principles and properties of digital waveguide modelling were discussed. While DWG modelling techniques are well-established in the context of physical modelling, previous applications of wave digital filter techniques (or techniques akin to these[11]) to musical acoustics have been very sporadic. The systematic application of WDF techniques to simulation of lumped elements in a model of an acoustical bore, as discussed in section 3.3, is a novelty. We have seen in section 3.4 that these techniques can be combined to form a more general discrete-time modelling approach ("wave digital modelling"), in which model units are discretised with WDF or DWG techniques according to whether they are best approximated as distributed or lumped elements, respectively.

[11] Van Duyne et al. [153] and Borin and Rochesso [31] have applied techniques that are similar to WDF techniques.

# Chapter 4

# Digital Waveguide Modelling of Non-Flaring Bores

In this chapter, discrete-time modelling of wave propagation in cylindrical and conical bores by means of digital waveguide (DWG) modelling techniques is discussed. The DWG modelling approach is based on efficient simulation of lossless wave propagation by means of delay-lines [130, 148, 119]). The main challenge within the approach is to maintain a good balance between accuracy, stability and efficiency when adding more complexities to the model, such as viscothermal losses and tubular junctions.

The chapter is organised as follows. In the first section we briefly discuss the application of digital waveguide modelling techniques to simulation of wave propagation in cylindrical bores. It is well known that the delay-lines that are employed in digital waveguide modelling need to be interpolated for simulation of wave propagation in bores of arbitrary length [130, 148]. Fractional delay filters can be used for this purpose, and we briefly review this topic in section 4.2. In the last two sections of the chapter we discuss discrete-time modelling of wave propagation in conical bores. The basic simulation principles and formulae are given in section 4.3, and in section 4.4 we investigate the stability properties of these simulations.

## 4.1 Cylindrical Bores

### 4.1.1 Lossless Wave Propagation

In section 2.2.1 we have seen that one-dimensional, lossless wave propagation in cylindrical bores is described by the equation:

$$\frac{\partial^2 p}{\partial x^2} = \frac{1}{c^2}\frac{\partial^2 p}{\partial t^2}. \tag{4.1}$$

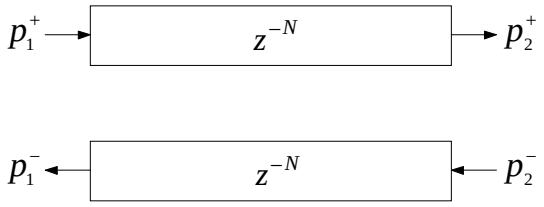


Figure 4.1: Wave propagation in a cylindrical bore simulated by means of a bi-directional delay-line. The $z^{-N}$ unit indicates a delay-line of length $N$.

As discussed in section 3.2, wave motion governed by this wave equation can be simulated by means of digital waveguide techniques. In the case of modelling a cylindrical pipe of length $L$, the delay-time associated with travelling from one end to the other is $L/c$. Given a sample period $T = 1/f_s$, wave propagation in the pipe is simulated with a bi-directional delay-line of length $N = L/(c\,T)$ (see figure 4.1). We note that the delay-lines can only be realised in discrete-time for integer values of $N$, hence this formulation has the limitation that the length of the pipe must be equal to a multiple of the spatial sampling interval $\Delta x = c\,T$. As discussed in section 3.2.1, the pressure at a specific point $x$ along the pipe axis is found by summing the forward- and the backward-travelling waves at that point.

### 4.1.2 A Junction of Two Cylindrical Sections

Some wind instrument bores contain a discontinuity in diameter. The wave scattering at the discontinuity can be modelled as a junction of the two cylindrical sections of different cross-section (see figure 4.2). In section 2.3.3, the scattering equations for this type of junction were found to be (equation (2.80)):

$$\begin{bmatrix} P_1^+ \\ P_1^- \end{bmatrix} = \frac{1}{2} \begin{bmatrix} 1 + \frac{Z_1}{Z_2} & 1 - \frac{Z_1}{Z_2} \\ 1 - \frac{Z_1}{Z_2} & 1 + \frac{Z_1}{Z_2} \end{bmatrix} \begin{bmatrix} P_2^+ \\ P_2^- \end{bmatrix}. \tag{4.2}$$

Computation of wave scattering in a discrete-time model has to be carried out in a causal order, hence we need to know how the *reflected* waves $P_2^+$ and $P_1^-$ are computed from the *incident* waves $P_1^+$ and $P_2^-$:

$$\begin{bmatrix} P_2^+ \\ P_1^- \end{bmatrix} = \begin{bmatrix} \frac{2Z_2}{Z_2+Z_1} & -\frac{Z_2-Z_1}{Z_2+Z_1} \\ \frac{Z_2-Z_1}{Z_2+Z_1} & \frac{2Z_1}{Z_2+Z_1} \end{bmatrix} \begin{bmatrix} P_1^+ \\ P_2^- \end{bmatrix}. \tag{4.3}$$

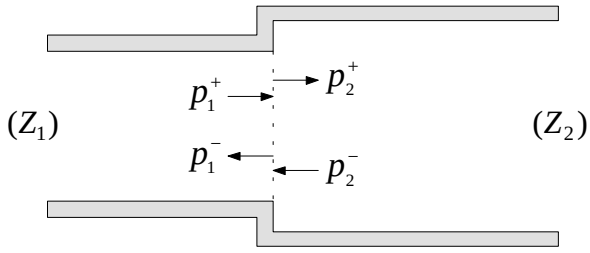


Figure 4.2: A junction of two cylindrical bore sections.

The scattering equation can be written in a more compact form if all matrix elements are expressed in terms of the *junction reflection coefficient* $k_j$:

$$\begin{bmatrix} P_2^+ \\ P_1^- \end{bmatrix} = \begin{bmatrix} 1+k_j & -k_j \\ k_j & 1-k_j \end{bmatrix} \begin{bmatrix} P_1^+ \\ P_2^- \end{bmatrix}, \tag{4.4}$$

with

$$k_j = \frac{Z_2 - Z_1}{Z_2 + Z_1}. \tag{4.5}$$

If viscothermal losses are neglected, then we may write:

$$k_j = \frac{S_1 - S_2}{S_1 + S_2}. \tag{4.6}$$

For computation in discrete-time, it is advantageous to formulate the scattering equations in one-multiplier form [148]:

$$P_2^+ = P_1^+ + W, \tag{4.7a}$$
$$P_1^- = P_2^- + W, \tag{4.7b}$$

with the intermediate variable

$$W = k_j \left[ P_1^+ - P_2^- \right]. \tag{4.8}$$

The signal flow diagram for wave scattering at a junction of two cylindrical tube sections is depicted in figure 4.3. As mentioned in section 3.2.4, this type of junction is often referred to as a *Kelly-Lochbaum* (KL) junction [92, 130, 148]. The one-multiplier form is typically useful in applications where the computational efficiency is a high priority.

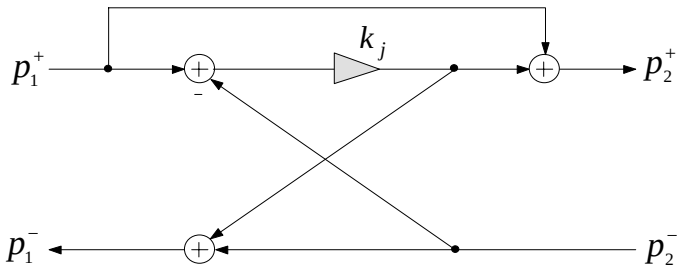


Figure 4.3: A Kelly-Lochbaum junction in one-multiplier form.

### 4.1.3 Inclusion of Viscothermal Losses

If viscothermal losses are taken into account, wave propagation over a length $L$ can be represented with the transfer function:

$$\hat{H}(\omega) = e^{-\Gamma L}, \tag{4.9}$$

where $\Gamma$ is the lossy propagation constant as defined in equations (2.57) in section 2.2.3. The lossy transfer function $\hat{H}(\omega)$ contains the same delay-term as the lossless transfer function $H(\omega) = e^{-j\,\omega\,L/c}$. As in the lossless case, this delay can be simulated by means of a delay-line. What remains is to model the propagation losses, which are defined as:

$$H_{loss}(\omega) = \frac{\hat{H}(\omega)}{H(\omega)} = \frac{e^{-\Gamma\,L}}{e^{-j\,\omega\,L/c}}. \tag{4.10}$$

We can approximate the propagation losses with a digital filter, and implement the complete propagation path by cascading this "loss-filter" with the delay-line. The resulting lossy digital waveguide structure is depicted in figure 4.4.

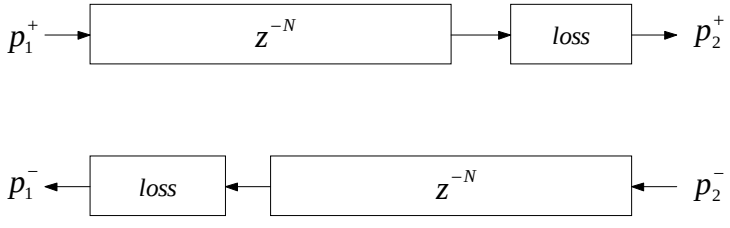


Figure 4.4: Digital waveguide model of a cylindrical bore taking into account viscothermal losses. Each *loss* unit indicates a digital filter approximation of the losses associated with travelling from one end of the bore to the other.

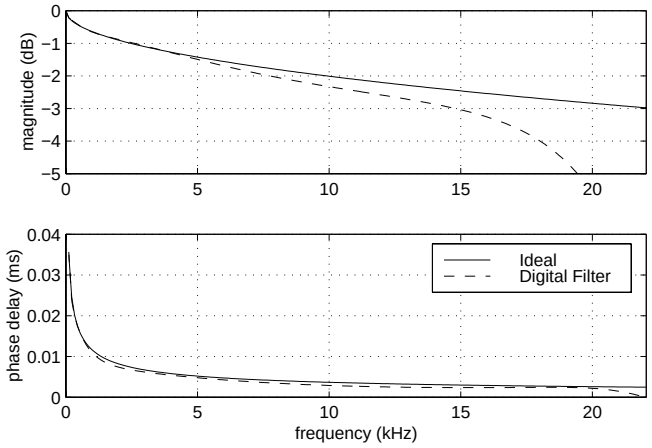


Figure 4.5: Digital filter approximation of the propagation losses of a cylindrical bore using the output-error minimisation method. The bore length was taken such that the propagation delay equals $50\,T$ seconds, which corresponds to a length of $L \approx 389$mm using a sample rate $f_s = 44.1$kHz. The minimisation was done using a weighted least-square error, whereby the weighting was chosen such that the digital filter will have a good fit at the lower frequencies.

The most straightforward way to approximate the propagation losses is by means of an FIR filter [151]. However, IIR filters are generally more powerful approximators [109], thus an IIR filter approximation is likely to result in a better balance between accuracy and efficiency. Since in wind instrument modelling, the lower frequencies (i.e. the frequencies below cut-off) are of more importance than the higher frequencies (i.e. the frequencies above cut-off), the IIR filter design must be carried out such that the resulting digital filter forms a good fit at the lower frequencies, possibly at the cost of increased discrepancy at the higher frequencies. This can be achieved with the use of iterative, frequency-weighted error minimisation techniques. Here we applied the *output-error minimisation* technique[1] [127], which uses iterative gradient descent search methods to minimise a weighted least-square approximation error. This method has previously been applied to modelling viscothermal wave propagation by Scavone [119]. The frequency response of a 5th-order IIR approximation designed using this technique is compared with $H_{loss}(\omega)$ in figure 4.5.

In order to model the scattering at a junction of two cylindrical tube sections while taking into account the effects of viscothermal losses, the scattering junction equations must be re-derived using lossy formulations of the characteristic impedances. Therefore we may model the junction as in figure 4.2, but with the junction reflection coefficient $k_j$ replaced with a digital junction reflection filter. The ideal response of the junction filter is:

$$K_j(\omega) = \frac{Z_2(\omega) - Z_1(\omega)}{Z_2(\omega) + Z_1(\omega)}, \tag{4.11}$$

[1] Implemented in *MATLAB*® with the function `invfreqz`.

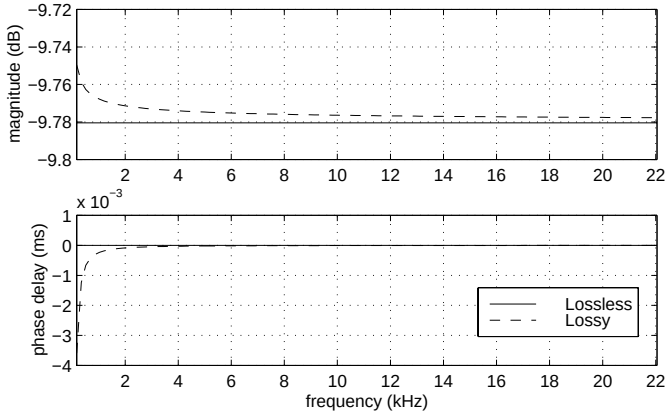


Figure 4.6: Frequency response of the reflection filter of a cylindrical junction, with radii $a_1 = 7mm$ and $a_2 = 5mm$. The figure makes clear that the discrepancy between the junction reflection filter $K_j(\omega)$ and the "lossless" junction reflection coefficient $k_j$ is extremely small.

where the characteristic impedances $Z_1$ and $Z_2$ are defined by (2.57). The frequency response of the junction reflection filter is compared with the junction reflection coefficient (as used in the lossless case) in figure 4.6. Because the discrepancy is extremely small, the effects of viscothermal losses on modelling cylindrical junctions are usually neglected. Hence in discrete-time modelling, the Kelly-Lochbaum model (see figure 4.3) can be applied without introducing any significant errors.

## 4.2 Fractional Delays

So far in this chapter, the length of a delay-line has been restricted to an integer multiple of the sample period. In other words, only a limited number of bore lengths (on a linear grid) can be simulated in this way (see figure 4.7). The length of a real acoustical instrument bore will in most cases not fall on this grid. Therefore interpolating methods are required in order to simulate a delay-line of non-integer or *fractional* length. This can be achieved by cascading the delay-line with a digital filter that has a *phase delay* that approximates the fractional delay in the important frequency range (see figure 4.8). A digital filter

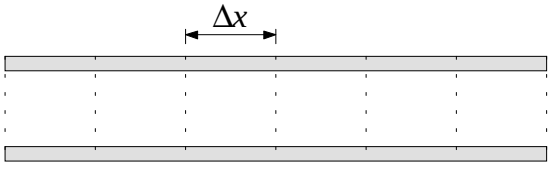


Figure 4.7: The length of bore simulated with the use of a delay-line has to be a multiple of the spatial sampling interval $\Delta x = cT$.

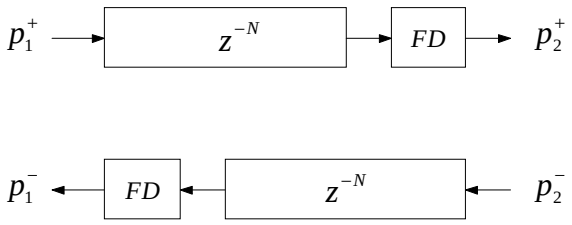


Figure 4.8: Digital waveguide simulation of a cylindrical bore of arbitrary length. The delay associated with wave propagation in backward- and forward-direction is modelled with a cascade of a delay-line ($z^{-N}$) and a fractional delay filter ($FD$).

applied in this way is referred to as a *fractional delay* (FD) filter. In general, an FD filter is designed to approximate the transfer function of the *ideal* fractional delay:

$$H_{id}(\omega) = e^{-j\omega d}, \tag{4.12}$$

which, at all frequencies, has a flat magnitude response that equals unity and a phase delay that equals $d$. Extensive research on the subject of FD filter design has been carried out in recent years [85, 86, 151, 147, 148]. In this section we will only review the most commonly applied types of fractional delay filters, namely *Lagrange FIR interpolation filters* and *Thiran allpass interpolation filters*.

### 4.2.1 Lagrange FIR Interpolation Filters

Lagrange FIR interpolation filters are based on the classical Lagrange interpolation method. Given a fractional delay $D = d/T$ (where $d$ is the actual delay-time), the FIR filter coefficients are computed [148]:

$$h(n) = \prod_{\substack{k=0 \\ k \neq n}}^{N} \frac{D-k}{n-k} \quad \text{for n = 0,1,2,...N,} \tag{4.13}$$

where $N$ is the order of the FIR filter. The main advantage of designing a FIR interpolator by means of classical Lagrange interpolation is that the resulting filter has a maximally flat error-function at $\omega = 0$ [148]. A possible disadvantage is that FIR interpolators are lowpass filters, i.e. the higher frequencies are attenuated, whereas the ideal delay has unity magnitude. Välimäki [148] has found that the Lagrange FIR filters are passive only for delays in a certain range that depends on the filter order. When $N$ is odd, the delay

should be chosen such that

$$(N-1)/2 \leq D \leq (N+1)/2, \tag{4.14}$$

and when $N$ is even, the delay should be chosen so that

$$(N/2) - 1 \leq D \leq (N/2) + 1. \tag{4.15}$$

An additional advantage of the restrictions set in (4.14) and (4.15) is that the FIR filter has the smallest approximation error at the lower frequencies for delays in these "optimum" ranges. Since the lower frequencies are the most vital to the tuning of an instrument bore, it makes sense to have an FD filter that approximates the ideal delay most closely in this frequency range.

### 4.2.2 Thiran Allpass Filters

Allpass filters are filters that have unity magnitude [109]. The transfer function of a digital allpass filter is:

$$H(z) = \frac{a_N + a_{N-1}z^{-1} + \ldots + a_1 z^{(N-1)} + z^{-N}}{1 + a_1 z^{-1} + \ldots + a_{N-1}z^{-(N-1)} + a_N z^{-N}}, \tag{4.16}$$

where $N$ is the order of the filter, and $a_k \quad (k = 1, 2, \ldots N)$ are the filter coefficients. The allpass filter design that is most suitable in the context of digital waveguide modelling is the *Thiran* allpass design, because the resulting filter has a maximally flat group delay at $\omega = 0$ [86, 148]. The coefficients of the Thiran allpass filter that implements a fractional delay $D$ are:

$$a_k = (-1)^k \left[ \begin{array}{c} N \\ k \end{array} \right] \prod_{n=0}^{N} \frac{D - N + n}{D - N + k + n} \quad \text{for} \quad k = 0, 1, 2, \ldots, N, \tag{4.17}$$

with the binomial coefficient

$$\left[ \begin{array}{c} N \\ k \end{array} \right] = \frac{N!}{k!(N-k)!}. \tag{4.18}$$

Such a filter is stable only when $D > N - 1$ [148]. Furthermore, the minimum average discrepancy between filter response and an ideal fractional delay is obtained for [148]:

$$N - 0.5 \leq D < N + 0.5. \tag{4.19}$$

Hence in the case of a Thiran allpass filter, the order $N$ is best chosen as the integer nearest to $D$.

### 4.2.3 Fractional Delay Filter Comparison

In order to carry out a meaningful comparison between the allpass IIR and the Lagrange FIR design approach, we require that within a 5kHz bandwidth the following criteria have to be met:

- The magnitude response discrepancy should not exceed 1dB.
- The phase delay response should not differ from the ideal delay by more than 2% of the sample period.

Given a sample rate of $f_s = 44.1$kHz, the lowest order filters that meet these conditions are the third-order Lagrange interpolator and the second-order Thiran allpass filter. The frequency responses of these filters are shown in figures (4.9) (4.10), and (4.11).

Frequency-Domain Comparison

A frequency-domain comparison does not seem to favour either of the two filters. The third-order Lagrange interpolation filter has a slightly better phase delay fit while on the other hand, the Thiran allpass interpolation filter has no frequency attenuation.

Time-Domain Comparison

A physical model of a musical instrument is usually computed in the time domain due to the nonlinearity of the sound generation mechanism. Figure 4.12 compares three different methods for digital approximation of a Dirac pulse delayed by the (fractional) time $d = 2.49T$ seconds. In all three cases, the response shows a kind of "rippled" distortion of the original (continuous-time) Dirac pulse, where the IFFT result clearly exhibits the strongest ripple.

Computational Efficiency Comparison

At first sight, it might appear that the third-order Lagrange FIR filter is computationally less expensive than the second-order Thiran allpass IIR filter, since in general, a direct-form filter realisation of an $Nth$-order IIR filter requires $2N+1$ multiplications, whereas an $Nth$-order FIR filter uses $N+1$ multiplications. However, due to the (Hermitian) mirror-image symmetry relation between the numerator and denominator polynomials of an allpass transfer function, the Thiran allpass filter can be computed using only $N$ multiplications [112]. In the case of the second-order Thiran allpass filter, the filter difference equation can be written:

$$y(n) = a_2\,[x(n) - y(n-2)] + a_1\,[x(n-1) - y(n-1)] + x(n-2), \qquad (4.20)$$

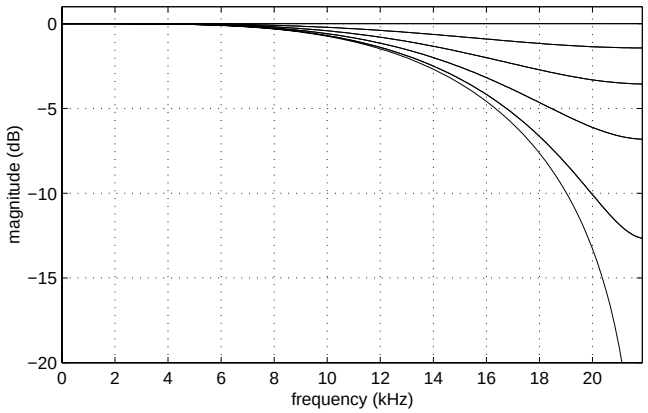


Figure 4.9: Magnitude response of a third-order Lagrange FIR interpolation filter, computed for eleven different delay values in its optimum range ($D = 1, 1.1, 1.2, ..., 2.0$). Note that the figure only exhibits five curves because the delays $D$ and $N - D$ result in the same magnitude response.

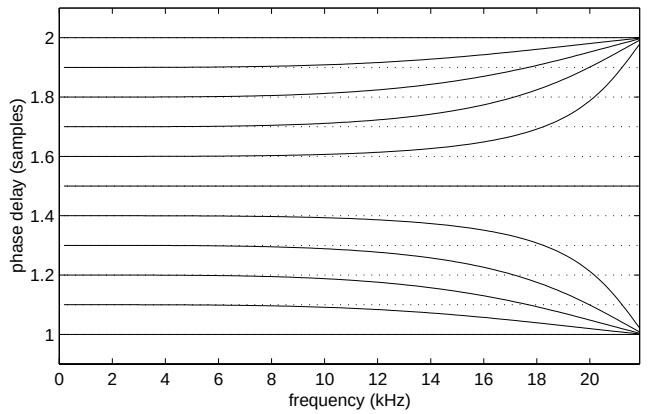


Figure 4.10: Phase delay response of a third-order Lagrange FIR interpolation filter, computed for eleven different delay values in its optimum range ($D = 1, 1.1, 1.2, ..., 2.0$).

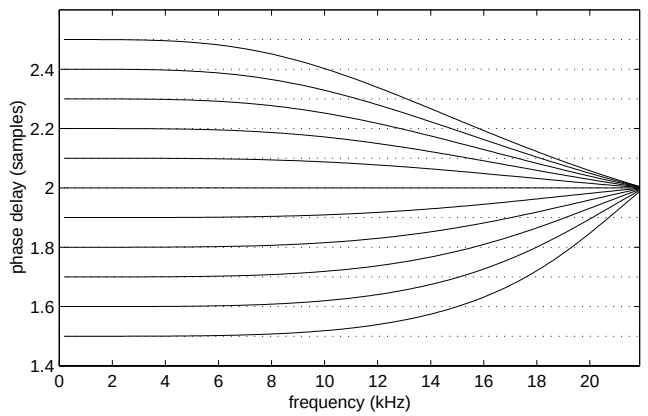


Figure 4.11: Phase delay response of a second-order Thiran allpass interpolation filter, computed for eleven different delay values in its optimum range ($D = 1.5, 1.6, 1.7, ..., 2.5$).

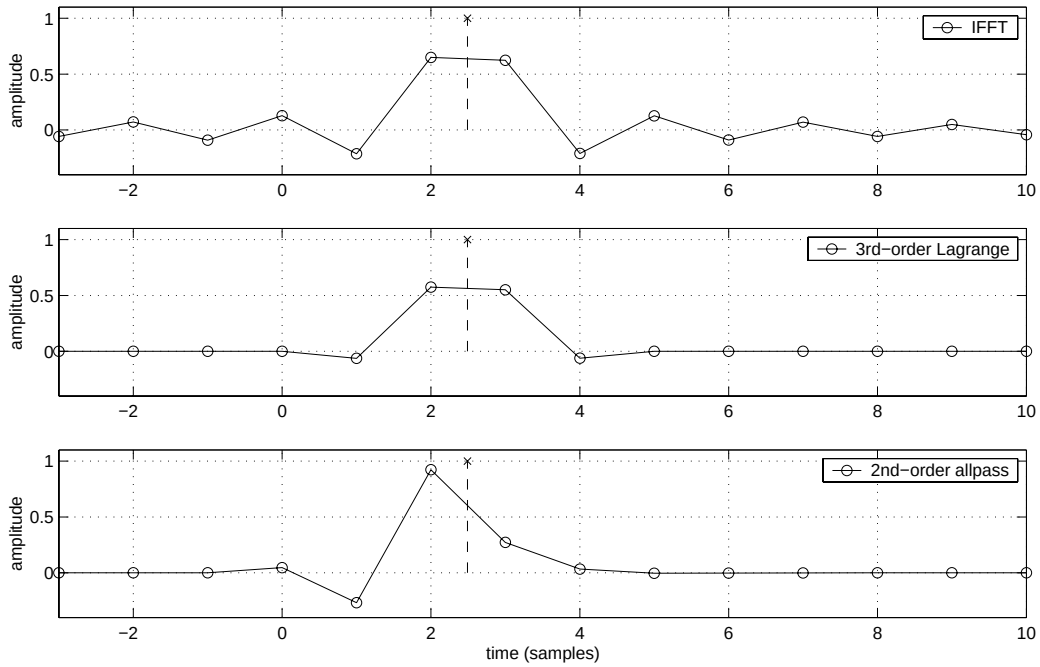


Figure 4.12: Digital approximation of an Dirac pulse delayed by $d = 2.49T$ seconds by means of an IFFT (top), a third-order Lagrange interpolator (middle), and a second-order Thiran allpass interpolator (bottom). The dashed line indicates the delayed Dirac pulse as it would be in continuous time. The sample rate is 44.1kHz.

where $a_1$ and $a_2$ are the filter coefficients as given by (4.17), and where $x(n)$ is the input and $y(n)$ is the output of the filter. The second-order Thiran allpass filter thus requires only two multiplications, two less than the third-order Lagrange FIR filter.

Time-Varying Fractional Delays

In some applications, the length of the bore needs to be gradually adjusted during operation. For example, this would be the case in a discrete-time simulation of a trombone slide. This means that the delay-time and as a consequence, the coefficients of the FD filter are time-varying. In the case of an FIR filter, varying the filter coefficients over time does not introduce any significant numerical problems. On the other hand, the output of an IIR filter exhibits transient effects whenever filter coefficients are updated. These transients can be largely suppressed using "transient-elimination techniques" [152, 148]. However, this increases the computational costs of the IIR filter implementation. Hence for time-varying applications, the Lagrange FIR design appears to be more suitable.

Suppression of Aliasing Effects

Simulation of sustained wind instrument oscillations inevitably involves some form of non-linear excitation of the air column resonances. As a consequence, a series of higher harmonics is generated. This may lead to aliasing effects, because the non-linearity can result in generation of frequencies above the Nyquist frequency. A possible way to suppress these aliasing-effects is to employ a lowpass filter. That is, if the frequencies close to Nyquist are strongly attenuated, then the multiples of these frequencies that are generated by the non-linear driving in the system will be of small amplitude. Thus, whilst the response of a wind instrument is already typically lowpass, the extra attenuation introduced when using Lagrange interpolators may further help to suppress aliasing effects.

In summary, the Lagrange FIR approach appears to be preferable to the Thiran allpass approach in designing fractional delay filters in application to physical modelling of wind instruments, because (1) FIR filters result in less numerical artefacts than IIR filters in time-varying applications, and (2) the lowpass magnitude response of Lagrange FIR filters is useful for the suppression of aliasing effects.

## 4.3 Conical Bores

### 4.3.1 Lossless Wave Propagation

As seen in section 2.2.2, the wave equation that describes lossless wave propagation in a conical bore is:

$$\frac{\partial^2 p}{\partial r^2} + \frac{2}{r}\frac{\partial p}{\partial r} = \frac{1}{c^2}\frac{\partial^2 p}{\partial t^2}, \tag{4.21}$$

where $r$ is the cone apex distance. The pressure-wave solution of this wave equation for frequency $\omega$ is:

$$\begin{aligned} p(r,t) &= p^+(r,t) + p^-(r,t) \\ &= \frac{A}{r}e^{j(\omega t - kr)} + \frac{B}{r}e^{j(\omega t + kr)}, \end{aligned} \tag{4.22}$$

where $A$ and $B$ are arbitrary amplitudes. This travelling-wave solution is the same as for plane waves in a cylindrical bore, apart from the scaling by $1/r$. The scaling may be interpreted as the decrease of amplitude of a pressure wave (due to the spreading of the wavefront over a larger surface) as it travels away from the cone apex (see figure 4.13). For simplicity, no backward reflections from the ends of the cone are included in the figure. As was found in section 2.2.2, the Fourier transforms of the forward- and backward-

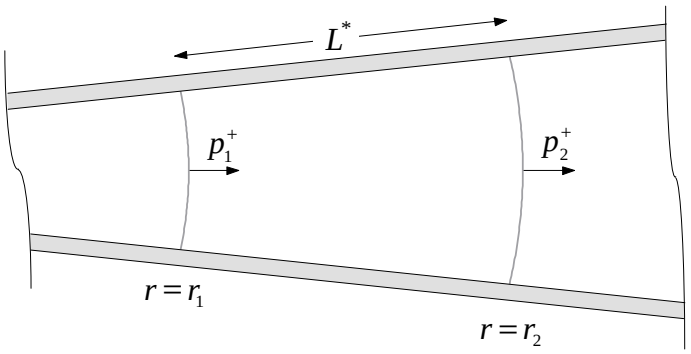


Figure 4.13: Wave propagation in a conical bore section. The amplitude of a forward-travelling wave decreases by $r_1/r_2$ as it travels the from $r_1$ to $r_2$.

propagating waves at two points $r_1$ and $r_2$ in a cone are related:

$$P_1^+(\omega) = \left(\frac{r_2}{r_1}\right)\left[e^{+j\omega L^*/c}\right]\, P_2^+(\omega), \tag{4.23a}$$

$$P_1^-(\omega) = \left(\frac{r_2}{r_1}\right)\left[e^{-j\omega L^*/c}\right]\, P_2^-(\omega). \tag{4.23b}$$

Reversing the upper equation in (4.23), and taking the inverse Fourier transforms yields

$$p_2^+(t) = g^{-1}\, p_2^+(t-D), \tag{4.24a}$$

$$p_1^-(t) = g\, p_2^-(t-D), \tag{4.24b}$$

where $g = r_2/r_1$ is a simple scaling factor, and $D = L/c$ is the delay-time, that equals the time it takes for a wave to propagate from $r_1$ to $r_2$. These relations can be modelled in discrete-time using a digital waveguide structure with added scaling by $1/g$ in the forward direction, and $g$ in the backward direction. The scaling factors may in fact be removed without changing the reflectance of the system. This is demonstrated in figure 4.14. Suppose that the conical waveguide is terminated with the spherical wave reflectance $R^*(z)$ (see figure 4.14a). The factors and delay-lines are linear and commutative, thus the order of units may be re-arranged without changing the system reflectance (see figure 4.14b). In this re-arranged system, the scaling factors clearly cancel each other out, and may be entirely removed from the system without changing the system reflectance. Note that with the scaling factors removed, the transmittance is not the same. Suppose that the forward-propagating wave $p_1^+$ has the correct amplitude, then if the actual physical value of the pressure at point $r = r_2$ of the cone is to be obtained, an "extrinsic" scaling by a factor $g$ has to be done (see figure 4.14c)).

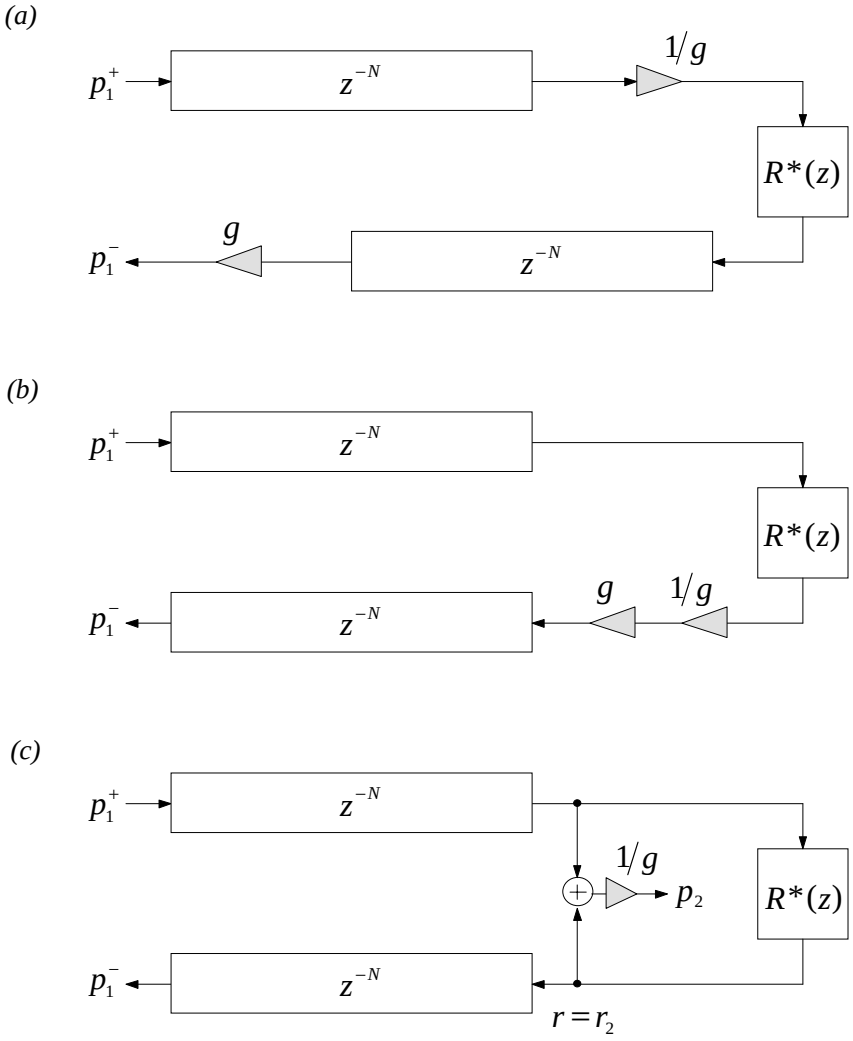


Figure 4.14: Discrete-time modelling of spherical wave propagation in a conical bore section. The cone is terminated with a spherical wave reflectance $R^*(z)$. Each $z^{-N}$ unit indicates a delay-line. The model units in (a) are linear and commutative, thus the system may be re-arranged such that the structure depicted in (b) results. For computing the reflected wave $p_1^-$, the scaling factors $g$ and $1/g$ in (b) cancel each other out, so may be removed from the system. With the scaling factors removed (c), the pressure at point $r = r_2$ is to be obtained with an "extrinsic" scaling.

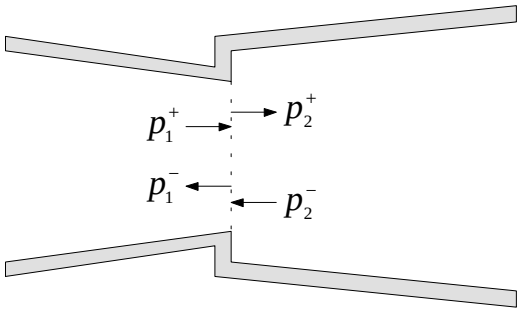


Figure 4.15: A junction of two conical bore sections.

### 4.3.2 A Junction of Two Conical Sections

The bi-directional delay-line structure in figure 4.14 implements spherical wave propagation in a conical bore section. In the case of a junction of two conical bores (see figure 4.15), the abrupt changes in diameter and taper cause wave scattering. The boundary conditions at the junction are:

$$P_1^+ + P_1^- = P_2^+ + P_2^-, \tag{4.25a}$$

$$Y_1^+ P_1^+ - Y_1^- P_1^- = Y_2^+ P_2^+ - Y_2^- P_2^-, \tag{4.25b}$$

where $Y_1^\pm = 1/Z_1^\pm$ and $Y_2^\pm = 1/Z_2^\pm$ are the characteristic admittances at the left and the right side of the junction. If viscothermal losses are neglected, these are:

$$Y_1^\pm = \left(\frac{S_1}{\rho c}\right)\left(\frac{j\omega r_1 \pm c}{j\omega r_1}\right), \tag{4.26a}$$

$$Y_2^\pm = \left(\frac{S_2}{\rho c}\right)\left(\frac{j\omega r_2 \pm c}{j\omega r_2}\right), \tag{4.26b}$$

where $S_1$ and $S_2$ are the wave areas and $r_1$ and $r_2$ are the cone apex distances at the left and right side of the junction, respectively. Solving for $P_1^+$ and $P_2^-$ gives the scattering equation:

$$\begin{bmatrix} P_2^+ \\ P_1^- \end{bmatrix} = \begin{bmatrix} T^+(\omega) & R^+(\omega) \\ R^-(\omega) & T^-(\omega) \end{bmatrix} \begin{bmatrix} P_1^+ \\ P_2^- \end{bmatrix}, \tag{4.27}$$

with the scattering matrix elements

$$T^+(\omega) = \frac{Y_1^+ + Y_1^-}{Y_1^- + Y_2^+}, \tag{4.28a}$$

$$R^+(\omega) = \frac{Y_1^+ - Y_2^+}{Y_1^- + Y_2^+}, \tag{4.28b}$$

$$R^-(\omega) = \frac{Y_2^- - Y_1^-}{Y_1^- + Y_2^+}, \tag{4.28c}$$

$$T^-(\omega) = \frac{Y_2^+ + Y_2^-}{Y_1^- + Y_2^+}. \tag{4.28d}$$

Since we have

$$T^+(\omega) = 1 + R^-(\omega), \tag{4.29a}$$

$$T^-(\omega) = 1 + R^+(\omega), \tag{4.29b}$$

the scattering equations can be re-written as:

$$P_2^+ = \left[1 + R^-(\omega)\right] P_1^+ + R^+(\omega)\, P_2^-, \tag{4.30a}$$

$$P_1^- = R^-(\omega)\, P_1^+ + \left[1 + R^+(\omega)\right] P_2^-. \tag{4.30b}$$

After substitution of (4.26), the reflectances $R^+(\omega)$ and $R^-(\omega)$ can be expressed:

$$R^+(\omega) = -\left(\frac{B-1}{B+1}\right) - \frac{2\alpha}{(B+1)\,(j\omega + \alpha)}, \tag{4.31a}$$

$$R^-(\omega) = \left(\frac{B-1}{B+1}\right) - \frac{2B\alpha}{(B+1)\,(j\omega + \alpha)}. \tag{4.31b}$$

where $B = S_1/S_2$ is the ratio of the wavefront areas at the junction, and $\alpha$ is given by

$$\alpha = \frac{2\,(\gamma_2 S_2 - \gamma_1 S_1)}{S_2 + S_1}, \tag{4.32}$$

where $\gamma_1 = c/2r_1$ and $\gamma_2 = c/2r_2$. The value of $\gamma_x$ (at point $r_x$ along the cone wall) is of the dimension of frequency, and $1/\gamma_x$ may be interpreted as the (virtual) *round-trip time* of a wave travelling from the cone apex to $r_x$ and back. For a diverging cone (small end on the left, large end on the right), $\gamma$ is positive, and for a converging cone (small end on the right, large end on the left), $\gamma$ is negative. For a cylindrical bore, which can be considered as a special case of a conical bore, we have $\gamma = 0$. The term $(B-1)/(B+1)$ in both reflectances in (4.31) results only from the wavefront area discontinuity, and vanishes if the wavefront areas are equal. The remaining terms in (4.31) mainly result from the taper

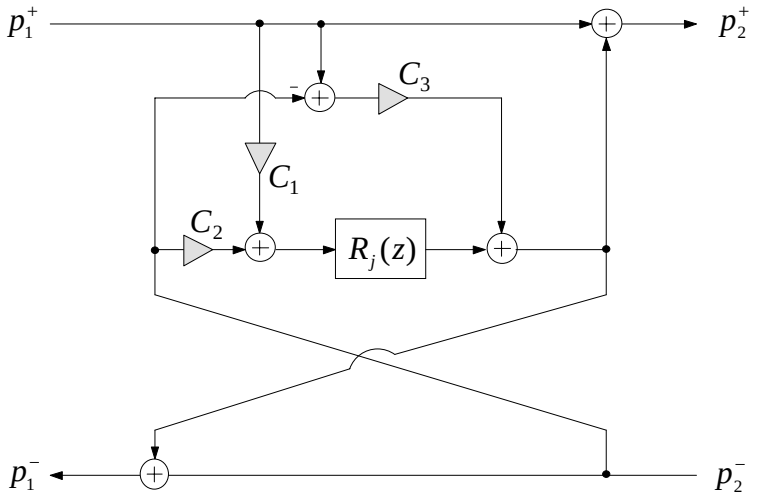


Figure 4.16: A digital waveguide junction in one-filter form.

discontinuity, and vanish for $\gamma_b = \gamma_c$. If we define the *junction filter*

$$R_j(\omega) = \frac{-\alpha}{j\omega + \alpha}, \tag{4.33}$$

and the coefficients

$$C_1 = \frac{2B}{B+1}, \tag{4.34a}$$

$$C_2 = \frac{2}{B+1}, \tag{4.34b}$$

$$C_3 = \frac{B-1}{B+1}, \tag{4.34c}$$

then the scattering equations can be written:

$$P_2^+ = P_1^+ + C_3\left[P_1^+ - P_2^-\right] + R_j(\omega)\left[C_1 P_1^+ + C_2 P_2^-\right], \tag{4.35a}$$

$$P_1^- = P_2^- + C_3\left[P_1^+ - P_2^-\right] + R_j(\omega)\left[C_1 P_1^+ + C_2 P_2^-\right]. \tag{4.35b}$$

This form is particularly efficient, since both reflected waves can be computed as the sum of an incident wave and the intermediate variable $W_1$:

$$P_2^+ = P_1^+ + W_1, \tag{4.36a}$$

$$P_1^- = P_2^- + W_1, \tag{4.36b}$$

with

$$W_1 = C_3\left[P_1^+ - P_2^-\right] + R_j(\omega)\, W_0, \tag{4.37}$$

| | impulse invariance method | time-interpolated convolution | bilinear transform |
|---|---|---|---|
| $b_0$ | $\left(-1+e^{\alpha T}\right)$ | $-1-\frac{e^{-\alpha T}-1}{\alpha T}$ | $\frac{\alpha}{\alpha+\beta}$ |
| $b_1$ | 0 | $e^{-\alpha T}+\frac{e^{-\alpha T}-1}{\alpha T}$ | $\frac{\alpha}{\alpha+\beta}$ |
| $a_1$ | $e^{-\alpha T}$ | $e^{-\alpha T}$ | $\frac{\alpha-\beta}{\alpha+\beta}$ |

Table 4.1: Coefficients of the digital junction filter. $\beta = 2/T$ is the bilinear operator.

and

$$W_0 = \left[C_1 P_1^+ + C_2 P_2^-\right]. \tag{4.38}$$

For computation in the discrete-time domain, the junction filter $R_j(\omega)$ has to be approximated with a digital filter $R_j(z)$. This filter is applied in the overall signal structure of the conical junction model as demonstrated in figure 4.16. This one-filter form of the general conical junction is more efficient than the two-filter form used in previous work [150, 148, 119] on this subject. We will refer to the structure in figure 4.16 as a *digital waveguide junction.*

What remains is the design of the digital junction filter $R_j(z)$. The problem consists of discretising the one-pole filter element

$$R_j(s) = \frac{-\alpha}{s+\alpha}. \tag{4.39}$$

It appears that in previous work on discrete-time simulation of conical bores, three different methods have been used to discretise this conical junction reflection filter. Välimäki [148] applied the impulse invariance method (IIM), whereas Scavone [119] and Amir [10] obtain a discrete-time version of the junction filter via the bilinear transform. A third method can be found in the work by Martínez et al. [94], who obtain the reflected wave by means of a recursive formulation of time-interpolated convolution of the junction filter impulse response with the incident pressure wave. We will refer to this method as the "time-interpolated convolution method" (TICM). In appendix G we show that all three methods

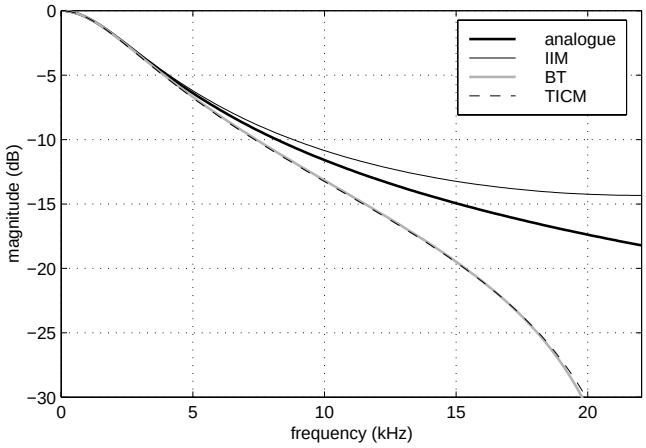


Figure 4.17: Digital approximation of the junction filter $R_j(\omega)$, with $r_1 = 10\text{mm}, r_2 = 5\text{mm}$, and $B = 1$. The sample rate is 44.1kHz.

are equivalent to passing the incident pressure wave through a first-order digital filter:

$$R_j(z) = \frac{b_0 + b_1 z^{-1}}{1 + a_1 z^{-1}}. \tag{4.40}$$

Table 4.1 summarises the coefficients as derived with the three different methods. In order to compare the different discretisation methods, the magnitude responses of the digital filters obtained with the different methods are computed for the dimensions $r_1 = 10\text{mm}$, $r_2 = 5\text{mm}$, and $B = 1$. Figure 4.17 compares the resulting magnitude responses. All three methods clearly result in a very close approximation at the lower frequencies. Note that the responses obtained with the TICM and the BT are extremely close (the curves overlap at most frequencies). We found that this is always the case except for extreme values of $\alpha$ that correspond to modelling extreme taper discontinuities.

Junction Stability

All three discretisation methods convert stable analogue filters into stable digital filters[2]. Hence if the analogue junction filter $R_j(\omega)$ is stable, then its discrete-time counterpart $R_j(z)$ is also stable. Unfortunately, $R_j(\omega)$ is not stable for all physically feasible cases. From (4.39) we can see that the analogue filter is only stable if $\alpha > 0$. This is true if

$$\frac{1}{r_2} > \frac{B}{r_1}. \tag{4.41}$$

The stability clearly depends on the values of $B$, $r_1$ and $r_2$. Välimäki [148] has indicated

[2] An analogue filter is said to be unstable when it has poles in the right-hand side of the $s$-plane, and a digital filter is said to be unstable if it has poles outside the unit circle of the $z$-plane [109].

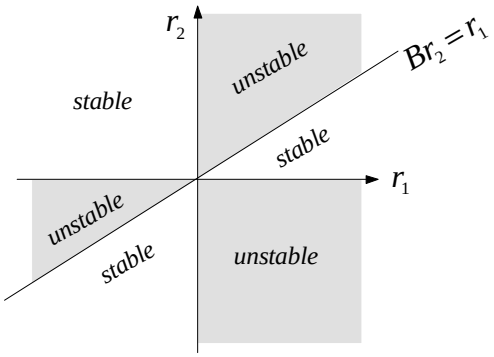


Figure 4.18: Regions of stability of the junction filter $R_j(\omega)$.

the regions of stability for the junction filter for the specific case of a junction with taper discontinuity only (i.e. $B = 1$). In figure 4.18, the regions of stability of the junction filter $R_j(\omega)$ are indicated for the general case, according to equation (4.41). The use of an unstable filter element is generally very problematic, since its impulse response exhibits unstable growth. However, it can be argued that a complete conical bore model should always be stable, since it represents a passive physical system [5, 60, 148]. The literature is not clear about whether this remains true in the case of a finite-precision implementation. Scavone [119] has reported that in finite precision implementations, the round-off errors of the unstable junction filters eventually become dominant, which leads to unstable growth. On the other hand, Martínez et al. [94] and Barjau et al. [19] have performed time-domain computations with the "multi-convolution algorithm", and have not reported any such numerical stability problems. This subject clearly deserves some more investigation, and is further discussed in section 4.4.

### 4.3.3 Fractional Delays and Viscothermal Losses

Fractional delay lengths can be simulated using fractional delay filters, as described in section 4.2. As with modelling cylindrical bores, these filters are placed within the delay-loop of a bore section. In section 4.1.3 it was explained that viscothermal losses can be included in a digital waveguide model of a cylindrical bore section by placing digital filters at appropriate points in the digital waveguide structure. The same method can be applied for simulation of lossy wave propagation in a conical section. For a bore section of length $L$, such a digital loss-filter approximates the response:

$$H(\omega) = e^{-\Gamma L} \cdot e^{j\omega L/c}. \tag{4.42}$$

For cones of sufficiently small taper and length, $\Gamma$ is computed as for a cylindrical bore section with a radius equal to the mean radius of the conical section, using equation (2.57).

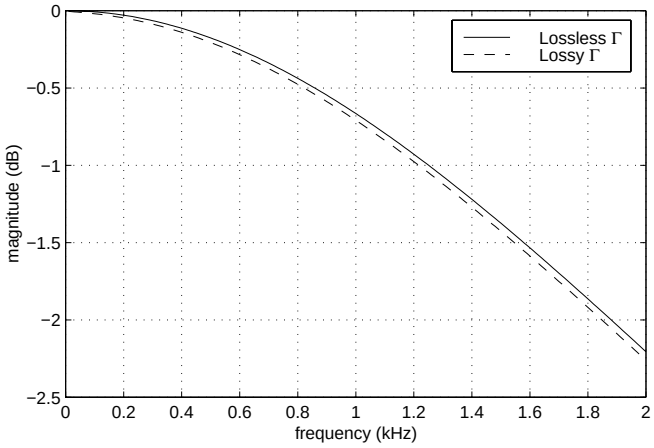


Figure 4.19: Magnitude response of the reflectance $R^-(\omega)$ for a junction with no diameter discontinuity, and with $r_1 = 10\text{mm}$ and $r_2 = 5\text{mm}$.

If viscothermal losses are taken into account, the characteristic admittances of the forward- and backward-travelling wave components are:

$$Y_0^+(r,\omega) = Y_0\left(1 + \frac{1}{\Gamma\, r}\right), \tag{4.43a}$$

$$Y_0^-(r,\omega) = Y_0\left(1 - \frac{1}{\Gamma\, r}\right), \tag{4.43b}$$

where $Y_0 = 1/Z_0$, where $Z_0$ is given by (2.57). Equations (4.43) can be combined with (4.28) in order to calculate the reflectances and transmittances associated with a junction of two conical bore sections. These reflectances and transmittances are not the same as those obtained without inclusion of viscothermal losses, although the deviation is generally very small. For example, figure 4.19 shows the reflectance $R^-(\omega)$ for a junction with taper discontinuity only, computed using the lossless $\Gamma = j\omega/c$ and also computed using the lossy formulation of $\Gamma$. In the context of time-domain modelling, the effect of including the viscothermal losses on the junction reflectance is usually neglected (see, e.g., [148, 10, 119, 94, 19]). The main reason for taking this approach is that the junction reflectances and transmittances are much harder to formulate in discrete-time form using the lossy formulation. The small deviation in figure 4.19 appears to justify this simplification. However, there are various consequences of this simplification that appear to be completely overlooked in the literature. Firstly, the error introduced by the simplification tends to have a small but noticeable effect on the height of the low-frequency impedance peaks of a conical bore system. For example, this can be observed in the input impedance of a truncated conical bore section of length $L^* = 700\text{mm}$ (see figure 4.20). Secondly, for some conical bore configurations, the inconsistent use of $\Gamma$ results in a conical bore model that exhibits a divergent reflection function. This particular effect is further discussed in

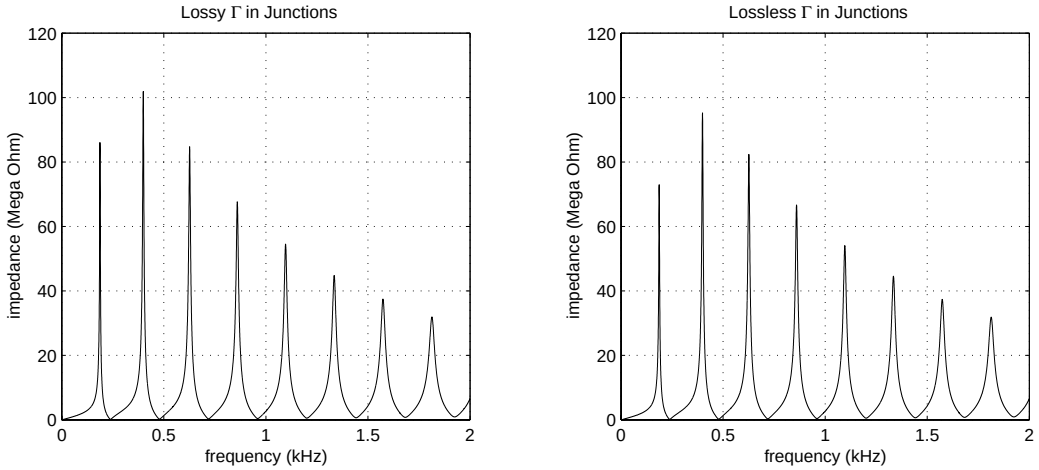


Figure 4.20: Input impedance of a truncated, open-ended conical section, as computed when using a lossy and a lossless version of the propagation constant in formulating the junctions. The cone length is 700mm, the radius at the input-end is 5mm, and the radius at the output-end is 20mm.

section 4.4.2. Thirdly, as will be seen in chapter 8, the simplification can lead to significant effective-length deviations at low frequencies.

## 4.4 Stability of Conical Bore Simulations

As seen in section 4.3.2, the junction filter associated with a taper discontinuity is unstable for certain bore conical configurations. The use of such unstable filters in digital signal processing systems is normally highly unadvisable, since numerical problems are likely to occur because of the unbounded exponential signal growth of the filter output. In the case of a conical bore model (i.e., a model of a bore that contains conical sections), a discrete-time model contains unstable one-pole filter elements that are directly derived from their analogue equivalents that appear in the continuous-time model. Gilbert et al. [60] and Agulló et al. [6] have demonstrated that the (continuous-time) impulse response of a one-dimensional conical bore model can be formulated as a sum of causal, growing exponentials. Numerical calculations of this sum have indicated, at least for physically feasible systems, that this impulse response is convergent, in other words that the system is stable. Viscothermal losses were not taken into account in any of these calculations.

Although a continuous-time conical bore model is stable in theory, this is not necessarily the case for a discrete-time implementation. In continuous-time, the reflected and transmitted waves can grow exponentially only for a limited time, because they are cancelled out by further (multiple) reflections. This "cancellation-mechanism" is very precise, i.e., it can be easily disturbed by small model deviations. Discrete-time models are only *approximations* of continuous-time models. The inevitable deviations introduced by simpli-

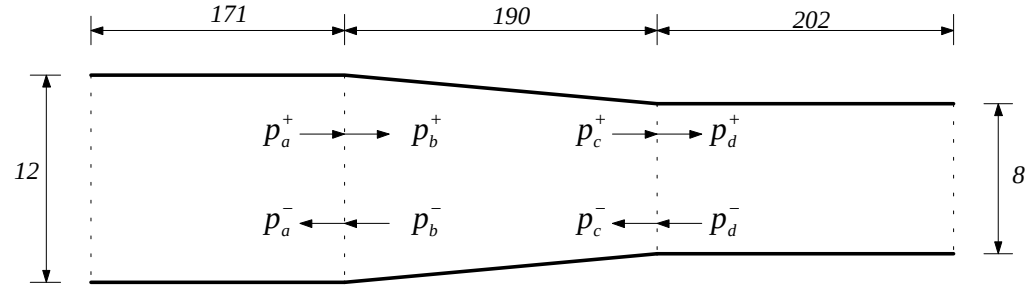


Figure 4.21: A single truncated cone system, connected on both sides to a cylindrical tube. The dimensions are given in mm.

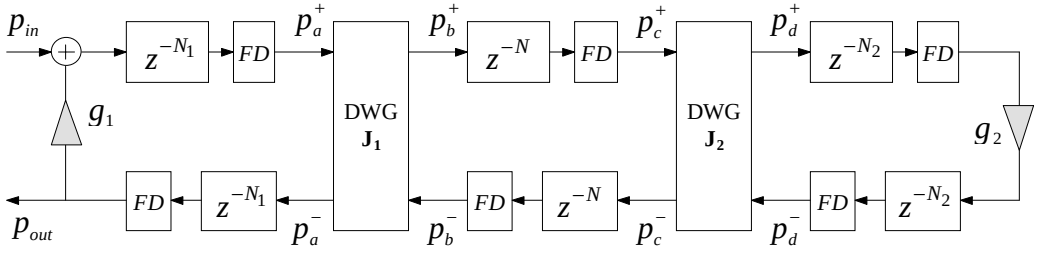


Figure 4.22: Digital waveguide implementation of the single truncated cone system. The $z^{-N}$ units indicate delay-lines, the *FD* units indicate fractional delay filters, and the DWG $\mathbf{J_1}$ and DWG $\mathbf{J_2}$ units indicate conical junctions. The multipliers $g_1$ and $g_2$ are introduced in the system to simulate end reflections in the cylindrical sections.

fications and discretisations may therefore disturb the cancellation-mechanism. Moreover, round-off errors occur in finite-precision implementations of discrete-time models, which could lead to further instability problems. In this section we investigate the stability of finite-precision implementations of conical bore simulations. The results presented here are calculated for the specific bore configuration in figure 4.21. Accuracy aspects of the simulation of this bore configurations are investigated in section 4.5.

### 4.4.1 Simulation without Propagation Losses

Using the techniques described in section 4.3.1 and section 4.3.2, the truncated cone system in figure 4.21 can be simulated in discrete-time with the digital waveguide model depicted in figure 4.22. Viscothermal losses are not taken into account at this point. In order to simulate end reflections in the cylindrical sections, the termination coefficients $g_1$ and $g_2$ are introduced. This system contains one unstable filter element, namely the junction filter of the DWG junction $\mathbf{J}_1$.

Anechoic Simulation

The impulse response of this system was calculated using the three different methods for discretising the junction filter introduced in section 4.3.2. The fractional delays were simulated with the third-order Lagrange interpolation filters discussed in section 4.2. Anechoic bore terminations are simulated by setting $g_1 = 0$ and $g_2 = 0$. The impulse response was also computed by applying an inverse Fourier transform (IFFT) to a frequency-domain result obtained using transmission-line matrices. Figure 4.23 shows the resulting impulse responses. The ripples in the inverse Fourier result are due to the frequency-domain window effect. The impulse responses obtained with the digital waveguide model also exhibit small ripples at points in time where strong reflections occur. These ripples are due to the use of fractional delay filters. We note that the results obtained using the BT and the TICM are extremely close.

Echoic Simulation

The same simulation can be carried out for an "echoic" truncated cone system. That is, we set $g_1 = 1$, which simulates a closed end at the left-hand side, and we set $g_2 = -1$, which simulates an open end at the right-hand side. Such a bore configuration is not dissimilar to a musical wind instrument air column. Of course, in a real wind instrument bore, the closed-end reflectance is frequency-dependent. The "$-1$" end reflectance is nevertheless suitable for the purposes of investigating the stability properties of the system. Figure 4.24 compares the IIM result to the BT result. The echoic simulation is entirely lossless (i.e., no wave energy is dissipated). Thus in theory, the waves propagating in the bore never decay to zero. The impulse response obtained using the BT demonstrates this, and a similar result was obtained using the TICM. However, the impulse response obtained using the IIM appears to be divergent. As can be seen in figure 4.24, the response is correct for the first few 100 milliseconds, but starts to exhibit unstable growth after about $t = 400$ms.

Further simulations were carried out with various other combinations of the termination coefficients $g_1$ and $g_2$. Table 4.2 (part A) summarises the results, which indicate that the IIM results in a convergent impulse response only when at least one of the bore terminations is anechoic. It must be noted that the stability is subject to the floating-point precision used in the calculations; all results presented in this section are calculated using 64-bit floating-point precision, unless mentioned otherwise. Simulations of a variety of different bore configurations (i.e., different diameters and bore lengths, as well as a larger number of sections), indicate that under these circumstances, stability is preserved with the BT and the TICM for all the possible passive[3] combinations of $g_1$ and $g_2$.

[3] The conical bore system is *a proiri* not passive whenever one of the termination coefficients has an amplitude larger than unity.

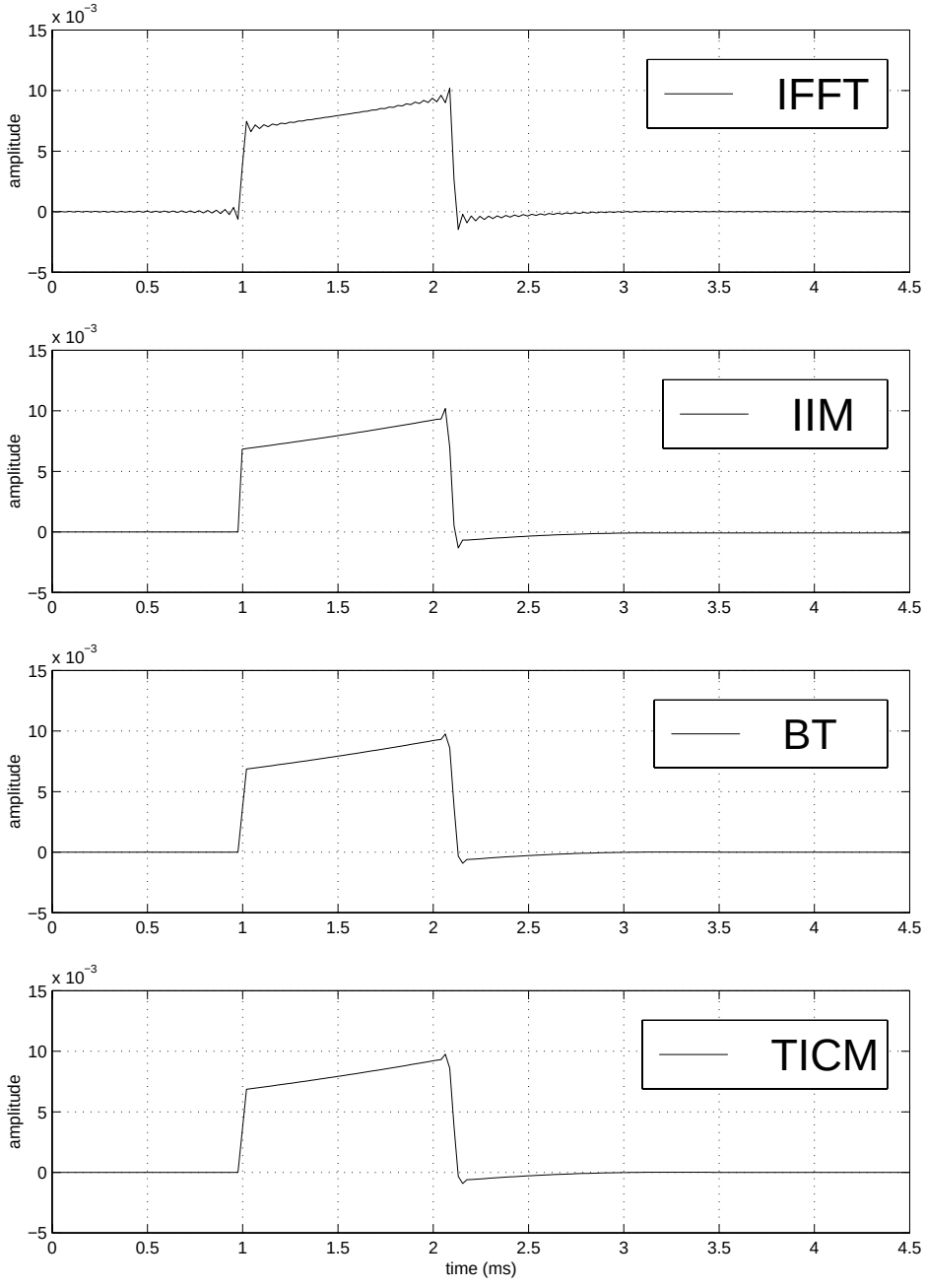


Figure 4.23: Impulse response of the (anechoically terminated) truncated cone system.

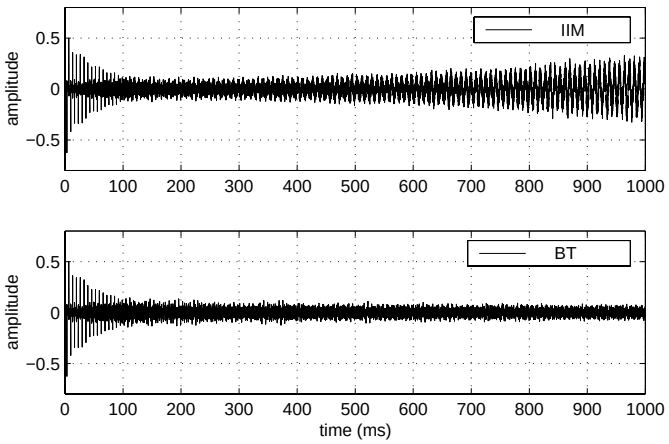


Figure 4.24: Impulse response of the (echoicically terminated) truncated cone system.

As mentioned before, setting one of the termination values to 1 corresponds to modelling a closed end, while a zero reflection simulates an anechoic termination. For a realistic open-end termination, one needs to replace the termination coefficient with a frequency-dependent filter. The results obtained with simulations with an open-end reflectance filter (in the form of a fourth-order IIR filter) were no different than those obtained with setting one of the termination coefficients to $-1$. That is, the simulations remained stable whenever the BT or the TICM was used with 64-bit precision.

The stability of the simulations without viscothermal losses was further tested by

- computing the impulse response for much longer simulation times (up to 200 seconds).
- using a variety of more complex input signals (such as sequences of rectangular pulses, repetitive noise bursts, and audio-signals from CD-recordings).
- simulating a variety of more complex piecewise conical bore models.
- using lower precision (32-bit and 16-bit).

All tests were carried out twice, first using the BT and then using the TICM. Whenever the coefficients and signal variables of the system were computed using 64-bit floating point precision, the simulation resulted in a convergent impulse response. However, lower-precision simulations can be unstable. For example, the impulse response computed with a 16-bit simulation of the truncated bore system with $g_1 = 1$ and $g_2 = 1$ exhibited unstable growth.

| Termination | | A: Simulation *without* VT losses | | | B: Simulation *with* VT losses | | |
|---|---|---|---|---|---|---|---|
| $g_1$ | $g_2$ | IIM | BT | TICM | IIM | BT | TICM |
| 0 | 0 | stable | stable | stable | unstable | unstable | unstable |
| 0 | 1 | stable | stable | stable | unstable | unstable | unstable |
| 0 | -1 | stable | stable | stable | unstable | unstable | unstable |
| 1 | 0 | stable | stable | stable | unstable | unstable | unstable |
| 1 | 1 | unstable | stable | stable | unstable | unstable | unstable |
| 1 | -1 | unstable | stable | stable | unstable | unstable* | unstable* |
| -1 | 0 | stable | stable | stable | unstable | unstable | unstable |
| -1 | 1 | unstable | stable | stable | unstable | unstable* | unstable* |
| -1 | -1 | unstable | stable | stable | unstable | unstable* | unstable* |

Table 4.2: Stability of the truncated cone system. Part A shows the simulation results without inclusion of viscothermal losses, and part B shows the results with inclusion of viscothermal losses. All results were obtained using a sample rate of 44.1kHz and a 64-bit floating-point precision. A simulation that is unstable but allows to calculate the (truncated) impulse response is indicated with "unstable*".

### 4.4.2 Inclusion of Viscothermal Losses

For accurate simulation of conical bore systems, viscothermal losses need to be taken into account. This can be done by placing loss-filters in the delay-loops in figure 4.22. As explained in section 4.1.3, these loss-filters approximate the propagation losses in each bore section. In this case we employed 4th-order IIR filters, which accurately model the propagation of low-frequency wave components. As explained in section 4.3.3, the junction models are based on a lossless formulation of the propagation constant. In order to investigate the effect this simplification has on the impulse response, we computed two different IFFT results: one in which the junctions were computed with a lossy propagation constant (IFFT (1)), and another in which the junctions were computed with a lossless propagation constant (IFFT(2)). In figure 4.25, these results are compared with the impulse responses computed with the digital waveguide simulation, respectively using the BT and the TICM. Apparently, using the lossless propagation constant causes some form of "DC-offset" in the impulse response. This effect is not the same for the IFFT(2) result as it is for the discrete-time simulation results, but in all three cases the multiple reflections clearly do not cancel each other out properly. This effect occured for all other bore configurations with anechoic terminations that were simulated. The effect can in fact not be considered as a DC-gain, because at DC, the model in which viscothermal

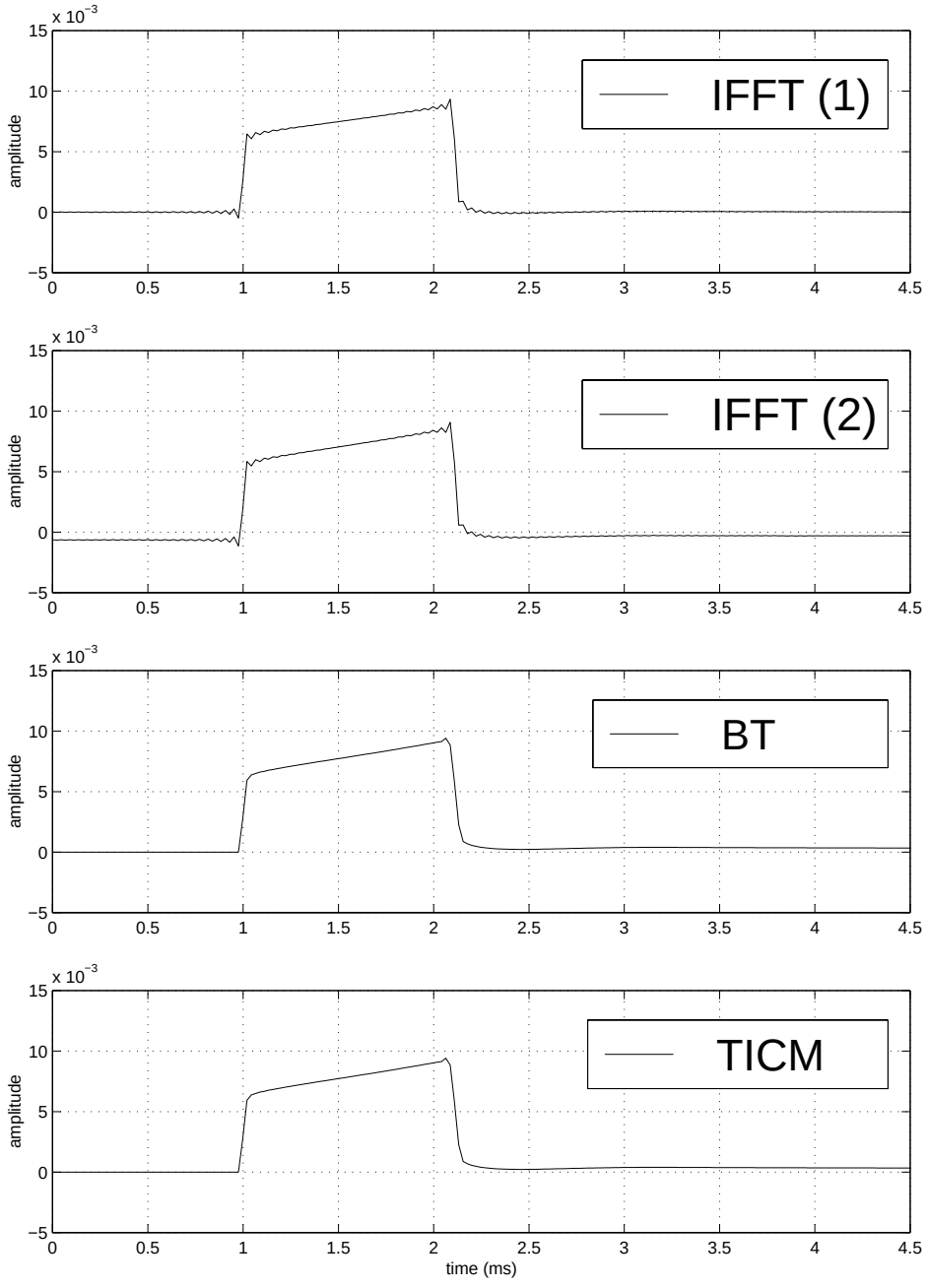


Figure 4.25: Impulse response of the (anechoically terminated) truncated cone system, as computed with inclusion of viscothermal losses.

losses are included is equivalent to the model with inclusion of those losses (i.e., there are no viscothermal losses at DC). Hence it must be considered as a disturbance of the cancellation-mechanism at frequencies other than DC. In both the BT and the TICM simulation, this results in a divergent impulse response. This is obviously a serious flaw of the simulation method; the difference between the results IFFT(1) and IFFT(2) in figure 4.23 strongly indicate that the cause of the instability is the inconsistency in the formulation of the propagation constant, rather than any errors introduced by the discretisation or by round-off errors.

As can be seen from part B of table 4.2, none of the simulations with inclusion of viscothermal losses are fully stable. However, it was found that when (1) setting one of the termination coefficient to $-1$, and (2) setting the other to either 1 or $-1$, one is able to run the simulation using the BT or the TICM long enough to compute the impulse response without any significant numerical problems. That is, numerical errors start to dominate only long after "normal" oscillations have decayed. Such "relative stability" is indicated with "unstable*" in table 4.2. With the calculations carried out for the bore configuration in figure 4.21, the signal growth typically starts to appear after more than 200 seconds of simulation time, which is many times longer than a typical effective length of the impulse response of an acoustical bore. As with the simulations in which viscothermal losses are excluded, the results obtained with one of the termination coefficient set to $-1$ are the same as those obtained with that coefficient replaced by a passive filter, with the added restriction that the response of this filter at $\omega = 0$ has to be exactly $-1$. That is, the truncated impulse response can be computed when at least one of the terminations corresponds to having a -1 reflection at DC, and neither of the terminations is anechoic.

In summary, the simulation results indicate that the none of the methods discussed result in a stable simulation when viscothermal losses are included. However, they also indicate that the truncated impulse response of the system can be computed whenever the bore contains (1) no anechoic terminations and (2) at least one termination for which the reflectance $R$ is $-1$ at $\omega = 0$. This is a useful property, because models of musical wind instruments are usually formulated such these conditions are fulfilled; the radiation impedance associated with an open end of an acoustical bore is by definition zero, which corresponds to open-end reflectance $R(\omega)$ for which $R(0) = -1$, practically all musical wind instrument that contain conical bore sections are open-ended, and the input-end is effectively closed by either the lips or the reed.

## 4.5 Accuracy of Conical Bore Simulations

For the purpose of investigating accuracy aspects, the truncated bore system depicted in figure 4.21 is simulated with the termination coefficients $g_1 = 0$ and $g_2 = 0.8$. The choice

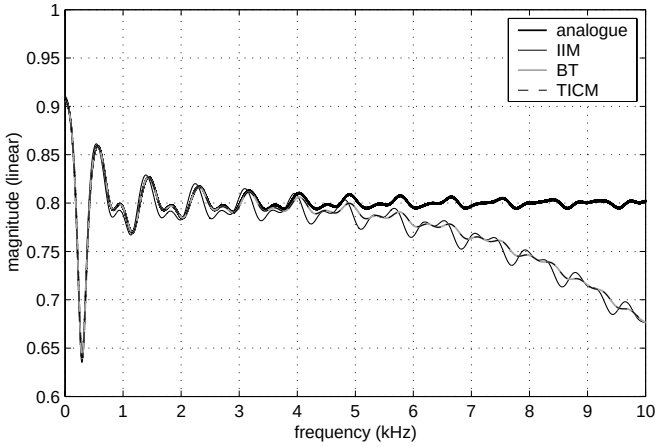


Figure 4.26: Reflectance magnitude of the truncated cone system, with $g_1 = 1$ and $g_2 = 0.8$.

of the latter coefficient corresponds to having a diameter discontinuity at the output-end, i.e., another cylindrical bore section attached to this end which is in turn anechoically terminated. This configuration is a suitable choice for the purpose of comparing how well the three different methods for discretisation of the junction filters perform; choosing $g_2 = 1$ or $g_2 = -1$ leads to a configuration for which the resonances are of infinite strength, while setting $g_2 = 0$ results into a small number of very weak resonances, for which the exact peak-frequencies are not well defined. On the other hand, setting $g_2 = 0.8$ amounts to having a certain amount of losses at all frequencies, which results in well-defined resonances, of which the peak amplitude and the frequency can be accurately determined. In order to focus the comparison on the discretisation methods, viscothermal losses were not included. As an "ideal reference", the result of a frequency-domain computation (i.e., a transmission-line model) of the truncated bore system was used. Figure 4.26 compares the three discrete-time modelling results to the ideal case in terms of the reflectance magnitude. As could be expected, all three methods are relatively accurate at low frequencies, but underestimate the ideal magnitude response at higher frequencies. This lowpass effect is mostly due to the use of Lagrange interpolators. As in the comparison of the junction filter magnitude in figure 4.17, the TICM and the BT give very similar results. Furthermore, it is noticable that the IIM result exhibits somewhat more deviation from the ideal case than the BT and the TICM.

In order to obtain a measure for the accuracy of the different discretisation schemes that can be related to the perceptual properties of the human ear, we computed for each case the input impedance from the reflectance using equation (2.40). The positions and heights of the input impedance peaks were determined, and the differences with the ideal case computed. These "tuning-errors" and "damping-errors" are listed in table 4.3 for the first 9 resonances of the system, for which the frequencies are below 3kHz. Resonances at

| | IIM | | BT | | TICM | |
|---|---|---|---|---|---|---|
| resonance no. | $\epsilon_t$ (cents) | $\epsilon_d$ (dB) | $\epsilon_t$ (cents) | $\epsilon_d$ (dB) | $\epsilon_t$ (cents) | $\epsilon_d$ (dB) |
| 1 | -1.23 | -0.08 | -1.23 | -0.02 | -1.23 | -0.02 |
| 2 | -1.07 | -0.28 | -1.41 | -0.04 | -1.41 | -0.04 |
| 3 | -1.23 | -0.29 | -1.40 | -0.03 | -1.40 | -0.03 |
| 4 | -1.48 | 0.24 | -1.44 | -0.02 | -1.44 | -0.02 |
| 5 | -1.33 | -0.54 | -1.43 | -0.04 | -1.43 | -0.04 |
| 6 | -1.43 | -0.28 | -1.43 | -0.04 | -1.43 | -0.04 |
| 7 | -1.40 | 0.43 | -1.40 | -0.04 | -1.41 | -0.04 |
| 8 | -1.40 | -0.70 | -1.45 | -0.06 | -1.45 | -0.06 |
| 9 | -1.44 | -0.28 | -1.42 | -0.06 | -1.42 | -0.07 |
| *mean* | -1.34 | -0.20 | -1.40 | -0.04 | -1.40 | -0.04 |

Table 4.3: Tuning and damping errors of the conical bore simulation. The tuning-error $\epsilon_t$ is computed as the interval between the simulation frequency and the ideal resonance frequency (in cents), and the damping-error $\epsilon_t$ is computed as the amplitudal difference (in dB) between the corresponding peak amplitudes. The last row in the table shows the mean errors over the 9 resonances. The difference in cents between the ideal frequency $f_1$ and the simulation frequency $f_2$ is calculated as $1200 \cdot log_2(f_2/f_1)$, thus a negative value in cents indicates that $f_2$ is smaller than $f_1$.

higher frequencies are considered as relatively unimportant in our comparison, since the air column of most wind instruments have a cut-off below 3kHz.

As can be seen from the mean value of these errors, the IIM causes somwhat less frequency warping than the BT and TICM. However, the frequency deviations are in all cases smaller than the "just noticable difference" detectable by te human ear. It is interesting to note that the warping introduced by discretising the junctions with the BT does not result in the typical warping effects associated with the BT; as can be seen from figure 3.19 the BT causes a highly non-linear form of warping which increases strongly with frequency. The results presented in table 4.3 show that the warping exhibited by the digital waveguide model of the truncated bore system is approximately linear. In terms of damping-error, the BT and TICM show considerably smaller values than the IIM, but also in this case the errors introduced with the three different schemes would not or hardly be detectable the human ear.

Hence it may be concluded that when using a 44.1kHz sample rate, all three schemes

introduce only very small errors in the important frequency range.

## 4.6 Conclusions and Future Work

We have seen that the propagation of waves in cylindrical and conical bore sections can be simulated by means of digital waveguide techniques. This involves digital approximation of fractional delays and frequency-dependent phenomena such as viscothermal losses, which can be realised with the use of digital FIR and IIR filters.

The results presented in the chapter indicate that if viscothermal losses are not included, stable digital waveguide simulations of conical bore systems appear to be possible when using the BT or the TICM for discretisation of the frequency-dependent scattering at the junctions; if the IIM is used, the simulations appear to be stable only for bore configurations that have at least one anechoic termination.

Unfortunately, none of the discretision schemes used in the present study appear to result in stable simulations of conical bore systems when viscothermal losses are included. Frequency-domain computations have indicated that the instability is at least partly due to an inconsistent formulation of the propagation constant. That is, the propagation constant is formulated taking into account the viscothermal losses when modelling the propagation of waves in a conical bore section, while such losses are ignored when modelling the scattering of waves at a conical junction. This inconsistent formulation appears to be common in previously developed time-domain models of conical bores (for example [5, 148, 10, 119, 19]). An interesting future topic would therefore be to determine the impulse response analytically, with taking into account viscothermal losses. Gilbert et al. [60] have performed this analysis without the inclusion of viscothermal losses, and have shown that the impulse response can be written as an infinite series of causal growing exponentials, the sum of which is convergent. Interestingly, their calculations were carried out with a *consistent* formulation of a "lossy" propagation constant $k = (j\omega+\alpha)/c$. As the authors have pointed out, such a formulation corresponds to taking into account losses, but of a different kind than the actual viscothermal losses. Extending their results towards frequency-dependent losses might prove rather complicated from a mathematical point of view, but may give a definite proof of divergence in certain cases where the junctions are formulated using the lossless version of the propagation constant.

Furthermore we envisage that in order to find a method for stable discrete-time simulation with inclusion of viscothermal losses, an interesting approach in future work would be to derive junction models in which the propagation constant is formulated in its lossy version.

# Chapter 5

# Wave Digital Modelling of Woodwind Toneholes

The pitch of woodwind instruments is controlled mainly via opening and closing toneholes. Toneholes are therefore essential tools for musical expression with woodwinds. The subject of this chapter is the simulation of toneholes in discrete-time. Given that the model is to be applied in the context of musical sound synthesis, a number of different requirements[1] have to be fulfilled. Firstly, the model should approximate the acoustic theories closely in the range of the instrument resonances, so that the sound generation mechanism is not distorted. Secondly, the model should allow dynamic control of its state. That is, a digital model should be formulated such that the process of opening and closing of the tonehole can be simulated. A third requirement of the tonehole model is that it can represent toneholes of a wide variety of physically and musically feasible dimensions. For example, it should be possible to model a narrow, long hole in the cylindrical bore of a clarinet as well as a short, wide hole in the conical bore of a saxophone. Finally, the model should be efficient in terms of computational costs, so that a real-time implementation on a standard processor is possible. Additionally, it would be desirable to be able to obtain the sound pressure that is radiated from the tonehole.

Tonehole models that were previously developed in the context of digital waveguide modelling [151, 122, 136, 121] do not meet all of the above requirements. The basic modelling approach is very similar to the approach taken in these prior studies, and can be considered as a logical further development of the subject.

The chapter is organised as follows. The first section is a review of tonehole theory, starting from a simple side branch model, and relating this to the more complex tonehole theories developed by Keefe [73, 72, 76]. Then in section 5.2, we present a novel method for modelling partially open holes. Finally in section 5.3, the partially open hole model is

[1] See chapter 1 for a more detailed explanation of the motivation and concepts behind these requirements.

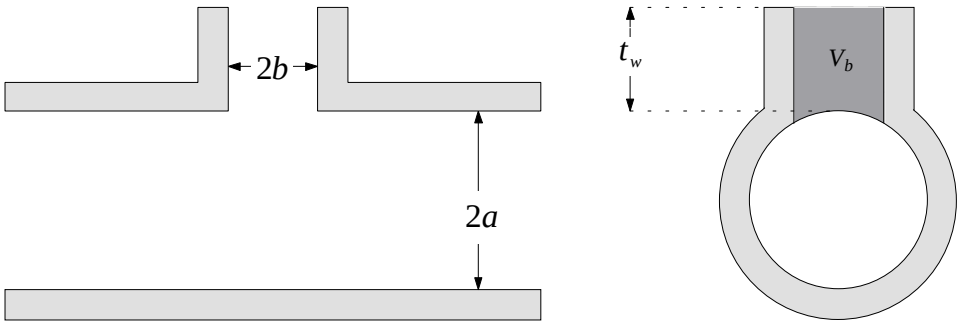


Figure 5.1: Cross-sections of a tonehole.

discretised by means of wave digital filter techniques.

## 5.1 Tonehole Theory

This section forms a brief review of basic acoustic theories of woodwind toneholes. For more advanced theories we refer to recent work on this subject by Nederveen et al. [102] and Dubos et al. [47].

### 5.1.1 The Side Branch Model

The simplest way of modelling a tonehole is to consider it as a simple side branch of the main bore. Figure 5.1 depicts this concept for a tonehole in a cylindrical bore. In this approach, the tonehole height $t$ is defined such that its product with the tonehole surface $S_b = \pi b^2$ equals the geometric volume $V_b$. It can be shown that $t$ is related to the shortest geometrical tonehole length $t_w$ by [76]:

$$t = t_w + 0.125b(b/a)\left[1 + 0.172(b/a)^2\right]. \tag{5.1}$$

In the low frequency-limit, the height of a tonehole is usually small in comparison to the wavelength[2], and therefore the side branch can be modelled as a lumped acoustic element. In the case of an open hole, the branch impedance may be formulated [84]:

$$\begin{aligned} Z_s^{(o)} &= \mathcal{R}_s + j\mathcal{X}_s \\ &= \frac{\rho\,\omega^2}{4\pi c} + j\,\frac{\rho\, t_e^{(o)}\,\omega}{\pi\, b^2}, \end{aligned} \tag{5.2}$$

[2]Some woodwinds, such as the bassoon, have toneholes that are drilled into the main bore at an angle. For such toneholes, the tonehole length can be considerably larger than usual, and may not be small in comparison with the acoustic wavelength, even at low frequencies.

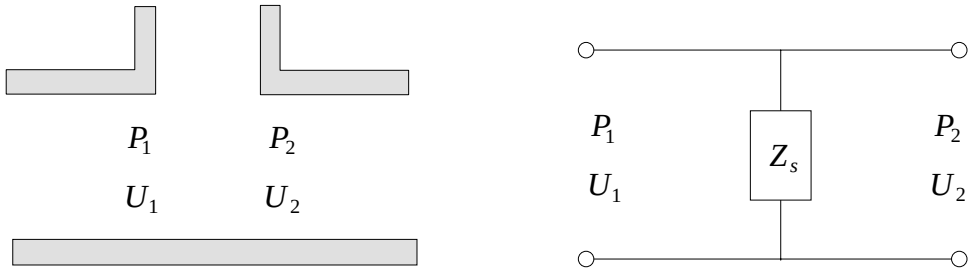


Figure 5.2: A tonehole in a cylindrical bore (left), and its equivalent network (right).

where $\mathcal{R}_s$ and $\mathcal{X}_s$ are the open side branch acoustic resistance and reactance, respectively, and $t_e^{(o)}$ is the open-hole effective length. The effective (acoustical) length $t_e^{(o)}$ differs from its effective (geometrical) height $t$ due to length-corrections at both the inner and outer end of the tonehole. In the low-frequency limit, the resistance is negligible ($\mathcal{R}_s << \mathcal{X}_s$), and the side branch approximately acts as an pure inertance:

$$Z_s^{(o)} = \frac{\rho t_e^{(o)}}{S_b} j\omega = j\omega L, \tag{5.3}$$

where $L = (\rho t_e^{(o)})/S_b$ is the acoustic inertance of the side branch, and $S_b = \pi\, b^2$ is the side branch cross-section. In the case of a closed hole, the branch impedance corresponds to the input impedance of a short cylindrical section with a closed end:

$$Z_s^{(c)} = -jZ_b \cot\left(kt_e^{(c)}\right), \tag{5.4}$$

where $Z_b = (\rho c)/S_b$ is the characteristic impedance of the branch, and $k$ is the free-space wave number. In this case, no outer length-correction is applied, thus the closed-hole effective length $t_e^{(c)}$ is the sum of the tonehole height $t$ and the inner-length correction. In the low-frequency limit, the closed branch impedance acts as an approximately pure compliance:

$$Z_s^{(c)} = \frac{\rho c^2}{j\omega S_b t_e^{(c)}} = \frac{1}{j\omega C}, \tag{5.5}$$

where $C = (S_b t_e^{(c)})/(\rho c^2)$. The equivalent network of a tonehole with impedance load $Z_s$ is depicted in figure 5.2. The shunt impedance is formulated with (5.3) for an open hole, and with (5.5) for a closed hole.

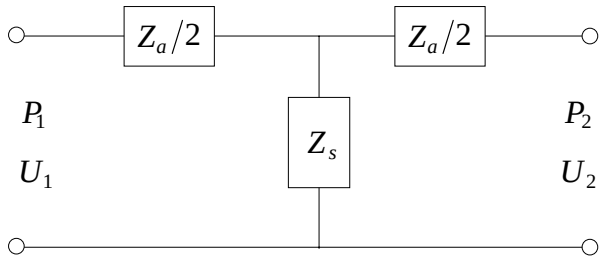


Figure 5.3: T-section network that represents a transmission-line model of a tonehole. The series impedances $Z_a/2$ represent the (negative) main bore length-corrections associated with be tonehole.

### 5.1.2 Keefe's *T*-section Model

The side branch model is formulated such that the tonehole has a zero geometric length along the main bore axis, and can be inserted at the point of a bore model that matches the centrepoint of the tonehole in the real bore. However, a real tonehole reduces the effective acoustic length of the main bore, thus length-corrections must be applied to the main bore due to the presence of the tonehole [20]. Moreover, since the direction of plane wave propagation within the tonehole is perpendicular to the direction of plane wave propagation in the main bore, there must be some bending of a wavefront travelling into a tonehole. The bending of the wavefront requires the contribution of secondary modes, which are evanescent in the main bore. Therefore an appropriate woodwind bore model may be derived by taking into account the influence of the secondary modes only in the vicinity of the toneholes. This approach was taken by Keefe [73, 72, 76], who used a variational formulation (developed within the context of electromagnetic waveguide theory [125]) to derive the transmission-line model parameters for a tonehole model based on a slightly more complex $T$-section network (see figure 5.3). The series impedance terms $Z_a/2$ correspond to the negative length-corrections. The full transmission-line matrix formulation of the single tonehole is:

$$\begin{bmatrix} P_1 \\ U_1 \end{bmatrix} = \begin{bmatrix} 1 & Z_a/2 \\ 0 & 1 \end{bmatrix} \begin{bmatrix} 1 & 0 \\ Z_s^{-1} & 0 \end{bmatrix} \begin{bmatrix} 1 & Z_a/2 \\ 0 & 1 \end{bmatrix} \begin{bmatrix} P_2 \\ U_2 \end{bmatrix}, \tag{5.6}$$

where the series impedance $Z_a$ and shunt impedance $Z_s$ for open ($o$) and closed ($c$) toneholes are defined:

$$Z_s^{(o)} = Z_0 \, (a/b)^2 \, (jkt_e + \xi_e) \, , \tag{5.7a}$$

$$Z_s^{(c)} = -jZ_0 \, (a/b)^2 \, (\cot(kt) + ykt) \, , \tag{5.7b}$$

$$Z_a^{(o)} = -jZ_0 \, (a/b)^2 \, kt_a^{(o)}, \tag{5.7c}$$

$$Z_a^{(c)} = -jZ_0 \, (a/b)^2 \, kt_a^{(c)}. \tag{5.7d}$$

The open-hole effective length $t_e$ is formulated:

$$t_e = \frac{(1/k)\tan(kt) + b\left[1.40 - 0.58(b/a)^2\right]}{1 - 0.61kb\tan(kt)}. \tag{5.8}$$

If a pad of diameter $2R$ is placed at a distance $h$ above the tonehole, this expression takes on a slightly different form:

$$t_e = \frac{(1/k)\tan(kt) + b\left(0.61\,(R/b)^{0.18}\,(b/h)^{0.39} + (\pi/4)\left[1 - 0.74(b/a)^2\right]\right)}{1 - 0.61(R/b)^{0.18}\,(b/h)^{0.39}\,kb\,tan(kt)}. \tag{5.9}$$

The parameter $\xi_e$ represents the specific acoustic resistance for the open tonehole:

$$\xi_e = 0.25(kb)^2 + \alpha t + (1/4)kd_v\, ln(2b/r_c), \tag{5.10}$$

where $r_c$ is the outer radius of curvature of the tonehole, $\alpha$ is the real part of the propagation wave number within the tonehole, and $d_v = \sqrt{\nu/(\rho\omega)}$ is the viscous boundary layer thickness[3]. For a closed hole, there is an additional term ($ykt$) due to the localised inhomogeneous acoustic field at the internal intersection of the tonehole with the main bore [76], where $y$ is:

$$y = 0.25(b/t)^2 + 0.58(b/a)^2 - (\pi b)/(4t). \tag{5.11}$$

The negative length-correction is represented by the series equivalent length[4] $t_a$. The open- and closed-hole series equivalent lengths are:

$$t_a^{(o)} = \frac{0.47\,b\,(b/a)^4}{\tanh(1.84t/b) + 0.62(b/a)^2 + 0.64(b/a)}, \tag{5.12a}$$

$$t_a^{(c)} = \frac{0.47\,b\,(b/a)^4}{\coth(1.84t/b) + 0.62(b/a)^2 + 0.64(b/a)}. \tag{5.12b}$$

[3] $\nu$ is the square root of the Prandtl number (see appendix A).

[4] The length-correction is negative for a positive value of $t_a$, hence the minus-sign in the formulation of $Z_a^{(o)}$ and $Z_a^{(c)}$ in (5.7).

The tonehole transmission-line matrix formulation may be used in combination with the transmission-line matrices for tubular sections as discussed in section 2.3 in order to model a complete tonehole lattice. In [72], results obtained with this approach were verified with experimental results for a bandwidth of 5kHz. The lattice formulation forms an accurate approximation of a woodwind bore provided that it can be assumed that there are no interactions between the toneholes. As mentioned earlier, secondary modes are active in the vicinity of tonehole discontinuities. As a consequence, tonehole interaction occurs when the disturbances due to the secondary modes of different toneholes overlap. As a rule of thumb, one may assume that the secondary modes decay over a length approximately equal to a duct diameter [74]. Thus the above lattice formulation remains valid as long as consecutive tonehole edges are separated by at least twice the duct diameter [119]. External interaction can also occur, though this phenomenon is usually relatively insignificant at the lower frequencies. In [74], Keefe outlines how the tonehole effective length and the effective interhole distances are affected by the presence of interaction.

## 5.2 A Lumped Element Model of a Partially Open Hole

### 5.2.1 Simplifications to Keefe's Model

In this section we set out to develop a simplified model that approximates Keefe's $T$-section model at the open and closed state. The first few simplifications involve the formulation of the shunt impedance. In the simplified model, we formulate $Z_s$ in the same way as in the side branch model (i.e., as a lumped element). Hence the open-hole shunt impedance is defined as in (5.3), and the closed-hole shunt impedance is defined according to (5.5). The main objective is to define the effective lengths $t_e^{(o)}$ and $t_e^{(c)}$ such that the simplified model forms a good low-frequency approximation of Keefe's formulation. For an open hole, the best low-frequency approximation results if we use an open-hole effective length that equals $t_e$ (according to equations (5.8) and (5.9)) at $\omega = 0$. If no pad is present, this yields:

$$t_e^{(o)} = t_e|_{\omega=0} = t + b\left(1.4 - 0.58(b/a)^2\right). \tag{5.13}$$

With pad above the hole, this expression takes the form:

$$t_e^{(o)} = t_e|_{\omega=0} = \frac{t + b\left(0.61\,(R/b)^{0.18}(b/h)^{0.39} + (\pi/4)\left[1 - 0.74(b/a)^2\right]\right)}{1 - 0.61(R/b)^{0.18}(b/h)^{0.39}\,b\,t}. \tag{5.14}$$

For a closed hole, we neglect the inner-length correction and use an effective length $t_e^{(c)} = t$. Keefe's formulation of the closed-hole shunt-impedance amounts to using a closed-hole

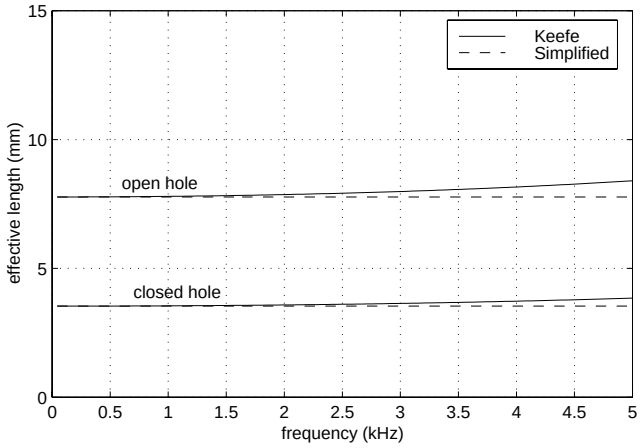


Figure 5.4: Open-hole and closed-hole effective length for a hole of dimensions $b = 3.2$mm and $t_w = 3.4$mm. There is no pad above the hole, and the main bore radius is 9.4mm.

effective length

$$t_e^{(c)} = \frac{\rho\, c^2}{j\omega S_b Z_s^{(c)}}, \tag{5.15}$$

where $Z_s^{(c)}$ is calculated with (5.7b). Figure 5.4 shows how the (constant-valued) open-hole and closed-hole effective lengths of the simplified formulation vary from the effective lengths according to Keefe's formulation.

The second set of simplifications involves the series impedance $Z_a$. This impedance depends mainly on the series equivalent length $t_a$. Unfortunately, $t_a$ is defined slightly differently for the closed state than it is for the open state (see equations (5.12)), which complicates the formulation of a unified tonehole model that can represent both states. Fortunately, it was found that the first term in the denominator in these expressions (i.e., $tanh(1.84t/b)$ for the open-hole and $coth(1.84t/b)$ for the closed-hole) takes a value that lies very close to 1 for practically all physically feasible tonehole dimensions. Therefore we may simplify (5.12) to:

$$t_a = \frac{0.47\, b\, (b/a)^4}{1 + 0.62(b/a)^2 + 0.64(b/a)}. \tag{5.16}$$

Furthermore, we anticipate a complication that arises when modelling the series impedances in discrete-time: they represent *negative* length-corrections, formulated in the form of a negative series inertance on either side of the shunt impedance (see figure 5.3). Simulation of a negative inertance network using WDF techniques normally leads to an unstable two-port filter [51]. Therefore we model the length-corrections by simply reducing the length of the main bore on either side of the tonehole. According to Barjau et al. [19], there is no significant loss of accuracy when using this alternative formulation for

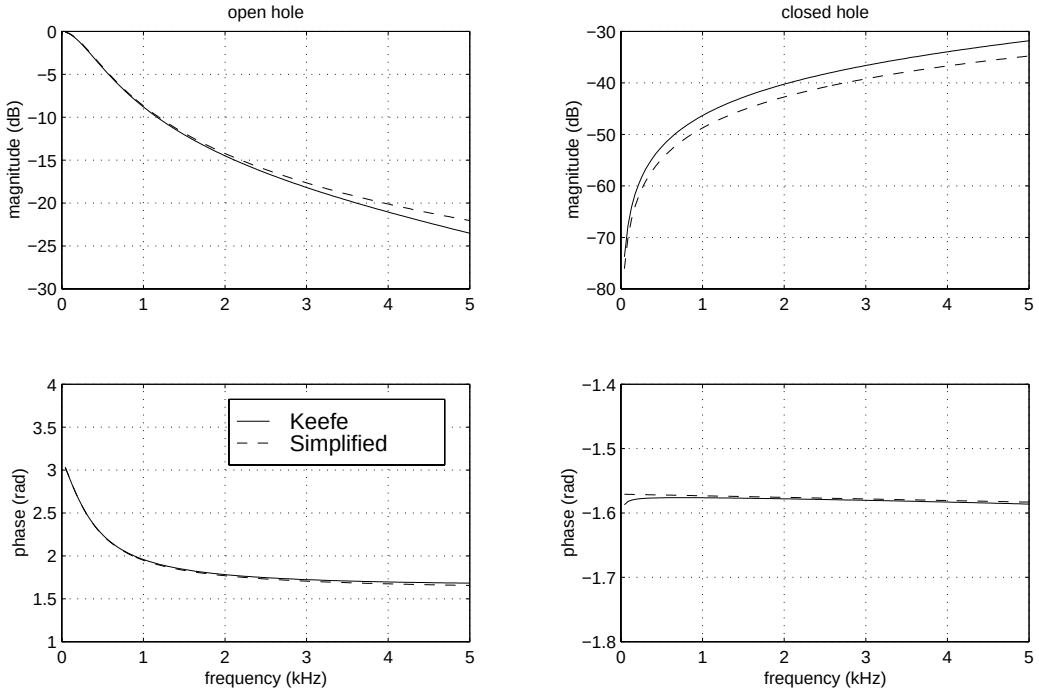


Figure 5.5: Plane wave reflectance magnitude (top) and phase (bottom) of an open hole (left) and a closed hole (right). The hole dimensions are $b = 3.2$mm and $t_w = 3.4$mm, and the main bore radius is 9.4mm.

musical wind instrument geometries. The total main bore negative length correction for a tonehole with series equivalent length $t_a$ is [76]:

$$l_a = -(a/b)^2 t_a. \tag{5.17}$$

Thus if the length of the main bore sections on either side of the tonehole are $l_1$ and $l_2$, they should be corrected to $l_1 + l_a/2$ and $l_2 + l_a/2$, respectively.

In order to investigate the combined effect of the simplifications, we computed the plane wave reflectance of the tonehole (as seen from the main bore). Figure 5.5 shows the reflectance magnitude and phase for the open and closed case.

### 5.2.2 Partially Open Holes

So far, we have discussed only the two extreme states of the tonehole (open and closed). However, musical sound synthesis applications require dynamic control of the tonehole state. In order to achieve this, we need to formulate a tonehole model that (1) can represent *partially open* states and (2) is fully parametric. In the ideal case, we end up with a model in which the tonehole state can be adjusted continuously through a single parameter.

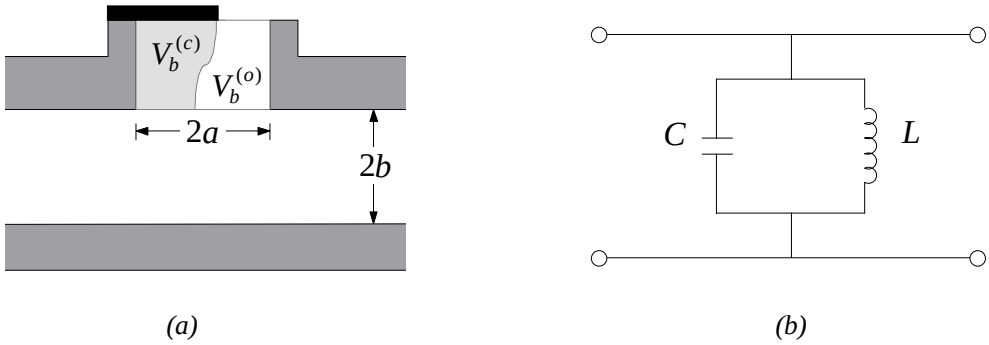


Figure 5.6: A partially open tonehole (left), and its equivalent network (right).

Consider the tonehole in figure 5.6a. With the hole partially closed off, we assume that the tonehole volume can effectively be divided into an "open part" $V_b^{(o)}$, that acts as an inertance, and a "closed part" $V_b^{(c)}$, that acts as a compliance. These volumes operate in parallel, thus the net shunt impedance is formulated:

$$Z_s = \frac{j\omega L}{1 - \omega^2 LC}. \tag{5.18}$$

The electrical network representation of the shunt impedance is depicted in figure 5.6b. If we define the ratio between open and total hole volume $g = V_b^{(o)}/V_b$, then the compliance and inertance are given by:

$$C = (1 - g) \cdot \frac{\pi b^2 t_e^{(c)}}{\rho c^2}, \tag{5.19a}$$

$$L = g^{-1} \cdot \frac{\rho t_e^{(o)}}{\pi b^2}, \tag{5.19b}$$

where $t_e^{(c)}$ and $t_e^{(o)}$ are defined as for the simplified tonehole model (see section 5.2.1). The tonehole state is controlled through the parameter $g$. When $g = 1$, the compliance is zero, and its impedance value goes to infinity, thus the model behaves as a pure inertance, which corresponds to a fully opened state. When $g = 0$, the inertance and its impedance value go to infinity, and the model thus behaves as a pure compliance, which corresponds to a fully closed state. Any value for $g$ in between zero and one represents a partially closed state: sweeping $g$ in time from one to zero corresponds to the process of closing a tonehole, and sweeping $g$ from zero to one corresponds to opening a tonehole.

It must be noted that there is a complication with the parametrisation of the model formulated above: the inertance defined in (5.19) uses the reciprocal of $g$, which excludes setting $g$ fully to zero without running into numerical problems. Therefore it is more convenient to formulate the shunt impedance using the reciprocal of the inertance. Suppose

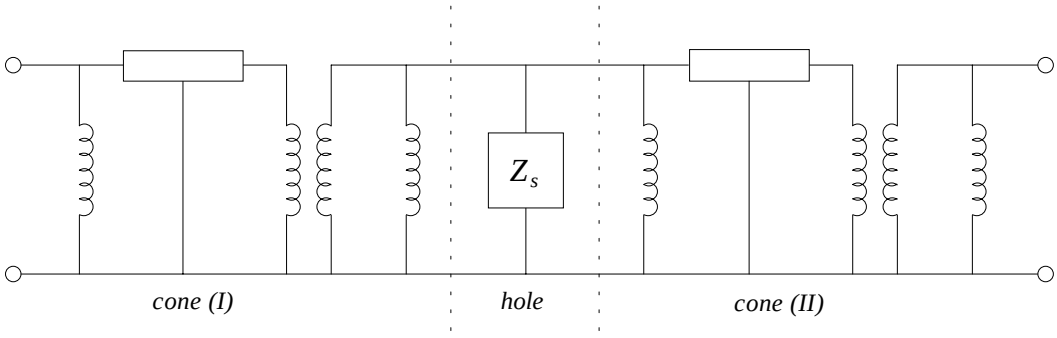


Figure 5.7: Equivalent network of a tonehole in a conical bore section.

that the inertance in the fully opened state is indicated with $L^{(o)}$, and the compliance in the fully closed state is indicated with $C^{(c)}$:

$$C^{(c)} = \frac{\pi b^2 t_e^{(c)}}{\rho c^2}, \tag{5.20a}$$

$$L^{(o)} = \frac{\rho t_e^{(o)}}{\pi b^2}. \tag{5.20b}$$

The elements of the partially opened hole can then be formulated:

$$C = (1-g)\, C^{(c)}, \tag{5.21a}$$

$$L^{-1} = \frac{g}{L^{(o)}}. \tag{5.21b}$$

Hence the shunt impedance is formulated:

$$Z_s(\omega) = \frac{j\omega}{L^{-1} - \omega^2 C}. \tag{5.22}$$

### 5.2.3 A Tonehole in a Conical Bore

As seen in section 2.3.4, a conical section may be modelled as a cylindrical waveguide in combination with two conicity inertances and an ideal transformer (see figure 2.17). We may consider a conical bore with a tonehole as a system of two conical sections separated by a tonehole. An equivalent network of this system may be derived by dividing the equivalent networks of the two bore sections by the shunt impedance of the hole (see figure 5.7). We note this formulation does not require that the conical taper on the left side of the hole equals the taper on the right side.

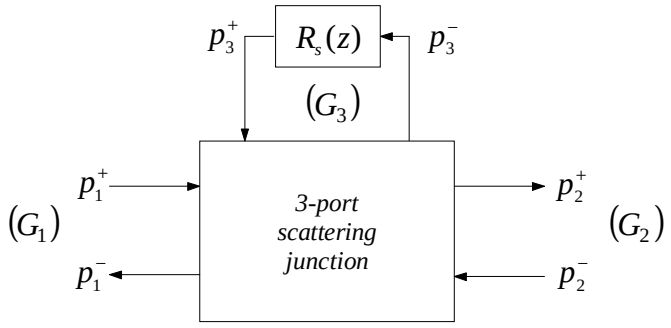


Figure 5.8: Wave digital modelling scheme for discrete-time simulation of the partially open hole. $G_1$, $G_2$ and $G_3$ are the port-admittances.

## 5.3 The Wave Digital Tonehole Model

### 5.3.1 Discretisation of the Partially Open Hole Model

The partially open hole model is a lumped element model that can be simulated in the discrete-time domain by means of wave digital filter (WDF) techniques. As discussed in sections 3.3 and 3.4, the first step in a WDF derivation is the decomposition of the acoustic variables $P$ and $U$ into wave variables (equation (3.60)). Applying this decomposition to the partially open-hole network in figure 5.6b results in the system depicted in figure 5.8. In this scheme, the three-port scattering junction models the wave interaction between the main bore and the tonehole. The scattering equations for such a junction are given in appendix E. In this case, we have

$$P_1^- = P_2^- + W, \tag{5.23a}$$

$$P_2^+ = P_1^+ + W, \tag{5.23b}$$

$$P_3^+ = P_1^+ + P_2^- + P_3^- + W, \tag{5.23c}$$

with

$$W = k_1 \left[ P_1^+ - P_3^- \right] + k_2 \left[ P_2^- - P_3^- \right], \tag{5.24}$$

where $k_1$ and $k_2$ are the junction coefficients. The value of these depend on the port-admittances of the acoustic ports:

$$k_1 = \frac{G_1 - G_2 - G_3}{G_1 + G_2 + G_3}, \tag{5.25a}$$

$$k_2 = \frac{G_2 - G_1 - G_3}{G_1 + G_2 + G_3}, \tag{5.25b}$$

where $G_1$ and $G_2$ are the port-admittances at the left and the right side of the tonehole respectively, and $G_3$ is the port-admittance of the hole. The way in which the port-admittances $G_1$ and $G_2$ are defined depends on whether the bore is cylindrical or conical. In the case of a cylindrical main bore, the hole is directly attached on either side to a distributed element, thus the port-resistances $G_1$ and $G_2$ must in that case be set equal to the main bore characteristic impedances at the left and right side of the bore, respectively. It is uncommon for a tonehole to be exactly placed at a discontinuity in diameter, thus usually we have $G_1 = G_2 = Y_0$, where $Y_0 = 1/Z_0$ is the characteristic admittance of the main bore. In the case of a conical main bore, the hole is connected directly on either side to a lumped element (see figure 5.7), thus the port-admittances are in that case arbitrary. The port-admittance $G_3$ is arbitrary for either a cylindrical or a conical main bore.

What remains is the derivation of the wave digital reflectance $R_s^{'}(z)$ that models the shunt impedance. The continuous-time "reflectance" $R_s^{'}(\omega)$ is:

$$R_s^{'}(\omega) = \frac{Z_s(\omega) - R_3}{Z_s(\omega) + R_3}, \tag{5.26}$$

where $R_3 = 1/G_3$. Note that unless we set $R_3 = (\rho c)/(\pi b^2)$, $R_s^{'}(\omega)$ does not correspond to the actual physical tonehole reflectance. Substitution of (5.18) and applying the bilinear transform gives the "wave digital reflectance" of the hole:

$$R_s^{'}(z) = -\frac{\alpha_1 + \alpha_2 z^{-1} + z^{-2}}{1 + \alpha_2 z^{-1} + \alpha_1 z^{-2}}. \tag{5.27}$$

This is a digital allpass filter with coefficients:

$$\alpha_1 = \frac{\left(L^{-1} + \beta^2 C\right) - G_3\beta}{\left(L^{-1} + \beta^2 C\right) + G_3\beta}, \tag{5.28a}$$

$$\alpha_2 = \frac{2\left(L^{-1} - \beta^2 C\right)}{\left(L^{-1} + \beta^2 C\right) + G_3\beta}, \tag{5.28b}$$

where $\beta = 2/T$ is the bilinear operator, and $T$ is the sample period. In order to avoid a delay-free loop, the port-admittance $G_3$ must be chosen such that $R_s^{'}(z)$ is non-immediate[5]. From equations (5.27) and (5.28) we can see that $R_s^{'}(z)$ is non-immediate only if $\alpha_1 = 0$.

[5] By "non-immediate", we mean that the inverse Fourier transform $r_s^{'}(t)$ has a zero instantaneous reflection, i.e. $r_s^{'}(0) = 0$. See section 3.3.1 for a detailed explanation.

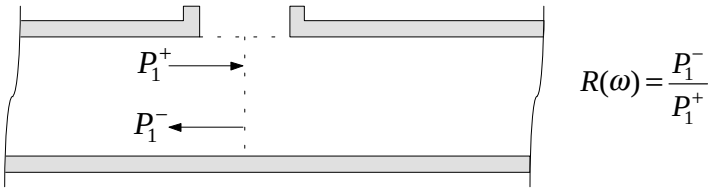


Figure 5.9: Plane-wave reflectance of a tonehole.

It follows that we must set

$$\begin{aligned} \left(L^{-1} + \beta^2 C\right) - G_3\,\beta &= 0 \\ & \textit{or} \\ G_3 &= \frac{L^{-1} + \beta^2 C}{\beta}. \end{aligned} \tag{5.29}$$

If we substitute (5.29) into (5.28), the wave digital reflectance becomes:

$$R_s^{'}(z) = -z^{-1}\ \left(\frac{\alpha_2 + z^{-1}}{1 + \alpha_2 z^{-1}}\right), \tag{5.30}$$

with

$$\alpha_2 = \frac{L^{-1} - \beta^2 C}{L^{-1} + \beta^2 C}. \tag{5.31}$$

This digital filter can be implemented using only one multiplication:

$$P_3^+ = -\alpha_2\left[P_3^- z^{-1} + P_3^+ z^{-1}\right] - P_3^- z^{-2} \tag{5.32}$$

The three-port equations in (5.23) in combination with (5.32) form the complete set of equations of the discrete-time version of the lumped element mode of the partially open tonehole. We will refer to this as the *wave digital tonehole model.*

In order to investigate the discretisation effects, the plane wave reflectance of the partially open hole was computed for a range of tonehole states ($g = 0, 0.1, 0.2, 0.3, ..., 1.0$). The plane wave reflectance is the quotient of the reflected and the incident pressure wave in the main bore, assuming anechoic main bore terminations (see figure 5.9). The resulting plane wave reflectance magnitude responses, as computed in continuous- and discrete-time are shown in figure 5.10. As can be expected, the discrete-time model closely approximates the continuous-time model at the lower frequencies. However, at the high end of the frequency-spectrum, the discrete response strongly deviates from the continuous response. It can be seen in figure 5.10 that the wave digital tonehole model has unity amplitude at $f = f_s/2$ whenever the compliance is not zero. As a result, the model strongly overestimates the reflectance at frequencies near the Nyquist frequency. Fortunately, this is

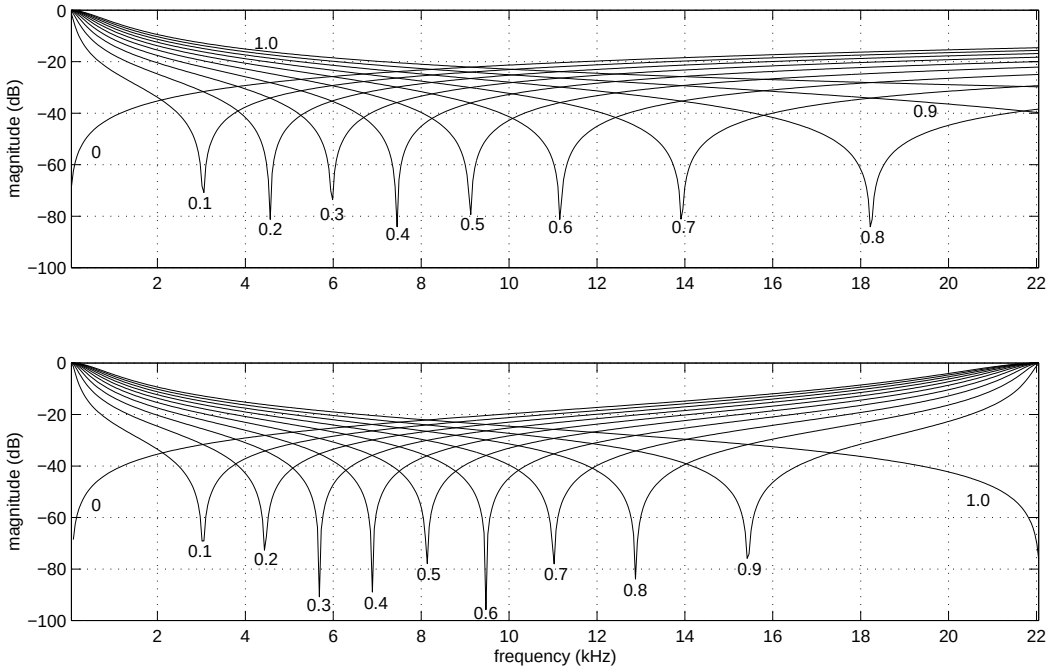


Figure 5.10: Plane-wave reflectance of the continuous-time model (top) and discrete-time model (bottom) of a partially open hole, as computed for a range of tonehole states ($g = 0, 0.1, 0.2, 0.3..., 1.0$).

usually not a problem in wind instrument modelling, because the boundary and radiation losses significantly attenuate the higher frequencies such that the overall bore reflectance maintains lowpass. Therefore this deficiency does not disturb the sound generation mechanism.

### 5.3.2 Application to a Six-Hole Flute

In this section we model a full tonehole lattice in discrete-time, and compare it with Keefe's transmission-line model in terms of the reflection function. In [76], Keefe's tonehole model was tested by computing the reflection function of a six-hole flute for a number of different fingerings, using the transmission-line matrix formulation. We computed the reflection function of the same flute bore (using transmission-line matrices), but in a slightly different way. Firstly, the boundary losses in the main bore were not included. This was done to ensure that the comparison is not "clouded" by discrepancies introduced by loss-filters, so that the focus of the comparison is firmly on tonehole modelling. Secondly, the equivalent length of the flute excitation mechanism was not taken into account in our computations. As a result of these two differences, the amplitude- and time-scale of the reflection functions deviate somewhat from the ones originally published by Keefe in [76].

The reflection function was also computed using a discrete-time model in which each of

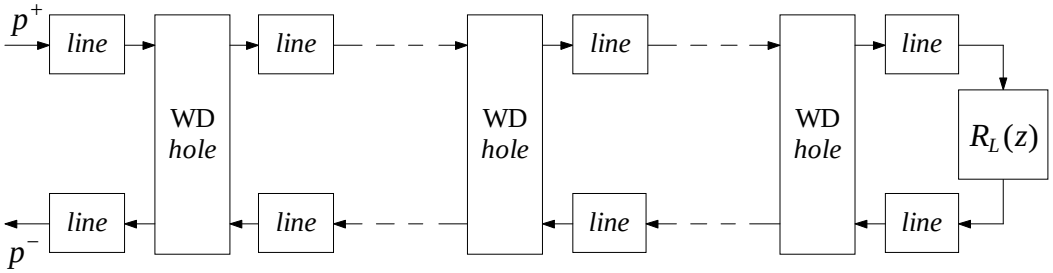


Figure 5.11: Wave digital model of a cylindrical bore with $N$ toneholes. Each *line* unit indicates a delay-line plus a fractional delay filter, and each WD *hole* block indicates a wave digital tonehole structure. $R_L(z)$ is the open-end reflectance filter.

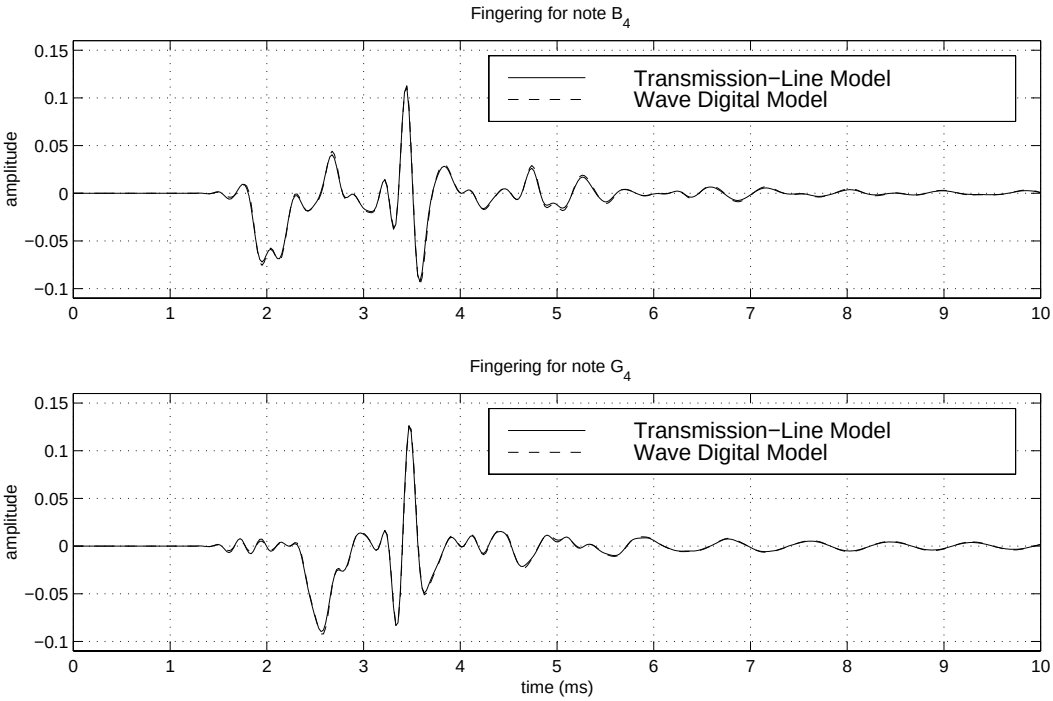


Figure 5.12: Six-hole flute (discrete-time) reflection function (lowpass filtered) for the note $B_4$ (top) and $G_4$ (bottom), as computed using Keefe's transmission-line model (solid) and the wave digital model (dashed). The sample rate is 44.1kHz. Note that in both cases, the difference between the curves is barely visible.

the holes is modelled with a wave digital tonehole model, i.e., a "wave digital model" of the flute bore. The cylindrical bore sections in between the holes are modelled as delay-lines in cascade with third-order Lagrange interpolation filters, and the open-end reflectance is modelled with a 4th-order IIR filter. Figure 5.11 shows the modelling structure for a cylindrical bore with $N$ toneholes. Lowpass filtering was applied to both reflection functions in order to focus the comparison on the lower frequency-range. A linear-phase FIR lowpass filter with a 5kHz cut-off was used for this purpose. Figure 5.12 shows the reflection functions computed for fingerings corresponding to the notes $B_4$ and $G_4$, respectively. The comparisons clearly indicate that the wave digital model forms a remarkably close low-frequency approximation of Keefe's transmission-line model.

### 5.3.3 Sound Radiation

In the formulation of the partially open hole, it is assumed that there are no radiation losses associated with the tonehole. This corresponds to assuming that the ambient air does not provide any resistance to the air motion within the tonehole, even if the tonehole is partially or fully opened. This assumption only holds approximately at low frequencies. At higher frequencies, the air just outside the hole is disturbed by the vibrational motion of the "open part" of the tonehole. Hence at high frequencies there is a conversion of acoustical energy from inside the tonehole to the outside environment (i.e., high-frequency components are radiated).

In order to get some insight into the amount of radiation losses at higher frequencies, we may employ Scavone's smooth extension of the Levine and Schwinger formulation of an open-ended tube[6]. Figure 5.13 shows the full audio rate bandwidth amplitude response of the open-end reflectance, calculated for a range of different tonehole radii.

Given that the radiation losses are small at the lower frequencies (less than 1dB up to 5kHz for a hole radii smaller than 5mm), it follows that the low-frequency components of the acoustic pressure $P_3$ just underneath a tonehole are closely approximated with the wave digital tonehole model. Hence we may deduce from $P_3$ the low-frequency components of the radiated pressure. The problem of deducing the higher frequency components of the radiated pressure is then treated separately. Following the approach in [22, 26, 52], we divide the problem into modelling the radiation below and above the tonehole lattice cut-off frequency ($f_c$). Benade [22] defines the cut-off frequency for a lattice of equally spaced and equally sized toneholes as:

$$f_c = 0.11\, c \left(\frac{b}{a}\right) \left(\frac{1}{s\, t_e}\right), \tag{5.33}$$

[6] See section 2.2.5 for a brief explanation of this open-end formulation.

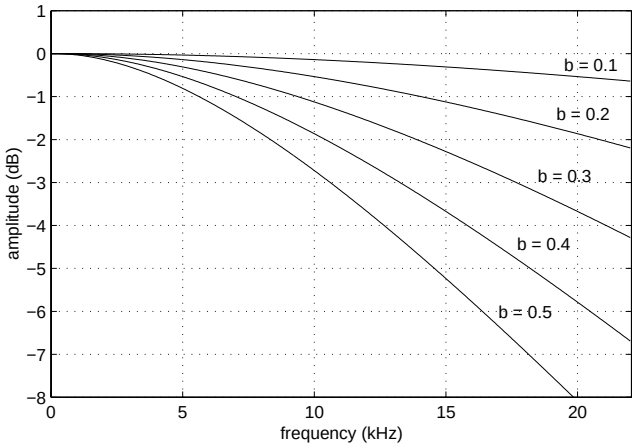


Figure 5.13: Open-end reflectance amplitude response for a range of tonehole radii ($a = 0.1, 0.2, 0.3, 0.4, 0.5$mm).

where the distance between the holes is $2s$. His measurements show that the cut-off of a real woodwind instrument is reasonably constant, despite that fact that the spacing and sizes vary for each hole.

Low-Frequency Components ($f \leq f_c$)

Because only the "mass-like" motion of the open part of the tonehole volume disturbs the ambient air (i.e., the "spring-like" motion of the closed-part of the tonehole volume does not contribute to the sound radiation), the flow $U_e$ exiting the hole equals the flow across the inertance:

$$U_e = \frac{P_3}{j\omega L}. \tag{5.34}$$

Because a woodwind tonehole is generally small, it may be considered as an isotropic source [52]. Given a source-strength $U_e$, the radiation pressure at a distance $r$ from such a source is:

$$P_{rad}(r) = \left(\frac{j\omega\rho}{4\pi r}\right) U_e \, e^{-jkr}, \tag{5.35}$$

where $k = \omega/c$ is the free space wave velocity. By combining (5.34) and (5.35), we can compute the pressure radiated from a woodwind tonehole as:

$$P_{rad}(r) = \left(\frac{\rho}{4\pi r L}\right) P_3 \, e^{-jkr}. \tag{5.36}$$

Note that the frequency term $j\omega$ has disappeared in the final result. The term $e^{-jkr}$ represents a pure time-delay (i.e., the time it takes for a radiated pressure wave to reach the "listening point"). Thus, the (low-frequency) radiated pressure at any distance from the tonehole can be computed by simply *scaling* and *delaying* the bore pressure $P_3$ just

underneath the tonehole. We can incorporate this in the wave digital tonehole model by formulating the digital domain version of (5.36) as:

$$P_{rad}(r) = \left(\frac{g}{r}\right) \xi \, P_3 \, z^{-N} \, H_{FD}(z), \tag{5.37}$$

where $z^{-N}$ represents a delay-line, $H_{FD}(z)$ indicates a fractional delay filter and $\xi = S_b/(4\pi t_e^{(o)})$ is a constant. It can be seen from (5.37) that the amplitude of the radiation pressure decreases with distance ($r$) and increases with open tonehole surface ratio ($g$). Furthermore, since the delay and fractional delay filter are essentially allpass, the radiation pressure apparently has, at least at low frequencies, the same frequency content as the bore pressure $P_3$.

High-Frequency Components ($f > f_c$)

As mentioned before, the lumped element model is inaccurate at higher frequencies. More precisely, the open-end resistance is not taken into account, thus all the internal bore variables (such as $P_3$) do not have the proper high-frequency content. Moreover, for low-frequency components we have assumed that the radiation is isotropic (i.e., the flow spreads out evenly in all directions). This assumption is not valid at high frequencies, because the effects of directivity need to be taken into account. Possible solutions to the problem of accurately modelling the high-frequency components are discussed in section 9.2.3.

## 5.4 Conclusions and Future Work

In this chapter we have seen that it is possible to accurately model the reflection function of a cylindrical woodwind bore by means of an efficient travelling-wave based discrete-time model. The toneholes in this model are represented with wave digital tonehole units, which use only two multiplications per sample (one for the three-port scattering and one for the reflectance filter). The wave digital tonehole model fulfils the essential requirements for application in the context of musical sound synthesis. Tonehole models that were previously developed in the context of digital waveguide modelling do not meet one or more of these requirements. For example, the "model for an open finger hole" presented in [151] does not accurately represent the closed-hole state. Various other models, such as the "two-port tonehole model" in [122] and its "one-filter version " presented in [136], do not allow for dynamic control of the tonehole state, and are therefore not useful in the case where musical control is required. The "three-port tonehole model" presented in [121] closely approximates the established theories on tonehole acoustics, allows dynamical control of its state and is also computationally efficient. However, whereas in the wave digital tonehole model the tonehole length can be chosen freely (the only restriction being

that it must be larger than zero), the three-port model is only computable for tonehole lengths that correspond to a round-trip time of at least one delay. This is because the model is based on a distributed modelling approach, i.e., the tonehole is modelled as a subsidiary waveguide. For an audio sampling frequency $f_s = 44.1$kHz and a wave velocity $c = 342$m/s, the tonehole length is thus restricted to a minimum of $t = c/(2f_s) \approx 3.8$mm. This excludes the possibility of simulation of woodwind instruments that contain holes of shorter length (such as the saxophone), unless the sample rate is increased. Furthermore, the three-port model requires the inclusion of a fractional delay filter for simulation of a tonehole of fractional delay length. In the wave digital modelling approach, the length of the hole can be adjusted without the use of additional filters. Another drawback is that the three-port tonehole model has not (yet) been formulated in such a form that it can be used for modelling toneholes in conical bores. The three-port tonehole model has one advantage though: it is more suitable for simulation of large toneholes. This is because the lumped element approach is valid only when the tonehole length is sufficiently short to allow the time delay for propagation down to the end of the hole and back to be neglected.

A useful improvement to the wave digital tonehole model could be to include some form of resistance. In the revised edition of [101], Nederveen includes a non-linear resistive term in the tonehole shunt impedance. Such a resistive term could explain particular phenomena observed with very small holes, and may need to be included for accurate simulation of register holes.

# Chapter 6

# Wave Digital Modelling of Woodwind Bores

A woodwind bore may be considered as a succession of conical and cylindrical bore sections with a set of open or closed holes in their sides [94]. Techniques for the simulation of wave propagation in cylindrical and conical sections were discussed in chapter 4, and methods for discrete-time modelling of woodwind toneholes were discussed in chapter 5. These techniques can be combined for discrete-time simulation of complete woodwind bores. This approach is straight-forward in the case of a cylindrical main bore, but application to tapered bore systems results in realisibility problems. That is, delay-free loops arise when connecting a digital waveguide model of a conical section to a wave digital tonehole model, because both the taper junction and the tonehole model have immediate reflectances in this case. Hence an alternative discrete-time formulation of the conical junction has to be developed in order to overcome this problem.

As pointed out by Benade [24], a junction of two conical sections can be modelled as a parallel inertance. This raises the possibility of applying wave digital filter (WDF) techniques for digital simulation of wave scattering at a junction between two conical sections. Unlike digital waveguide modelling techniques, wave digital modelling techniques allow for the adjustment of the port-resistance values such that delay-free loops are avoided. In section 6.1, we discuss how this approach can be used in woodwind bore modelling.

The remaining part of this chapter is organised as follows. In section 6.2, we demonstrate the wave digital modelling approach with two example applications, and in the final section of the chapter (section 6.3), we compare the wave digital approach to the "multi convolution approach".

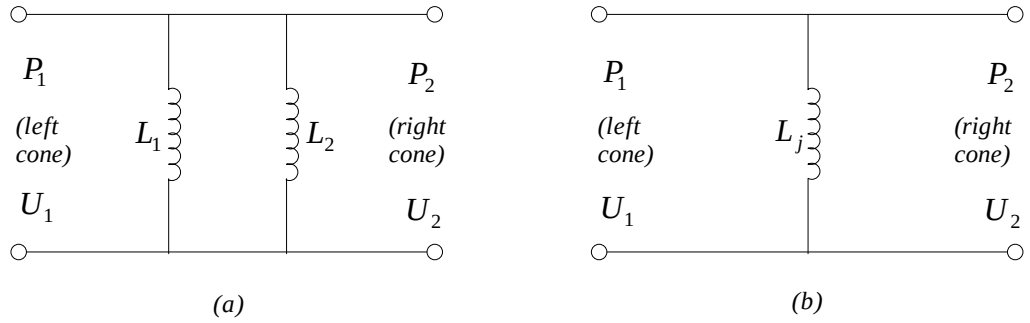


Figure 6.1: Network representation of a junction of two conical sections (a), and the equivalent network (b).

## 6.1 The Wave Digital Junction

### 6.1.1 A Junction of Two Conical Sections

An equivalent network of two coupled conical bore sections can be constructed by attaching two networks of the kind depicted in figure 2.17. A junction of two conical sections is thus described with a network which has the right inertance ($L_1 = -(\rho r_1)/S_1$) of the left cone in parallel with the left inertance ($L_2 = (\rho r_2)/S_2$) of the right cone (see figure 6.1a), where $r_1$ and $r_2$ are the apex distances of the left and the right cone, respectively. The junction network is equivalent to the single inertance network in figure 6.1b, where the "equivalent junction inertance" is:

$$L_j = \frac{L_1 L_2}{L_1 + L_2} = \frac{\rho r_1 r_2}{r_1 S_2 - r_2 S_1}. \tag{6.1}$$

This network can be simulated in the digital domain by means of WDF techniques. The WDF structure is derived in a fashion similar to the WDF structure for simulation of a parallel compliance in section 3.3.2, and takes the form as depicted in figure 6.2. The "inertance reflectance" is:

$$R_{inr}(\omega) = \frac{j\omega L_j - G_3^{-1}}{j\omega L_j + G_3^{-1}}. \tag{6.2}$$

Discretisation of (6.2) via the bilinear transform (BT) gives the wave digital reflectance:

$$R_{inr}(z) = \frac{\beta L_j \left(\frac{1-z^{-1}}{1+z^{-1}}\right) - G_3^{-1}}{\beta L_j \left(\frac{1-z^{-1}}{1+z^{-1}}\right) + G_3^{-1}}, \tag{6.3a}$$

$$= \frac{-\phi - z^{-1}}{1 + \phi z^{-1}}, \tag{6.3b}$$

with the coefficient

$$\phi = \frac{1 - \beta L_j G_3}{1 + \beta L_j G_3}. \tag{6.4}$$

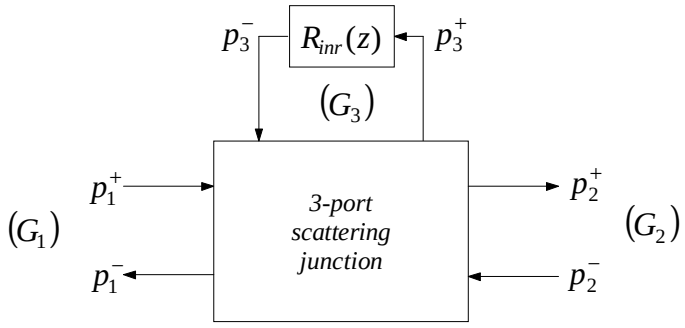


Figure 6.2: WDF modelling structure for digital simulation of the parallel inertance network in figure 6.1b. The port-admittances are indicated with $G_1$, $G_2$ and $G_3$.

In order to ensure that the inertance-loop in figure 6.2 is not delay-free, the wave digital reflectance $R_{inr}(z)$ has to be non-immediate, thus the coefficient $\phi$ has to be zero. It follows that the port-admittance has to be chosen

$$G_3 = \frac{1}{\beta L_j}. \tag{6.5}$$

After substitution of (6.5) into (6.3), it is found that the wave digital reflectance reduces to a delay plus a change of sign:

$$R_{inr}(z) = -z^{-1}. \tag{6.6}$$

The three-port scattering junction in figure 6.2 is a form of a branching junction, for which the scattering equations are given in equations (E.8) in appendix E. Combining these three-port equations with (6.6) gives the final set of equations for the wave digital (WD) junction:

$$\begin{aligned} P_3^- &= -P_3^+ \, z^{-1}, \\ W &= k_1 \left[P_1^+ - P_3^-\right] + k_2 \left[P_2^- - P_3^-\right], \\ P_1^- &= P_2^- + W, \\ P_2^+ &= P_1^+ + W, \\ P_3^+ &= P_1^+ + P_2^- + P_3^- + W, \end{aligned} \tag{6.7}$$

with

$$k_1 = \frac{G_1 - G_2 - G_3}{G_1 + G_2 + G_3}, \tag{6.8a}$$

$$k_2 = \frac{G_2 - G_1 - G_3}{G_1 + G_2 + G_3}. \tag{6.8b}$$

The WD junction signal flow structure is depicted in figure 6.3. We note that only two

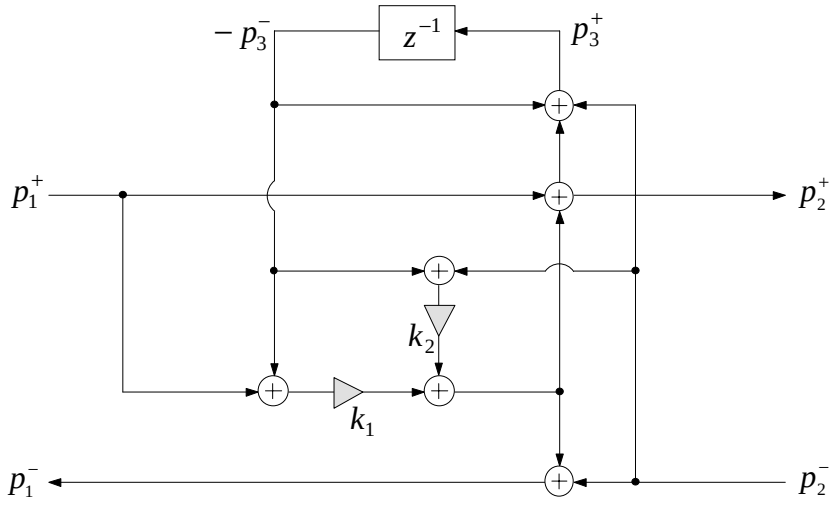


Figure 6.3: Signal flow structure of the wave digital junction.

multiplications are required for implementation of this conical junction model, which is less than required for implementation of the digital waveguide junction model discussed in section 4.3.2. From a mathematical point of view, the WD junction is equivalent to the digital waveguide junction discretised with the BT. From a digital signal processing perspective, the two are *not* equivalent, because different finite precision realisations of mathematically equivalent discrete-time systems have different properties due to signal quantisation effects [109]. However, no significant differences between the two forms were found in the simulations results.

### 6.1.2 A Conical Section Connected to a Lumped Element

Consider the network in figure 6.4. This network is the electrical equivalent of a conical section that is terminated by a load impedance $Z_L(\omega)$. The value of the parallel inertance (2) is $L_j = -(\rho r)/S$, where $r$ is the distance from the cone apex to the end of the cone, and $S$ is the wave area at the cone end. Figure 6.5 shows the discrete-time model of this system. The scaling factors that model the ideal transformer have been omitted, and viscothermal losses have not been taken into account. The term $R_L^{'}(z)$ indicates a digital filter approximation of the reflectance

$$R_L^{'}(\omega) = \frac{Z_L(\omega) - R_2}{Z_L(\omega) + R_2}, \tag{6.9}$$

where $R_2$ is the port-resistance as defined for the travelling waves $p_2^+$ and $p_2^-$. We note that $R_L^{'}(\omega)$ equals the actual physical reflectance of the lumped element only if we set $R_2$ equal to the characteristic impedance $(\rho c)/S$ at the cone end. If the taper junction modelled by

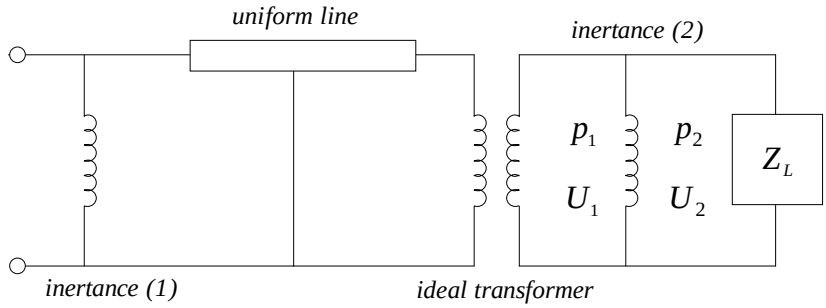


Figure 6.4: The equivalent network of a truncated cone that is terminated by a lumped element with impedance load $Z_L$.

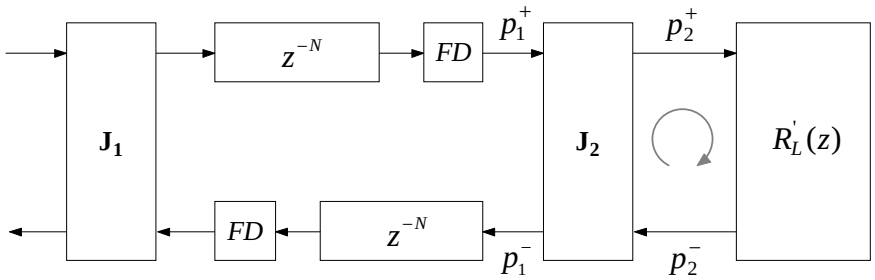


Figure 6.5: Discrete-time model of a cone terminated by a lumped element. The $\mathbf{J_1}$ and $\mathbf{J_2}$ units indicate conical junctions, the $z^{-N}$ units indicate delay-lines,and the $FD$ units represent fractional delay filters. The grey arrow indicates the loop that becomes delay-free when the junction (2) is modelled as a digital wvaeguide junction or a normal WD junction.

inertance (2) is simulated in discrete-time by means of a DWG junction, or a "normal" WD junction, then the system would exhibit a delay-free loop, because both the junction and the lumped element have an immediate reflectance. One way to solve this problem would be to lump the conical junction (2) together with the lumped element reflectance, and approximate the resulting spherical wave reflectance with a digital filter. However, in many applications the lumped element is connected to another waveguide section on the right-hand side, in which case the lumped reflectance becomes rather complex. Therefore we prefer an approach in which the lumped element is modelled separately from the conicity inertance. In order to avoid a delay-free loop, we have to model the inertance (2) as a special wave digital junction that is designed such that its reflectance in the right-going direction is non-immediate. We will therefore refer to it as a "WD-$r$ junction", where the letter $r$ indicates that the junction has a non-immediate reflectance at its right-hand side. Similarly, in the case of modelling a lumped element attached to the left side of the cone, a WD-$l$ junction (that has a non-immediate reflectance in the left-going direction)

is required. The signal flow structures of the WD-$r$ and WD-$l$ junctions are depicted in figure 6.6. The derivation of these junction structures is given below.

The WD-$r$ Junction

The first few steps in the derivation is the same as in the case of the normal WD junction. That is, the basic structure is again a three-port junction (see figure 6.2), with an inertance reflectance

$$R_{inr}(\omega) = \frac{j\omega L_j - G_3^{-1}}{j\omega L_j + G_3^{-1}}. \tag{6.10}$$

attached to one of its ports (see figure 6.2). After applying the BT, we find that in order to avoid a delay-free inertance-loop, the port-admittance $G_3$ should relate in the same way to the inertance as for the normal WDF junction, i.e.:

$$G_3 = \frac{1}{\beta L_j}. \tag{6.11}$$

The wave digital reflectance again reduces to a negative delay. Also, the same three-port equations apply here. Written in the general form of (E.5), these are:

$$\begin{bmatrix} P_1^- \\ P_2^+ \\ P_3^+ \end{bmatrix} = \begin{bmatrix} \frac{G_1-G_2-G_3}{G_1+G_2+G_3} & \frac{2G_2}{G_1+G_2+G_3} & \frac{2G_3}{G_1+G_2+G_3} \\ \frac{2G_1}{G_1+G_2+G_3} & \frac{-G_1+G_2-G_3}{G_1+G_2+G_3} & \frac{2G_3}{G_1+G_2+G_3} \\ \frac{2G_1}{G_1+G_2+G_3} & \frac{2G_2}{G_1+G_2+G_3} & \frac{-G_1-G_2+G_3}{G_1+G_2+G_3} \end{bmatrix} \begin{bmatrix} P_1^+ \\ P_2^- \\ P_3^- \end{bmatrix}. \tag{6.12}$$

Because the cone is terminated by a lumped element, we may choose an arbitrary value on the side it is attached to. In the case of a termination load on the right side, this is the port-admittance $G_2$. The cone itself is a distributed element, thus the value of the port-admittance $G_1$ has to be set to the local characteristic admittance $Y_1 = S_1/(\rho\, c)$. It can be seen from (6.12) that the instantaneous reflection of the wave $P_2^-$ is $(-G_1 + G_2 - G_3)/(G_1+G_2+G_3)$. In order to derive a realisable structure, this instantaneous reflection should be zero, thus we must set

$$G_2 = G_1 + G_3. \tag{6.13}$$

After substitution of (6.13) into (6.12), the three-port equations become:

$$\begin{bmatrix} P_1^- \\ P_2^+ \\ P_3^+ \end{bmatrix} = \frac{1}{G_1+G_3} \begin{bmatrix} (-G_3) & G_1+G_3 & G_3 \\ G_1 & 0 & G_3 \\ G_1 & G_1+G_3 & (-G_1) \end{bmatrix} \begin{bmatrix} P_1^+ \\ P_2^- \\ P_3^- \end{bmatrix}. \tag{6.14}$$

If we define the junction coefficient

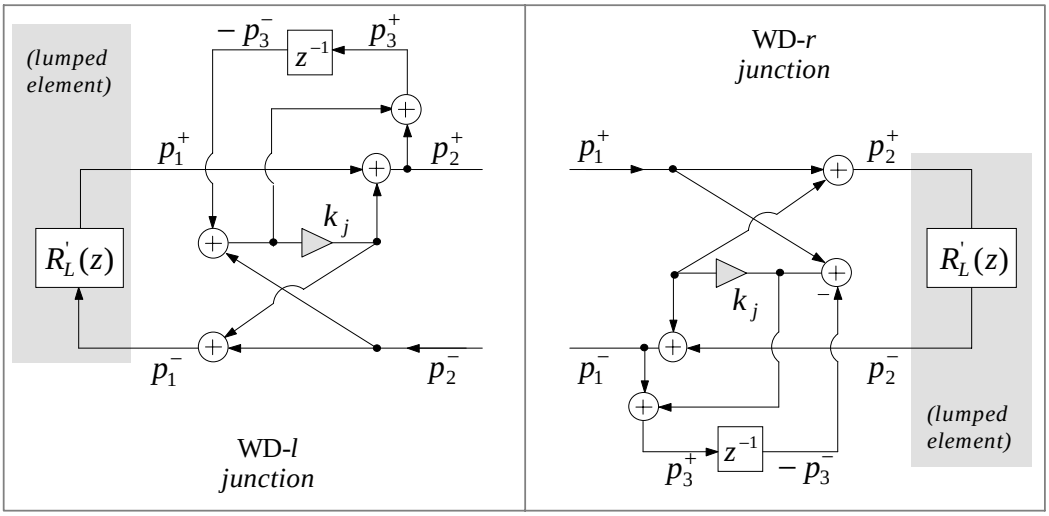


Figure 6.6: Signal flow structure of the WD-$l$ and the WD-$r$ junction.

$$k_j = -\frac{G_3}{G_1 + G_3}, \tag{6.15}$$

the three-port equations can be written:

$$P_1^- = P_2^- + k_j\,[P_1^+ - P_3^-], \tag{6.16a}$$
$$P_2^+ = P_1^+ + k_j\,[P_1^+ - P_3^-], \tag{6.16b}$$
$$P_3^+ = P_2^- + [P_1^+ - P_3^-] + k_j\,[P_1^+ - P_3^-]. \tag{6.16c}$$

After some further algebra, the final WD-$r$ equations can be written as:

$$\begin{aligned} P_3^- &= -P_3^+\,z^{-1}, \\ W_1 &= P_1^+ - P_3^-, \\ W_2 &= k_j\,W_1, \\ P_1^- &= P_2^- + W_2, \\ P_2^+ &= P_1^+ + W_2, \\ P_3^+ &= P_2^- + W_1 + W_2. \end{aligned} \tag{6.17}$$

The WD-$l$ Junction

The signal flow structure of the WD-$l$ junction can be directly obtained from the signal flow of the WD-$r$ junction. That is, one can simply interchange the incident waves ($p_1^+$ and $p_2^-$) and the reflected waves ($p_1^-$ and $p_2^+$). The port-admittance $G_2$ now has to be set equal to the local characteristic admittance $Y_2 = S_2/(\rho\,c)$, and the port-admittance $G_1$ has to be set $G_1 = G_2 + G_3$ in order to avoid a delay-free loop. The junction coefficient

in this case is:

$$k_j = -\frac{G_3}{G_2 + G_3}. \tag{6.18}$$

The final set of equations for the WD-$l$ junction is:

$$\begin{aligned} P_3^- &= -P_3^+ z^{-1}, \\ W_1 &= P_2^- - P_3^-, \\ W_2 &= k_j W_1, \\ P_1^- &= P_2^- + W_2, \\ P_2^+ &= P_1^+ + W_2, \\ P_3^+ &= P_1^+ + W_1 + W_2. \end{aligned} \tag{6.19}$$

The definition of the reflectance $R_L^{'}(z)$ of the lumped elements in figures (6.5) and (6.6) depends on the value of the port-resistance. Given a lumped element with impedance $Z_L(\omega)$ and a port-resistance $R$, this "wave digital reflectance" is designed to approximate the reflectance:

$$R_L^{'}(\omega) = \frac{Z_L(\omega) - R}{Z_L(\omega) + R}. \tag{6.20}$$

We note that this reflectance only corresponds to the actual physical reflectance in the case where the port-resistance equals the local characteristic impedance.

### 6.1.3 Stability Properties

For certain types of conical junctions, the junction inertance $L_j$ is negative. From equations (6.5) and (6.11) it can be seen that the port-admittance $G_3$ will then also be negative. The use of negative port-admittances normally leads to an unstable WDF structure [51, 87]. For a normal WD junction (inertance given by (6.1)), the inertance remains positive for

$$\frac{S_2}{r_2} > \frac{S_1}{r_1}, \tag{6.21}$$

which is exactly the same as the condition under which the junction filter associated with a DWG junction remains stable (see equation (4.41)). The normal WD junction, the WD-$r$ junction, and the WD-$l$ junction are all junctions where the frequency-dependent element is discretised using the BT. It can be expected that bore simulations formulated with such wave digital junctions have similar stability properties to the DWG junction formulated using the BT [1]. This was tested, and indeed it was found that conical bore simulations using wave digital junction remain stable only if viscothermal losses are excluded; simulations with inclusion of such losses can usually only be employed for the calculation of the (truncated) system impulse response.

[1] The stability properties of conical bore simulations using DWG junctions are discussed in section 4.4.

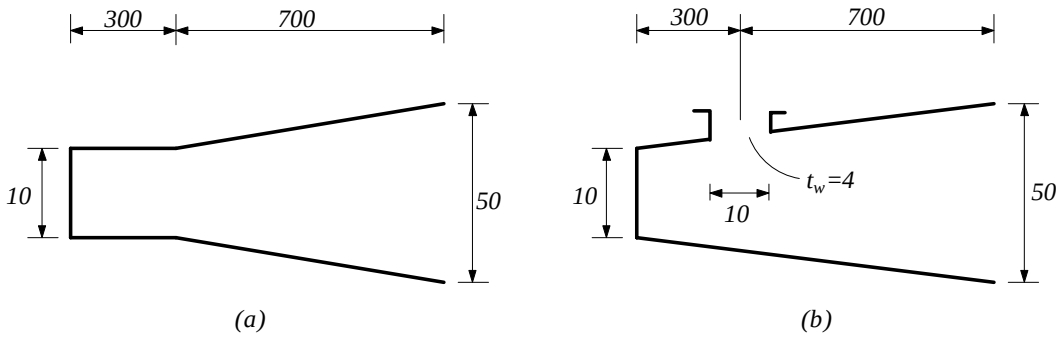


Figure 6.7: Example bore dimensions (After Martínez et al. [94]).

## 6.2 Example Applications

In one of the classical articles on time-domain modelling of acoustical bores, Martínez et al. [94] demonstrate the use of the multi-convolution method with a number of example applications. In this section we demonstrate the use of the wave digital modelling approach using the bore configurations of the first two examples in [94].

### 6.2.1 The Cylinder-Cone System

In the first example (figure 7 in [94]) we simulate a conical section attached to a short cylindrical section (see figure 6.7a). This bore configuration also served as an example in [19]. The computations in both references result in an impulse response that corresponds to the inverse Fourier transform of the input impedance of the bore, i.e., what is defined as "Green's function" in section 3.1.

In the wave digital modelling approach, wave propagation in cylindrical or conical sections is simulated in the same way as in digital waveguide modelling (see chapter 4). That is, propagation in the bore from one end to the other is simulated with a delay-line in cascade with two digital filters. In this case we used third-order Lagrange interpolation filters for modelling fractional delay lengths and fourth-order IIR filters to approximate the viscothermal losses of each bore section. Tubular junctions are modelled with the wave digital junction model presented in section 6.1.1. The open-end reflectance of the bore in section 6.7a can be considered as a lumped element. As explained in section 6.1.2, the reflectance at the end of the cone can therefore be simulated with a WD-$r$ junction in combination with a reflectance filter. Hence the complete wave digital model takes the form as depicted in figure 6.8. The wave digital reflectance $R_L'(z)$ was implemented using a third-order IIR filter.

In order to compute Green's function, a volume flow input pulse is injected into the system (i.e., $u(t) = \delta(t)$), and the pressure $p(t)$ at the input is obtained by summing the

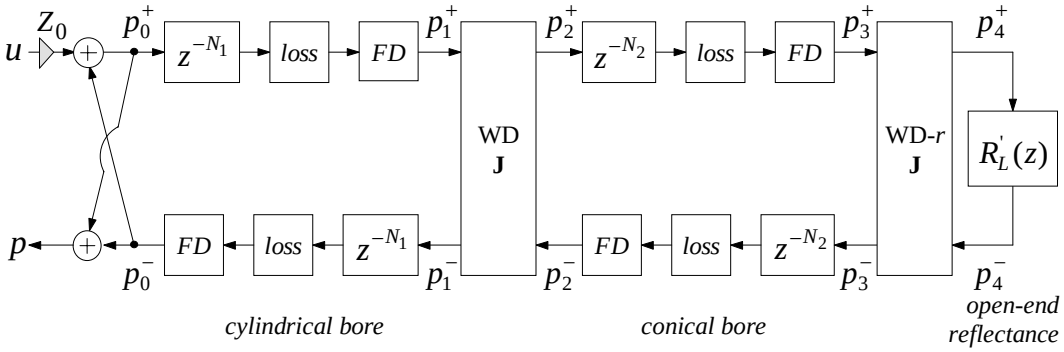


Figure 6.8: Wave digital model of the bore in figure 6.7a. The $z^{-N}$ units indicate delay-lines, the *FD* units indicate fractional delay filters, the *loss* units indicate loss-filters, and $R_L'(z)$ indicates the (wave digital) open-end reflectance. The WD **J** and the WD-$r$ **J** units are wave digital junctions.

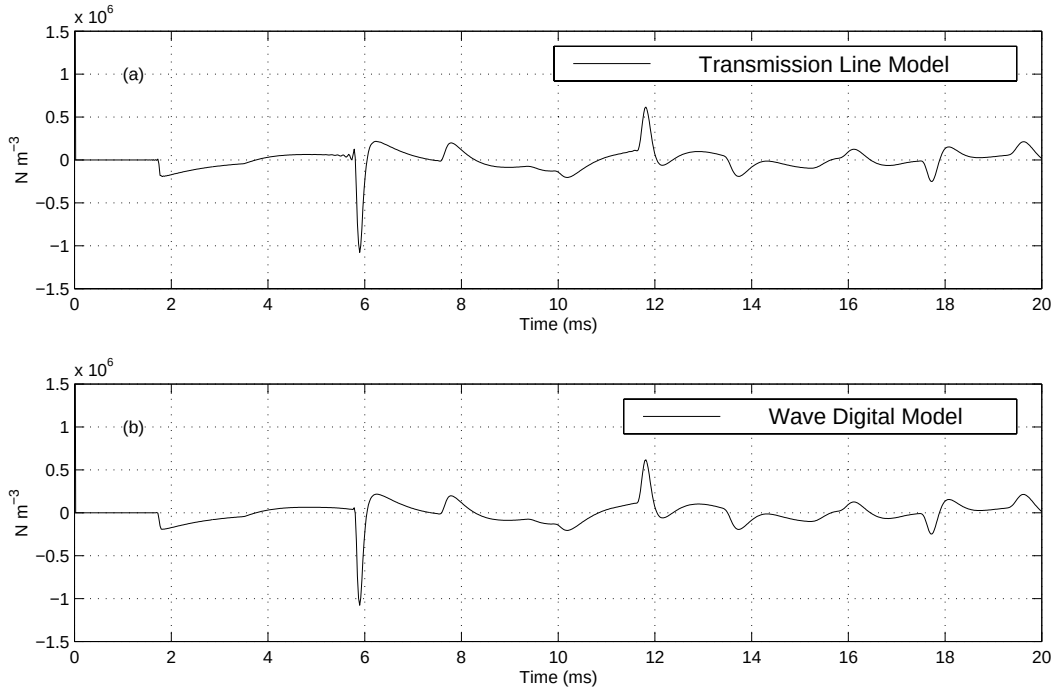


Figure 6.9: Discrete-time Green's function of the bore depicted in figure 6.7a. The sample rate is 44.1kHz.

waves $p_0^+$ and $p_0^-$ at each time-step. Figure 6.9b shows Green's function as calculated with the wave digital model. Green's function in Figure 6.9a was computed by taking the inverse Fourier transform of a frequency-domain computation using transmission-line matrices[2]. These time-domain signals can also be compared by ear[3]. We note that while the bore configuration is quite similar to the truncated bore system simulated in section 4.4.2, the error due to not using the "lossy" propagation constant in the junction formulation is significantly smaller in this case.

### 6.2.2 The Cone with Open Tonehole

The second example application, the bore configuration (figure 9 in [94]) consists of a conical section with an open hole in its side (see figure 6.7b). Discretisation is slightly more complicated than in the previous example, because we have to model a tonehole discontinuity. In the wave digital modelling approach, this is done by splitting the cone into two separate sections, and modelling the tonehole as a lumped element placed in between those sections. The open hole is simulated in discrete-time with the wave digital tonehole model discussed in chapter 5. Delay-free loops can be avoided in the system by using a WD-$r$ junction on the left-hand side and a WD-$l$ junction on the right-hand side of the tonehole, as depicted in figure 6.10. Because in this case the bore is immediately conical at its entry, a WD-$l$ junction is required at this point. The length-corrections associated with the tonehole are taken into account by reducing the length of the bore on either side of the hole. The losses, fractional delay-lengths, and the open-end reflectance are modelled in the same way as in the first bore example.

Green's functions of the cone with open hole, as computed with the transmission-line model and with the wave digital model, are depicted in figure 6.11. The main deviation between the two curves stems from the differences with respect to tonehole modelling. As seen in chapter 5, these differences occur mainly at high frequencies, and are therefore of secondary importance because (1) the transmission-line model employs Keefe's formulation of the tonehole shunt and series impedance, which have been verified experimentally only up to 5kHz, and (2) high frequencies have a negligible influence on the sound generation mechanism. The fact that there are only very small difference between the transmission-line model and the wave digital model can also be experienced through audio[4].

[2] See section 2.3 for frequency-domain computations with transmission-line matrices.
[3] Sound examples **(ex1)** and **(ex2)** in appendix K.
[4] Sound examples **(ex3)** and **(ex4)** in appendix K.

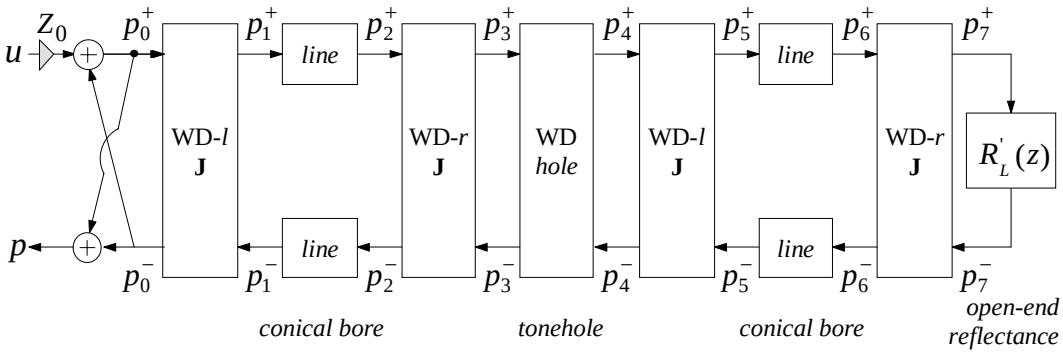


Figure 6.10: Wave digital model of the bore in figure 6.7b. Each *line* unit indicates a cascade of a delay-line, a loss-filter, and a fractional delay filter. The WD-$l$ **J** units indicate wave digital junctions with non-immediacy on the left-hand side, and the WD-$r$ **J** units indicate wave digital junctions with non-immediacy on the right-hand side.

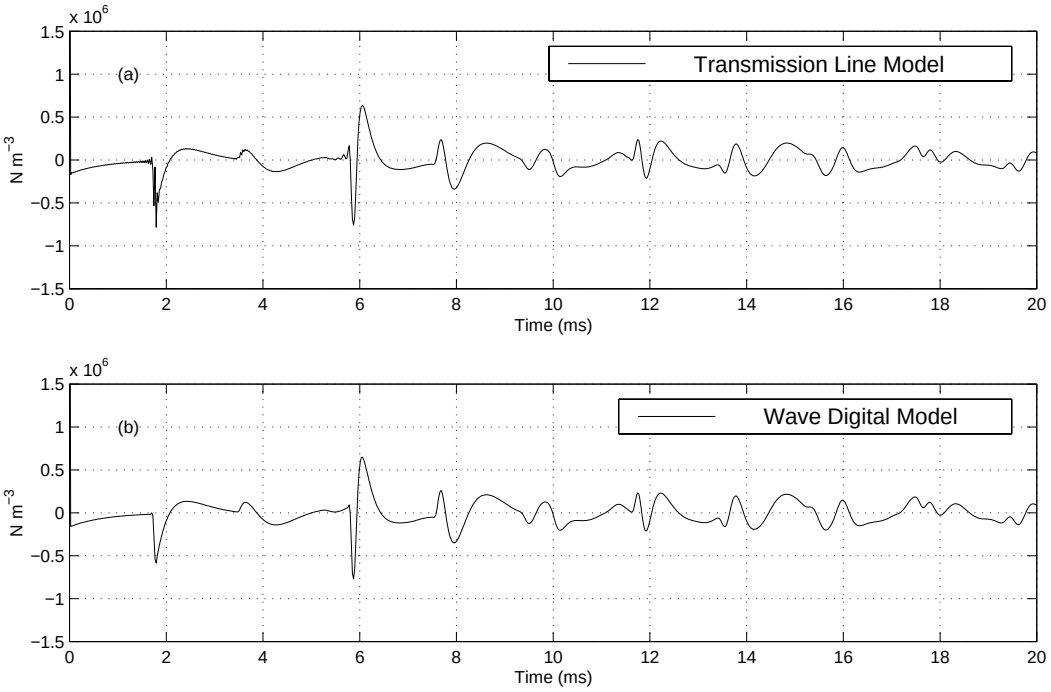


Figure 6.11: Discrete-time Green's function of the bore depicted in figure 6.7b. The sample rate is 44.1kHz.

## 6.3 Comparison with the Multi Convolution Approach

Some decades ago, Martínez et al. [94] developed methods for time-domain modelling of woodwind bores. In their original "multi convolution algorithm", the spacing between discontinuities is constrained to be a multiple of the spatial sampling interval. This limitation was later removed by Barjau et al. [19]. There are strong similarities between the wave digital modelling approach and the multi convolution approach. Firstly, the approaches employ the same modelling framework. That is, the response of a woodwind bore is computed by explicitly simulating the transmission, reflection and propagation of pressure waves in the bore. Secondly, many of the typical bore discontinuities (such as toneholes and taper changes) are based on equivalent continuous-time models. In this section, we compare the two approaches in terms of the reflection, transmission and propagation functions that are employed in the multi-convolution approach.

### 6.3.1 Calculation of Reflection and Transmission of Waves with the Time-Interpolated Convolution Method

In the multi convolution approach, the reflection and transmission functions are always of the form [19] ($t \geq 0$):

$$f(t) = a_0\delta(t) + a_1 e^{b_1 t} + a_2 e^{b_2 t} + a_{31} e^{b_3 t} + a_{32} t e^{b_3 t}, \tag{6.22}$$

where $a_i$ and $b_i$ are coefficients. These functions are convolved with pressure waves by means of the time-interpolated convolution method (TICM). The TICM computes a reflected or transmitted output-signal $y(t)$ by means of a convolution of the input signal $x(t)$ with the function $f(t)$:

$$\begin{aligned} y(t) &= f(t) * x(t) \\ &= \int_0^{+\infty} f(\tau)\, x(t-\tau)\, d\tau. \end{aligned} \tag{6.23}$$

This convolution is determined analytically, usually by assuming a linear evolution of the input-signal between successive discrete-time instants [94, 19].

### 6.3.2 Modelling First-Order Reflectance and Transmittance Filters

The last two terms in equation (6.22) only apply when modelling an open-end reflectance discontinuity (see section 6.3.3). Hence for all other types of discontinuities, the reflection and transmission functions are described as the sum of a Dirac pulse and two exponential

functions of the type

$$r(t) = a\, e^{bt}, \tag{6.24}$$

where the Dirac pulse part is usually computed separately. For example, the convolution of $x(t)$ with a function of the form

$$f(t) = \delta(t) + a\, e^{bt}, \tag{6.25}$$

is computed

$$y(t) = x(t) + a\, e^{bt} * x(t). \tag{6.26}$$

Reflection and transmission functions of this type are obtained by taking the inverse Fourier transform of a frequency-domain expression. For example, the result in equation (6.24) is obtained by taking the inverse Fourier transform of the frequency-domain function

$$F(\omega) = \frac{a}{j\omega - b}. \tag{6.27}$$

This frequency-domain expression corresponds to the transfer function of a one-pole filter element. Functions of this type also in appear in the underlying models of the wave digital modelling approach. In appendix I we show that for simulation of bore discontinuities of the types listed below, the two approaches are in fact based on equivalent continuous-time models:

- diameter and taper discontinuities
- open- and closed-hole discontinuities
- closed-end discontinuities

However the approaches are different in the way these first-order reflectances and transmittances are discretised. In the wave digital modelling approach, the bilinear transform (BT) is used, whereas a recursive formulation of the TICM is applied in the multi convolution approach [94, 19]. In appendix G we show that both these discretisation methods amount to passing the input-signal through a first-order digital filter. Although there is a difference in the way the filter coefficients are formulated, there tends to be a negligible difference between the responses obtained using the BT and using the TICM. Hence we may conclude that for discrete-time modelling of woodwind bore discontinuities that can be represented by reflection and transmission functions of the exponential type (or a sum of such functions and a Dirac pulse), the multi convolution approach and the wave digital modelling approach are practically equivalent. There are two remaining types of functions that appear in the multi convolution approach:

- the reflection function associated with an open-end discontinuity.

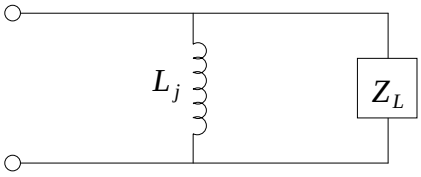


Figure 6.12: Equivalent network of the open end of a conical section. The conicity inertance is $L_j = -(\rho r)/(S)$, where $r$ is the apex distance and $S$ is the cross-section at the open end. $Z_L$ is the open-end radiation impedance.

- conical bore propagation functions.

These are discussed in the next two sections.

### 6.3.3 The Open-End Reflection Function

Martínez and Agulló [93] base their open-end reflectance formulation on an open-end radiation impedance formula by Morse [97]:

$$Z_L(\omega) = Z_0 \left(\Theta_0 + j\chi_0\right), \tag{6.28}$$

where $\Theta_0$ is the resistive and $\chi_0$ the reactive part of the impedance[5]. For application within the multi convolution approach, they employed an "ad hoc" formulation that was designed to approximate the inverse Fourier transform of the corresponding (spherical wave) reflectance:

$$r\,(t) \approx -\epsilon(t)\,\alpha_e^2\,te^{-\alpha_e\,t}, \tag{6.29}$$

with

$$\alpha_e = \frac{c}{2}\left[\frac{0.787\,e}{a} - \frac{1}{r}\right]. \tag{6.30}$$

where $a$ and $r$ are the radius and apex distance at the open end. It can be shown that computing the convolution of $r(t)$ with a pressure wave signal by means of a recursive formulation of the TICM amounts to passing the pressure wave through a second-order digital filter with a (double) pole at $z = e^{-\alpha_e T}$.

The wave digital formulation of the open end is based on a conicity inertance in parallel with the open-end radiation impedance $Z_L(\omega)$ (see figure 6.12). In principle, any formulation of $Z_L(\omega)$ can be used. As explained in section 6.1.2, the conicity inertance is modelled with a WD-$r$ junction. The port-resistance ($R_0$) is then determined, and we may derive the reflectance

$$R_L^{'}(\omega) = \frac{Z_L(\omega) - R_0}{Z_L(\omega) + R_0}. \tag{6.31}$$

[5] See [97] or [93] for the formulae for $\Theta_0$ and $\chi_0$.

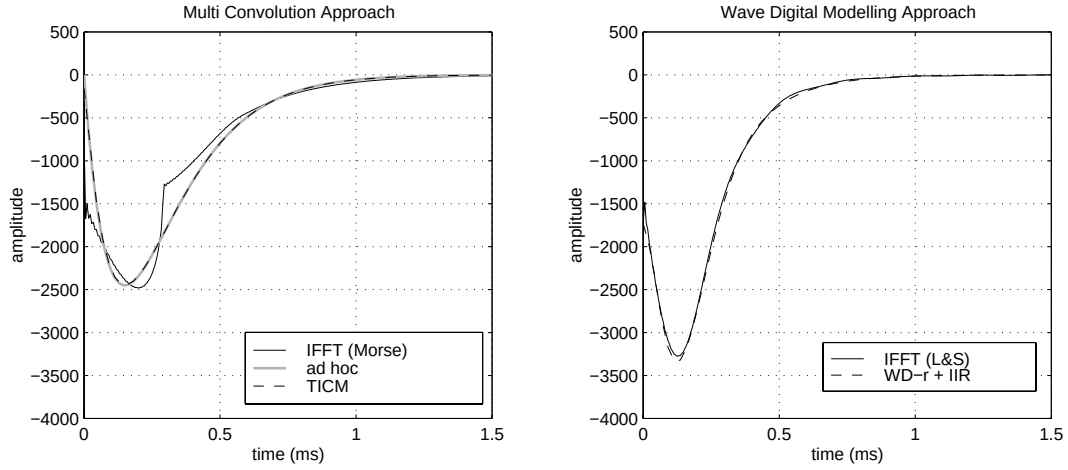


Figure 6.13: Spherical wave open-end reflection function as calculated with various different methods. Left: the inverse Fourier transform of the (spherical wave) reflectance according to Morse's frequency-domain formulation (solid, black), the "ad-hoc" formulation (solid, grey) and its discrete-time model using the TICM (dashed). Note that the latter two almost entirely overlap. Right: the inverse Fourier transform of the (spherical wave) reflectance according to the Levine and Schwinger formulation (solid), and the wave digital formulation (dashed).

This reflectance is then approximated with a digital filter. Scavone's extension of the open-end reflectance formulae by Levine and Schwinger[6] was used as our frequency-domain formulation of the open-end reflectance. For digital approximation of $R_L^{'}(\omega)$, a third-order IIR filter was used.

In order to compare the two approaches, we computed the (spherical wave) reflection function of the open end of a cone with $a = 50$mm and $r = 250$mm. These dimensions are of the same order as those found in woodwind instruments. The effective spherical reflection function of the wave digital modelling open-end formulation is computed by simply injecting an input pulse in the wave digital simulation of the network in figure 6.12. In the right-hand plot of figure 6.13, this result is compared to the inverse Fourier transform of the spherical wave reflectance according to the open-end formulation by Levine and Schwinger. In order to compare with the multi convolution approach, we compared the spherical wave reflection function as computed with (6.29) to the inverse Fourier transform of the spherical wave reflectance according the open-end formulations by Morse in the left plot of figure 6.13. Apparently, the "ad hoc" formulation does not approximate its target-response as closely as does the wave digital model. Whether this matters is questionable, because the ad hoc formulation possibly results in a more accurate open-end reflection function than Morse's formulation. More important to our comparison is that the ad hoc formulation is "fixed" into a certain form, and its accuracy can therefore not be increased in any way. In contrast, the wave digital approach allows for using any kind of formulation

[6] See section 2.2.5 for an explanation of this open-end formulation.

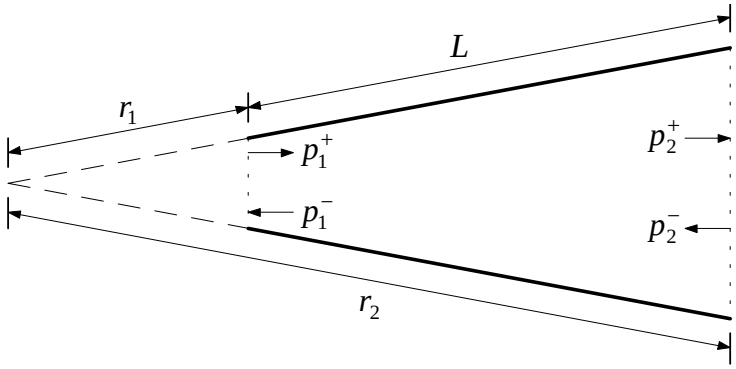


Figure 6.14: Conical bore geometry.

of $Z_L(\omega)$, and also allows for any order and type of digital filter approximation of the corresponding wave digital reflectance $R_L^{'}(\omega)$.

### 6.3.4 Propagation Functions

Consider the propagation of waves in the conical section depicted in figure 6.14. In the multi convolution approach, the propagation of waves in a conical bore section is modelled by means of a convolution with the bore propagation functions. Martínez and Agulló [93] implement this method in a form in which the pressure wave on the input-side is first delayed and then convolved with a propagation function $\sigma(t)$ that represents the viscothermal losses:

$$p_2^+(t) = p_1^+(t - L/c) * \sigma^+(t), \tag{6.32a}$$

$$p_1^-(t) = p_2^-(t - L/c) * \sigma^-(t), \tag{6.32b}$$

with

$$\sigma^{\pm}(t) = B^{\pm}\,\epsilon(t)\,\left(\frac{\xi}{2\sqrt{\pi}\,t^{3/2}}\right)\,e^{-\xi^2/4\,t}, \tag{6.33}$$

where $B^- = r_2/r_1$ and $B^+ = r_1/r_2$. These propagation functions are computed by taking the inverse Fourier transforms of the frequency-domain functions [94]:

$$\sigma^{\pm}(\omega) = B^{\pm}\,e^{-(\zeta + j\,\omega/c)L}, \tag{6.34}$$

where $\zeta$ is the viscothermal damping coefficient as used by Nederveen (Nederveen1969) for cylindrical bores. However, as pointed out in [19], this method does not allow accurate simulation of propagation in bore sections of arbitrary length. As explained in section 4.2, this problem can be solved by means of fractional delay filters. Barjau et al. use an alternative method, by re-formulating (6.32) such that the propagation-delay $L/c$ is included

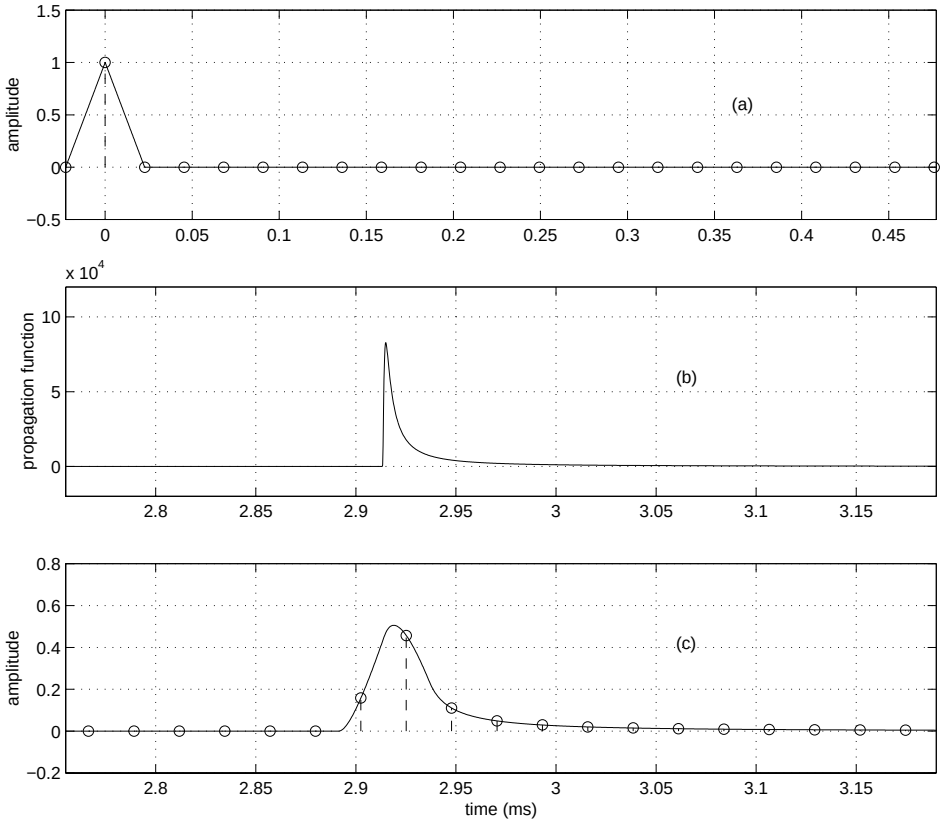


Figure 6.15: Time-domain signals involved in applying the TICM to modelling wave propagation in a cylindrical bore of length $L = 1$m and radius $a = 5$mm. Top: a Dirac pulse (circles) and the corresponding time-interpolated Dirac Pulse signal (solid). Middle: the continuous-time propagation function $\sigma(t)$. Bottom: the discrete-time impulse response $h(t)$ as computed with the TICM (circles) and the convolution product of $\sigma(t)$ with the time-interpolated Dirac pulse signal (solid).

in the propagation functions:

$$p_2^+(t) = p_1^+(t) * \sigma^+(t - L/c), \tag{6.35a}$$

$$p_1^-(t) = p_2^-(t) * \sigma^-(t - L/c). \tag{6.35b}$$

The convolutions in (6.35) are calculated by means of the TICM, which involves the calculation of the analytical integrands of the functions $\sigma^+(t)$ and $\sigma^-(t)$. The TICM effectively samples the continuous-time products of $\sigma^+(t)$ and $\sigma^-(t)$ convolved with a linearly interpolated Dirac pulse signal. We demonstrate this for the specific case of a cylindrical bore section of length $L = 1$m and radius $a = 5$mm. For a cylindrical section, the propagation functions are equal ($B^{\pm} = 1$). Therefore we denote both propagation functions with $\sigma(t)$. The continuous-time function $\sigma(t - L/c)$ may be approximated by evaluation at a very high sample rate $f_s = 4.41$MHz (see figure 6.15b). Next, an input-signal that approximates the continuous-time interpolated version of a 44.1kHz Dirac

pulse signal was generated at the same high sample rate (see figure 6.15a (solid line)). The approximation of the continuous-time convolution product of these two signals can be computed with a straight-forward discrete-time convolution at 4.41MHz, and is plotted in figure 6.15c (solid line). The discrete-time response $h(t)$ in figure 6.15c (circles) was computed with the TICM at 44.1kHz, using a Dirac pulse signal as the input-signal.

An efficient way of implementing the time-interpolated convolution method is by means of an FIR filter. That is, we compute the impulse response $h(t)$, and use this series as the coefficients of an FIR filter implementation of the convolution product. In theory, $h(t)$ is of infinite time-length, but in practice it has to be computed for a finite time-length. The finite nature of the convolution-length does not affect the accuracy of the simulation much because in application to musical instrument air columns, $h(t)$ always decays rapidly [19]. For a conical section, the coefficients $B^{\pm}$ may be applied separately or, as explained in section 4.3.1, may be left out altogether without affecting the reflection function.

In the wave digital modelling approach, the propagation of waves in a conical or cylindrical section is implemented with the techniques discussed in chapter 4. That is, the full propagation-path is simulated with a cascade of a delay-line, a fractional delay filter, and a loss-filter. This cascade is designed to approximate the "ideal" frequency response as calculated with Keefe's theory for viscothermal losses in acoustical bores (see section 2.2.3 and section 4.1.3). In order to test the approximation error, we computed the frequency response according to Keefe's theory for a cylindrical bore (of the same dimensions as in the above example), and compared this to the response of the cascade of a delay-line and two filters that is used in the wave digital modelling approach (see the right-hand plot in figure 6.16). A 4th-order IIR filter was used to approximate the viscothermal losses, and a third-order Lagrange interpolator was employed for simulation of the fractional delay length. For a similar test of the multi convolution approach, we compared equation (6.34) with the Fourier transform of the impulse response $h(t)$ (see the left-hand plot in figure 6.16). Apparently, both approaches result in a lowpass filtering effect. As with the simulation of the open-end reflectance, the main difference between the two approaches is the greater freedom within the wave digital modelling approach. That is, any type of discrete-time approximation of any type of frequency-domain formulation can be employed within the approach. For example, we may want to apply specific filter design methods in which emphasis can be put on accuracy at lower frequencies. Accuracy can be improved by increasing the order of the digital filter approximations. In the multi convolution approach, the continuous- and discrete-time formulations are "fixed". The accuracy of the discrete-time approximation can be improved by increasing the length of the convolution and by using a higher-order polynomial time-interpolation. While the discrete-time formulation by means of propagation functions already leads to an approximation that is more accurate at the lower frequencies, it can not be "navigated" towards accuracy in

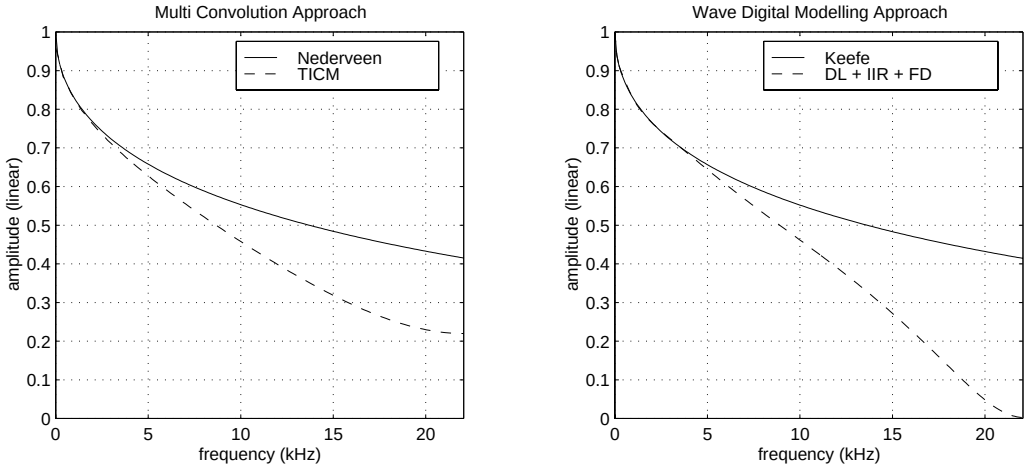


Figure 6.16: Magnitude response of the propagation function. Left: Nederveen's frequency-domain formulation (solid), and its discrete-time approximation using the time-interpolated convolution method (TICM). Right: Keefe's frequency-domain formulation, and its discrete-time formulation in the form of a delay-line and two digital filters in cascade.

specific frequency ranges.

## 6.4 Conclusions

In this chapter we have discussed methods for discrete-time modelling of woodwind bores. By formulating conical junctions in terms of equivalent inertance networks and discretising these by means of wave digital filter techniques, we have developed a novel method for discrete-time modelling of conical bore systems. The main advantage of the wave digital modelling approach over the more traditional digital waveguide modelling approach is that no realisability problems occur when a conical section is directly connected to a lumped element (such as a tonehole).

Furthermore, we have shown that strong similarities exist between the wave digital modelling approach and the multi convolution approach. Via a detailed comparison it was found that the wave digital modelling approach mainly differs in the manner in which (1) the open-end discontinuity is formulated, and (2) the viscothermal losses are taken into account. We have seen that there is a greater freedom of choice in basic formulation as well as digital approximation of these phenomena within the wave digital modelling approach.

# Chapter 7

# Digital Approximation of a Brass Bell Reflectance

A brass bell functions as a reflector of waves, trapping energy inside the instrument in such a way that standing waves of precisely defined frequencies can be build up [22]. The brass bell is therefore vital to the tuning of the instrument. In this chapter we investigate how a brass bell can be modelled in discrete-time such that the essential acoustic characteristics of the bell are preserved. A particularly efficient scheme is possible in which lumped filters model the bell reflection and transmission characteristics. This concept is discussed in section 7.1. The main task then consists of formulating appropriate digital approximation techniques. In section 7.2 we briefly review some previously applied methods as well as conventional filter design techniques. Then in section 7.3, we study the use of "one-pole TIIR filter elements". These are a special type of digital filters that are particularly efficient when applied to impulse responses that exhibit temporary exponential growth. Finally in section 7.4, the TIIR approach is applied to an experimentally determined trumpet bell reflectance.

## 7.1 Simulation using Lumped Filters

### 7.1.1 The Bell Reflectance

Consider the simplified representation of a brass air column depicted in figure 7.1. We note that the main bore of a brass instrument is usually only approximately cylindrical, and in some cases approximately conical, but the arguments brought forward in this section equally apply to these cases. Suppose that the objective is to compute the frequency-domain response at the air column entry. Because brass bells are usually strongly flared, the acoustic wave motion *inside* the bell is rather complicated due to coupling between the

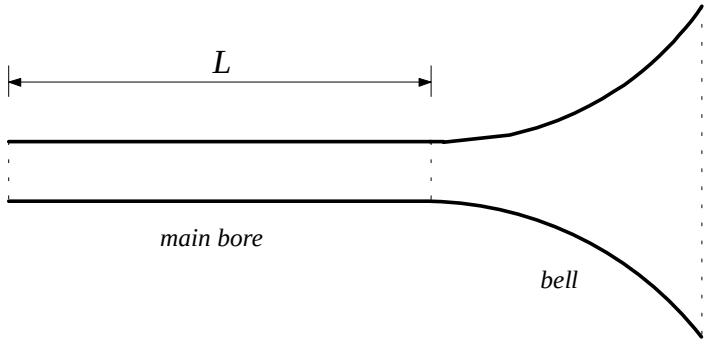


Figure 7.1: Schematic model of a simplified brass instrument air column.

various propagation modes. On the other hand, all propagation modes except the plane wave mode are evanescent at low frequencies in a main bore of sufficiently small diameter. This also holds if the main bore contains small cross-sectional discontinuities. For a brass instrument bore, the higher modes typically do not propagate at frequencies within the range of the musically important resonances. Hence if the plane-wave reflectance $R_L(\omega)$ of the bell is known (for example, via measurement or multi-modal analysis), then the entry reflectance of the complete instrument can be computed via a simple one-dimensional formulation:

$$R_f(\omega) = e^{-2\Gamma L} \cdot R_L(\omega), \tag{7.1}$$

where $\Gamma$ is the plane wave propagation constant. This concept can be used to construct an efficient discrete-time model of the air column. The system in figure 7.1 can be modelled in discrete-time with the structure depicted in figure 7.2. As explained in chapter 4.1, a

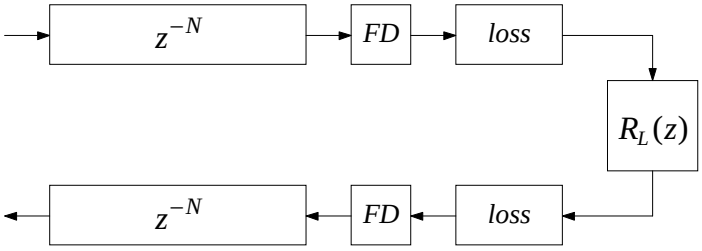


Figure 7.2: Discrete-time simulation scheme of the model depicted in figure 7.1. Each *FD* unit indicates a fractional delay filter, each *loss* unit represents a loss-filter, $z^{-N}$ indicates a delay-line, and $R_L(z)$ is the digital filter that approximates the plane wave horn reflectance.

cylindrical bore section can be modelled with a simple delay-line plus some filters for simulation of boundary losses and fractional delays. The bell reflectance can be approximated with a digital filter $R_L(z)$. The simulation efficiency can be improved by first lumping the

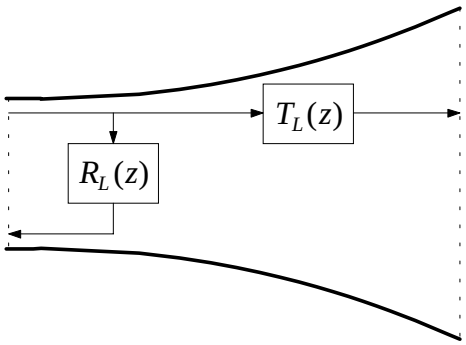


Figure 7.3: Simulation of the bell with two lumped filters.

boundary losses and fractional delays together with the bell reflectance:

$$\hat{R}_L(\omega) = \left( \frac{e^{-2\Gamma L}}{e^{-2\omega L/c}} \right) \cdot R_L(\omega), \tag{7.2}$$

and then approximating the lumped reflectance $\hat{R}_L(\omega)$ with a digital filter. In this way no loss-filter is required in the simulation.

The higher-modes are also evanescent in the lower frequency range in the case of a conical main bore. The bell may still be modelled as a plane wave reflectance in this case, although discrete-time modelling becomes slightly more complex, and has to be realised as explained in section 6.1.2.

### 7.1.2 The Bell Transmittance

The sound pressure at the end of the bell can be computed via the bell transmittance $T_L(\omega)$. The bell may thus be modelled in discrete-time by means of two lumped filters that approximate the reflectance and transmittance (see figure 7.3). For digital approximation, we employ the output-error method for IIR filter design. As seen in section 4.1 this method allows us to emphasise accuracy at low frequencies. If viscothermal losses in the bell are neglected, we have conservation of energy within the bell:

$$|R_L(\omega)|^2 + |g\, T_L(\omega)|^2 = 1, \tag{7.3}$$

where for a bell with entry radius $a_1$ and end radius $a_2$, $g = a_2/a_1$; this amplitude scaling is required to take into account the decrease of pressure with increasing bell cross-section. The relationship in (7.3) allows us to deduce the transmittance magnitude from a given bell reflectance $R_L(\omega)$. The phase-information, which can not be deduced from (7.3), is relatively unimportant because it does not influence the sound generation of the instrument. Moreover, since the mechanisms of human sound perception are relatively

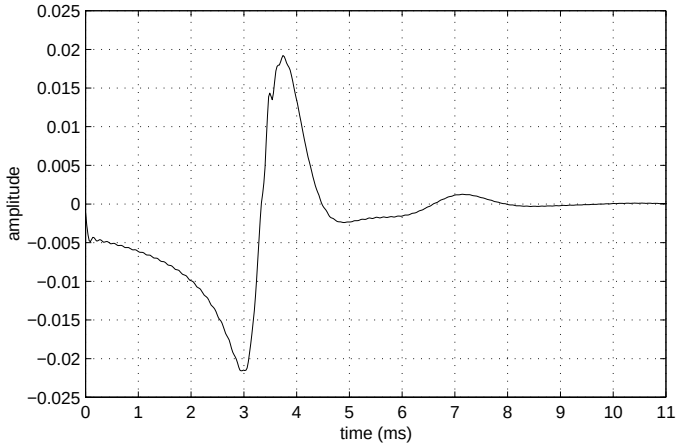


Figure 7.4: Discrete-time reflection function of the Bessel horn approximation of a trombone bell, as computed via multi-modal analysis.

insensitive to phase information [108], we may "reconstruct" an arbitrary transmittance phase without affecting the sound quality of the physical model. Here we apply the method of minimum-phase reconstruction using the real cepstrum method described in [50]. With respect to digital filter approximation of the transmittance, the minimum-phase reconstruction is a particularly suitable choice, because the output-error method for IIR filter design gives the best results if the target-response is minimum-phase [127].

## 7.2 Digital Approximation Techniques

### 7.2.1 A Generalised Target Response

A general characteristic of musically useful brass horns is that their internal bore profile is well approximated by a Bessel horn [25]. Although almost any real brass bell will show some deviations from this approximation in its bore shape and acoustic reflectance, a theoretically derived Bessel horn reflection function may serve as a suitable generalised target-response for developing effective digital filter design techniques. In order to obtain such a target-response, the reflectance of a Bessel horn that approximates the trombone bell profile depicted in figure 2.19 was computed using the multi-modal method that is described in [105] (see also section 2.3). In this case, the horn was assumed to be open-ended with infinite flange. The open-end radiation impedance was computed using the formulation in [169]. Figure 7.4 shows the resulting trombone bell reflection function.

### 7.2.2 Previously Developed Approximation Techniques

It appears that only two methods for digital approximation of the open-ended brass bell reflectance have been applied in previous research. The most simple method is to use an


Figure 7.5: Two ways of modelling a bell reflectance in discrete-time used in previous research. (a) convolution with the bell reflectance, implemented using a FIR filter. (b) piecewise cylindrical approximation of the bell, implemented using a waveguide filter (WGF).

$N$th-order FIR filter, where a vector of $(N+1)$ filter coefficients equals the truncated impulse response of the bell (see figure 7.5a). This method is equivalent to convolution with the discrete-time reflection function of the bell. Msallam [99] employed this method for modelling of the trombone bell. Using a sample rate $f_s = 44.1$kHz, the bell reflection function can usually be truncated to about 100 to 300 samples [158]. The FIR approach gives accurate results, but must be considered as computationally expensive in the context of musical sound synthesis.

Another method that has been applied previously is to approximate the bell profile with a piecewise cylindrical model and implement this model in discrete-time using a waveguide filter (WGF)[1] (see figure 7.5b). For example, this approach has been taken in [45, 46] for simulation of the trumpet. As seen in section 2.3, the reflectance of a strongly flaring tube such a brass bell is not modelled particularly accurately using the piecewise cylindrical approximation, even if the number of sections taken is very high. Moreover, even if only a moderately accurate bell reflectance is required, a relatively high number of sections still has to be used. Taking into account that the waveguide filter requires one multiplication per bore section, it may be concluded that this approach is neither accurate nor efficient.

### 7.2.3 IIR Approximation

It is clear that the bell-modelling techniques used in previous research are open to improvement. What is needed is a digital model that computes an accurate bell reflectance, but has relatively low computational costs. An obvious approach would be to employ an IIR filter instead of an FIR filter, because IIR filters are generally more powerful digital approximators [109]. The transfer function of an IIR filter that has $N$ zeros and $M$ poles is:

$$H(z) = \frac{b_0 + b_1 z^{-1} + .... + b_{N+1} z^{-(N+1)}}{a_0 + a_1 z^{-1} + .... + a_{M+1} z^{-(M+1)}}. \tag{7.4}$$

[1] The waveguide filter is discussed in section 3.2.4.

Several IIR filter design techniques are available in the literature (see [104, 127, 106, 109] for detailed discussions on IIR filter design methods. Here we will apply the *output-error method* [127], also referred to as the *Steiglitz-McBride algorithm* [138, 89]. This is an iterative method that minimises a least-square error between $H(z)$ and the target-response $H_t(\omega)$. The error may be calculated either in the frequency-domain[2] or in the time-domain[3], where the frequency-domain method allows for frequency-weighting. For both types of error-minimisation, the method is phase-sensitive (i.e. both magnitude and phase are approximated). Smith [127] has pointed out that the output-error method is not guaranteed to iterate to an optimum solution. Therefore some additional "fine-tuning" of the filter design parameters is often needed in order to obtain good results [133]. The main possibility of such fine-tuning can be achieved via frequency-weighting.

In figure 7.6, the IIR filter approximation obtained using the frequency-domain implementation of the output-error method with filter order 5 and 10 respectively, is compared with the target-response. A $(1/\omega)$ frequency-weighting was applied to emphasise accuracy for the lower frequencies. As a result, the higher frequencies are overestimated. Perhaps a more significant error is that the IIR impulse response exhibits a spurious oscillative pattern in the first few milliseconds, whereas the real horn reflectance exhibits a typically smooth build-up. We note that increasing the order of the filter from 5 to 10 does not improve the fit significantly.

Figure 7.7 compares the target-response with the response of an IIR filter for which the filter coefficients were obtained using the time-domain implementation. The 5th-order filter response is quite similar to the response obtained with the results obtained with the frequency-domain implementation, but this time an improved fit is obtained using a 10th-order filter. However we note that the response still exhibits spurious oscillations in the build-up.

Apparently it is difficult to get a good fit to the target-response using conventional phase-sensitive filter design methods: it appears that the search for the optimum parameters is "ill-conditioned", which leads to the procedure converging to a local minimum. Empirically we found that this tends to be the case whenever the response has a long, slowly rising, quasi-exponential start. A possible explanation for this is that the poles of a stable IIR filter (which are located inside the unit circle) cannot contribute to such a growing trend. The filter design algorithm is, as it were, "set" to search for pole locations outside the unit circle while being constrained to locations inside the unit circle.

[2]Implemented in *MATLAB*© with the function `invfreqz`.
[3]Implemented in *MATLAB*© with the function `stmcb`.

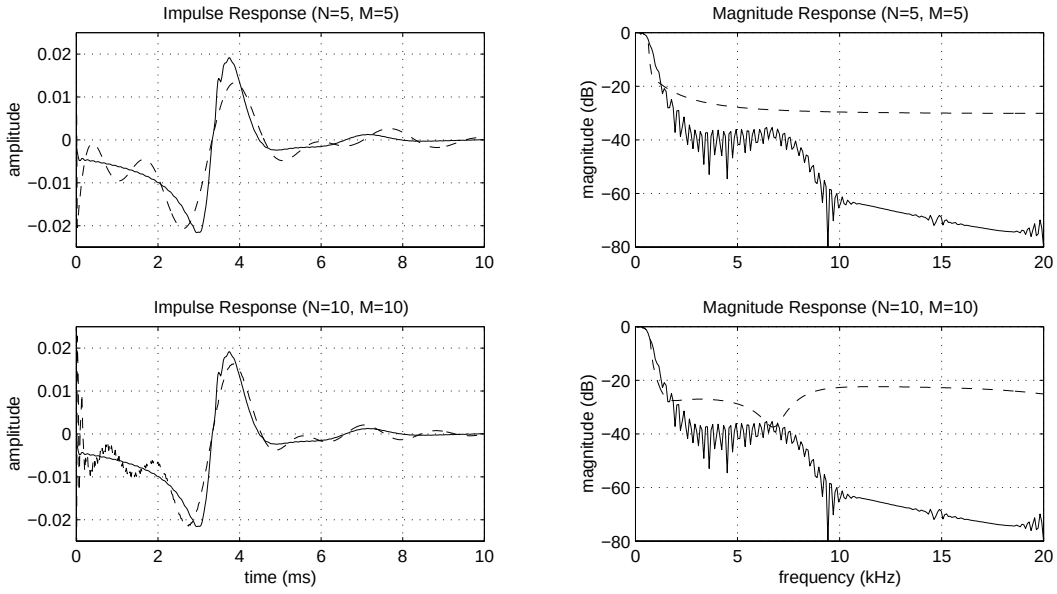


Figure 7.6: The IIR filter (dotted), designed using the frequency-domain implementation of the output-error method, compared to the Bessel horn target-response (solid).

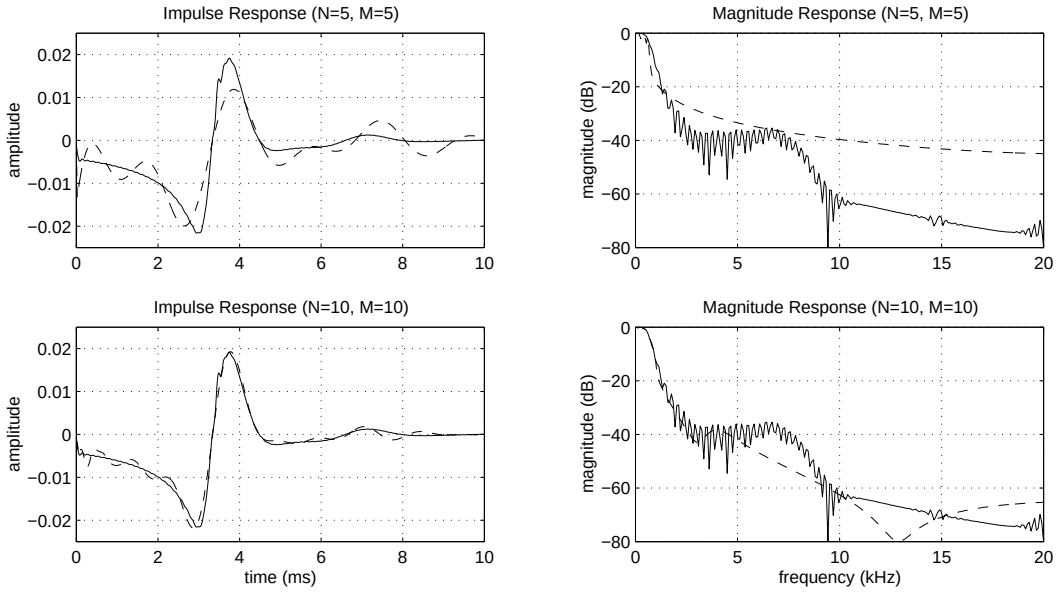


Figure 7.7: The IIR filter (dotted), designed using the time-domain implementation of the output-error, compared to the Bessel horn target-response (solid).

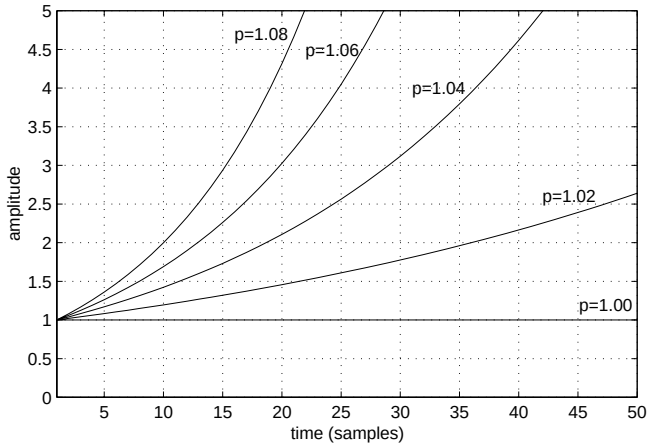


Figure 7.8: Impulse response of an unstable one-pole filter, for a range of pole coefficients. The sample rate is 44.1kHz.

## 7.3 Use of One-Pole TIIR Filter Elements

Given that the exponentially growing portion of the impulse response is what causes the problems, it is interesting to note that a one-pole filter withh its pole outside the unit circle has exactly such a response. For example, consider the one-pole filter with the transfer function

$$H(z) = \frac{1}{1 - pz^{-1}}. \tag{7.5}$$

Figure 7.8 shows the impulse response of this filter for a number of different pole coefficients ($p \geq 1$). It is well known that such a filter is unstable, which usually excludes it from application in the time-domain. While the impulse response of a filter with $p > 1$ exhibits infinite growth, we would only need temporary growth for the horn reflection function approximation. If somehow a special technique can be applied in which the growth of this response can be stopped after a certain number of samples, then the resulting *truncated* impulse response could be used for approximation of the start of the horn impulse response. Fortunately, such a technique indeed exists, and the filters that result from applying this technique are referred to as *truncated infinite impulse response* (TIIR) filters. Smith [133, 157] has suggested to use one-pole TIIR filter elements for the approximation of a brass bell reflectance.

### 7.3.1 Truncated Infinite Impulse Response Filters

The basic idea of a truncated infinite impulse response (TIIR) filter is to synthesise a FIR filter as the difference of two IIR filters [162]. That is, the tail of the first IIR filter is "cancelled" by the second IIR filter, such that the overall response is FIR. In order to realise this cancellation, the second IIR filter has to be designed such that it generates a

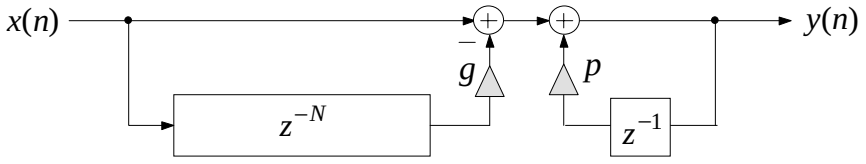


Figure 7.9: Implementation of a one-pole TIIR filter. This implementation is only suitable in the case of a filter with a pole inside the unit circle.

copy of the tail of the first IIR filter. For example, consider the first-order IIR filter with a transfer function as given in equation (7.5). This one-pole filter has an impulse response

$$h_1(n) = p^n * \epsilon(n), \tag{7.6}$$

where the operator "$*$" denotes convolution, and where $\epsilon(n)$ is the Heaviside unit-step function:

$$\epsilon(n) = \begin{cases} 1, & n \geq 0 \\ 0, & n < 0 \end{cases} . \tag{7.7}$$

Suppose that we want to truncate the impulse response $h_1(n)$ after $N$ samples. With the first sample occurring at $t = 0$s, this means that we have to find an IIR filter that has an impulse response:

$$h_2(n) = \begin{cases} 0, & n < N \\ p^n\,\epsilon(n), & n \geq N \end{cases} , \tag{7.8}$$

and subtract the output of this filter from the output of the first filter. We can write (7.8) as:

$$\begin{aligned} h_2(n) &= p^n * \epsilon(n-N), && \text{(7.9a)} \\ &= p^N * p^{n-N} * \epsilon(n-N), && \text{(7.9b)} \\ &= g * h_1(n-N), && \text{(7.9c)} \end{aligned}$$

where $g = p^N$. Thus $h_2$ is simply $h_1$ scaled by $g$ and delayed by $N$ samples! We can now write the TIIR filter transfer function as:

$$\begin{aligned} H(z) &= H_1(z) - H_2(z), && \text{(7.10a)} \\ &= \frac{1}{1-pz^{-1}} - \frac{gz^{-N}}{1-pz^{-1}}, && \text{(7.10b)} \\ &= \frac{1-gz^{-N}}{1-pz^{-1}}. && \text{(7.10c)} \end{aligned}$$

This filter can be implemented with the structure in figure 7.9. For a pole that is located

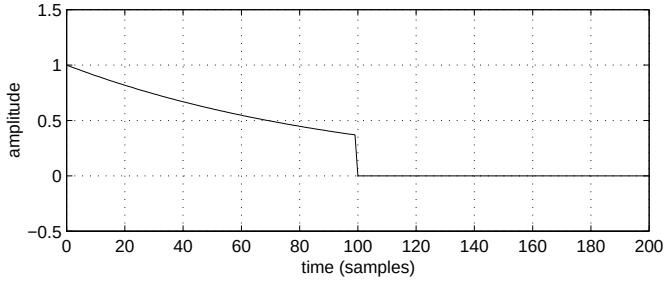


Figure 7.10: Impulse response of a one-pole TIIR filter with $p = 0.99$. The (decaying) tail is cancelled after $N = 100$ samples.

*inside* the unit-circle ($|p| < 1$), the impulse response is an exponentially decaying curve that is truncated after $N$ samples. Figure 7.10 shows the impulse response for $p = 0.99$ and $N = 100$. In theory, a TIIR filter always has a finite impulse response, even in the "unstable" case in which the pole is located *outside* the unit-circle ($|p| > 1$). The impulse response then is an exponentially growing curve that is truncated after $N$ samples (see figure 7.11). However, in this case the straight-forward implementation fails numerically. While the tail-cancelling concept always functions in principle, the exponential growth of the round-off error eventually starts to dominate. Thus, although this problem might perhaps not occur within the first few hundred samples, it *will* eventually occur if we keep computing the impulse response.

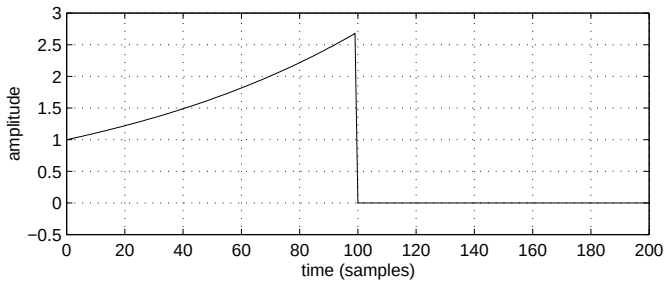


Figure 7.11: Impulse response of a one-pole TIIR filter with $p = 1.01$. The exponentially growing tail is cancelled after $N = 100$ samples.

Clearly, such a numerical failure complicates the use of this filter model. Fortunately, this problem can be solved by using two alternating instances of the TIIR filter. That is, we effectively run two versions of the TIIR filter in parallel (filter (I) and filter (II)), where only one of them (e.g., filter (I)) is producing the current output. However filter (II) receives the same input signal as filter (I). After $M$ samples, we "switch" the two filters, so now filter (II) produces the output. Directly after switching, the state of filter (I) is cleared. This means that all the values of the delay-line as well as the memorised value of the filter are set to zero. Filter (I) then starts to receive the normal input signal,

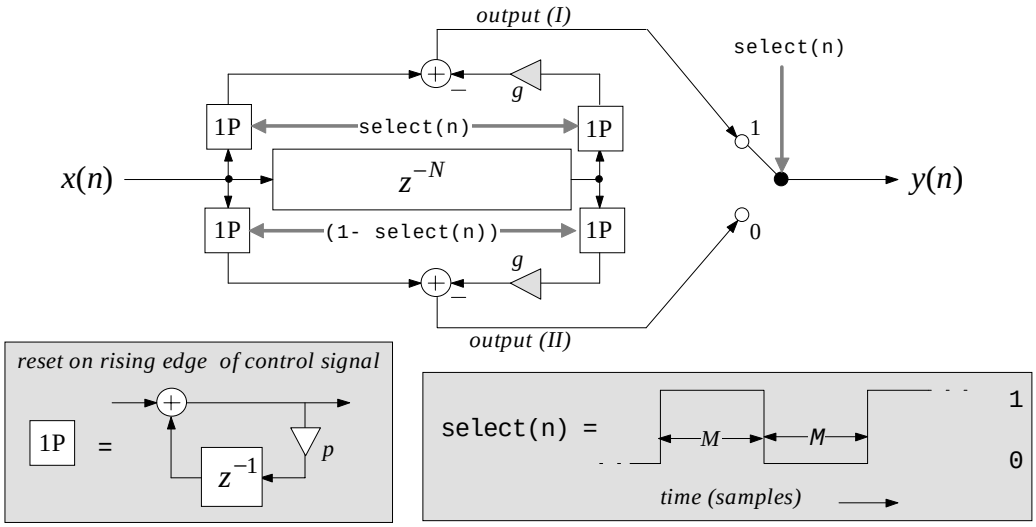


Figure 7.12: A one-pole switched TIIR filter. The grey arrows indicate control signals. `Select(n)` is the main control signal that determines whether output(I) or output(II) is used.

and "warms" up for a period of $M$ samples. The key observation is that, because the desired TIIR filter functions as an FIR filter, it reaches an exact "steady state" after only $N$ samples, where $N$ is the length of the synthesised FIR filter. As a result, a "fresh instance" of the TIIR filter, when "ramped up" from the zero state, is ready to be switched in after only $N$ samples, even though the filter has not yet reached the same internal state as the one being switched out. Hence as long as we choose $M > N$, the switching should not produce any discontinuities in the output signal.

Figure 7.12 shows one of the possible ways of implementing such a "switched" one-pole TIIR filter. Here we use the "shared delay" form. By conceptually "pushing" all four one-pole filters forward through the subtraction block, one obtains additionally the "shared dynamics" form suggested in [162]. For simplicity, however, we will describe the version in figure 7.12. Referring to figure 7.12, suppose the upper pair of one-pole filters is switched in (as the figure indicates). When the `Select` signal undergoes transition, the alternate one-pole pair below is selected, and the upper one-poles can be cleared and halted (or simply not computed in a software implementation). If the TIIR impulse-response length is $N$ samples, then the first upper filter on the left is restarted $N$ samples before it is to be switched back in, while the second upper filter is restarted on the *same* sample as it is switched back in. This works because, even though the upper pair will not be in the same state as the lower pair after $N$ times steps, its tail-cancelling difference, which synthesizes an FIR filter, *is* identical (ignoring round-off errors). Therefore, the switching resets can be as often as every $N$ samples. It is desirable, however, to switch much less often than every $N$ samples in

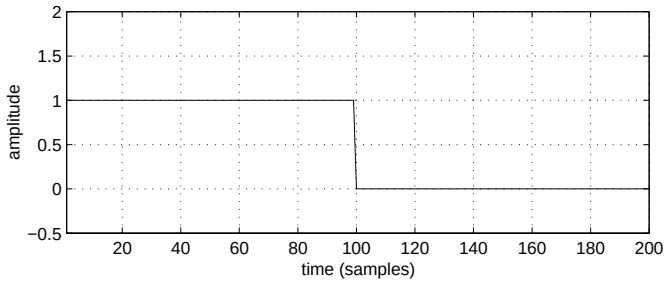


Figure 7.13: Impulse response of a one-pole TIIR filter that has its pole on the unit-circle ($p = 1$). The "constant function" is truncated after 100 samples.

order to minimise computations. The minimum switching rate, at the other extreme, is determined by the exponential growth rate and available dynamic range [162]. Finally, we note that when the poles are set to $p = 1$, the one-pole filter elements become digital integrators, and the TIIR filter impulse response is a truncated constant function (see figure 7.13). The tail-cancelling multiply-subtract in that case becomes only a subtraction. We note that the resets for digital integrators can be considerably less often than for growing exponentials, because the round-off error grows more slowly in an integrator [162].

In summary, a one-pole TIIR filter can be used for making

- a truncated decaying exponential ($p < 1$, no switching required).
- a truncated constant function ($p = 1$, switching at a "low" rate required ($M \gg N$)).
- a truncated rising exponential ($p > 1$, switching at a "normal" rate required ($M > N$)).

TIIR filters can be computed at a cost close to that of a one-pole filter and a multiply-add, plus some associated switching and control logic. Higher order TIIR filters are also possible [162]. However, the one-pole filter is sufficiently general for the purposes of the present study.

### 7.3.2 Bessel Horn Application

As shown in figure 7.4, the Bessel horn impulse response has a slow, quasi-exponentially growing portion at the beginning, corresponding to the smoothly increasing taper angle of the horn. A one-pole TIIR filter gives a truncated exponential impulse response $y(n) = ae^{cn}$, for $n = 0, 1, 2, \ldots, N-1$, and zero afterwards. We can use this truncated exponential to efficiently implement the initial growing trend in the horn response ($c > 0$). We found empirically that improved accuracy is obtained by using the *sum* of an exponential and a

*constant* function, i.e.,

$$y(n) = \begin{cases} ae^{cn} + b, & n = 0, 1, 2, \ldots, N-1 \\ 0, & \text{otherwise} \end{cases} . \tag{7.11}$$

In order to find appropriate values for the parameters $a$, $b$ and $c$, an optimisation routine[4] that minimises the error between $y(n)$ and the exponentially growing part of the horn is used. As seen in the section 7.3.1, a truncated constant function $f(n) = 1$ can be generated using a one-pole TIIR filter with its pole set to $p = 1$. We only have to multiply such a filter with $b$ to obtain a truncated constant function $f(n) = b$. This TIIR filter operates in parallel with the TIIR filter that generates an exponentially growing response. Hence the transfer function of the overall TIIR filter for modelling the start of the horn impulse response can be written as[5]

$$H(z) = b\left[\frac{1 - z^{-N}}{1 - z^{-1}}\right] + a\left[\frac{1 - p^N z^{-N}}{1 - pz^{-1}}\right] . \tag{7.12}$$

Note that both one-pole TIIR filter elements in (7.12) are implemented in "switched" form, as explained in section 7.3.1.

The remaining part of the reflection function has a decaying trend, and can therefore be modelled accurately with a conventional IIR filter design technique. In this case we applied the Steiglitz-McBride algorithm. The input to the IIR filter has to be delayed for $N$ samples, so that the tail it generates starts exactly after the truncation-point of the TIIR filter. Hence the final filtering structure takes the form depicted in figure 7.14.

In figure 7.15, the TIIR horn filter structure (using a 3rd-order IIR tail filter approximation) is compared with the theoretical response. We included the open-end effective length[6] in the comparison, since it gives us a good indication of how well the positions of the resonances of the horn are preserved. Apparently, the TIIR+IIR filter scheme approximates both the magnitude and the effective length closely at frequencies below the bell cut-off.

## 7.4 Trumpet Bell Application

The impulse response of the Bessel horn used in the computations in section 7.2.1 is an "idealised", target-response. It was found that this response can be simulated in discrete-time with the use of an offset-exponential TIIR section (that models the impulse response start) plus an IIR filter (that models the impulse response tail). In this section we

[4] A simplex search method was used, implemented in *MATLAB*© with `fmins`.
[5] This type of filter will be referred to as an "offset-exponential TIIR section".
[6] see appendix C for the definition of the open-end effective length of an acoustical system.

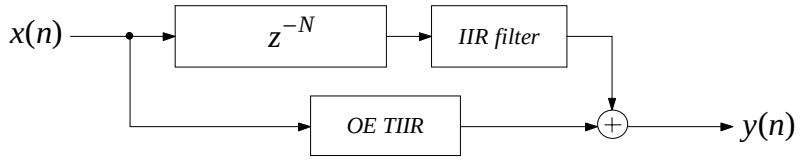


Figure 7.14: TIIR+IIR Filter scheme for modelling the Bessel horn reflectance. The offset-exponential TIIR section is indicated with OE TIIR.

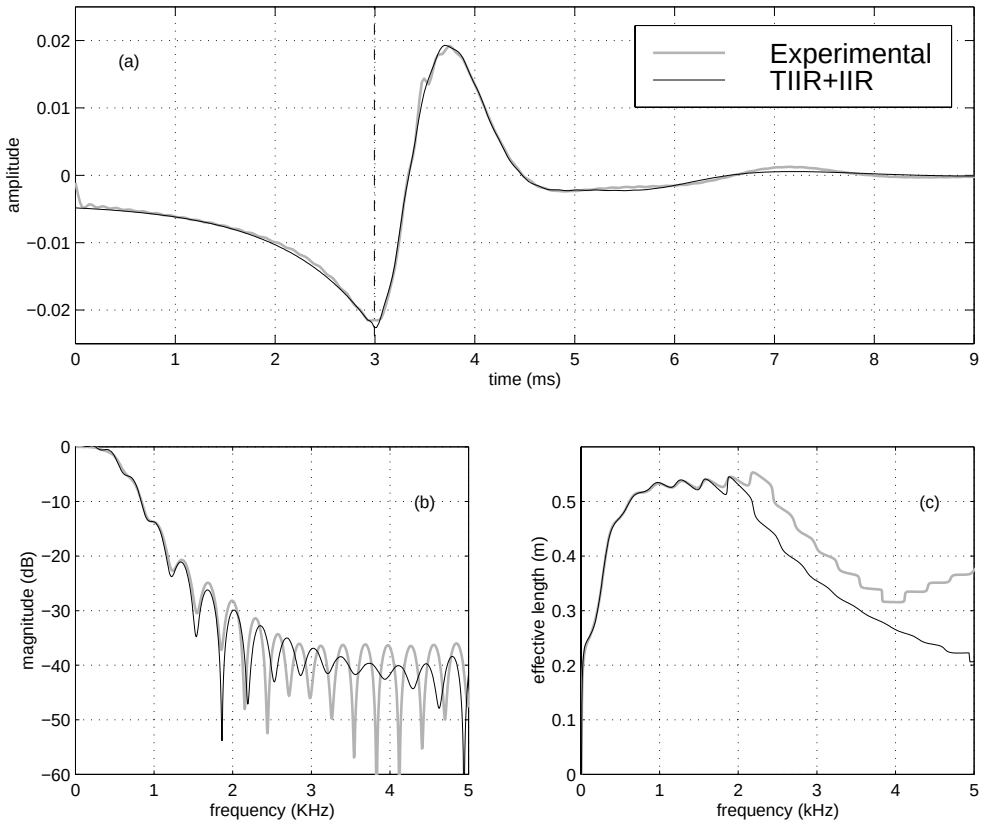


Figure 7.15: Bessel horn response (solid) compared with the TIIR+IIR filter approximation (dashed) in terms of (a) impulse response, (b) magnitude and (c) open-end effective length. The vertical line in (a) indicates the segmentation into an growing exponential and a decaying tail. The sample rate is 44.1kHz.

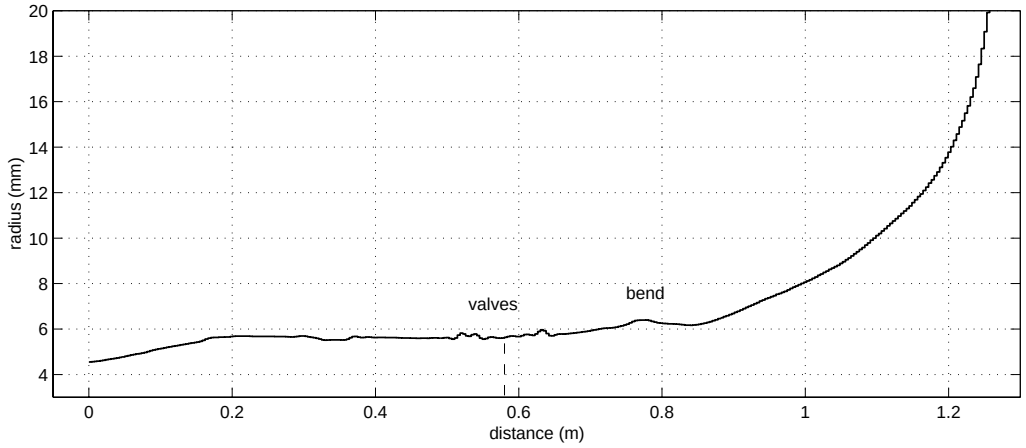


Figure 7.16: Trumpet bore profile reconstruction. The valves and the final tubular bend show as "dents" in the profile. The dashed line indicates the point where the bell starts.

investigate the possibilities of using the TIIR approach in modelling of an experimentally determined trumpet bell response.

### 7.4.1 Experimental Determination of the Bell Reflectance

Acoustic pulse reflectometry techniques[7] were applied to obtain the impulse response of a Boosey and Hawkes trumpet (without mouthpiece). A piecewise cylindrical section model of the bore profile was then reconstructed using an inverse-scattering method [10, 126], taking into account the viscothermal losses (see figure 7.16). The piecewise cylindrical model corresponds well to the physical bore profile for non-flaring tube-segments, thus giving a good physical model up to the bell. The remaining cylindrical sections do not provide valid geometrical information, but they retain all relevant acoustical information of the bell reflectance, including the complex influences of the higher transversal modes and the open-end radiation impedance. We note that the profile has been reconstructed beyond the physical end of the trumpet. Because the transition to open air is very smooth, the profile shows no taper discontinuity at this point. The bell reflectance $R_L(\omega)$ is computed as the reflectance of that part of the piecewise cylindrical model that corresponds to reconstruction of the bell.

### 7.4.2 TIIR+IIR Filter Model

The trumpet bell reflection function $r_L(t)$ is obtained by taking the inverse Fourier transform of $R_L(\omega)$. This reflection function (see figure 7.18a, solid grey line) differs from the theoretical Bessel horn response (see figure 7.4) primarily in its two-stage build-up

[7] See appendix J for a short description of this experimental technique.

towards the main reflection peak. By adding another offset-exponential TIIR section (equation (7.12)) to the basic horn filter structure, the filter design methodology is sufficiently flexible to cover the two-stage build-up. That is, each of the two build-up stages is modelled using an offset-exponential TIIR section, and the tail is modelled using an IIR filter (see figure 7.17).

### 7.4.3 FIR+IIR Filter Model

The growing part of the bell reflection function may also be approximated using an FIR filter. Such an approach leads to an FIR+IIR filter model, which may be expected to be more accurate than the TIIR+IIR filter model. The computational costs of this model will be considerably higher than that of the TIIR+IIR model, but significantly smaller than that of a FIR model of similar accuracy. For example, using a 44.1kHz sample rate, the growing part of the trumpet bell reflection function is about 175 samples, while a good FIR response is about 400 samples long. The FIR+IIR model may thus be considered as a good solution in the case where a high level of precision is required.

The time and frequency responses of the TIIR+IIR model and the FIR+IIR model are depicted in figure 7.18. As can be seen in figure 7.18, the TIIR+IIR model exhibits small differences with the experimentally determined response in the growing part of the reflection function. This is because the TIIR approximation of the initial slow rise is insensitive to reflections caused by bore profile dents. Naturally, these problems do not occur with the FIR+IIR model, since it effectively samples the growing part of the reflection function. We note that the FIR+IIR model is extremely accurate at frequencies below cut-off, and that the TIIR+IIR model response exhibits only small magnitude deviations in this frequency range.

## 7.5 Conclusions

In this chapter we have seen that a brass bell can be modelled efficiently and accurately by means of a digital reflectance filter. This filter is designed to approximate an experimentally determined or calculated plane wave bell reflectance. With respect to filter design, it was found that conventional phase sensitive IIR filter design techniques typically perform poorly when applied to a brass bell reflectance. More accurate results were obtained using a modelling scheme in which the decaying tail is modelled with an IIR filter, and the exponentially rising start of the brass bell reflectance is modelled either with TIIR one-pole filter elements or an FIR filter.

In summary, we recommend the TIIR+IIR model for applications in which efficiency is a high priority. While this approach accurately preserves the essential properties of a brass horn (such as the effective length), it does not model the more subtle features (such as

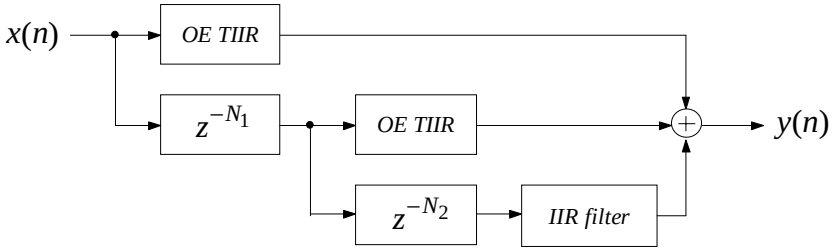


Figure 7.17: TIIR+IIR model for computing the trumpet bell reflectance. The offset-exponential TIIR sections are indicated with OE TIIR. The $z^{-N_1}$ unit indicates the delay-line that is required to delay the input to the second OE TIIR section, and the $z^{-N_2}$ unit indicates the delay-line that is required to delay the input to the IIR filter.

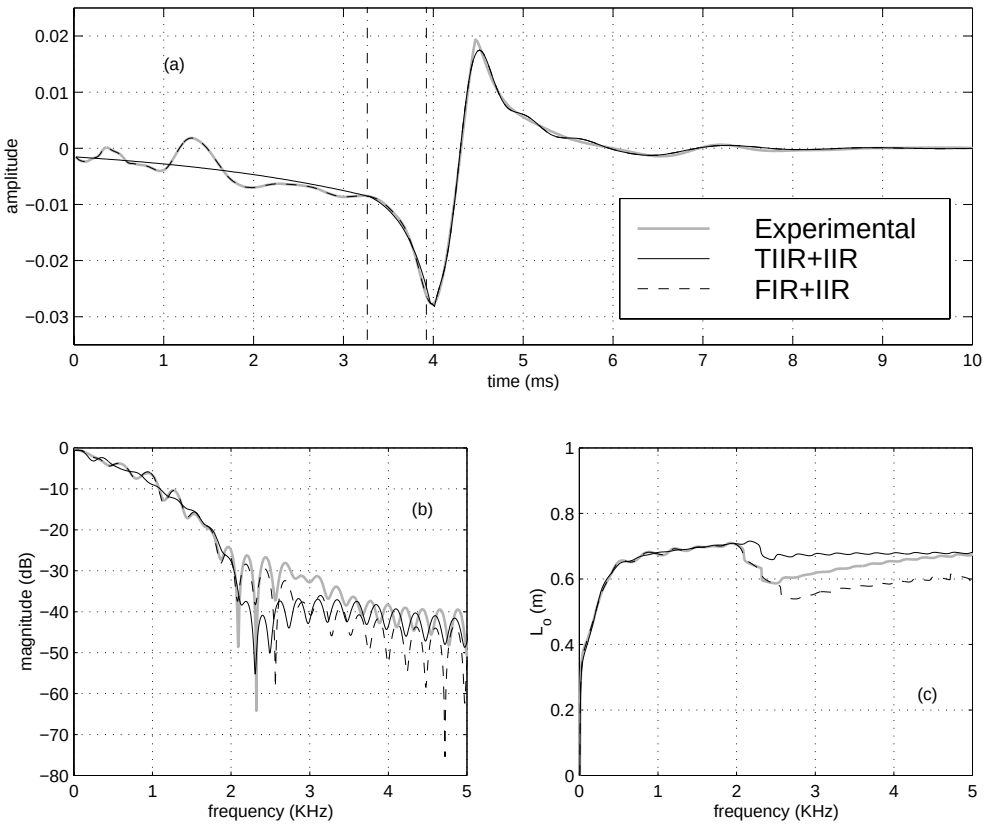


Figure 7.18: TIIR+IIR filter model and FIR+IIR filter model compared to the experimentally determined bell reflectance, in terms of (a) impulse response, (b) magnitude response, and (c) open-end effective length. The vertical (dash-dot) lines in (a) indicate the response segmentation into 2 growing exponentials and a tail. In both filter models, the tail is approximated with a 6th-order IIR filter. The sample rate is 44.1kHz.

small reflections due to dents and bends). Simulations in which accuracy is a high priority can be achieved using of the computationally more expensive FIR+FIR filter model.

# Chapter 8

# Mouthpiece Modelling

The airway of the mouthpiece of a brass or woodwind instrument forms the acoustical channel through which the reed or the lips communicate with the air column. The mouthpiece design therefore usually has a strong influence on the oscillations that are generated in the instrument. For a detailed discussion on the acoustical function of wind instrument mouthpieces, we refer to [22]. In this chapter we develop techniques for modelling the mouthpiece in discrete-time. A general modelling scheme for brass instrument mouthpieces is developed in section 8.1. For woodwinds, the variety of mouthpiece designs is such that for each instrument a separate modelling approach is required. We therefore limit ourselves to modelling the clarinet mouthpiece (section 8.2).

## 8.1 Brass Mouthpieces

Brass mouthpieces come in a great variety of shapes. For example, a trumpet mouthpiece is typically cup-shaped (see figure 8.1a), whereas a more funnel-shaped mouthpiece is characteristic for horns (figure 8.1b). A common characteristic for all brass mouthpieces is that they have a tubular constriction (the backbore) through which the cup volume and

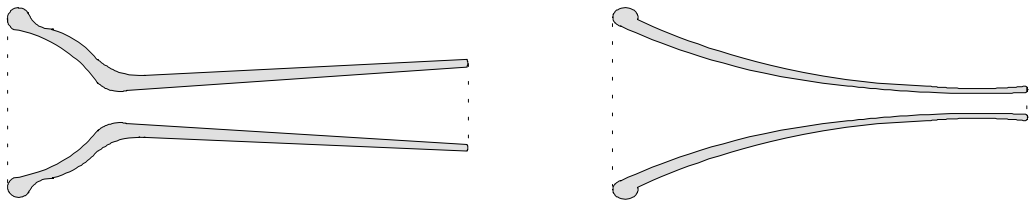

*(a) Trumpet* *(b) Horn*

Figure 8.1: Cross-section of typical brass instrument mouthpieces. (After Campbell and Greated [33]).

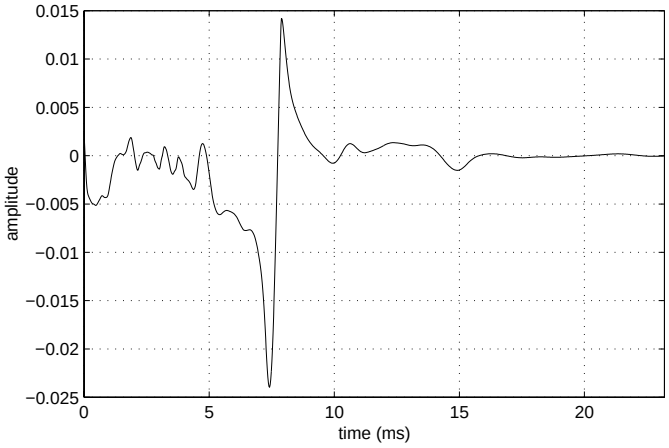


Figure 8.2: Reflection function of a trumpet (without mouthpiece), obtained using pulse reflectometry measurement techniques.

main bore of the instrument communicate. It is generally assumed that the exact shape of the cup is relatively unimportant to the acoustical function of the mouthpiece [22, 18, 91, 33, 52]. Inserted into a brass instrument, the mouthpiece performs its resonating function such that the amplitudes of the musically important resonance frequencies are enhanced. In other words, it acts as an *impedance multiplier* [33]. The mouthpiece also slightly shifts the frequencies of the air column resonances. This effect is usually expressed in the mouthpiece *effective length*[1]. In this section we work towards a discrete-time model of the brass mouthpiece. The modelling approach is verified using measurements on a particular (trumpet) mouthpiece[2].

### 8.1.1 Measurements

Two types of experiments[3] were carried out in order to measure the acoustical behaviour of the trumpet mouthpiece. First, the plane wave reflection function of the trumpet (without mouthpiece) was obtained using pulse reflectometry techniques (see figure 8.2). The input impedance $Z_{tr}(\omega)$ of the trumpet (without mouthpiece) can be derived from the measured reflection function:

$$Z_{tr}(\omega) = Z_0 \left( \frac{1 + R_f(\omega)}{1 - R_f(\omega)} \right), \tag{8.1}$$

where $Z_0$ is the characteristic impedance at the trumpet bore entry, and $R_f(\omega)$ is the Fourier transform of the reflection function. Figure 8.3a depicts the resulting input impedance curve. Next, the input impedance of the same trumpet *with* mouthpiece was obtained via direct input impedance measurement. The magnitude of the measured input

[1] See appendix C for an explanation of the concept of effective length.
[2] A Wick 3E trumpet mouthpiece.
[3] See appendix J for a short description of the acoustic measurement techniques used in this study.

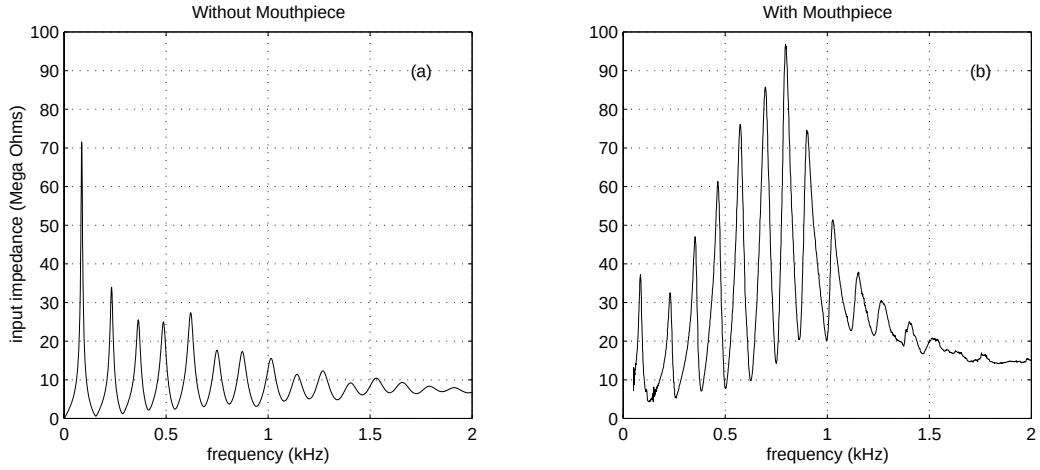


Figure 8.3: Input impedance (magnitude) of a trumpet without mouthpiece (left) and with mouthpiece inserted (right).

impedance is depicted in figure 8.3b. A comparison between the two impedance curves in figure 8.3 confirms the theory that (1) the mouthpiece acts as an impedance-multiplier, and (2) the mouthpiece adds a certain (effective) length to the instrument, i.e. one can see a downward shift of the resonance frequencies. The first task is to find a simple mouthpiece model with which both these observed features are well approximated.

### 8.1.2 The Cylinder-Cone Model

In several studies it has been suggested that the brass mouthcup can be modelled as a simple cylindrical section of equivalent volume[4] [22, 91, 99]. This approach is based on the low-frequency behaviour of the mouthcup, since in the low-frequency limit, a cavity is characterised by its volume whereas the high-frequency behaviour also depends on its shape. Hence a simple model of the brass mouthpiece consists of a cylindrical section (representing the mouthcup) plus a conical section (representing the backbore).

Figure 8.4 shows the model dimensions that result when applying this approach to the trumpet mouthpiece. In theory, the exact dimensions of the cylindrical section should not make much difference as long as it has the correct volume. However in practice we found that the highest modelling accuracy is obtained using a cylinder with a cross-section that is of the same order as the average cross-section of the real mouthcup.

Using the piecewise modelling techniques described in section 2.3, we can compute the input impedance of the trumpet fitted with this theoretical mouthpiece. This was carried out using transmission-line matrices (as described in section 2.3), and using the measured trumpet reflectance $R_f(\omega)$ as the end-reflectance of the mouthpiece system. We

[4] The volume of the real mouthcup was measured to be $1.1 \pm 0.05$ml.

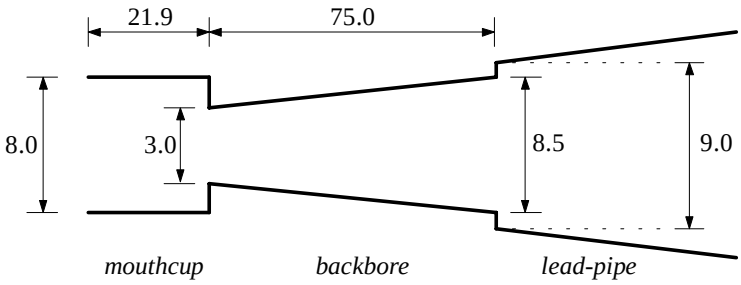


Figure 8.4: Cylinder-cone model of the trumpet mouthpiece. The volume of the cylindrical section equals the volume of the mouthcup. The dimensions are given in mm.

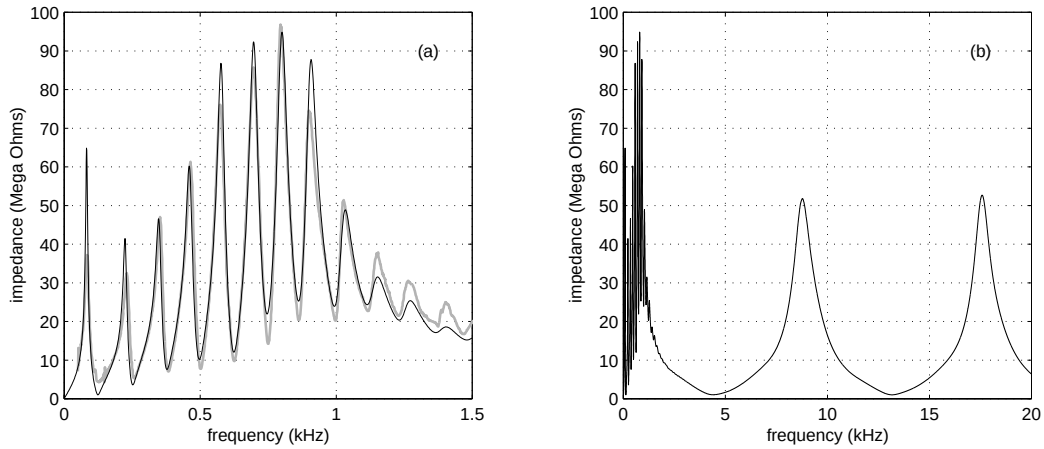


Figure 8.5: Input impedance (magnitude) of the trumpet with mouthpiece, as calculated using the cylinder-cone model for a bandwidth of 1.5kHz (left) and 20kHz (right). The measured input impedance (grey line) is plotted for comparison in the left figure.

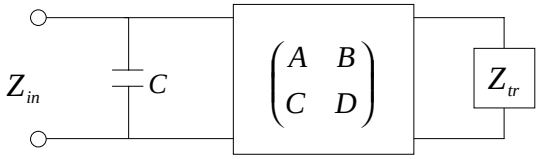


Figure 8.6: Equivalent network representation of the hybrid model. The mouthcup is modelled as a compliance, and the backbore is modelled as a conical section. The four-terminal unit indicated with the *ABCD*-matrix represents the conical section.

note that it is important to take into account the small difference in cross-section between the backbore and the lead-pipe. The resulting input impedance curve is compared with the measured input impedance in figure 8.5a. The calculated impedance curve exhibits an approximately correct multiplier-effect as well as a well-matched set of resonance frequencies. However, plotting the impedance for a wider bandwidth (see figure 8.5b) reveals that extra impedance-multiplier regions exist. These extra regions are due to the large discontinuity at the boundary between the cylinder and the cone. No such step occurs in the bore profile of the real mouthpiece, therefore it may be assumed that the extra impedance-multiplier regions are not a feature of real brass instruments. The extra resonances form an unwanted model feature, since they will cause a significant change to the sound of a full instrument simulation.

Although the cylinder-cone model is partly based on a low-frequency approximation, it is essentially a *distributed* model. The extra unwanted feature of higher frequency enhancements could be avoided by using a more refined distributed model, in which the mouthcup bore profile is approximated with a piecewise series of very short tube sections. However, in order to realise such a piecewise model in discrete-time, a very high spatial resolution (and thus a very high sample rate) is required. Given that the computational costs are further increased due to the large number of cylindrical scattering junctions that are required to implement such a piecewise model, it may be concluded that this is not a particularly efficient approach.

### 8.1.3 The Hybrid Model

As discussed in section 3.4, a small volume is more efficiently simulated using a *lumped element model*, which can be discretised using wave digital filter (WDF) techniques. Hence we suggest a "hybrid" mouthpiece model, in which the cup volume is modelled as a lumped element (a pure compliance), and the backbore is modelled as a distributed element (a conical section). Figure 8.6 shows the equivalent network of this arrangement. The acoustical behaviour of the conical backbore can be described with a transmission-line matrix (see equation (2.93)). Given that $A$, $B$, $C$ and $D$ are the elements of this matrix,

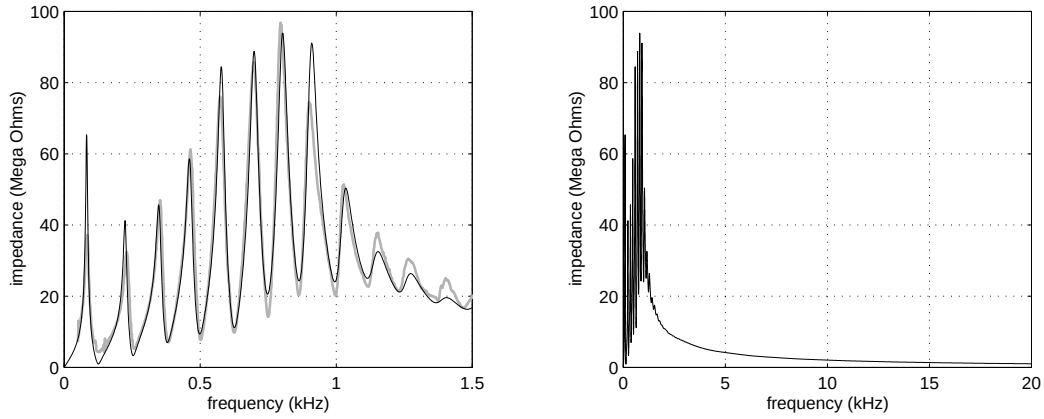


Figure 8.7: Input impedance (magnitude) of the trumpet with mouthpiece, as calculated with the hybrid model for a bandwidth of 1.5kHz (left) and 20kHz (right). The measured input impedance (grey line) is plotted for comparison in the left figure.

the input impedance $Z_{bb}(\omega)$ as seen from the backbore entry is:

$$Z_{bb}(\omega) = \frac{AZ_{tr}(\omega) + B}{CZ_{tr}(\omega) + D}. \tag{8.2}$$

The input impedance $Z_{in}(\omega)$ at the mouthpiece entry is simply a parallel combination of $Z_{bb}(\omega)$ and the impedance $Z_{cup}(\omega) = 1/(j\omega C)$ of the mouthcup:

$$Z_{in}(\omega) = \frac{Z_{cup}(\omega) \cdot Z_{bb}(\omega)}{Z_{cup}(\omega) + Z_{bb}(\omega)}. \tag{8.3}$$

Figure 8.7a compares $Z_{in}(\omega)$ to the measured input impedance. As could be expected, the hybrid model results in an impedance curve that is very similar to the curve obtained with the cylinder-cone model. However, the hybrid model does not have the disadvantage of the extra impedance-multiplier regions at the higher frequencies (see figure 8.7b). We note that the hybrid model corresponds exactly to the mouthpiece model presented by Lurton in [91].

### 8.1.4 Discretisation

The hybrid model can be simulated in discrete-time by employing the wave digital modelling techniques outlined in section 3.4. The final "wave digital brass mouthpiece model" takes the form depicted in figure 8.8. As discussed in section 3.3, an acoustic volume can be modelled using WDF techniques. In a full instrument model (one that includes lip excitation), the left port of the system communicates directly with the unit that computes the non-linear flow through the lips[5]. Because the lips will have an instantaneous reflection, the

[5] This unit will be referred to as "the lips".

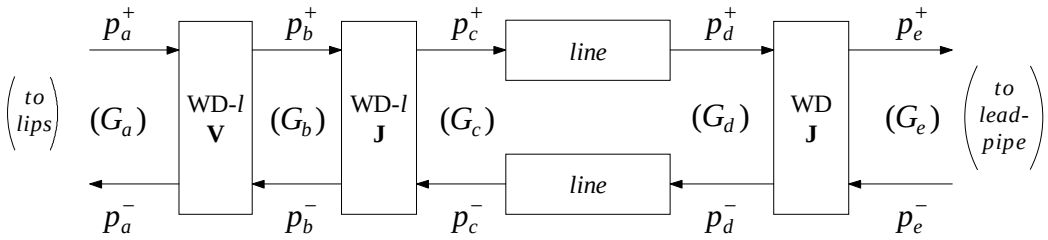


Figure 8.8: Discrete-time modelling structure of the hybrid mouthpiece model. Each *line* unit indicates a cascade of delay-line, a fractional delay filter and a loss-filter. The WD-$l$ **V** unit models the cup volume as a pure compliance, and the WD-$l$ **J** and WD **J** units model the junctions of the conical backbore with the cup volume and the lead-pipe, respectively. $G_a, G_b, G_c, G_d, G_e$ are the local port-admittances.

"cup volume unit" will have to have a non-immediate reflectance towards the left, which can be realised by choosing the appropriate value for $G_a$. This results in a WD-$l$ volume structure (see figure 8.10), for which the derivation is given in section 8.1.5. Discrete-time modelling of conical bores was discussed in chapters 4 and section 6. Wave propagation in a conical section can be simulated using a delay-line, while the wave scattering at both the entry- and the end-junction can be simulated using the wave digital junction models described in section 6.1. Viscothermal losses are approximated with 5th-order IIR filters, and fractional delays with 3rd-order Lagrange interpolators. The WD-$l$ volume unit has an immediate reflectance towards the right, thus in order to avoid a delay-free loop, the left junction of the conical section needs to be modelled as a WD-$l$ junction. The other junction (between the backbore and the lead-pipe) can be modelled with a normal WD junction, as described in section 6.1.1.

For determination of the values of the port-admittances $G_a$, $G_b$, $G_c$, $G_d$ and $G_e$, one has to work from right to left. The value of the port-admittances $G_e$, $G_d$ and $G_c$ are fixed because the lead-pipe and the conical backbore are distributed systems. The values of $G_b$ and $G_a$ are arbitrary from a physical point of view but must be set to a specific value in order to ensure the realisability of the system. $G_b$ only depends on $G_c$ and the junction inertance, and the value of $G_a$ depends on $G_b$ and the volume compliance.

### 8.1.5 The WD-$l$ Volume

As seen in section 3.3.2, the acoustic behaviour of a small volume can be modelled as a parallel compliance network that may be considered as a three-port with a compliance load at one of its ports. The basic WDF structure for simulation of such a network is as depicted in figure 8.9.

The three-port equations are as given in equations (3.51). As with the example ex-

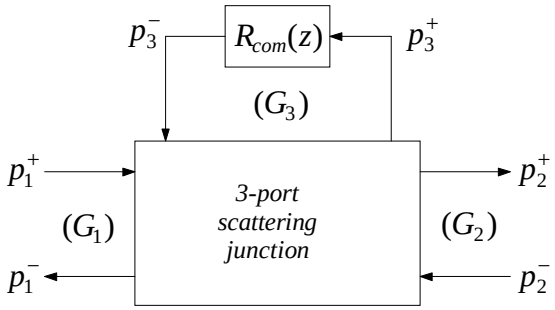


Figure 8.9: Basic structure for WDF modelling of the parallel compliance.

plained in section 3.3.2, we have to set the port-admittance of the compliance-loop such that a delay-free path is avoided. This amounts to setting $G_3 = \beta C$, and the compliance reflectance $R_{com}(z)$ is then modelled as a single delay:

$$P_3^- = P_3^+ \, z^{-1}. \tag{8.4}$$

However, the current case differs from the WD volume derived in section 3.3.2, because a non-immediate reflectance towards the left is required. This is realised by setting:

$$G_1 = G_2 + G_3. \tag{8.5}$$

After substitution of (8.5) into the three-port equations, the final set of equations for the WD-$l$ volume can be written:

$$\begin{aligned} P_3^- &= P_3^+ \, z^{-1}, \\ W_1 &= P_2^- - P_3^-, \\ W_2 &= k_j \, W_1, \\ P_1^- &= P_2^- + W_2, \\ P_2^+ &= P_1^+ + W_2, \\ P_3^+ &= P_1^+ + W_1 + W_2. \end{aligned} \tag{8.6}$$

where

$$k_j = -\frac{G_3}{G_2 + G_3}. \tag{8.7}$$

The signal flow of the WD-$l$ volume is depicted in figure 8.10.

### 8.1.6 Discretisation Effects

In order to examine the effects of discretisation, we need to compare the discrete-time model with its continuous-time counterpart in terms of a certain response. We choose here

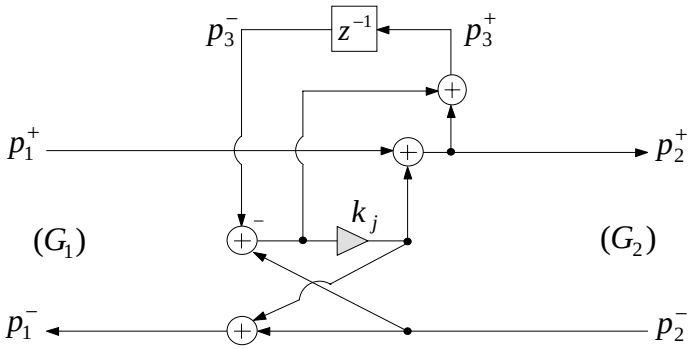


Figure 8.10: Signal flow of the WD-$l$ volume.

to compute the mouthpiece effective length, since it has proved to be a useful measure in brass instrument research (see, for example, [110, 22, 33, 15]). The effective length of the mouthpiece can be derived from the reflectance $R_{mp}(\omega)$ as seen from the instrument[6]. In this case we compute the "closed-end" effective length, which means that it is assumed that the mouthcup is rigidly terminated at the end (see figure 8.11).

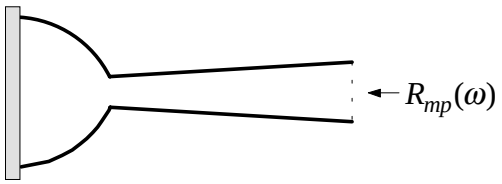


Figure 8.11: The "closed-end" effective length of the mouthpiece can be derived from the "closed-end" reflectance as seen from the instrument.

Figure 8.12 compares the effective lengths as computed with a transmission-line model and with two versions of the wave digital model. In version (I), we included loss-filters, while in version (II) these were omitted. The second version thus amounts to neglecting the viscothermal losses. We can see from figure 8.12 that the effective length of the first version exhibits large deviations at the lower frequencies ($f < 400$Hz) with the transmission-line model. This is a typical example of the problem of using an inconsistent formulation of the propagation constant[7]. On the other hand, version (II) exhibits a small deviation at all frequencies, but does not exhibit any frequency attenuation. Which version is most suitable depends on the lowest pitch playable on the instrument. For many brass instruments, the first resonance of the air column is "out of tune" with the higher resonances and is rarely used in musical practice. Therefore the deviation at the lower frequencies may in some cases be of small relevance to the tuning of the instrument.

[6] This is explained in appendix C.

[7] This problem is discussed in section 4.3.3.

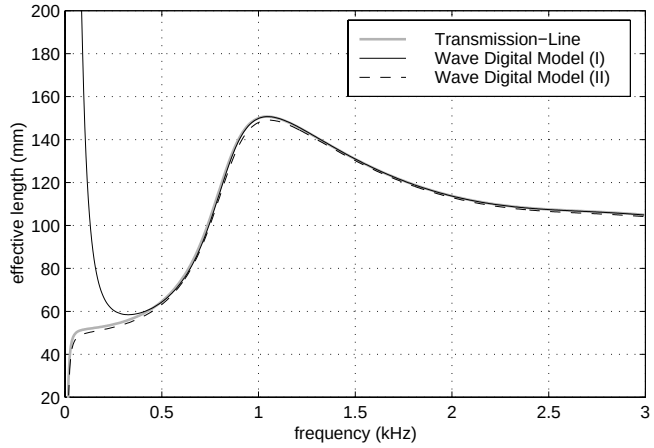


Figure 8.12: Effective length of the hybrid mouthpiece model.

## 8.2 Clarinet Mouthpieces

In this section we set out to develop a discrete-time model of the clarinet mouthpiece. The modelling approach is tested with experiments on a particular mouthpiece[8]. We take the view that the geometrical differences between various clarinet mouthpiece designs are generally small enough to assume that the resulting model is sufficiently flexible for simulation of a wide variety of clarinet mouthpiece designs.

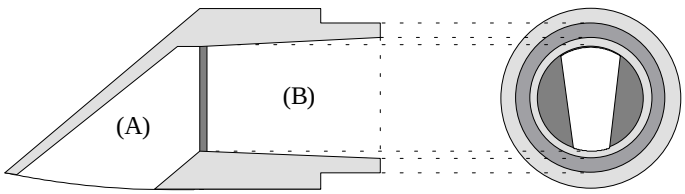


Figure 8.13: Cross-section of the mouthpiece used in the measurements (not to scale).

A schematic cross-sectional view of the mouthpiece is depicted in figure 8.13. The shape of the interior of this mouthpiece can be divided into two parts, (A) and (B). Part (B) is slightly tapered, and approximately functions as an extension of the main bore. Part (A) has a more complicated shape, in which the cross-section at most places has an approximately rectangular shape. At the boundary between (A) and (B), there is a transition from an approximately rectangular to a circular cross-section. In this particular design, this cross-sectional "step" is very abrupt. Other mouthpiece designs might differ from this mouthpiece in two ways. Firstly, part (B) is sometimes purely cylindrical.

[8] A Bundy clarinet mouthpiece.

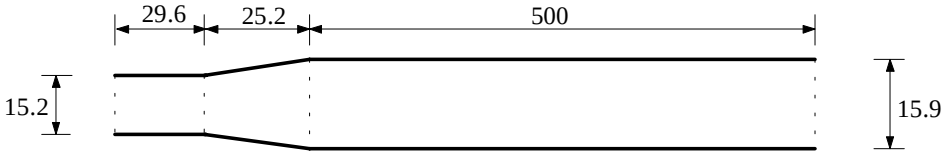


Figure 8.14: The tubular assembly that was used in the measurements. The assembly was designed such that the clarinet mouthpiece could be fitted at the entry. The dimensions of the assembly are comparable to those of a real clarinet. Dimensions are given in mm.

Secondly, the transition from (A) to (B) is much more smooth in certain designs[9]. Given these possible variations in mouthpiece designs, the following theories apply to clarinet mouthpieces in general:

- The position of the resonance frequencies of the clarinet are mainly controlled by the total *volume* of the mouthpiece interior.
- The heights of the impedance peaks of the clarinet are mainly controlled by the particular *shape* of the mouthpiece interior.

For a broader discussion on the acoustical function of woodwind mouthpieces, we refer to [101, 22, 33].

### 8.2.1 Measurements

Input impedance measurements were carried out in order to investigate the acoustical behaviour of the clarinet mouthpiece. The main strategy is the same as that applied to brass instruments. That is, an instrument was measured, with and without mouthpiece inserted, and the resulting responses were then compared. However, the approach differs in two respects. Firstly, this time both experiments were direct input impedance measurements. Secondly, the mouthpiece was not fitted to a real instrument but instead to an assembly of tubular sections (see figure 8.14). The main reason for using this assembly is that leakages occurred during experiments with the real clarinet, which greatly complicated the task of obtaining consistent and reliable results. Another advantage of using the tubular assembly is that the complex input impedance can be obtained via calculation, whereas the current experimental setup only allows for determination of the impedance magnitude.

Figure 8.15 shows the measured input impedance of the tubular assembly. For comparison, the calculated input impedance is also plotted. The good match between theory

[9] A sharp step in the mouthpiece cross-section leads to separation of the air stream from the wall [33], which has consequences to the functioning and the sound of the instrument. However, this topic is not addressed in the present study.

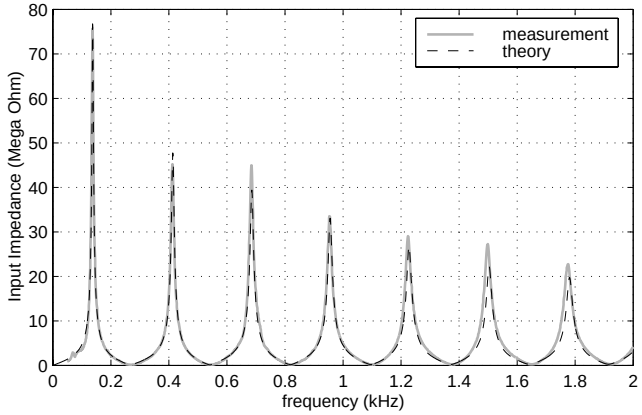


Figure 8.15: Input impedance of the tubular assembly.

and experiment justifies the use of the calculated impedance in computations with a tubular assembly fitted with a (theoretical) mouthpiece. That is, given that the acoustical function of the mouthpiece is expressed with a transmission-line matrix, we may compute the input impedance of the assembly fitted with the mouthpiece as:

$$Z_{in}(\omega) = \frac{A\,Z_{as}(\omega) + B}{C\,Z_{as}(\omega) + D}, \tag{8.8}$$

where $Z_{as}(\omega)$ is the calculated complex input impedance of the assembly and $A$, $B$, $C$, and $D$ are the elements of the transmission-line matrix.

### 8.2.2 The Cylinder-Cone Model

A simple model of the clarinet mouthpiece is constructed by joining a conical section (of the dimensions of part (B)), with a cylindrical section of the same volume as the volume of part (A) (see figure 8.16). The cylindrical section was chosen such that the step is the same as at the boundary between (A) and (B) in the real mouthpiece. This way it is ensured that the main difference between this simple model and the real mouthpiece is due only to the difference in shape of part (A).

Ideally, one would like to create a more refined distributed model of the mouthpiece, in the form of an axially-symmetric model approximation of the mouthpiece profile. However, it is rather difficult to predict exactly how waves propagate through part (A) under playing conditions (with the reed closing off most of the mouthpiece). Hence there are no clear guidelines as to how to construct an axially-symmetric bore shape that properly represents the intricate acoustic behaviour of (A). However, since the dimensions of (A) are rather small in comparison with the smallest wavelength for frequencies below the clarinet tonehole lattice cut-off frequency, the simple model should at least suffice with respect to obtaining the correct resonance frequencies of a clarinet with mouthpiece. The

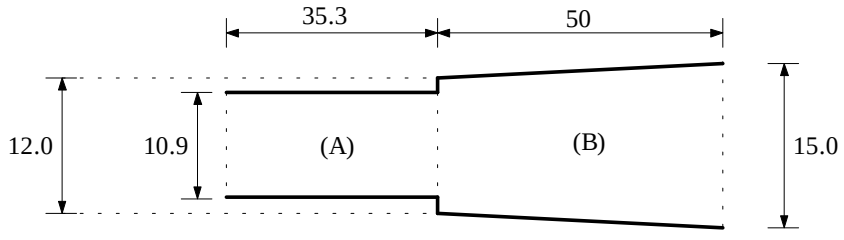


Figure 8.16: Cylinder-cone model of the clarinet mouthpiece. Dimensions are given in mm.

elements of the transmission-line matrix of this model can be obtained with the piecewise modelling techniques explained in section 2.3.

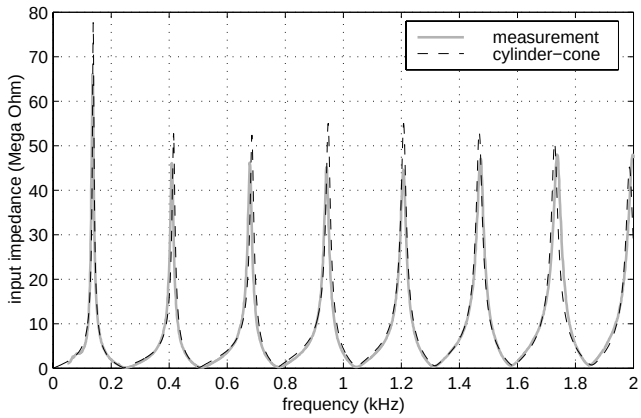


Figure 8.17: Input impedance of the assembly fitted with mouthpiece. The dashed curve was computed using the cylinder-cone mouthpiece model.

Figure 8.17 compares the input impedance computed using equation (8.8) with the measured input impedance of the tubular assembly with the real mouthpiece fitted. Clearly, the mouthpiece significantly enhances some of the input impedance peaks. The effect is such that most resonances now have approximately equal amplitude, apart from the fundamental. This effect is closely emulated by the cylinder-cone model.

### 8.2.3 Discretisation

The cylinder-cone mouthpiece model can be implemented using the techniques described in chapters 4 and 6. Using the wave digital junction for implementation of wave scattering at the junctions, the wave digital model in figure 8.18 results. As with the wave digital brass mouthpiece model, the fractionality of the propagation-delays was achieved using third-order Lagrange FIR interpolation filters, and the viscothermal losses were approximated with 5th-order IIR filters.

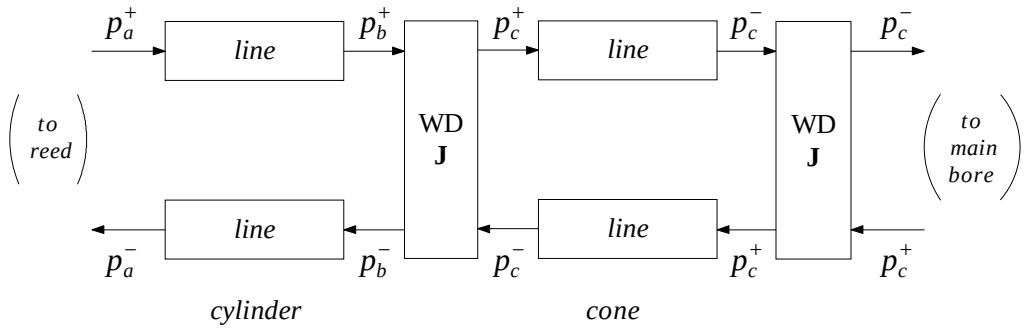


Figure 8.18: Wave digital clarinet mouthpiece model. The $WD$ **J** units indicate wave digital junctions, and each *line* units represents a cascade of a delay-line, a fractional delay filter and a loss-filter.

We can investigate the effects of discretisation by computing the mouthpiece reflectance as seen from the main bore (and assuming a closed end), and deriving the (closed-end) effective length from this reflectance using (C.5). Figure 8.19 compares the effective length curves as computed with transmission-line matrices and with two versions of the wave digital model. As with the brass mouthpiece model, version (I) exhibits strong deviations with the transmission-line model for $f < 0.25$kHz. The lowest pitch on a clarinet is usually well below 0.25kHz, thus the range of notes in the lowest octave (register) of the instrument will be out of tune with version (I). With version (II), in which the viscothermal losses are neglected, the effective length is slightly too small at all frequencies, thus all notes will be a little out of tune. Furthermore, version (2) does not implement any losses.

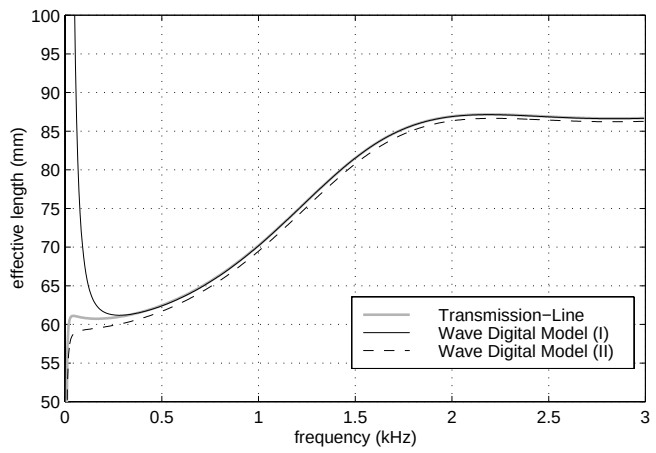


Figure 8.19: Closed-end effective length of the cylinder-cone mouthpiece model.

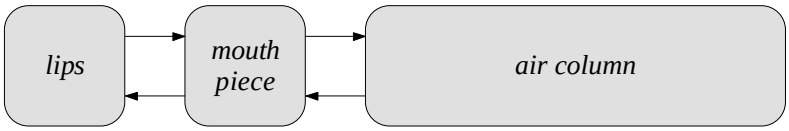


Figure 8.20: Travelling-wave based simulation of a wind instrument, using a two-port unit for modelling the mouthpiece.

## 8.3 Conclusions and Future Work

In this chapter, we have seen that brass and clarinet mouthpieces can be simulated efficiently in the digital domain using wave digital modelling techniques. The resulting two-port mouthpiece units can be employed in a modular way in a travelling-wave based simulation (see figure 8.20).

For simulation of the clarinet mouthpiece, this two-port unit takes the form of a cylinder-cone model. With minor adaptations, this basic approach can also be applied to discrete-time modelling of various other woodwind mouthpieces.

In section 8.1, it was found that a hybrid mouthpiece model (containing both lumped and distributed elements) accurately simulates the acoustical function of the brass mouthpiece. This model was discretised using wave digital modelling techniques. In comparison with the lumped element mouthpiece models presented by Dietz [45], the acoustical function of the backbore is modelled more accurately. This is because in Dietz' models, the backbore is modelled as a pure inertance, or alternatively as an inertance and a compliance, and neither of these models properly incorporates the conicity of the backbore.

An interesting direction for future work on this subject is to investigate the effect of the mouthpiece design on the radiated sound. A recent psycho-acoustic study by Wright and Campbell [168] has indicated that the perceived timbre of cup-mouthpiece wind instruments may be altered significantly when different mouthpieces are used. Furthermore, a study by Gilbert [56] on the influence of the mouthpiece on the sound of the saxophone has indicated that several "formants" can be identified in the radiated spectrum, and that the strength and position of these formants depend strongly on the shape of the mouthpiece interior. Since our modelling approach is strongly based on low-frequency approximations, it would be complicated, and indeed unnecessary to take into account directly all the higher frequency characteristics of the radiated sound when modelling the internal oscillations of the instrument (see sections (9.1.3) and (9.2.3) for a further discussion on modelling the radiated sound). However, the low-frequency approach should produce a reasonably good approximation for the frequency range in which the first few spectral formants (and indeed all the significant resonance peaks) of a wind instrument

fall.

# Chapter 9

# Full Bore Simulations

Most musical wind instruments have evolved quite slowly towards their present form, with minor tonal or technical improvements reflecting the gradually changing mental image of the ideal instrument of that type [52]. The specific sound produced with these instruments is thus to a significant extent captured within the intricate physicalities of the instrument. It is therefore interesting to try and simulate these instruments in a precise way, not only in order to reproduce the sounds, but also as an exercise to gain insight into what features give the instrument its specific sonoric qualities.

In this relatively short chapter, we bring together the techniques described in previous chapters in order to simulate the air columns of two particular wind instruments, namely that of a *Boosey and Hawkes* trumpet[1] and a *Selmer* clarinet[2]. The principal reason for using these two specific instruments is that they were available for measurements during the period of study.

## 9.1 The Boosey and Hawkes Trumpet

The trumpet is a brass instrument with a bore that is largely cylindrical and flares out towards the end. The flaring bell is actively involved as a resonator for every note played on the instrument, and adds an effective length to the instrument such that the bore has an approximately even series of harmonics. The length of the bore can be adjusted by means of three valves, which insert extra lengths of tubing into the cylindrical part of the bore. The instrument is played by buzzing the lips while holding them pressed against the mouthpiece such that a coupling between the lip and the air column vibrations develops.

[1] A Boosey and Hawkes "78".
[2] A Selmer clarinet no. 1400.

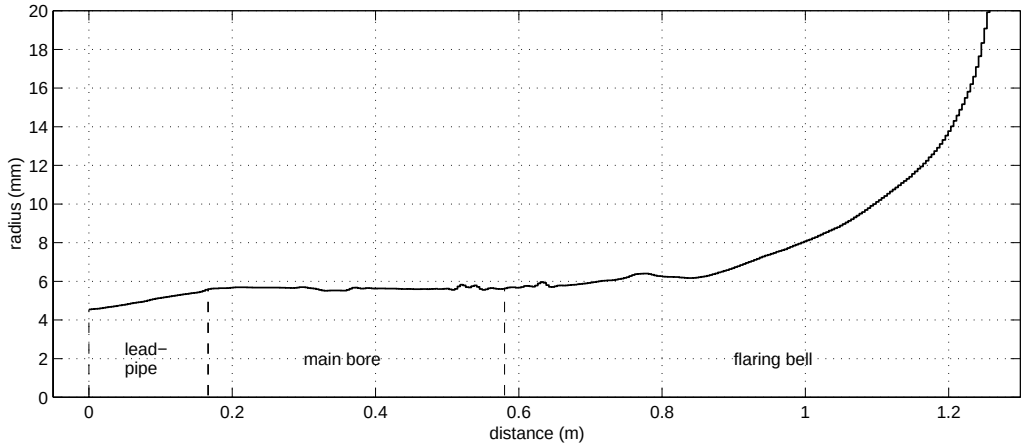


Figure 9.1: Trumpet bore profile reconstruction. The dashed lines indicate the division of the trumpet bore into a tapered section (the lead-pipe), a cylindrical section (the main bore), and a flared section (the bell).

### 9.1.1 Transmission-Line Model

Results of measurements on the Boosey and Hawkes trumpet were presented in sections 7.4.1 and 8.1.1. Figure 8.2 shows the reflection function of the trumpet (without mouthpiece), and figure 7.16 shows the bore reconstruction as calculated from this reflectance using the inverse scattering techniques described in [126]. For convenience, this piecewise cylindrical reconstruction is plotted again in figure 9.1. As we can see from the bore profile, the main bore of the trumpet is essentially cylindrical, with an initial taper widening. This initial tapered section, which is usually referred to as the *lead-pipe*, is approximately conical. With the mouthpiece inserted, this part communicates with the backbore of the mouthpiece. Thus, an accurate model of the trumpet can be derived by approximating the bore profile data with a cylindrical bore, plus a conical section to model the lead-pipe, and modelling the remaining part of the reconstruction as the bell reflectance $R_L(\omega)$. As seen in section 8.1.3, the trumpet mouthpiece may be modelled with a hybrid model. With a model available for all parts of the trumpet, the reflection function and input impedance of the transmission-line model of the complete trumpet with mouthpiece can be computed with the piecewise modelling techniques explained in section 2.3, using either transmission-line or waveguide matrices. This transmission-line model forms the continuous-time model from which we derive the discrete-time model.

### 9.1.2 Wave Digital Model

The conical and cylindrical sections of the trumpet bore can be modelled in discrete-time with the techniques described in chapters 4 and 6. Here we employed the "wave digital junction" (described in section 6.1.1) rather than the "digital waveguide junction"

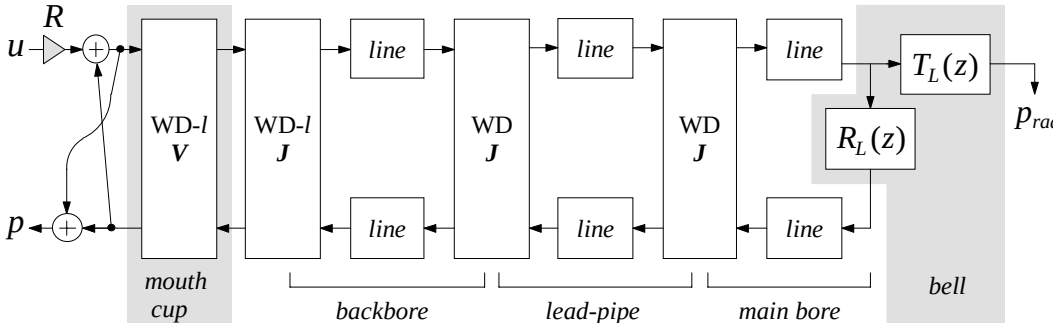


Figure 9.2: Wave digital model of the trumpet. The WD-$l$ **V** unit indicates the wave digital volume structure that models the mouthpiece cup. The WD-$l$ **J** unit indicates a wave digital junction that models the scattering of waves at the boundary between the mouthcup and the backbore. The WD **J** units indicate normal wave digital junctions, which model the taper discontinuities at either end of the lead-pipe. The *line* units implement wave propagation. $R$ is the port-resistance at the input-end.

(described in section 4.3.2) for simulation of wave scattering at the junctions at both ends of the lead-pipe. The bell reflectance is modelled with a digital filter scheme such as that explained in section 7.4, and the hybrid mouthpiece model is discretised with wave digital modelling techniques as described in section 8.1.4. The complete wave digital model of the trumpet then takes the form depicted in figure 9.2. A 44.1kHz sample rate was used. Fourth-order IIR filters were used for approximation of viscothermal losses in the main bore, and fractional delays were simulated by means of third-order Lagrange interpolators. The bell is modelled with a reflectance filter $R_L(z)$ and a transmittance filter $T_L(z)$, where the latter approximates the transmittance as obtained from the reflectance via equation (7.3), and using a minimum-phase reconstruction to deduce a suitable transmittance phase (see section 7.1.2).

Figure 9.3 shows the amplitude response of the bell reflectance and transmittance. For comparison, we also plotted the magnitude response of a third-order IIR filter approximation of the transmittance. The FIR+IIR filter scheme explained in section 7.4 was employed for digital approximation of the bell reflectance. As discussed in section 4.4 and 6.1, a wave digital model is not stable if viscothermal losses are included in the conical sections (i.e., the lead-pipe and the backbore). Therefore we do not include loss-filters in these sections. The backbore is very narrow at the input-end (2mm), and both the lead-pipe and the backbore are narrow in comparison with the main bore, so viscothermal losses per unit length are relativaly high in these sections. On the other hand, both the lead-pipe and the backbore are signifiantly shorter than the main bore, so it may be expected that the neglected losses are still small in comparison with the overall losses.

Figure 9.4a shows the input impedance of the trumpet, as computed with the

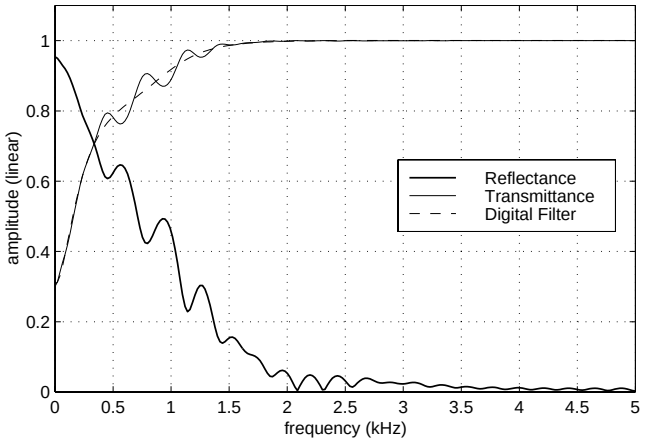


Figure 9.3: Reflectance and transmittance of the trumpet bell.

transmission-line model and the wave digital model. The wave digital model result was obtained by simply injecting a volume flow pulse into the mouthcup and tracing the mouthcup pressure. An FFT of the resulting discrete-time signal then gives the input impedance. The discrepancy between these results is almost entirely due to not taking into account the viscothermal losses in the conical sections of the system; if we calculate the transmission-line model with the same simplification (i.e., with no losses in the lead-pipe and the backbore), then the resulting input impedance curve (see figure 9.4b) closely matches that of the wave digital model.

### 9.1.3 Sound Radiation

The sound pressure $p_{rad}$ just outside the bell may be used as a first approximation of the sound radiated from the instrument, where we may expect that low-frequency components are more accurately modelled than high-frequency components. This is due to various simplifications used in the derivation of the wave digital model. Firstly, low-frequency approximations are employed in the digital approximation of the bell reflectance as well as in the derivation of the mouthpiece model. As a consequence, the internal bore pressure does not have the correct high-frequency content, and it is therefore not straightforward to deduce the high-frequency components of the radiation pressure from the internal bore pressure. Secondly, the effects of directivity would have to be taken into account for accurate determination of the radiated sound at a specific angle and distance from the bell. These effects are very small at low frequencies but are significant at higher frequencies [52]. We emphasise here that explicit inclusion of directivity effects would lead to precise computation of the radiation pressure only at frequencies within the bandwidth for which the instrument response is modelled accurately in the first place. With respect to obtaining a "perceptually representative" sound signal, it can in fact be argued that a

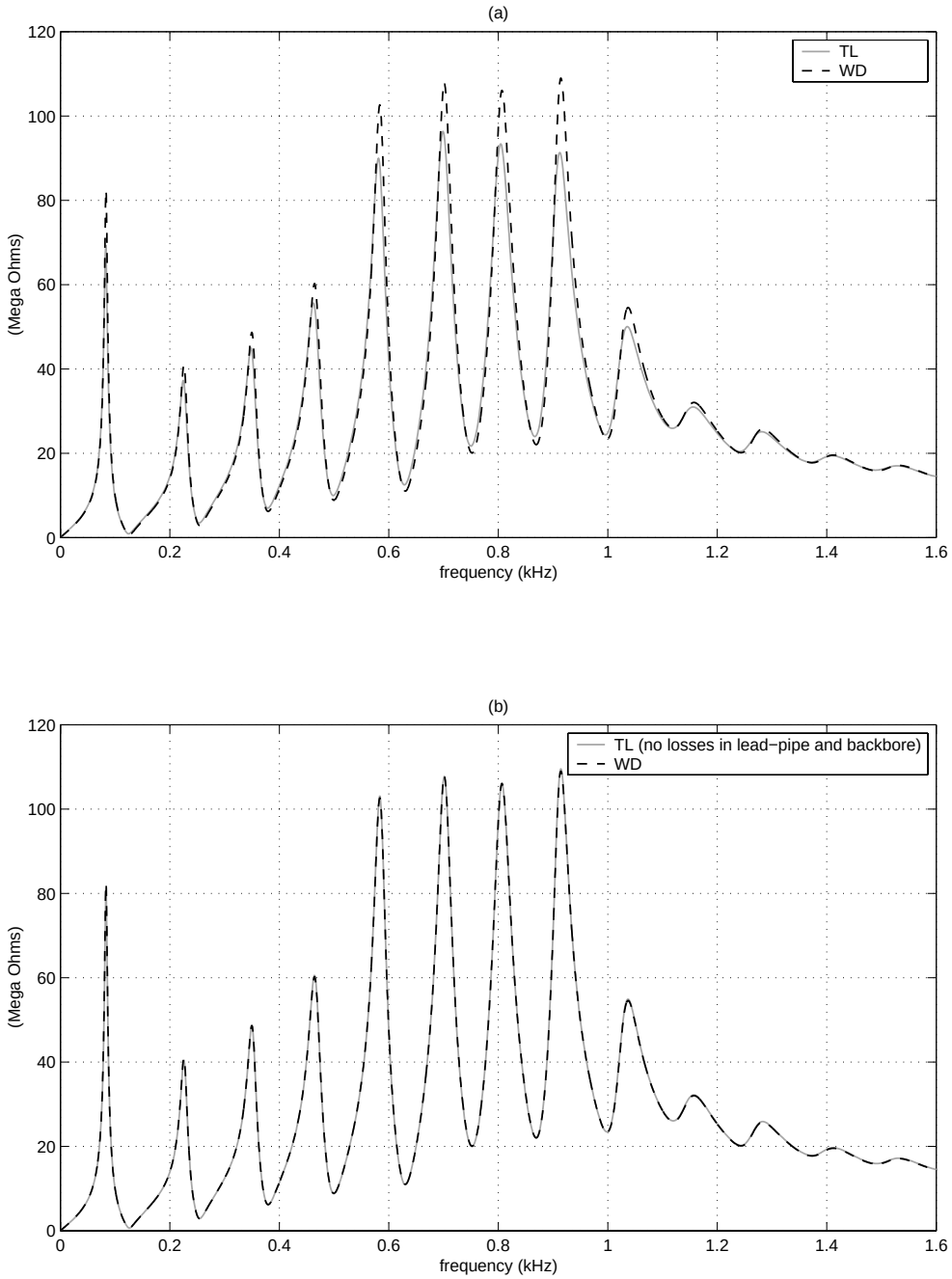


Figure 9.4: Input impedance of the Boosey and Hawkes trumpet. (a) The transmission-line model compared to the wave digital model. (b) The same comparison, but using an adapted transmission-line model in which no losses are taken into account in the lead-pipe and the mouthpiece backbore.

more suitable signal is obtained *without* taking into account the directivity effects. That is, musical sounds are usually produced in a reverberant environment, and in such circumstances the sound quality that is heard at a reasonable distance from the instrument is quite close to the spectral balance of the total radiated power [52]. The sound signal obtained without taking into account the effects of directivity thus has approximately the same spectral characteristics as the sound perceived under "normal" listening conditions. This does not include the phase effects that are associated with sound reverberation, but these can be modelled separately with the use of reverberation simulation techniques. Appendix K contains two sound examples of the wave digital model of the Boosey and Hawkes trumpet[3].

## 9.2 The Selmer Clarinet

The clarinet and its ancestor the Chalumeau are essentially cylindrical instruments and possess an odd-harmonic series, despite the small flaring bell at the foot of the instrument [52]. The modern clarinet usually contains a series of 24 holes which are controlled by means of a key system that is arranged according to the principles developed by Boehm [33].

### 9.2.1 Transmission-Line Model

In order to model the Selmer clarinet, the dimensions of the bore and the toneholes were measured. The geometrical data of the toneholes is given in table 9.2.1. We consider the remaining part of the bore (that is, the part starting directly after hole no. 1) as the bell. The bore in fact starts to flare before this point: this can be modelled by assuming a conical taper between the holes. The bell profile is depicted in figure 9.5. The instrument is fitted with the Bundy mouthpiece that was used in the experiments in section 8.2.

The input impedance of the complete instrument can be calculated with a transmission-line model. That is, the mouthpiece is modelled with the cylinder-cone model discussed in section 8.2.2 and the toneholes are modelled with Keefe's transmission-line formulae as discussed in section 5.1.2. The interhole bore sections are assumed to be either cylindrical or conical and are modelled as lossy transmission-lines as explained in section 2.3. The bell is modelled as a piecewise series of conical sections that is terminated by the open end impedance. We note that the holes are in some cases spaced extremely closely. As discussed in section 5.1, this means that we can not assume that there are no interactions between the holes. However, for the clarinet these interactions are typically very small

[3] The signal of **(ex5)** is the impulse response (Green's function), and signal of **(ex6)** is the corresponding radiation pressure.

| hole no. | $x$ | $2a$ | $2b$ | $t_w$ | $2R$ | $h$ | state ($F_3$) |
|---|---|---|---|---|---|---|---|
| 24 | 68.4 | 15.0 | 2.1 | 12.7 | 10.4 | 3.1 | (c) |
| 23 | 78.7 | 15.0 | 4.0 | 7.3 | 10.4 | 3.3 | (c) |
| 22 | 104.3 | 15.0 | 5.5 | 7.0 | 10.2 | 2.6 | (c) |
| 21 | 114.0 | 15.0 | 5.5 | 7.0 | 10.3 | 3.4 | (c) |
| 20 | 127.9 | 15.0 | 5.7 | 7.0 | 10.4 | 3.4 | (c) |
| 19 | 142.6 | 15.0 | 4.0 | 6.5 | 9.8 | 3.1 | (c) |
| 18 | 153.2 | 15.0 | 7.6 | 10.3 | - | - | (c) |
| 17 | 157.2 | 15.0 | 5.0 | 7.0 | 10.1 | 2.3 | (c) |
| 16 | 165.6 | 15.0 | 5.0 | 8.3 | - | - | (c) |
| 15 | 185.2 | 15.0 | 5.0 | 7.0 | 10.3 | 2.4 | (c) |
| 14 | 198.3 | 15.0 | 6.4 | 8.3 | - | - | (c) |
| 13 | 202.9 | 15.0 | 6.1 | 7.0 | 10.2 | 3.0 | (c) |
| 12 | 203.7 | 15.0 | 6.3 | 7.0 | 10.2 | 3.1 | (c) |
| 11 | 221.8 | 15.0 | 8.2 | 7.5 | - | - | (c) |
| 10 | 232.6 | 15.0 | 5.0 | 7.0 | 10.3 | 3.7 | (c) |
| 9 | 296.6 | 15.0 | 7.2 | 6.0 | 12.0 | 2.4 | (c) |
| 8 | 312.6 | 15.0 | 8.6 | 7.8 | - | - | (c) |
| 7 | 314.6 | 15.0 | 6.3 | 6.5 | 17.1 | 2.5 | (c) |
| 6 | 339.0 | 15.0 | 8.5 | 7.8 | - | - | (c) |
| 5 | 362.0 | 15.0 | 9.3 | 7.8 | - | - | (c) |
| 4 | 391.6 | 15.0 | 10.3 | 5.0 | 17.1 | 2.5 | (c) |
| 3 | 420.2 | 15.0 | 12.6 | 5.0 | 17.1 | 3.3 | (o) |
| 2 | 453.6 | 17.3 | 11.3 | 4.5 | 17.2 | 3.5 | (c) |
| 1 | 486.8 | 21.0 | 10.1 | 4.5 | 17.2 | 3.8 | (o) |

Table 9.1: Tonehole and bore dimensions of the Selmer clarinet. All dimensions are given in millimeters. $x$ is the distance between the mouthpiece and the hole along the bore axis, $a$ is the main bore radius, $b$ is the hole radius, and $t_w$ is the geometrical effective hole height. If a pad is placed above the tonehole, the pad radius is given by $R$, and the distance between the pad and the hole is indicated with $h$. The last column represents the fingering for the note $F_3$, where ($c$) and ($o$) stand for "closed" and "open", respectively.

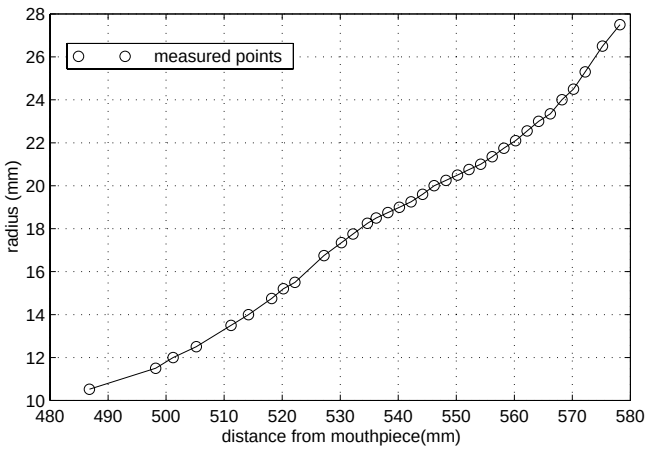


Figure 9.5: Profile of the clarinet bell.

at low frequencies [74]. We therefore model the bore without taking into account those interactions.

### 9.2.2 Wave Digital Model

The main bore of the clarinet can be modelled in discrete time using the wave digital modelling techniques discussed in chapter 6. The sample rate choice in this case depends on the inter-hole bore distances. The shortest inter-hole bore section ($L_{min} = 0.8$mm) is that in between hole no. 12 and no. 13. To enable discrete-time modelling of this section, the minimum allowable sample rate would be $(c/L_{min}) \approx 430$kHz. To allow for a lower sample rate, hole no. 13 was omitted from the model. Since this hole is part of a series of three small-sized and closely spaced holes, we may expect that this simplification (1) causes only a small change to the instrument response, and (2) does not greatly reduce the range of possible notes on the instrument. The second smallest inter-hole distance is 2mm: the sample rate was then taken equal to be the smallest allowable multiple of 44.1kHz, which is $f_s = 176.4$kHz. This sample rate choice allows for a simple conversion to a conventional audio rate, so that audio playback of output signals on standard audio equipment is possible.

As seen in section 2.3.5, wave propagation in a flared bore section may be modelled with a small number of piecewise conical sections. Here we approximate the clarinet bell profile with six sections, while the open-end reflectance and transmittance are modelled with a 5th and a 3rd order filter, respectively. The cylinder-cone mouthpiece is modelled in discrete-time as explained in section 8.2.3. Figure 9.6a shows the input impedance of the complete clarinet bore as computed with the transmission-line model and the wave digital model. The curves exhibit a slight difference in the position of the impedance peaks, which is mainly due to the different way in which the negative length-corrections associated with the toneholes are modelled. That is, if one computes the transmission-line model taking into account the length-corrections by reducing the bore lengths (as is done in the wave digital model), the resulting impedance curve has peak frequencies that match those of the wave digital model result (see figure 9.6b). The remaining difference in amplitude of the first impedance peak is due to the use of an inconsistent formulation of the propagation constant[4].

We note that the wave digital model results in figure 9.6a and figure 9.6b were computed with inclusion of viscothermal losses in the conical sections of the model, and as a consequence this model can only be used for computing the truncated impulse response. In order to derive a model that contains no loss-filters in any of the conical sections, each conical section in the main bore was replaced with a cylindrical sections of mean radius.

[4] This problem has been discussed in section 4.3.3.

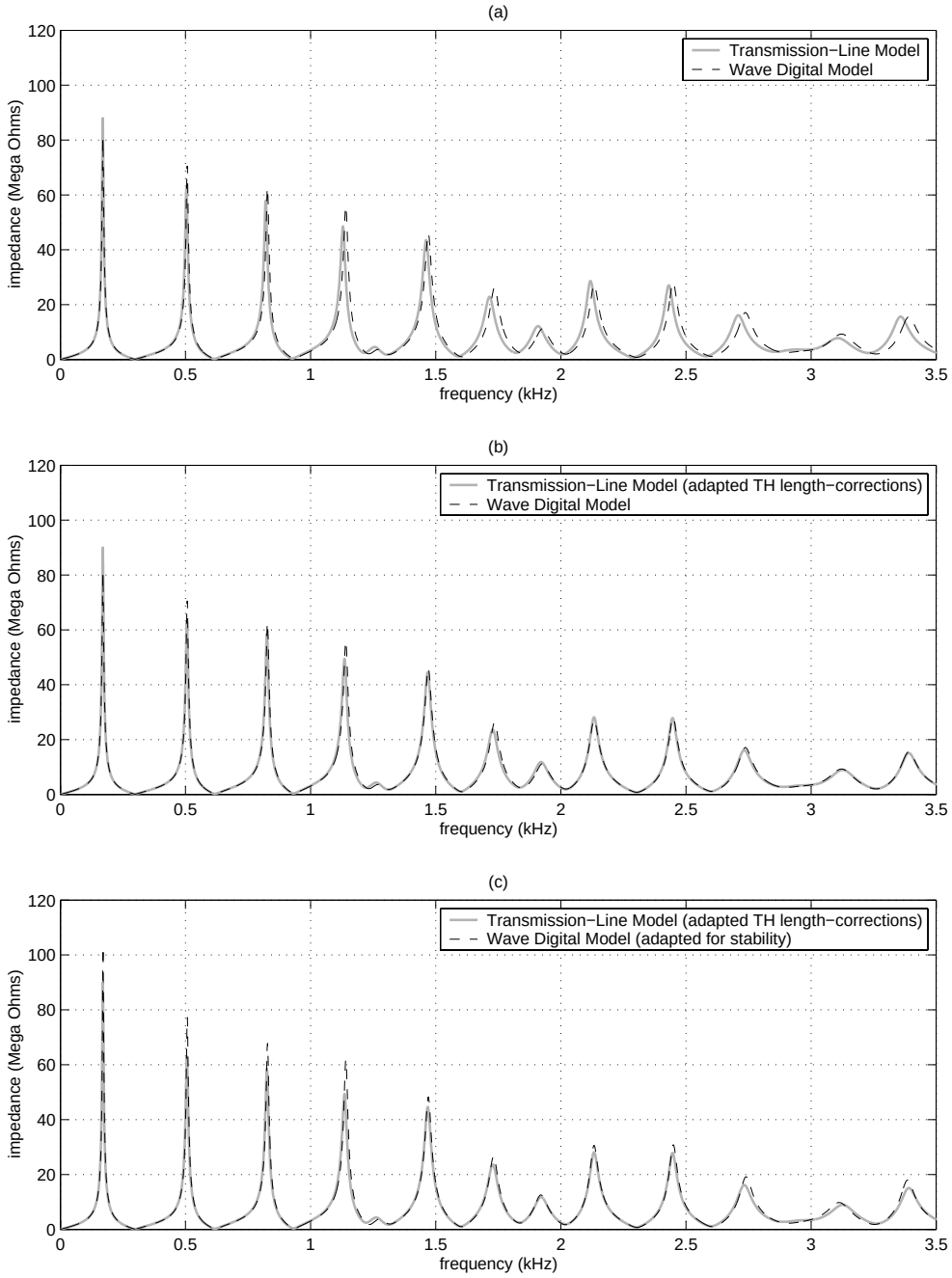


Figure 9.6: Input impedance of the Selmer clarinet, with fingering for note $F_3$. (a): the transmission-line model compared to the wave digital model where viscothermal losses are included in all bore sections. (b): the same comparison, but with the transmission-line model adapted such that the length-corrections associated with the toneholes are taken into account in the same way as in the wave digital model. (c): the same comparison, with the wave digital model with all conical sections in the main bore replaced by cylindrical sections, and no viscothermal losses taken into account in the remaining conical sections in the bell and the mouthpiece.

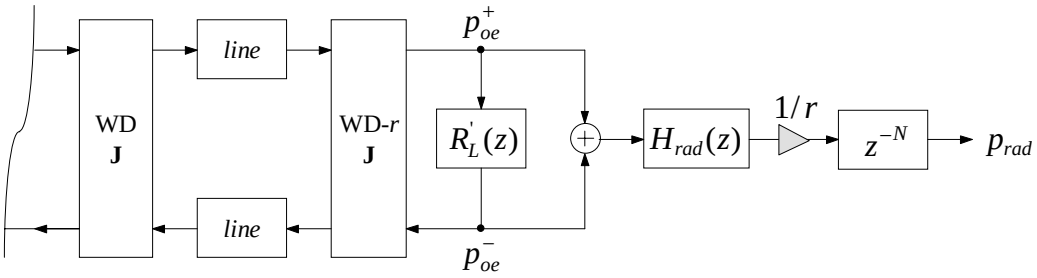


Figure 9.7: Wave digital modelling of the open-end of the clarinet bell.

The remaining conical sections (that in the mouthpiece part and those in the bell) were modeled without loss-filters. The comparison in figure 9.6c shows that these adaptations have extremely little effect on the accuracy of the model. This could be expected because (1) the losses in the very short conical section in the mouthpiece are small in comparison with the overall losses, (2) the angle of conicity of the conical sections in te main bore is very small, and (3) the influence of the bell on the input impedance is usually very small.

### 9.2.3 Sound Radiation

As explained in section 5.3.3, the pressure radiated from a tonehole can be modelled by simply delaying and scaling the pressure in the bore at the position of the tonehole. Apart from the toneholes, a woodwind instrument also radiates sound from the open end of the bell. It was shown in section 6.1.2 that an open end in a conical bore can be modelled using a wave digital reflectance filter in combination with a WD-$r$ unit (see figure 6.5). Figure 9.7 depicts the structure that results when we apply this method to discrete-time modelling of the last section in the piecewise conical series model of the clarinet bell. Although the wave variables $P^+_{oe}$ and $P^-_{oe}$ are not equal to the actual travelling waves at the open-end boundary, we may still compute the pressure at this point as the sum of these wave variables:

$$P_{oe} = P^+_{oe} + P^-_{oe}. \tag{9.1}$$

In order to compute the radiation pressure at a certain distance $r$ from the bell, we consider the bell as an isotropic source. The source-strength is then calculated as the flow across the open-end radiation impedance:

$$U_{oe} = \frac{P_{oe}}{Z_L(\omega)}, \tag{9.2}$$

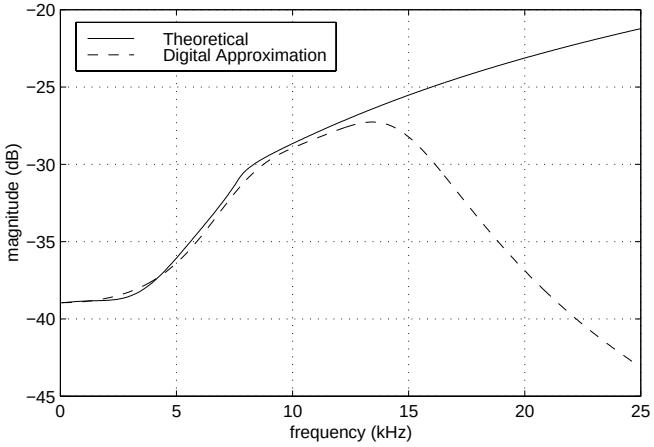


Figure 9.8: Magnitude response of the bell radiation filter.

where $Z_L(\omega)$ is the radiation impedance as discussed in section 2.2.5. The radiation pressure at a distance $r$ may be computed in the same way as for a tonehole (see equation (5.35)):

$$P_{rad}(r) = \left(\frac{j\omega\rho}{4\pi r}\right) U_{oe}\, e^{-jkr}. \tag{9.3}$$

Substitution of (9.2) into (9.3) yields:

$$P_{rad} = \left(\frac{1}{r}\right) H_{rad}(\omega)\, e^{-jkr}\, P_{oe}, \tag{9.4}$$

where $H_{rad}(\omega)$ represents the frequency-dependent element of the radiation, i.e., the *radiation filter*:

$$H_{rad}(\omega) = \frac{j\omega\rho}{4\pi Z_L(\omega)}. \tag{9.5}$$

Given that the term $e^{-jkr}$ represents pure propagation of the radiated wave into space, the radiation pressure $p_{rad}(r)$ may be modelled in discrete time by means of a cascade of a filter ($H_{rad}(z)$), a scaling factor ($1/r$) and a delay-line (see figure 9.7). The scaling factor may be joined with the radiation filter expression but is kept separate here in order to allow for continuous adjustment of the "listening point". What remains is the design of the digital radiation filter $H_{rad}(z)$. For this purpose, we first lowpass filter the theoretical radiation filter $H_{rad}(\omega)$, using a cut-off frequency of about 20kHz. As a result, high-frequency components are strongly attenuated, which helps with suppression of the aliasing effects that might occur in a full simulation. Both the amplitude-effects and the phase-effects of the lowpass filtering have very minor influences on the perception of the final radiated sound pressure[5]. Figure 9.8 shows the magnitude response of the theoretical

[5] The upper limit of the human hearing range is about 20kHz, and the human hearing system is relatively insensitive to phase-effects [108].

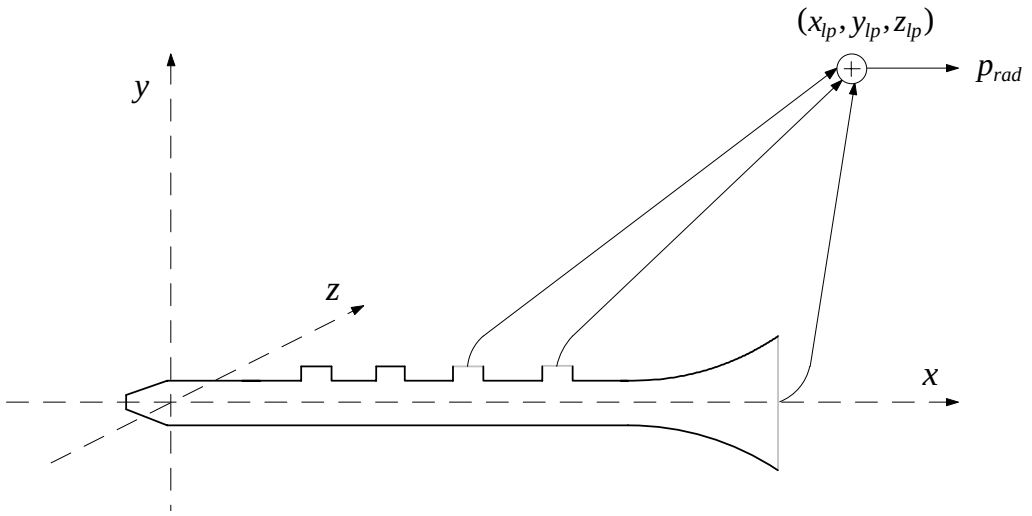


Figure 9.9: Scheme for computation of the total radiated pressure as perceived at a specific point in a non-reverberant space.

radiation filter and a fourth-order IIR filter approximation of the lowpass filtered radiation filter.

The total radiated pressure as perceived at a particular "listening point" in a non-reverberant space may be computed as the sum of the contributions of all toneholes and the bell (see figure 9.9). In principle, one delay-line is required for modelling the propagation from source to listening-point for each of the sound sources. However, if the distance between the listening-point and the instrument is sufficiently large, the differences in propagation time become very small and a single, shared delay-line may be used for all sources.

We note that, as in all previous wave digital model applications, we have omitted the scaling factors that model the decrease of pressure as a wave travels away from the cone apex. As explained in section 4.3.1, this does not affect the reflectance at the bore entry. For the trumpet simulation in section 9.1, the omission of the scaling factors causes the radiated sound to have an incorrect amplitude, but since there is only one single sound source, the spectral balance is unaffected. The clarinet on the other hand has a number of different sound sources. A simple way to take into account the effect of the scaling factors on the radiated sound is to multiply the output of each sound source by the ratio $a_e/a_k$, where $a_e$ is the bore radius at the mouthpiece entry, and $a_k$ is the bore radius at the location of the sound source. For toneholes, this can be done by first multiplying the value of $\xi$ with this ratio[6], so that the computational load of the tonehole models is not

[6] $\xi$ is a constant scaling factor for computing the pressure radiated from a tonehole (see section 5.3.3, equation (5.37)).

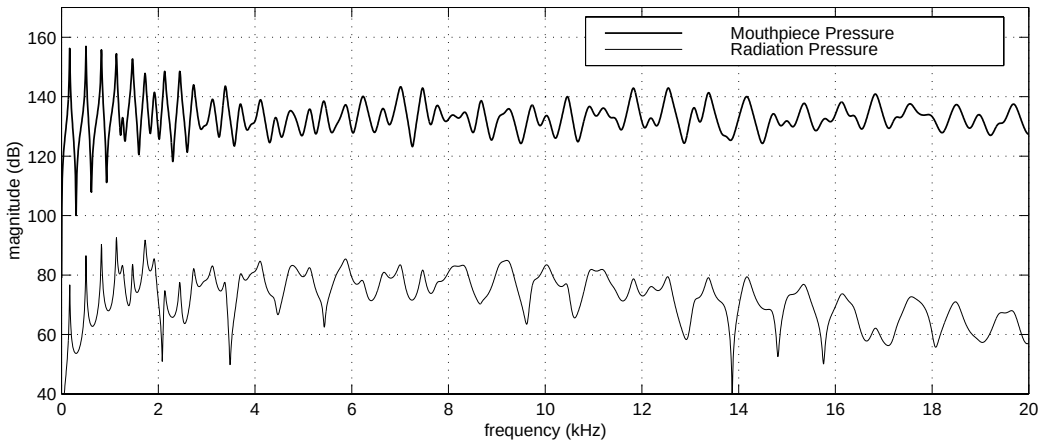


Figure 9.10: Spectral magnitude of the mouthpiece and radiation pressure of the Selmer clarinet, with fingering for note $F_3$.

affected.

Figure 9.10 displays a spectral comparison between the radiation pressure and the mouthpiece pressure. These curves were computed as the Fourier transforms of the signals obtained by injecting a flow (Dirac) input pulse into the mouthpiece (i.e., the mouthpiece pressure spectrum is in fact equivalent to the input impedance). Referring to the coordinate system in figure 9.9, the listening-point was taken $x_{lp} = 0.5\text{m}$, $y_{lp} = 0.5\text{m}$, $z_{lp} = 0\text{m}$. As can be seen from figure 9.10, the radiated pressure is highpass in comparison with the mouthpiece pressure. Below cut-off (about 1.5kHz for the clarinet), the radiation spectrum exhibits a steady increase with frequency relative to the internal bore spectrum, which is very much in agreement with the results reported by Fletcher and Rossing [52]. As with the trumpet model in section 9.1, it may in fact be expected that the various simplifications made in the derivation of the wave digital model result in an approximation of the radiated pressure that is good at low frequencies but poor at high frequencies. In this case, the main deviations at high frequencies are introduced by simplifications concerning the functioning of the toneholes. As discussed in chapter 5, we based our tonehole model on Keefe's transmission-line formulation, which was verified by Keefe with experimental results only up to 5kHz. Therefore, as in the case of the trumpet model, the internal bore pressure does not have the proper high-frequency content, and deducing the radiation pressure from the internal bore pressure will not give accurate results at high frequencies. The reasons brought forward in section 9.1.3 for not including the effects of directivity also apply to the clarinet. That is, we postulate that a perceptually representative sound signal may be obtained without taking these effects into account. Appendix K contains two sound examples of the wave digital model of the Selmer clarinet[7].

[7] The signal of **(ex7)** is the impulse response (Green's function), and signal of **(ex8)** is the corresponding radiation pressure.

## 9.3 Conclusions and Future Work

A trumpet and a clarinet bore have been simulated in this chapter. The techniques used for this purpose largely fall within the "wave digital modelling approach" outlined in section 3.4, hence we may refer to these models as "wave digital models". Various measurements were carried out in order to capture a number of acoustical properties of these instruments. The dimensions of the bore and the bell of the Boosey and Hawkes trumpet were determined experimentally by applying bore reconstruction techniques to pulse reflectometry measurement results. The dimensions of the bore, the toneholes and the bell of the Selmer clarinet were directly obtained via geometrical measurement. Comparisons were made between the input impedance as calculated with a transmission-line model and results obtained from a wave digital model. For both instruments, a reasonable agreement between continous-time results (i.e. the transmission-line model) and discrete-time results (i.e. the wave digital model) was found, and the causes of the small differences between these results have been indicated. We emphasise that although we have limited ourselves to simulation of the trumpet and the clarinet, most techniques that have been employed here are also directly applicable to the simulation of other wind instruments.

With respect to improving the wave digital model of the trumpet bore, two issues come to mind. Firstly, the accuracy would be increased significantly if viscothermal losses were taken into account in the lead-pipe and the mouthpiece backbore. As explained in section 4.4, the methods employed in the presented study do not result in a stable discrete-time model when such losses are included in the delay-loops of the conical sections. Secondly, a complete simulation should contain a model of the valves, so that the bore length can be adjusted in a realistic way. In the current simulation, the bore length is varied by simply adjusting the lengths of the delay-lines that implement wave propagation in the main bore. This method is in fact suitable for simulation of a trombone slide, but clearly forms only an approximate solution to modelling the functioning of the three piston-controlled valves of the trumpet.

The wave digital model of the clarinet bore could also be improved. As seen in section 9.2.2, the resonance frequencies appear to be sensitive to the way in which the length-corrections associated with the toneholes are taken into account. In the original transmission-line model, the length-corrections are incorporated using a series inertance formulation, while the simpler solution of decreasing the bore length on either side of the hole is used in the wave digital model. However the possibility of direct simulation of the series inertances is not investigated here. According to regular wave digital theory, this would lead to instabilities because the inertances associated with the length-corrections are negative. However, the inertances associated with bore conicities in some cases also become negative, and in cases where viscothermal losses are ignored, this does not lead

to any instability problems in the current simulations. So perhaps the inclusion of the length-corrections by means of negative inertances would not destabilise the wave digital model. The fact that the reflection function as computed with the transmission-line model is always convergent is a hint that this might indeed be possible.

Finally, we envisage that for both instruments a more accurate radiation pressure can be obtained by applying a filter that compensates for high-frequency deviations due to the low-frequency approximations used in the wave digital model derivation. This filter could for example be designed to approximate the quotient of a measured and a simulated sound spectrum.

# Chapter 10

# Single Reed Excitation

The sound production mechanism of single reed woodwind instruments has been widely studied in the past century. Many features that were observed in experiments with real woodwinds, can be explained using relatively simple models of the interaction between the excitation system (the reed) and the resonator (the air column). The first steps in developing theories on this interaction were made by musical acoustics pioneers such as Helmholtz [62], Lord Rayleigh [111] and Bouasse [32]. This research is for a large part characterised by qualitative descriptions of the sound production mechanism in woodwinds. Starting in the early 1960s, the research progressed towards the development of a solid mathematical framework for the theory of sustained oscillations in woodwinds, with contributions by various researchers, such as Backus [16, 17], Nederveen [101], Benade [22], Worman [167], Wilson and Beavers [166] and Thompson [144]. More recently, Hirschberg et al. [65, 64] provided some essential insight about these theories by looking at the problem from an aero-acoustical point of view, and Grand et al. [61] have improved on theoretical derivation of the clarinet spectrum. However, most of these theories are limited to the regime of small vibrations. This strongly simplifies the mathematics, and allows for a relatively straight-forward analysis of non-linear woodwind oscillations. The reed in this approach is usually represented by a linear oscillator. While such analysis provides significant insight in the basic mechanisms of self-sustained oscillation, it does not include the phenomenon of "reed beating", which occurs at larger amplitudes. Schumacher [123, 124], Gilbert [59] and more recently Kergomard et al. [83] provide methods for analysing non-linear oscillations taking into account the reed beating phenomenon. In these studies, the reed is still represented by a simple linear oscillator, but inelastic collisions with the mouthpiece are now assumed to occur under beating conditions. However, as was already suggested by Thompson [144], the reed may not behave as a linear oscillator even when it is not beating. Nevertheless this work provides fundamental insight into the behaviour of single reed woodwinds at large amplitude vibrations. Stewart and Strong [140] and Sommerfeldt

and Strong [137] developed the first *distributed* reed model of the reed, in which many fewer simplifying assumptions were made about the mechanical behaviour of the reed. In particular, their models include the effect of the reed curling up to the mouthpiece lay, which is a non-linear phenomenon. Starting from the work by Meynial [96], Ducasse [48] and Gilbert [57], Gazengel [55] has formulated theories for an "equivalent harmonic oscillator model". That is, he has presented a method for determining how the parameters of a the lumped oscillator model vary over time, if this model is to behave in a similar (non-linear) way as a distributed reed model. However, his study is rather global and theoretical, not taking into account various characteristic details of the reed/mouthpiece system of a particular woodwind instrument.

The main aim of the research presented in this chapter is to develop a non-linear lumped oscillator model that accurately describes the behaviour of the reed/mouthpiece system of a clarinet. The approach we take is to combine the distributed modelling techniques developed in [140, 137] with the parameter determination methods developed in [55]. The chapter is structured as follows. In section 10.1, the basic mechanisms involving the interaction between the reed and the air column are discussed. In section 10.2, a distributed model of the reed/mouthpiece system, including a detailed description of the techniques for numerical simulation and parameter determination, is presented. Then in section 10.3, the principles of the lumped oscillator model parameter determination are discussed, and the method is applied to the distributed model. Finally in section 10.4, the resulting non-linear reed oscillator is applied in a full simulation of a pipe blown by a reed, and various aspects and properties of this system are discussed.

## 10.1 Reed and Air Column Interaction

### 10.1.1 The Basic Mechanism

In single reed woodwinds the oscillations are excited by means of a reed that is clamped to the mouthpiece of the instrument (see figure 10.1). The reed is usually made of cane, although plastic versions exist. The generation of sustained oscillations in reed-driven instruments is based on the interaction between the air column and the reed. The basic mechanism works as follows. The mouth pressure ($p_m$) provided by the player causes an airflow through the reed aperture. This mouth pressure tends to close the reed, so that the aperture starts to decrease while a pressure wave ($p^+$) is "released" into the air column. Reflections of this pressure wave occur at various discontinuities in the bore of the instrument, which results in pressure waves travelling back and forth through the air column. Hence the total pressure $p$ in the mouthpiece, which is the sum of the forward- and backward-propagating waves ($p = p^+ + p^-$), starts to vary. This leads to the reed

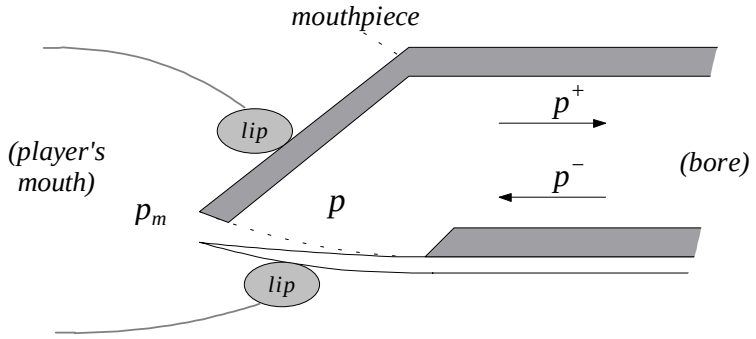


Figure 10.1: Cross-sectional view of a single reed woodwind mouthpiece.

being driven into motion by the pressure difference $(p_m - p)$ across it. Periodic oscillations can be sustained at frequencies near the resonance frequencies of the air column. For an inward-striking reed (such as a woodwind single reed), the fundamental frequency of a sustained oscillation lies just below one of the input impedance maxima of the air column [52]. Excitation is not possible under all circumstances: only when the player's embouchure tension and blowing pressure are such that the flow through the reed channel decreases with blowing pressure are oscillations sustained [22]. Also, if the mouth pressure exceeds a certain level, the reed is blown to full closure [52, 167].

### 10.1.2 An Elementary Valve Model

The interaction between the reed and the air column can be described mathematically with an elementary valve model that was originally proposed by Hirschberg et al. [65], and has since been applied for both synthesis [54] and analysis [81] purposes. A schematised view of this model is depicted in figure 10.2. The reed is represented by a mechanical oscillator that acts as a pressure-controlled valve. The equation of motion for this system is[1]:

$$\frac{d^2y}{dt^2} + g\,\frac{dy}{dt} + \omega_0^2\,y = \frac{\Delta p}{\mu}, \tag{10.1}$$

where $y$ is the reed displacement, $g$ is the reed damping factor, $\omega_0$ is the angular resonance frequency, and $\mu$ is the mass per unit area. The flow of air that is blown into the instrument is regulated by the varying gap between the reed and the mouthpiece. Note that equation (10.1) in fact describes the behaviour of the reed/mouthpiece system, which is rather different than the behaviour of a clamped reed on its own. In particular, the motion of the reed is restricted as it is in contact with both the mouthpiece and the lip. As a result,

[1] We note that the direction of the reed motion is chosen as positive when the reed moves towards closure, which is the same as in the distributed model presented in section 10.2, but opposite to what is conventionally used for the elementary valve model.

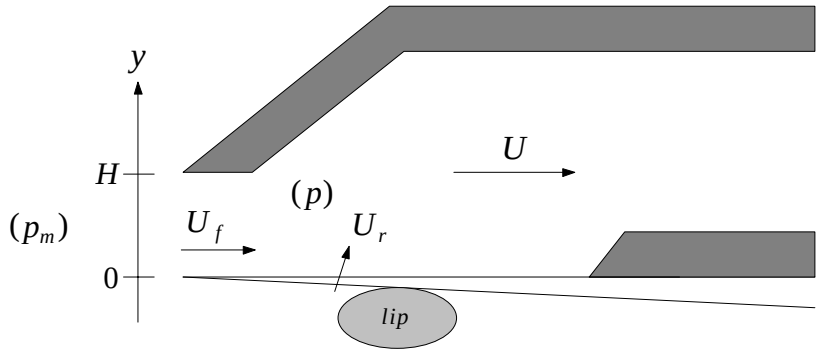


Figure 10.2: Schematised view of a single reed woodwind mouthpiece.

the determination of the parameters $g$, $\omega_0$ and $\mu$ is far from trivial.

The acoustic pressure can be calculated as the linear response of the instrument air column. The total air flow $u$ into the instrument is the sum of two components, the flow $u_f$ entering through the reed channel, and the flow $u_r$ that is induced by the motion of the reed:

$$u = u_f + u_r. \tag{10.2}$$

It is assumed that the reed-induced flow is proportional to the velocity of the reed:

$$u_r = S_r \cdot \frac{\partial y}{\partial t}, \tag{10.3}$$

where $S_r$ is defined as the effective or equivalent flow surface of the reed. The flow through the reed channel is assumed to obey:

$$p_m - p = \frac{\rho}{2} \left[ \frac{u_f}{w\, h} \right]^2, \tag{10.4}$$

where $w$ the width and $h = H - y$ is the height of the reed channel. By means of experiments with a clarinet mouthpiece, Backus [17] derived a semi-empirical version of equation (10.4):

$$(p_m - p)^{2/3} = \frac{u_f}{B\, h^{4/3}}, \tag{10.5}$$

where $B$ is a constant. The different relation between flow, pressure drop and reed opening was assumed by Backus to be due to the particular wedge-shape of the slit of the clarinet reed/mouthpiece system, in combination with the flexibility properties of the reed. However, measurements by Gilbert [57] did not confirm this result. Instead it was found that equation (10.4) applies, although no reliable dynamic data was found for very small reed openings. Hirschberg et al. [64] have pointed out that an empirically derived exponent does not have any simple physical meaning or universal value. Equation (10.4) describes the flow behaviour in the static regime, and it is assumed that it remains valid in the

dynamic regime. However, in the dynamic regime the inertia of the air in the reed channel needs to be taken into account [17]:

$$p_m - p = \frac{\rho}{2}\left[\frac{u_f}{w\,h}\right]^2 + M_{slit}\frac{\partial u_f}{\partial t}. \tag{10.6}$$

Backus [17] measured the reed channel inertia as a function of the reed opening. According to Nederveen [101], Thompson [144] and Gazengel [55], this inertia is generally small in comparison with the acoustic resistance implied in (10.4), and may therefore be neglected.

Worman [167] assumes that there is also a "Bernoulli force" acting on the reed. However, Hirschberg et al. [65] have pointed out that the calculation of this force in [167] is questionable, since it is based on the assumption that there is a pressure recovery in the mouthpiece. The use of equation (10.4) implies that flow separation occurs at the end of the reed channel, which results in the formation of an air jet. Due to turbulent mixing of the jet with the air in the mouthpiece, the kinetic energy in the jet is dissipated, and as a consequence, there is no pressure recovery in the mouthpiece. While it is not excluded that forces of the Bernoulli type are present in the reed channel, it is not directly clear over what length of the reed channel they are active, and whether they increase or decrease with channel aperture [65]. Following the studies in [65, 64], we therefore choose to use an elementary valve model in which no Bernoulli forces are taken into account.

Finally we note that for a pressure difference that can become both positive and negative, (10.4) is written:

$$p_m - p = Sgn\,\frac{\rho}{2}\left[\frac{u_f}{w\,h}\right]^2, \tag{10.7}$$

where $Sgn$ is the sign of the pressure difference. If channel inertia is neglected, the pressure difference and the flow through the channel always have the same direction, thus $Sgn$ is in this case also the sign of $u_f$.

### 10.1.3 Reed Beating

There are two non-linearities in the excitation system described above. For small oscillations, the reed is relatively free to move, and the only non-linearity arises from the relation between flow, reed opening and pressure difference (equation (10.7)). For large oscillations however, the reed starts "beating" against the mouthpiece lay. The common method for simulating reed beating is based on the assumption that when the reed closes, an inelastic collision occurs. This is usually implemented by imposing the following scheme:

$$h = \begin{cases} H - y, & \text{if} \quad y \leq H \\ 0, & \text{if} \quad y > H \end{cases}. \tag{10.8}$$

In case of full closure (i.e., $h = 0$), the velocity of the reed is usually also set to zero. This scheme introduces a discontinuity in the time derivative of $u$, $y$ and $p$ [81], and represents a second non-linearity of the system. While this reed-beating model has been applied frequently [124, 77, 59, 81, 55, 54], it is widely recognised that the interaction between reed and mouthpiece is in reality more complicated [101, 144, 57, 81, 55, 140, 137]. As the reed moves to closure, it must bend against the lay. In other words, there is not a fixed point at which the reed can not move further, but instead the reed is gradually stopped while *curling up* to the lay. During this process, the part of the reed that is pressed against the lay is effectively immobilised, so that the properties of the reed continuously vary over time.

Stewart and Strong [140] point out that the curling phenomenon would have to be explicitly added to the elementary model, by varying the parameters in (10.1), whereas a distributed model of the reed/mouthpiece system would incorporate it automatically. The distributed modelling approach is the subject of the next section.

## 10.2 A Distributed Model of the Reed/Mouthpiece System

### 10.2.1 The Single Reed Modelled as a Non-Uniform Bar

Consider a straight bar of uniform thickness $b$ and width $w$ (see figure 10.3). Suppose that this bar is driven by a force per unit length $F(x,t)$, where $x$ indicates the position along the bar length, and $t$ indicates time. If damping effects are ignored, and the bar is made of homogeneous and isotropic material, the transverse vibrations are governed by the following equation [116]:

$$\rho A \frac{\partial^2 y}{\partial t^2}(x,t) + \frac{\partial^2}{\partial x^2}\left[Y I \frac{\partial^2 y}{\partial x^2}(x,t)\right] = F(x,t), \tag{10.9}$$

where $y(x,t)$ denotes the transverse displacement of the bar, $A = w\,b$ is the cross-section, $\rho$ is the density, and $Y$ is the Young's modulus. The term $I = A\,\kappa^2$ is a mathematically convenient term, where $\kappa = b/\sqrt{12}$ is the radius of gyration of the bar. The contribution of torsional and longitudinal waves as well as flexural waves in the $xz$-plane are neglected in this formulation.

A woodwind reed may be considered as a bar of length $L$ and non-uniform thickness, clamped at one end ($x = 0$) and free on the other ($x = L$). For such a system, the boundary conditions are [52]:

$$\begin{aligned} y(0,t) = 0 \quad &, \quad \frac{\partial y}{\partial x}(0,t) = 0, \\ \frac{\partial^2 y}{\partial x^2}(L,t) = 0 \quad &, \quad \frac{\partial^3 y}{\partial x^3}(L,t) = 0. \end{aligned} \tag{10.10}$$

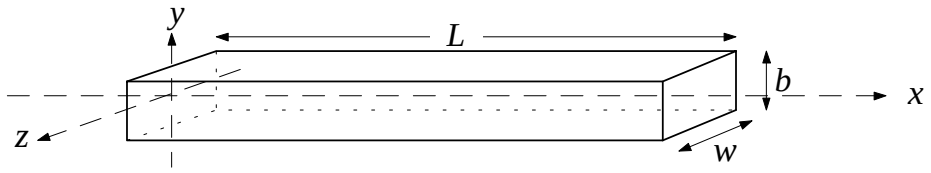


Figure 10.3: Bar Dimensions.

The reed thickness is a slowly varying function of the spatial coordinate $x$, which may be taken into account by simply writing the cross-section $A$ and moment $I$ as a function $x$ [116]. Furthermore, a realistic model of the reed involves some form of damping. A freely vibrating bar is subject to two different types of damping. The main damping is due to viscoelastic friction within the bar, and further losses occur due to damping by the fluid surrounding the bar. In a study on transverse vibrations of a xylophone bar [36], it is shown that these two damping effects may be incorporated by adding two terms to eq. (10.9):

$$\rho A(x) \left[ \frac{\partial^2 y}{\partial t^2}(x,t) + \gamma_B \frac{\partial y}{\partial t}(x,t) \right] + \frac{\partial^2}{\partial x^2} \left[ Y I(x) \left( 1 + \eta \frac{\partial}{\partial t} \right) \frac{\partial^2 y}{\partial x^2}(x,t) \right] = F(x,t), \quad (10.11)$$

where $\eta$ and $\gamma_B$ are coefficients that represent the magnitude of the viscoelastic losses and the fluid damping, respectively.

### 10.2.2 Numerical Formulation

In order to simulate the distributed reed model in discrete-time, finite difference methods are applied. This involves spatial and temporal discretisation: the bar is divided into $N$ sections, which corresponds to a spatial grid of $(N+1)$ grid-points. Extra grid-points are added at both ends in order to enable numerical formulation of the boundary conditions. The spatial sampling step is then $\Delta x = L/N$ and the temporal sampling step (sampling period) is $T = 1/f_s$, where $f_s$ is the sampling frequency. In our notation, the index $i$ indicates the spatial coordinate $x_i = i\,\Delta x$, and the discrete-time point $n$ indicates the time $t_n = n\,T$.

Both explicit and implicit finite difference schemes can be used in order to approximate the spatial and temporal derivatives of the bar equation. In the case of a non-uniform bar, an implicit finite difference scheme is required in order to preserve stability [36]. Here we will apply the "$\theta$-scheme" described in [36], in which the second term on the left-hand

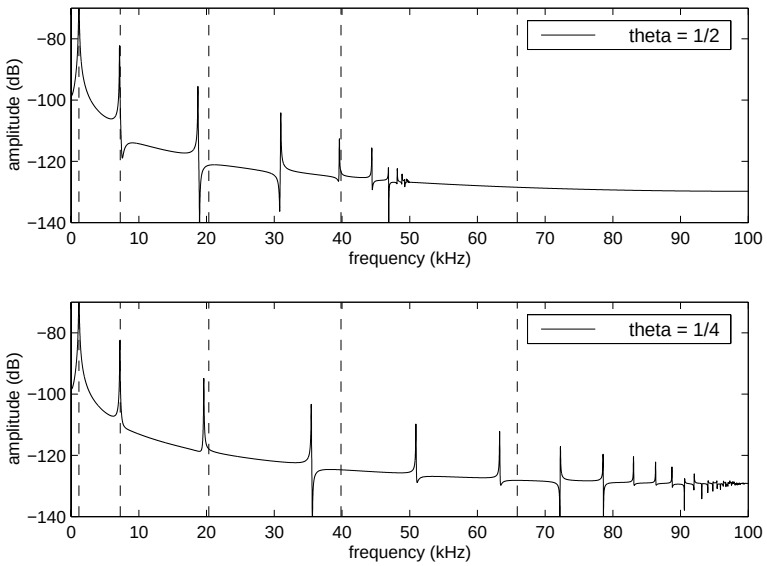


Figure 10.4: Comparison between using $\theta = 1/4$ and $\theta = 1/2$. Both figures show the spectral magnitude of the impulse response of a straight uniform bar clamped at one end, as computed using the numerical model. The dashed lines indicate the positions of the natural frequencies of the bar, as predicted by theory. The impulse responses were computed using $f_s = 200$kHz and $N = 200$.

side of equation (10.11) is approximated by:

$$\frac{\partial^2}{\partial x^2}\left[I_i\left(1+\eta\frac{\partial}{\partial t}\right)\frac{\partial^2 y}{\partial x^2}(x_i,t_n)\right] \approx \theta\left[(1+\beta)\,\delta_x^2[I_i(\delta_x^2 y)_i]^{n+1} + (1-\beta)\,\delta_x^2[I_i(\delta_x^2 y)_i]^{n-1}\right]\cdots + (1-2\theta)\,\delta_x^2[I_i(\delta_x^2 y)_i]^n, \quad (10.12)$$

with $\beta = \eta\, f_s$ and where

$$\delta_x^2[I_i(\delta_x^2 y)_i]^n = [I_{i+1}y_{i+2}^n - 2(I_{i+1}+I_i)y_{i+1}^n + (I_{i+1}+4I_i+I_{i-1})y_i^n \cdots -2(I_i+I_{i-1})y_{i-1}^n + I_{i-1}y_{i-2}^n]/\left(\Delta x^4\right). \quad (10.13)$$

It can be shown when such a scheme is used, the numerical simulation remains unconditionally stable if $\theta \geq 1/4$ [36]. The main advantage of an unconditionally stable scheme is that it allows to us to choose $N$ and $f_s$ independently.

It is well known that any discretisation process involves frequency warping effects. It is important to minimise these effects such that the natural frequencies of the bar are well approximated. Using a $\theta$-scheme, the minimum warping for unconditionally stable simulations is achieved with $\theta = 1/4$. It is interesting to note that $\theta = 0$ corresponds to using an explicit scheme, and that the finite-difference scheme used in the numerical simulations in [140, 137] corresponds to $\theta = 1/2$. Figure 10.4 demonstrates the difference in warping effects between using $\theta = 1/4$ and $\theta = 1/2$ for the case of a uniform bar

with fluid damping only (i.e., $\eta = 0$). For this case the exact resonance frequencies can be analytically determined [84]. Apparently, the 1/4-scheme "maps" the complete continuous-time frequency-axis on to the complete discrete-time frequency axis. In this respect, the 1/4-scheme resembles the use of the bilinear transform (see, e.g., [109]). On the other hand, the 1/2-scheme maps the continuous-time frequency-axis on to only half of the discrete-time frequency-axis, which corresponds to about "twice" the amount of frequency warping.

Using the approximation in (10.12), and applying simple central difference formulae for the time-derivatives in (10.11), a numerical formulation of the system is obtained (see appendix H):

$$\rho A_i \left[(1+\gamma)\, y_i^{n+1} - 2y_i^n + (1-\gamma)\, y_i^{n-1}\right] + T^2\, Y \mathcal{D}_i^n = T^2\, F_i^n, \tag{10.14}$$

with $\gamma = \frac{1}{2}\gamma_B\, T$ and where $\mathcal{D}_i^n$ denotes the spatial derivative approximation in (10.12). The implicity of this equation requires the solution of the system in matrix form. The final matrix equation takes the form:

$$\mathbf{y}(n+1) = \mathbf{A}_n \cdot \mathbf{y}(n) + \mathbf{A}_{n-1} \cdot \mathbf{y}(n-1) + \mathbf{A}_F \cdot \mathbf{F}(n), \tag{10.15}$$

where $\mathbf{y}(n+1)$, $\mathbf{y}(n)$ and $\mathbf{y}(n-1)$ represent the displacement vector at successive time instants, and $\mathbf{F}(n)$ is the force per unit length vector. The coefficients of the matrices $\mathbf{A}_n$, $\mathbf{A}_{n-1}$ and $\mathbf{A}_F$ are obtained by solving the initial system of simultaneous equations that results from combining the boundary equations with the difference equation (10.14), for the vector $\mathbf{y}(n+1)$ (see appendix H).

### 10.2.3 The Interaction with the Mouthpiece and the Lip

In a single reed woodwind instrument, the reed is clamped to the mouthpiece by means of a ligature (see figure 10.5). Furthermore, the player pushes the lip against the reed, such that when the reed is in rest position, a small gap (about 0.4mm) between the reed tip and the lay remains. These reed/mouthpiece and reed/lip interactions cause the reed to behave significantly differently to a reed that is simply clamped at one end and free to move at the other.

As the reed oscillates, collisions occur between sections of the reed and the mouthpiece. It is usually assumed that these collisions are fully inelastic [140, 137, 81]. This corresponds to a dissipative force applied to a section of the reed over the period that it collides with the lay. However, the interaction between reed and mouthpiece can never be fully explained in terms of dissipative forces. In the case of static contact (in which case no dissipative forces exist), some form of contact-forces (that is, external forces exerted on the reed by

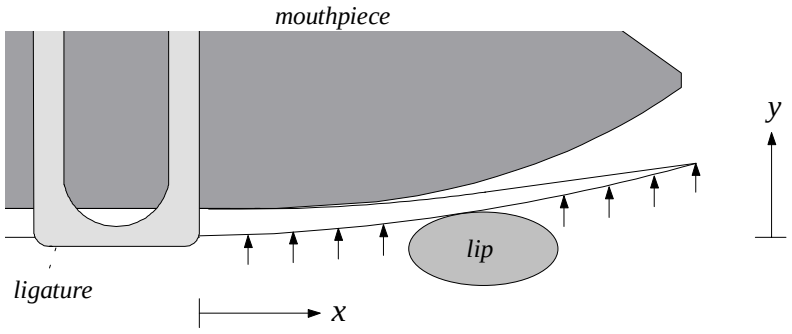


Figure 10.5: Schematic representation of the reed/mouthpiece system. The reed is clamped with the ligature at $x = 0$. The small arrows indicate the forces acting upon the reed due to a pressure difference across it.

the lip and the mouthpiece) must be present in order to hold the reed in place. If we assume that the permanent deformation of either the reed or the mouthpiece due to these static contact-forces is negligible[2], then it follows that, at least in the static case, the contact-forces must be elastic. Since part of the reed is effectively immobilised by the lip (and pressed against the mouthpiece lay), elastic forces must be continuously present in the reed/mouthpiece system.

The lip is assumed to be in continuous contact with the reed over a certain length, which provides extra damping to the reed/mouthpiece system. Following the approach taken in [137], we take this extra damping into account by increasing the fluid damping value of those parts of the reed that are in contact with the lip. Apart from damping, the lip also exerts an elastic restoring force on the part of the reed with which it is in contact.

The exact form of the contact-forces that model the interaction with the lip and the mouthpiece is presented here directly in numerical form. Recall equation (10.15), that gives the final numerical formulation of the reed/mouthpiece system. The force vector $\mathbf{F}(n)$ in this equation contains several components:

$$\mathbf{F}(n) = \mathbf{F}_{\Delta p}(n) + \mathbf{F}_{lay}(n) + \mathbf{F}_{lip}(n), \tag{10.16}$$

where $\mathbf{F}_{\Delta p}(n)$ is a vector that represents the force per unit length due to the pressure difference $\Delta p(n)$ across the reed. This pressure difference is assumed to be uniformly distributed over the reed surface. Thus for all sections $(i)$ we have:

$$(F_{\Delta p})_i^n = \frac{\Delta p(n)}{w}. \tag{10.17}$$

[2] This is a reasonable assumption, because otherwise it would have to be assumed that either the reed or the mouthpiece exhibits significant permanent deformation each time they are pressed together.

The vectors $\mathbf{F}_{lay}(n)$ and $\mathbf{F}_{lip}(n)$ represent the contact-forces that model the interaction with the mouthpiece and the lip, respectively. The lip-forces are modelled according to linear elasticity:

$$(F_{lip})_i^n = \begin{cases} K_{lip}\ \left[(y_{lip})_i - b_i - y_i^{n-1}\right], & \text{if} \quad i \in \mathbf{i}_{lip} \\ 0, & \text{otherwise} \end{cases}, \tag{10.18}$$

where $(y_{lip})_i$ and $b_i$ respectively are the vertical lip position and reed thickness at section $(i)$, $K_{lip}$ is the lip stiffness per unit length, and $\mathbf{i}_{lip}$ is a vector that indicates the reed sections that are in contact with the lip. We do not claim that modelling the lip with $F_{lip}$ forms a realistic simulation of the interaction between a human player's lip and the reed. It is merely the simplest possible restoring force, which is intended as a first-order approximation in the case of using an artificial lip (see section 10.2.4).

The interaction with the mouthpiece is slightly more complicated, because collisions occur during reed oscillation. The contact-forces contain a dissipative as well as an elastic component:

$$(F_{lay})_i^n = (F_{el})_i^n + (F_{dis})_i^n, \tag{10.19}$$

where $(F_{el})_i^n$ is an elastic restoring force per unit length, and $(F_{dis})_i^n$ is a dissipative force per unit length. The elasticity term is nonzero only in the case of *contact* between the reed and the mouthpiece, and the dissipative term is nonzero only when a *collision* is anticipated. The condition of contact is:

$$y_i^{n-1} > (y_{lay})_i, \tag{10.20}$$

and the elastic restoring force is formulated

$$(F_{el})_i^n = \begin{cases} K_{lay}\ \left[y_i^{n-1} - (y_{lay})_i\right], & \text{if condition (10.20) is fulfilled} \\ 0, & \text{otherwise} \end{cases}, \tag{10.21}$$

where $K_{lay}$ is the mouthpiece contact stiffness per unit length[3] and $(y_{lay})_i$ is the local position of the mouthpiece.

The dissipative force $(F_{dis})_i^n$ is chosen such that it nullifies the kinetic energy of any reed section $(i)$ that is "about to collide" with the mouthpiece. This force, that is applied over a single sampling period, is computed as follows. At each instant of the numerical simulation, we predict the next value of the displacement vector:

$$\hat{\mathbf{y}}(n+1) = \mathbf{A}_n \cdot \mathbf{y}(n) + \mathbf{A}_{n-1} \cdot \mathbf{y}(n-1) + \mathbf{A}_F \cdot \hat{\mathbf{F}}(n), \tag{10.22}$$

[3] It is assumed here that when the reed and the mouthpiece are pressed together, the mouthpiece compression is negligible compared to the reed compression. Hence the mouthpiece contact stiffness represents an elasticity coefficient that corresponds to compression of the reed.

where $\hat{\mathbf{F}}(n) = \mathbf{F}_{\Delta p}(n) + \mathbf{F}_l(n)$ contains only the forces due to the lip and the driving pressure difference. Using this displacement prediction, we compute a velocity vector:

$$\hat{\mathbf{v}}(n) = \frac{\hat{\mathbf{y}}(n) - \mathbf{y}(n-1)}{T}. \tag{10.23}$$

Note that eq. (10.23) gives a reasonable prediction of the velocity for the time period $t = nT$ to $t = (n+1)T$. Suppose now that an inelastic collision occurs within this time period. We can check whether a collision actually takes place for each section $(i)$ with the condition:

$$\hat{y}_i^{n+1} > (y_{lay})_i \quad \text{and} \quad y_i^n < (y_{lay})_i. \tag{10.24}$$

For the purpose of calculating $(F_{dis})_i^n$, we only need to take into account the kinetic energy of the reed section. Therefore we may temporarily assume that no forces are currently acting upon a particular reed section $(i)$ (i.e., we ignore the shear forces, the driving forces and the lip forces). In that case an inelastic collision with the mouthpiece is characterised by the total reduction of velocity of this reed section. That is, just before the section collides with the mouthpiece it has a velocity $v_i^n$, and directly after the collision, it has a zero velocity:

$$v_i^{n+1} = 0. \tag{10.25}$$

The most straight-forward way to model this would be to apply an impulsive force per unit length $F_{imp}(t)$ for the duration of the collision. In that case, the impulse-momentum theorem law applies [165]:

$$M_i \, \Delta v = \int_{t=t_1}^{t=t_2} F_{imp}(t) dt, \tag{10.26}$$

where $\Delta v$ is the change in velocity over a period of collision ($t = t_1$ to $t = t_2$), and $M_i$ is the mass per unit length:

$$M_i = \rho \, w \, b_i. \tag{10.27}$$

In the numerical model, we can only change the force at discrete-time instants. Avanzini [12] has suggested to nullify the kinetic energy of the reed by applying a constant dissipative force over the period $t = nT$ to $t = n(t+T)$:

$$M_i \left( v_i^{n+1} - v_i^n \right) = (F_{dis})_i^n \cdot T. \tag{10.28}$$

Substitution of (10.25) and solving (10.28) for $(F_{dis})_i^n$ gives:

$$(F_{dis})_i^n = - \left( \frac{M_i}{T} \right) v_i^n. \tag{10.29}$$

Thus an inelastic collision of a reed section with the mouthpiece can be simulated within the numerical model by applying a damping $-M_i/T$ at the moment that the reed hits the mouthpiece:

$$(F_{dis})_i^n = \begin{cases} -\left(\frac{M_i}{T}\right)\hat{v}_i^n, & \text{if condition (10.24) is fulfilled} \\ 0, & \text{otherwise} \end{cases} . \qquad (10.30)$$

In summary, the method applies a dissipative force at $t = (n)T$ to a certain reed section $(i)$, if it is anticipated (according to (10.24)) that this reed section will hit the mouthpiece between $t = (n-1)T$ and $t = nT$. Note that this nullifies the current kinetic energy of the reed section, but does not necessarily prevent it from moving "into" the mouthpiece. This is because the section also has potential energy, provided by the shear and external forces applied to it. The elasticity term in (10.19) represents the restoring forces that are required to hold the reed section in place when in contact with the mouthpiece.

### 10.2.4 Determination of the Model Parameters

The equations presented in the last section yield the basic numerical model of the reed/mouthpiece system. In order to simulate the motion of a particular woodwind reed, it is essential to run the simulation with appropriate physical parameters. Some of these parameters can be derived directly from measurements on reeds and mouthpieces of a real woodwind instrument. Other parameters, such as the damping provided by the lip, are more difficult to establish via measurement. For such parameters, we resort to the method of running the numerical simulation and adjusting the parameter such that the simulation exhibits a behaviour similar to the behaviour observed in real reed/mouthpiece systems. Here we applied this approach to the clarinet.

Measurements on the Mouthpiece

A clarinet mouthpiece lay typically has a relatively flat part at the end that connects to the instrument. When in rest position, and with no lip pressure supplied, the reed is pressed to this flat part. The remaining part of the lay is slightly curved, such that when in motion, the reed curls up to the lay. Using a travelling microscope, the profile of the curved part of the lay of three different mouthpieces was measured[4]. The spatial coordinates were defined such that the clamping point corresponds to $x = 0$. The data for each mouthpiece was fitted with a fourth-order polynomial function. In order to ensure that the resulting fitting curve smoothly connects to the flat part of the lay, the following

[4] A *Bundy*, a *Calteau*, and a *Reginald Kell* mouthpiece.

conditions were imposed on the polynomial fitting function $G(x)$:

$$G(x_c) = 0 \quad \text{and} \quad \frac{dG}{dx}(x_c) = 0, \tag{10.31}$$

where $x = x_c$ is the point where the flat and the curved part connect. The measured profile data and the polynomial fits are depicted in figure 10.6. The measured mouthpieces have an overall similar shape. It must be noted however that our simulation results indicated that small differences in shape can have a quite dramatic effect on the curling behaviour of the reed.

Measurements on the Reed

Various measurements were carried out in order to determine the properties of a clarinet reed. A plastic-coated reed was preferred instead of cane reed, because it has the properties of a "wet" reed[5].

The reed thickness cannot be measured directly as a function of $x$, since it is not constant over its width $w$ (see figure 10.8). Therefore we measured both the minimum thickness (at the edges) and the maximum thickness (central). This was done for 18 points along the length of the reed. For each point, an *effective* thickness, i.e. the thickness of the reed shape with equivalent rectangular cross-section, can be calculated. This calculation was based on the assumption that for each point along the length, the curvature over the width has a circular shape. Figure 10.7 shows the obtained data points and the corresponding effective thickness curve. The density of the reed material was determined by weighing the total reed and dividing this by its volume.

For the measurements of the elastic and damping properties of the reed, experiments were carried out with a reed clamped between two perspex plates, with a thin piece of hard rubber fitted in between on the curved side of the reed (see figure 10.8). The reed was excited using a horn driver at a distance of about 2mm. The response of the reed to a sinusoidal pressure signal was measured using an infra-red sender/receiver system, placed on the other side of the reed, and this signal was digitally recorded for further analysis. Hence both the driving and the detection are non-contact in this setup. The experiments were carried out in an anechoic chamber.

In the first step of the experiment, the reed was simply excited by plucking, and a rough estimation of the positions of the first three resonance frequencies was made with the use of a Fourier transform of the resulting response. In the second step, the reed was driven at the first mode frequency (1.4kHz), using a high-amplitude signal from the horn driver. The

[5] A normal, non-coated cane reed has different elastic and damping properties when humid (such as under playing conditions) from when it is dry. A plastic-coated reed is designed to have properties similar to the properties of a normal reed under playing conditions, independent of humidity.

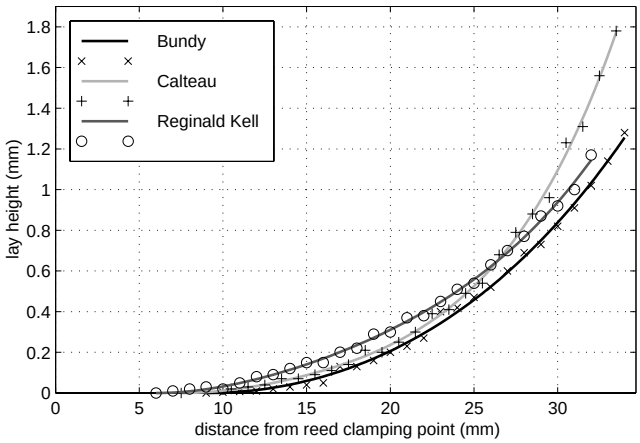


Figure 10.6: Lay profile of three different clarinet mouthpieces.

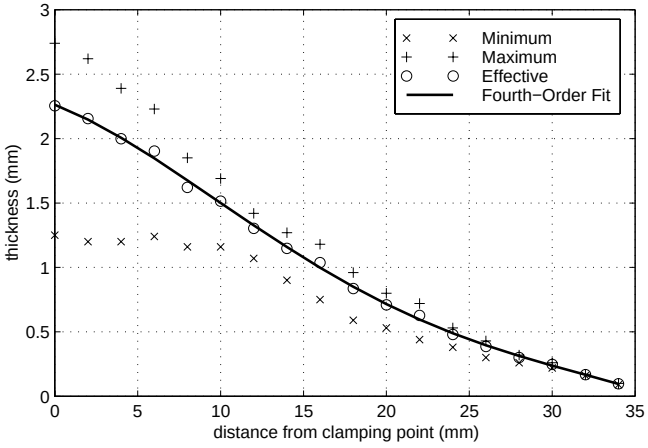


Figure 10.7: Maximum (central), minimum (edges) and effective thickness of a clarinet reed. The latter is computed as the thickness of the reed shape with equivalent rectangular cross-section.

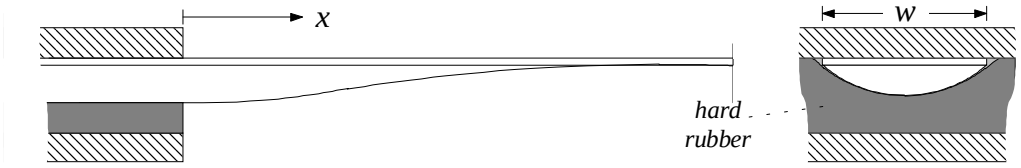


Figure 10.8: Cross-sectional views of the clamping arrangement used in the experiments on the clarinet reed.

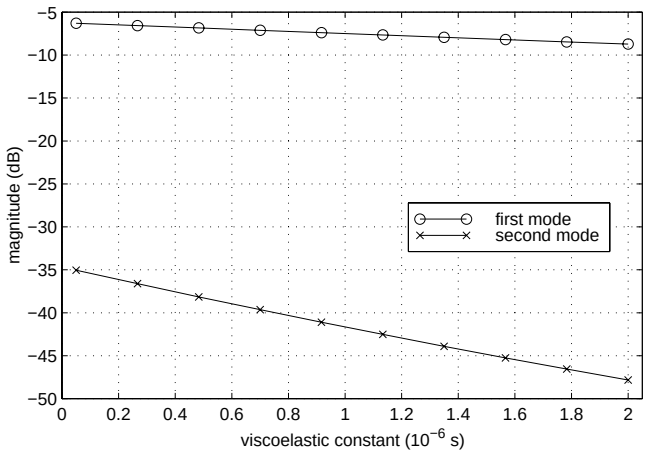


Figure 10.9: Dependence of the amplitude of the first two modes of the reed/mouthpiece system on the viscoelastic constant $\eta$, as computed with the numerical simulation.

frequency of the driving signal was fine-tuned until the reed response reached a maximum, after which the amplitude of the driving signal was measured with a microphone. Then, after sudden suppression of the driving signal, the damping factor of the first mode was derived from the decay pattern of the measured waveform. In a third step, the reed was driven at its second resonance frequency, using the same driving amplitude as was used in the second step. The second and higher modes are very strongly damped however, and it was found that the amplitude of the horn driver at this frequency is simply insufficient for higher-mode excitation that can be measured with the experimental setup. In the last step of the experiment, the minimum amplitude that is required to excite the first mode was measured. Taking into account the frequency-dependence of the microphone, the difference between that amplitude and the amplitude that was used in the attempt to excite the second mode was found to be about 32dB. Given that the infra-red receiver system has a flat magnitude response in the frequency area of interest, it follows that the response at the first mode must be at least 32dB stronger in amplitude than the response at the second mode.

The obtained information was used to fine-tune the numerical simulation as follows. The only unknown parameter which influences the first resonance frequency of the reed

is the Young's modulus. Hence we adjusted $Y$ until the simulation (with the lip- and the lay-interaction de-activated) exhibited the proper first mode frequency when excited with an impulse. Next, the influence of the damping constants $\eta$ and $\gamma_B$ on the damping of individual modes was established. Empirically it was found that the fluid damping constant $\gamma_B$ has approximately the same damping effect on all frequencies. On the other hand, the viscoelastic damping causes a distinctly frequency-dependent damping effect. The damping effect it has on the first two modes of the reed was determined by running the simulation several times, keeping $\gamma_B$ constant and varying $\eta$. Figure 10.9 shows the resulting amplitudes for both mode frequencies as a function of $\eta$. In the experimental stage, it was found that the difference in amplitude between the first and the second mode must be at least 32dB. In the numerical model, this difference only depends on $\eta$, and from the data displayed in figure 10.9, it can be deduced that the viscoelastic damping factor must be at least $\eta = 6.0^{-7}$s in order to have the same difference in dB. The fluid damping value was then determined by adjusting it until the simulation exhibited the appropriate damping behaviour at the first resonance frequency.

Measurements on the Artificial Lip

The properties of the human lip are not easily determined, due to its complex substance and structure. Moreover, an *artificial lip* is usually employed in experimental setups in which the clarinet is machine-blown (see, e.g., [16, 137, 57, 67]). We therefore resort to modelling the "lip" of a particular artificial blowing system[6]. The lip in this system is represented by a balloon filled with water. We assume that the use of the balloon-lip is justified to some extent by the fact that musically acceptable notes can be produced with the artificial blowing system, although it is obviously inferior compared to a human lip in terms of embouchure control.

The elastic properties of the balloon-lip were determined by measuring the compression $\Delta y_{lip}$ of the balloon due to the gravitational force per unit length $F_g$ of a known weight. The weight consisted of a clarinet reed with a piece of metal on top of it, and was placed on the balloon-lip such that the pressure distribution on the lip is the same as it is under normal playing conditions. The compression of the balloon due to the weight was measured using a travelling microscope. This procedure was carried for various weights, and the stiffness per unit length of the lip was determined as a the steepness of a linear fit to the data $F_g$ versus $\Delta y_{lip}$.

In the simulation, the lip was positioned 12mm from the reed tip, which is similar to

[6] Currently, an artificial blowing system for the clarinet is being used in the historical museum of musical instruments in Edinburgh, for the purpose of demonstration of the functioning of musical wind instruments [34]. This system has been used in the present study for qualitative observation of the behaviour of the clarinet reed.

| |
|---|
| Reed - (RICO plasticover, hardness 2) |
| Length (free part when clamped) $L = 34\,\mathrm{mm}$ |
| Width $w = 13\,\mathrm{mm}$ |
| Density $\rho = 500\,\mathrm{kG\,m^{-3}}$ |
| Young's Modulus $Y = 5.6 \times 10^{9}\,\mathrm{N\,m^{-2}}$ |
| Viscoelastic constant $\eta = 6.0 \times 10^{-7}\,\mathrm{s}$ |
| Fluid damping coefficient $\gamma_B = 100\,\mathrm{s^{-1}}$ |
| |
| Artificial lip (water-filled balloon) |
| Length of the contact segment $L_{lip} = 10\,\mathrm{mm}$ |
| Position of the centre of the contact segment $x_{lip} = 22\,\mathrm{mm}$ |
| Vertical position $y_{lip} = 5.65\,\mathrm{mm}$ |
| Stiffness per unit length $K_{lip} = 6.5 \times 10^{4}\,\mathrm{N\,m^{-2}}$ |
| Additional fluid damping $\gamma_{B,lip} = 16000\,\mathrm{s^{-1}}$ |
| |
| Mouthpiece (Bundy) |
| Lay length (total) 34 mm |
| Lay length (curved part) 25 mm |
| Contact stiffness per unit length $K_{lay} = 1.0 \times 10^{8}\,\mathrm{N\,m^{-2}}$ |
| |
| Discretisation |
| Number of sections $N = 200$ |
| Sample rate $f_s = 200\,\mathrm{kHz}$ |

Table 10.1: Parameter values used in the simulations.

the position of the balloon-lip in the artificial blowing system. The vertical position of the lip was then adjusted such that the gap between the reed tip and the lay is $0.4mm$. These positions are normally part of the player's embouchure, and may vary from note to note.

The damping that the lip adds to the system was determined by adjusting it until the simulation exhibited a damping behaviour similar to the behaviour observed in experiments by Worman [167], i.e., a reed damping factor $g \approx 3000$ rad/s.

The parameter $K_{lay}$, that indicates the stiffness per unit length associated with the elastic restoring force of the reed/mouthpiece interaction, is difficult to determine via measurement. Instead, we have chosen $K_{lay}$ as the highest possible value that does not cause any numerical instability problems in the simulation. This choice amounts to assuming

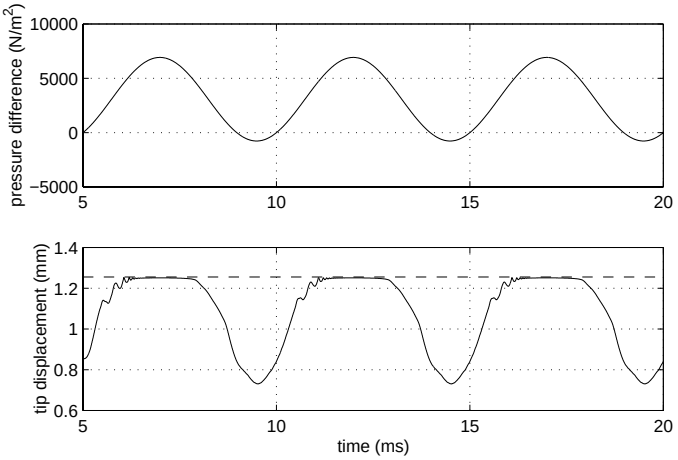


Figure 10.10: The pressure difference signal applied to the numerical simulation of the distributed model (top), and the resulting reed tip displacement (bottom).

that the reed and the mouthpiece are made of strong materials and may be regarded as incompressible in comparison with the lip.

### 10.2.5 Initial Results

Using the parameters determined as described in the last section, a number of initial results were obtained from running the simulation of the distributed reed model simulation (with no acoustical feedback). Firstly, the simulation was run using a sinusoidal driving pressure difference, and the resulting tip displacement was traced (see Figure 10.10). The reed tip is clearly "stopped" from exceeding a certain displacement level. This corresponds to the reed curling up to the mouthpiece lay. Another interesting feature of the displacement signal in figure 10.10 is that the displacement signal exhibits small additional oscillations just before it reaches it maximum. This corresponds to a point where the mass makes a rather sudden "jump" to a smaller value, which incites a decaying oscillation at the new resonance frequency of the system. These waveform features have been observed to some extent in various artificial blowing experiments with clarinet reeds [16, 96, 57, 67].

Secondly, the simulation was run in a "quasi-static" manner. That is, a series of simulations was run, where in each simulation a different (constant) driving force was applied. The simulation duration was chosen such that all oscillations have decayed at the end, at which point the position of each reed section (i.e., the reed deformation state) is measured. Figure 10.11 shows a representative set of deformation states.

The quasi-static simulation allows us to determine the elastic properties of the reed/mouthpiece system. In general, the reed motion is dominated by the pressure difference that drives it, and the driving signal contains frequency components that are mostly below the resonance frequency of the reed/mouthpiece system [101, 144]. For such a sys-

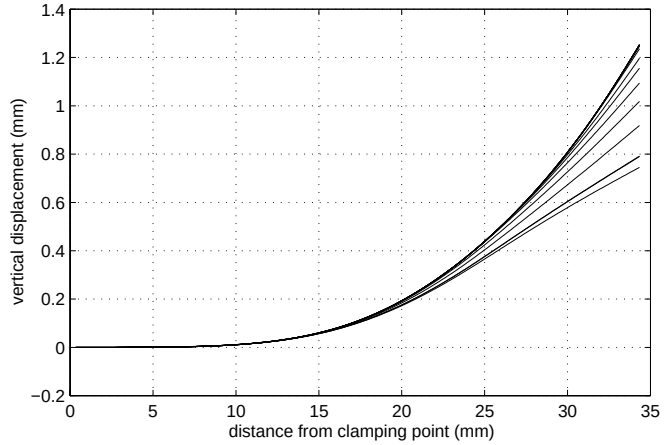


Figure 10.11: Reed deformation states, as measured from the quasi-static simulation.

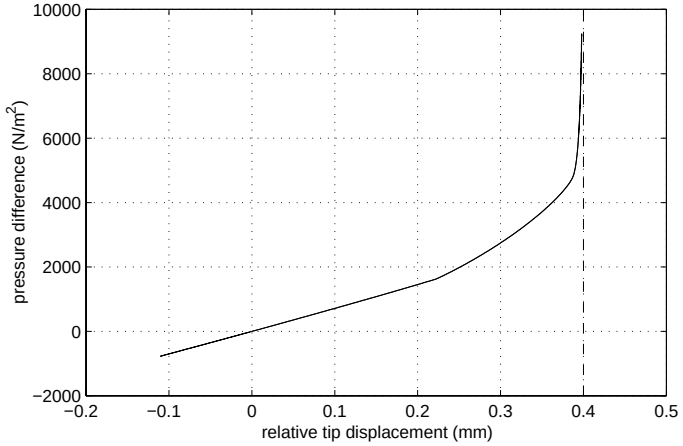


Figure 10.12: Elastic behaviour of the reed/mouthpiece system, as measured from the quasi-static simulation. The dashed line indicates the relative position of the mouthpiece tip.

tem, the inertia properties of the reed may be considered as of secondary importance to the elastic properties [52]. Hence the elastic properties give us a good first approximation of the behaviour of the reed/mouthpiece system. In the literature, the elasticity of the reed/mouthpiece system is often referred to in terms of the equivalent *stiffness per unit area*[7] (see, e.g., [140, 144, 22]). This quantity indicates how much pressure difference is required to achieve a certain (relative) displacement of the reed tip:

$$\Delta p = K_{ae} \left( y_L - y_0 \right) . \tag{10.32}$$

In figure 10.12, $\Delta p$ is plotted against $(y_L - y_0)$. As may be expected, the elasticity behaviour of the reed/mouthpiece system is approximately linear for small displacements, and becomes increasingly non-linear as the reed is pushed towards closure.

### 10.2.6 Comparison with Previously Developed Models

Numerical simulations of a distributed model of the reed/mouthpiece system have been developed in two earlier studies [140, 137]. The main differences in comparison with the numerical model presented in the present study are:

- In [140, 137], the viscoelastic friction within the reed is not considered, and the damping observed in experiments with the reed is taken into account by setting the fluid damping to a certain value such that the simulation exhibits the appropriate damping at the resonance frequency of the reed/mouthpiece system. Since fluid damping is practically frequency-independent, this results in underdamping of the higher frequencies.

- The numerical formulation in [140, 137] corresponds to using a $\theta$-scheme with $\theta = 1/2$. As seen in section 10.2.2, this results in significantly larger warping effects than with $\theta = 1/4$. Furthermore, the simulations in [140, 137] use $\Delta x = 1$mm, which corresponds to a much lower spatial resolution than that is used in the present study (200 sections, which corresponds to $\Delta x = 0.17$mm).

- In [140], the sample rate is $f_s = 400$kHz, whereas in [137] a sample rate of $f_s = 48$kHz is reported. In the present study it was found that with $N = 200$, a sample rate $f_s = 200$kHz gives sufficiently accurate results.

- In [140, 137], the effective thickness $b(x)$ of the reed was approximated with a linear function, whereas in the present study a fourth-order polynomial was used. It was not

[7] In [101], the elastic properties are referred to in terms of the reed *compliance*, which is the inverse of the stiffness per unit area.

tested here whether the use of a more the more precise fourth-order approximation results in a significant improved simulation accuracy.

- In [140, 137], it is assumed that the lay is flat up to a certain point, and that the remaining part of the lay is well approximated with a parabolic function. For this reason, it was assumed that it is sufficient to model only the motion of that part of the reed that curls up to the curved part of the lay. However, the measurements on various clarinet mouthpieces carried out in the present study indicate that the lay starts to curve from a point much closer to the clamping point. Therefore, our model includes all parts of the reed that are not clamped by the ligature.

- In [140, 137], collisions between the reed and the mouthpiece are simulated by simply stopping any reed section from moving any further than the position of the mouthpiece. That is, if a section of the reed collides with the mouthpiece, that section is held at its position for as long as the reed tends to move into the mouthpiece. In other words, a "stop" is *imposed* on that reed section. It can be easily shown that this method causes *immediate* accelerations to neighbouring reed sections that are not in contact with the mouthpiece. Since these immediate accelerations can not be caused by lip or shear forces[8], they must considered as artificial (i.e., contact-forces are applied to reed sections that are not in contact with the mouthpiece). The collision model presented in section 10.2.3 is based on conditional contact-forces, and by definition does not exhibit such artificial accelerations.

## 10.3 An Equivalent Lumped Model

In this section we explore the possibility of modelling the mechanical behaviour of the reed as a driven harmonic oscillator. The main assumption on which this approach is based is that the reed/mouthpiece system is well characterised by its first mode of vibration, and driven below the frequency of that mode [17, 144, 22, 81]. From a mechanical point of view, a harmonic oscillator corresponds to an ideal mass-spring-damper system driven by a certain force, for which the displacement of the mass is governed by a second-order differential equation (see appendix F). In application to the reed/mouthpiece system, this model describes only the motion of the reed tip ($y_L$), i.e., it is a *lumped* model of the reed:

$$M_e \frac{d^2 y_L}{dt^2} + R_e \frac{dy_L}{dt} + K_e(y_L - y_0) = F_e, \tag{10.33}$$

[8] Shear forces travel through the reed at a finite speed, and can not travel from one section to another in zero time.

where $M_e$, $R_e$, $K_e$ and $F_e$ are the equivalent mass, damping, stiffness, and driving force, respectively, and $y_0$ is the equilibrium position of the reed tip. The driving force is defined as the product of the equivalent driving surface and the pressure difference across the reed:

$$F_e = S_e \cdot \Delta p. \tag{10.34}$$

Dividing all terms in (10.33) by $M_e$ yields the reduced form of equation (10.1):

$$\frac{d^2 y_L}{dt^2} + g_e \frac{dy_L}{dt} + \omega_e^2 (y_L - y_0) = \frac{\Delta p}{\mu_e}, \tag{10.35}$$

where

$$\omega_e = \sqrt{\frac{K_e}{M_e}}, \quad g_e = \frac{R_e}{M_e}, \quad \mu_e = \frac{M_e}{S_e}. \tag{10.36}$$

Furthermore, the reed motion produces a certain volume flow. In the equivalent oscillator model, this flow is computed

$$U_{re} = S_r \cdot \frac{dy_L}{dt}. \tag{10.37}$$

Because the reed curls up against the mouthpiece lay as it moves towards closure, the parameters $M_e$, $R_e$, $K_e$, $S_e$ and $S_r$ continuously change during oscillation. Hence if (10.33) is to be used for realistic simulation of sound generation in reed woodwinds, the variation of these parameters over time has to be established.

Gazengel [55] has shown that the variation of the lumped model parameters can be derived from a distributed model of the reed/mouthpiece system. However, the distributed model used in this study is rather theoretical. Firstly, both the shape of the mouthpiece as well as the shape of the reed that was used in the calculations were only rough approximations to their real geometries. Secondly, it is assumed that the role of the lip is no more than effectively clamping the reed at some point along the mouthpiece lay. Such a model cannot explicitly take into account some of the properties of the lip, such as damping and stiffness. Thirdly, the geometry of a real woodwind mouthpiece is such that when the player's lip presses the reed against the lay, potential energy is stored in the "immobilised part" of the reed (see figure 10.13). The effective stiffness of the reed/mouthpiece system is not independent from this potential energy. In comparison, the numerical simulation presented in section 10.2 represents a more accurate distributed model. Hence it can be expected that an improved estimation of the parameters of the equivalent lumped model can be obtained by applying Gazengel's method to results computed with the numerical simulation.

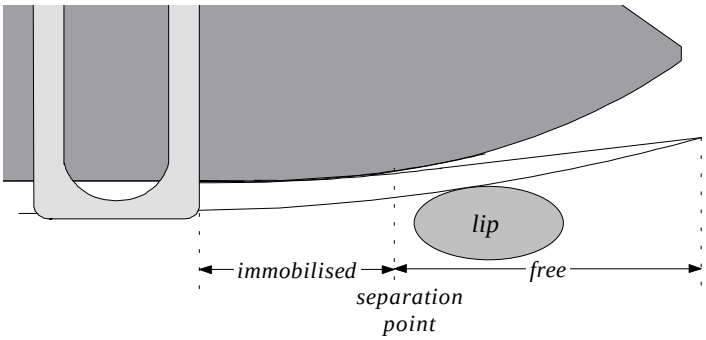


Figure 10.13: The reed mouthpiece system with the reed in rest position. The separation point defines the part of the reed that can freely vibrate. The remaining part of the reed is effectively immobilised, though potential energy is stored there.

### 10.3.1 Principles of the Parameter Determination

The parameter determination method in [55] is mainly based on the assumption that at each time instant, the harmonic oscillator has the same potential and kinetic energy as does the distributed model. This approach is similar to Rayleigh's method for determining the eigenfrequencies of a beam under flexure as explained in [116], and has been applied previously for the determination of the first resonance of an organ reed [143] and a clarinet reed [57]. While the reed was assumed to have the form of a straight bar in [143, 57], Gazengel [55] also provided results for a wedge-shaped bar. In the case of a numerical model, the method can easily be applied to the general case of a bar with varying thickness. Given a displacement $y(x,t)$ and velocity $v(x,t) = \partial y/\partial t(x,t)$, the potential and kinetic energy of a reed modelled as a non-uniform bar are [98]:

$$E_{pr} = \frac{1}{2} \int_0^L Y\, I(x) \left( \frac{\partial^2 y}{\partial x^2}(x,t) \right)^2 dx, \tag{10.38a}$$

$$E_k = \frac{1}{2} \int_0^L \rho\, A(x)\, (v(x,t))^2 \, dx. \tag{10.38b}$$

However, due to the action of the lip and the mouthpiece, the equilibrium position of the reed is such that (10.38) does not properly express the potential energy of the reed/mouthpiece system. For this reason, we follow the suggestion by Avanzini [12] to define the potential energy of the reed/mouthpiece system such that action of the lip and mouthpiece are included:

$$E_p = E_{pr} + E_{lip} + E_{lay} - E_{p0}, \tag{10.39}$$

where $E_{p0}$ is defined such that the potential energy is zero at $y_L = y_0$:

$$E_{p0} = \left[E_{pr} + E_{lip} + E_{lay}\right]_{y_L = y_0} . \tag{10.40}$$

The potential energies due to the lip and mouthpiece action are:

$$E_{lip} = \frac{1}{2} K_{lip} \int_0^L \Delta y_{lip}^2(x,t)\, dx, \tag{10.41a}$$

$$E_{lay} = \frac{1}{2} K_{lay} \int_0^L \Delta y_{lay}^2(x,t)\, dx, \tag{10.41b}$$

where

$$\Delta y_{lip}(x,t) = \begin{cases} y(x,t) - b(x) - y_{lip}(x), & \text{if} \quad y(x,t) < y_{lip}(x) + b(x) \\ 0, & otherwise \end{cases} . \tag{10.42}$$

and

$$\Delta y_{lay}(x,t) = \begin{cases} y(x,t) - y_{lay}(x), & \text{if} \quad y(x,t) > y_{lay}(x) \\ 0, & otherwise \end{cases} . \tag{10.43}$$

The potential and kinetic energy of the equivalent lumped model are:

$$E_{pe} = \frac{1}{2} K_e \, (y_L - y_0) , \tag{10.44a}$$

$$E_{ke} = \frac{1}{2} M_e \, v_L^2. \tag{10.44b}$$

The equivalent stiffness and mass are computed as the stiffness and mass for which $E_p = E_{pe}$ and $E_k = E_{ke}$:

$$K_e = \frac{2\, E_p}{(y_L - y_0)^2}, \tag{10.45a}$$

$$M_e = \frac{2\, E_k}{v_L^2}. \tag{10.45b}$$

The equivalent driving surface is determined from the static case, where we have:

$$K_e \, (y_L - y_0) = \Delta p \, S_e . \tag{10.46}$$

It follows that

$$S_e = \frac{K_e}{K_{ae}}, \tag{10.47}$$

where $K_{ae}$ is the equivalent stiffness per unit area (see (10.32)). As seen in section 10.2.5, we can "measure" $K_{ae}$ directly from the quasi-static simulation. The volume flow produced

by the reed moving with velocity $v(x,t)$ is:

$$U_r = w \int_0^L v(x,t)\, dx. \tag{10.48}$$

Combining with (10.37) gives the equivalent flow surface, which is the surface for which $U_{re} = U_r$:

$$S_r = \frac{U_r}{v_L}. \tag{10.49}$$

In [55], no method for determination of the equivalent damping is given. Instead, this parameter is assumed to be constant during oscillation. We will follow this approach, except for small reed openings (see section 10.3.3).

### 10.3.2 Dynamic versus Static Deformation

Gazengel's method for parameter determination is based on the assumption that the deformation of the reed is the same for the dynamic case as it is for the static case. The main advantage of this approach is that there is a one-to-one relation between the deformation state and tip displacement, which means that the equivalent lumped model parameters can be determined as a unique function of $y_L$. Note that there is a "jump" in the separation point, which corresponds to a part of the reed closer to the reed tip touching the lay before the part just next to it (on the instrument side) has fully curled up to the lay (see figure 10.15). We used our numerical simulation of a clarinet reed/mouthpiece system to

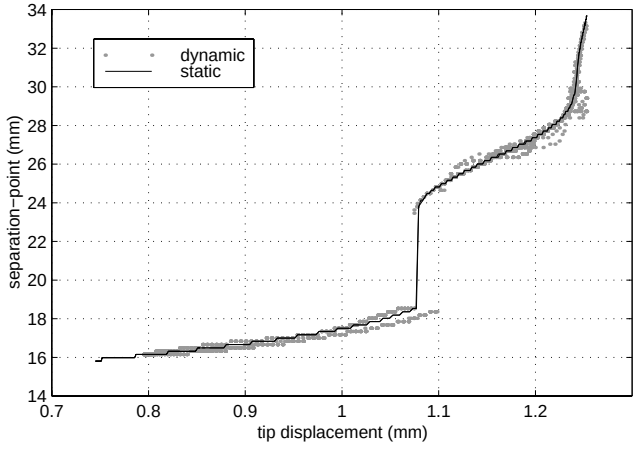


Figure 10.14: Separation point versus tip displacement.

verify whether this is a reasonable assumption. This was done measuring the *separation point* (i.e., the first point of contact between the lay and the reed, as seen from the reed tip), as a function of tip displacement, using first a static and then a dynamic simulation. We may expect that there is a strong correlation between the separation point and the

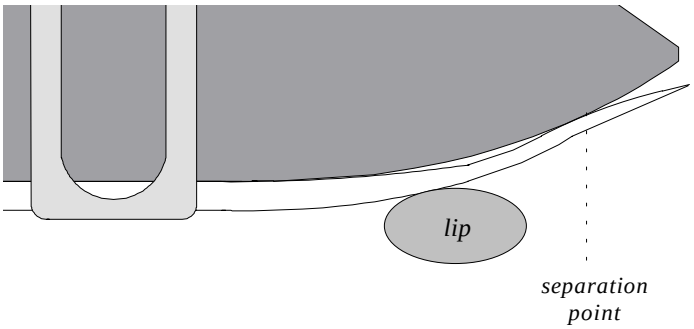


Figure 10.15: Case in which the reed does not smoothly curl up to the mouthpiece, which corresponds to a jump in the separation point.

lumped model parameters, because the separation point defines the part of the reed that can move freely. In the dynamic simulation, the reed was driven by a sinusoidal pressure difference at a frequency $f_d = 200$Hz, while in the static simulation a linear increasing scale of pressure differences was applied. Figure 10.14 compares the resulting separation point versus tip displacement.

Around this discontinuity, the dynamic simulation exhibits a form of hysteresis. However, the deviation from the static curve is generally quite small. We found similar results for frequencies up to 1500Hz, although the hysteresis effect does increase somewhat with frequency. Since the signal that drives the clarinet reed usually has a lowpass character with a cut-off of about 1500Hz, it may be concluded that there is generally only a small difference between the dynamic and static deformation of the reed[9].

### 10.3.3 Parameter Determination with the Quasi-Static Simulation

For estimation of the equivalent parameters, a *quasi-static* simulation is used. The main reason for using a quasi-static rather than the intuitively more correct dynamic simulation is that hysteresis effects are avoided. The use of the quasi-static case is based on two assumptions:

- The reed deformation is approximately the same in the quasi-static case as in the dynamic case. This assumption has been analysed in section 10.3.2.
- The equivalent parameters are independent of frequency. This assumption is likely to hold if it may be assumed that the higher modes of the reed are strongly damped. The observations made in the experiments described in section 10.2.4 confirm this.

[9] In [65], it is argued that hysteresis in the forces on the reed (although due to a hydrodynamic rather than a mechanical phenomenon) may explain particular features of reed behaviour. This subject is, however, considered to be beyond the scope of the present study.

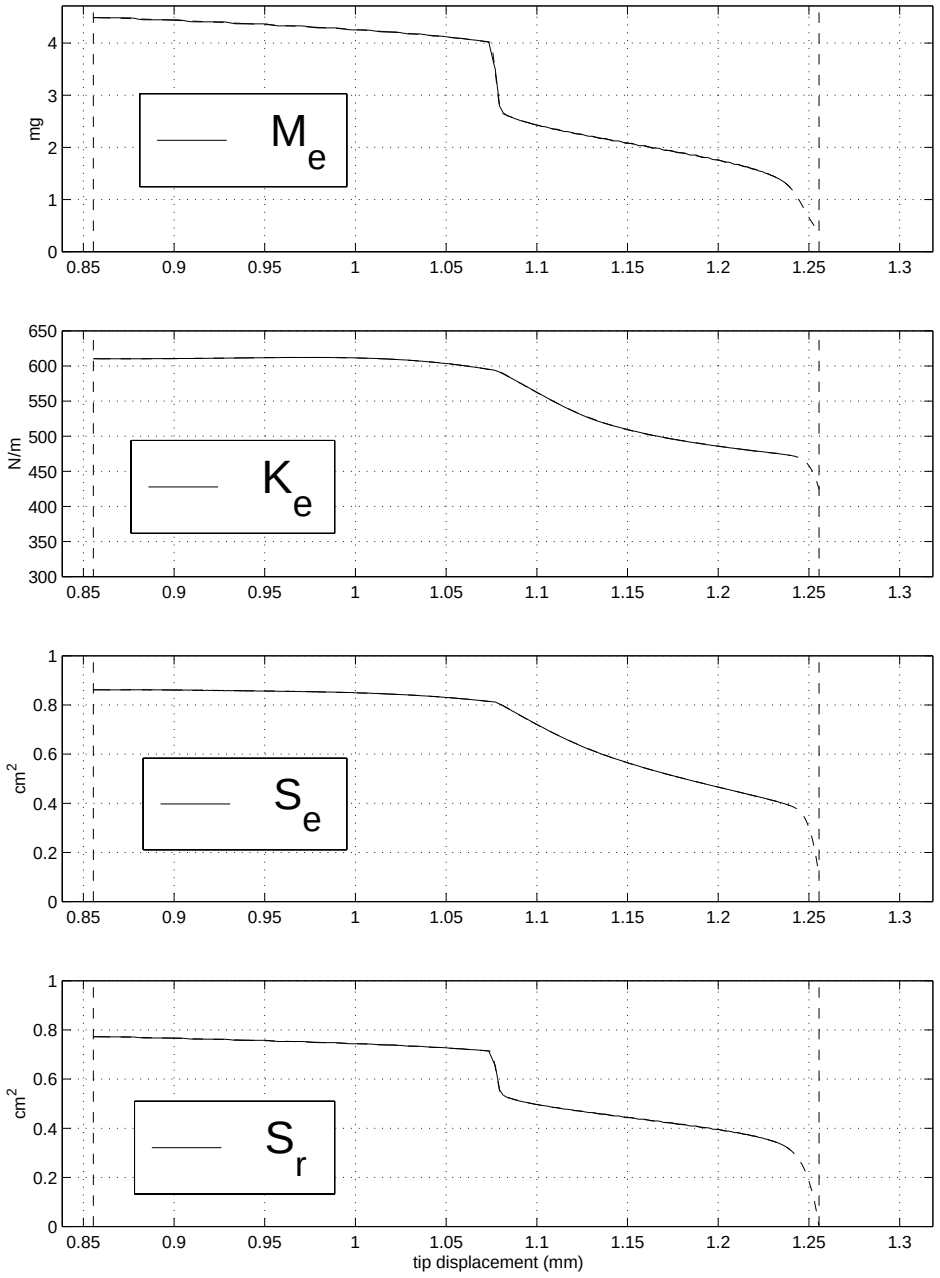


Figure 10.16: Parameters of the equivalent lumped model of a clarinet reed/mouthpiece system as a function of reed tip displacement. The straight, vertical dashed line on the left side of each plot indicates the equilibrium $y_L = y_0$, and the straight, vertical dashed line on the right side of each plot indicates the mouthpiece position at the reed tip $y_L = y_{lay}(L)$. The dashed part of each parameter curve indicates the extrapolation of the data towards a "logical" value, as explained in the text.

The method works as follows. First, one period of a sinusoidal driving pressure difference is created in discrete-time form[10]. The sampled values of this pressure difference signal are then applied in successive steps to the numerical simulation as a constant force, where in each simulation step the system is run for a sufficiently high number of samples $N_{qs}$ such that all oscillations decay before $t = N_{qs}T$. For each pressure difference $(\Delta p)^m$, the following quantities are traced:

- the reed deformation $y_i^m$. From this we can deduce the discrete-time velocities $(\delta y/\delta t)_i^m$ of the reed sections, which are required to compute the kinetic energy with a numerical version of (10.38) and the volume flow with a numerical version of (10.48). We also deduce the "reed-bend" $(\delta^2 y/\delta x^2)_i^m$, which is required to compute the potential energy of the reed with a discrete version of (10.38). Furthermore, the reed tip displacement $(y_L)^m$ at the reed tip is used to compute the equivalent stiffness per unit area with (10.32).

- the lip compression $\Delta(y_{lip})_i^m$ and the mouthpiece contact compression $\Delta(y_{lay})_i^m$, which are required to compute the lip and mouthpiece potential energy with discrete versions of equations (10.41).

The sinusoidal driving pressure difference varied between $-770\,\mathrm{N/m^2}$ and $+9230\,\mathrm{N/m^2}$, and the driving frequency was $f_d = 200\,\mathrm{Hz}$. The variation over time of the parameters $M_e$, $K_e$, $S_e$ and $S_r$ was estimated this way, using the formulae presented in (10.3.1). In some cases these computations result in a division in which both numerator and denominator are very close to zero. This can lead to numerical problems that result in inaccuracies in the parameter determination. This turned out to be especially problematic with calculating the equivalent stiffness for small deflections. Therefore, we compute the stiffness with a method that cross-fades between the results obtained by direct division $E_p/(y_L - y_0)^2$ and the steepness of a linear fit to the data $[(y_L - y_0)^2, E_p]$ in the region where $(y_L - y_0)$ is close to zero. The same method was applied to compute the equivalent stiffness per unit area. For the remaining parameters ($M_e$, $g_e$, $S_e$ and $S_r$), numerical problems only occurred for very small tip velocities. Therefore, no data was obtained directly for very small openings, but instead we extrapolated the obtained data in a logical manner. That is, the driving and flow surfaces are assumed to go to zero for $y_L = y_0$. To avoid division by zero, $S_e$ was set to a very small positive value at closure. Using (10.47), we can then deduce the equivalent stiffness for small openings. How the equivalent mass varies near closure is less obvious. Intuitively, one is led to assume that $M_e$ goes towards zero as the

[10] Note that the sample rate $f_s^*$ of this signal may be chosen independently from the sample rate $f_s$ of the quasi-static simulation. Increasing $f_s^*$ results in a higher number of estimation points. It was found that, with applying a driving frequency $f_d = 200\,\mathrm{Hz}$, using $f_s^* = f_s = 200\,\mathrm{kHz}$ gives a sufficient number of estimation points. The time-index of the driving signal is indicated with $m$.

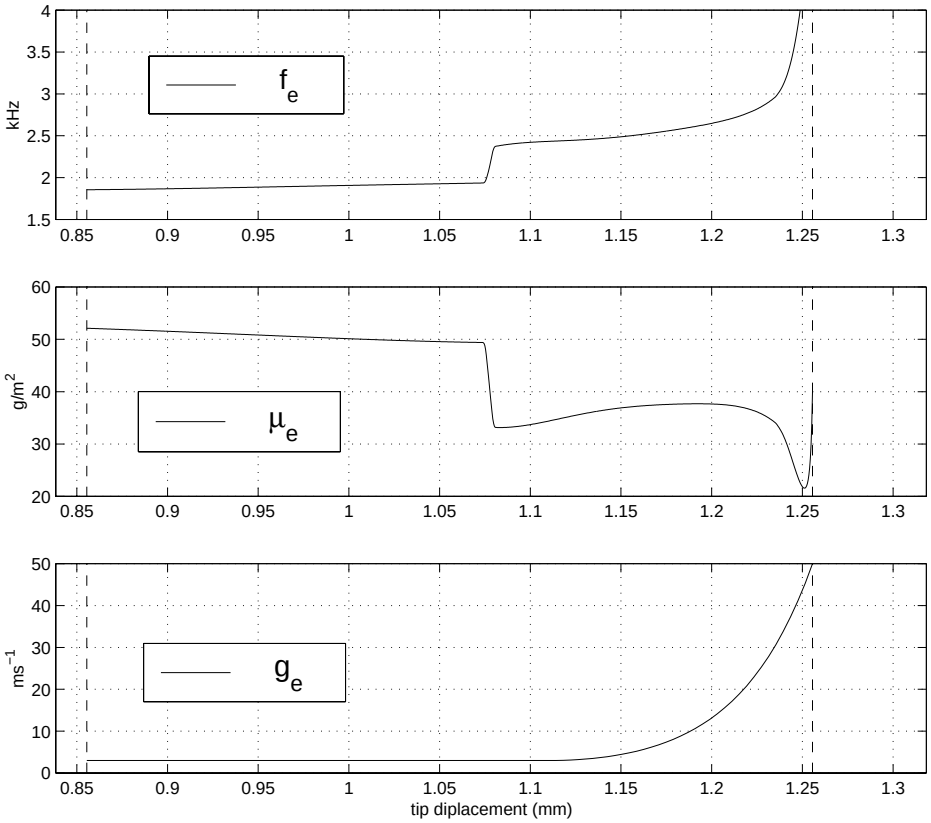


Figure 10.17: Parameters of the reduced equation of the equivalent lumped model, as a function of tip displacement. $f_e$ is the resonance frequency, $\mu_e$ is the mass per unit area and $g_e$ is the damping factor.

reed moves towards full closure. However, it was found that using an infinitely small mass leads to instability problems in the final lumped model. Therefore we extrapolated the mass towards a small positive value at $y_L = y_0$. Figure 10.16 shows the resulting estimated parameters as a function of reed tip displacement. The corresponding parameters $f_e$ $g_e$ and $\mu_e$ of the reduced equation are plotted versus tip displacement in figure 10.17. Note that the damping factor $g_e$ was not derived from the distributed model. It was found empirically that in order for the lumped model to be stable, the damping needs to increase strongly for small reed openings. The damping was therefore held constant up to a certain displacement $y_L = y_c$, while for larger displacements the damping was set to increase with displacement according to a *cosh* function.

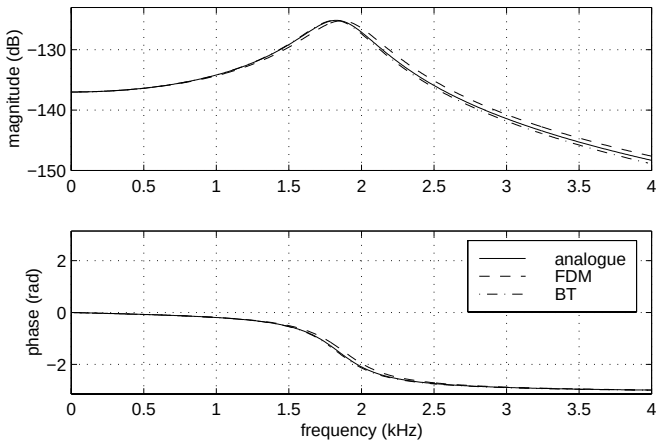


Figure 10.18: Discrete-time approximation of the reed response, using 44.1 kHz sample rate.

### 10.3.4 Numerical Formulation

For discrete-time simulation of the equivalent lumped oscillator, a numerical formulation of (10.35) has to be found. To simplify this task, we rewrite (10.35) as:

$$\frac{d^2y}{dt^2}(t) + g_e(t)\,\frac{dy}{dt}(t) + \omega_e^2(t)\,y(t) = \frac{\Delta p(t)}{\mu_e(t)}, \tag{10.50}$$

where $y(t) = y_L(t) - y_0$ is the relative tip displacement. A numerical formulation of (10.50) is relatively straightforward in the case of constant parameters. In appendix F, three different methods for discretisation are compared. In the case of simulating an oscillating reed, emphasis should be put on accuracy in the lower frequency response, since the reed is driven mainly below its resonance. From the comparisons in figure F.2 it can be seen that the impulse invariance method is therefore the least suitable method. Of the remaining methods, the bilinear transform (BT) more closely approximates the ideal reed response than the finite difference method (FDM) (see figure 10.18). However, the difference equation using the FDM only contains delayed input-terms, which simplifies the final numerical formulation of a complete simulation of a pipe excited with a single reed (see section 10.4), and is therefore preferred. Application of the finite difference scheme in (F.32) yields the difference equation for the equivalent harmonic oscillator:

$$y(n+1) = b_1(n) \cdot \Delta p(n) - a_1(n) \cdot y(n) - a_2(n) \cdot y(n-1). \tag{10.51}$$

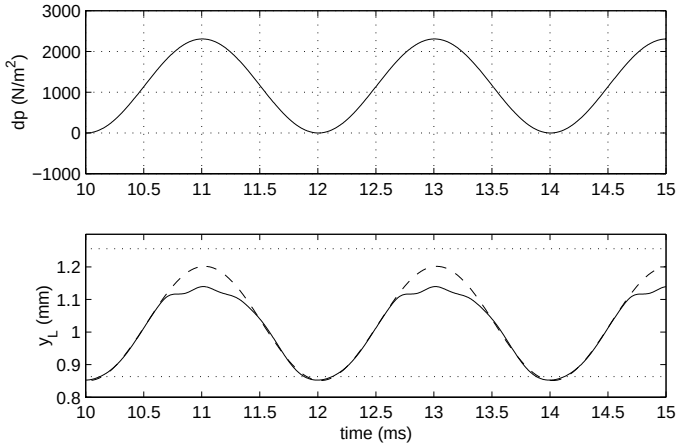


Figure 10.19: Pressure difference signal (top), and the resulting output waveform of reed oscillator model (bottom), using equivalent parameters (solid) and constant parameters (dashed). The vertical dotted lines in the bottom figure indicate the mouthpiece tip position (upper) and equilibrium position (lower). The driving frequency is 500 Hz.

with the coefficients:

$$b_1(n) = \frac{T^2}{\mu(n)}, \tag{10.52a}$$

$$a_1(n) = T^2\,\omega_0^2(n) + T\,g_e(n) - 2, \tag{10.52b}$$

$$a_2(n) = 1 - T\,g_e(n). \tag{10.52c}$$

Note that in order to compute $y$ at time $t = (n+1)T$, the coefficients as known at time $t = nT$ are used. This allows us to simply update the coefficients at each sample with the use of lookup-tables in which the values of the coefficients are stored as a function of $y$.

As discussed in section 10.1.3, a simpler reed model employs a harmonic oscillator with constant parameters, while reed beating is simulated by imposing a stop when the reed aperture becomes negative. Such a model behaves as a linear oscillator as long as the reed does not fully close. In contrast, the equivalent lumped model starts to behave in a non-linear way at much smaller reed displacements. This is demonstrated in figure 10.19, in which the simple model is compared to the equivalent lumped model. The coefficients of the simple model were set at the values of the equivalent lumped model at equilibrium.

### 10.3.5 Comparison with the Distributed model

In order to test if the behaviour of the lumped model approximates that of the distributed model, various comparisons were made. Firstly, the pressure difference as depicted in figure 10.19 was also applied to the distributed model. The resulting tip motion and reed-induced volume flow are compared with the those obtained with the lumped model

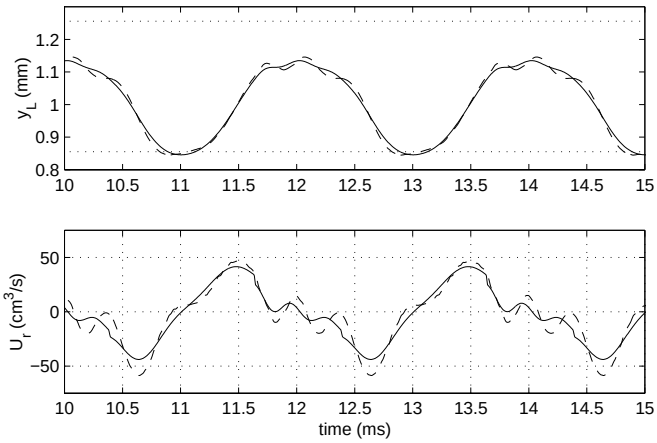


Figure 10.20: Reed tip motion (top) and reed-induced flow (bottom) of the distributed model (solid) and the lumped model (dashed).

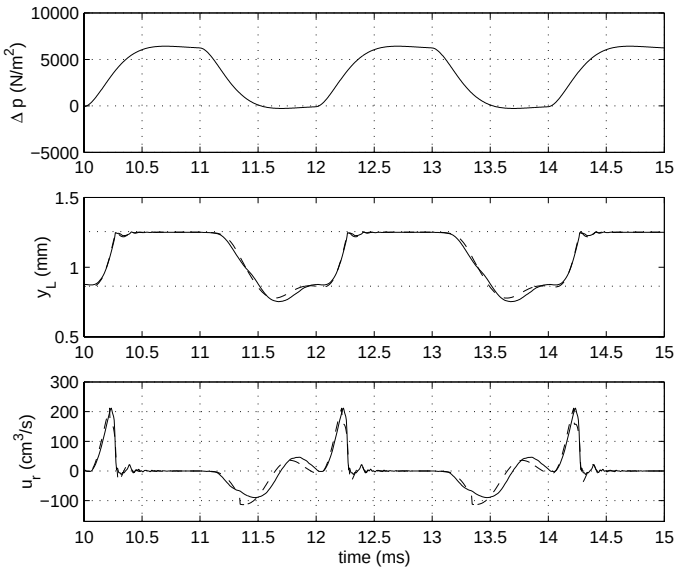


Figure 10.21: Pressure difference (top) and the corresponding reed motion (middle) and reed-induced volume flow (bottom), as computed with the distributed model (solid) and the lumped model (dashed).

in figure 10.20.

Apparently, the lumped model approximates the distributed model, though the waveforms differ slightly. These differences can be explained in terms of different damping behaviour, i.e., the "extra oscillations" that occur at the jump in separation point tend to be somewhat less damped in the lumped model. The fact that the damping behaviour deviates somewhat is not surprising, given that the damping as a function of $y_L$ was imposed rather than derived.

Secondly, a different driving signal, that more resembles the kind of pressure difference signal in a clarinet under playing conditions, was applied. This driving signal was generated by lowpass filtering a square wave, and the amplitude was chosen such that the reed exhibits beating behaviour. Figure 10.21 shows the resulting reed motion and volume flow. Apparently the equivalent lumped model also approximates the distributed model quite well in the case of a signal that contains several frequency components, such as the clarinet-like signal used in this example. Hence the term "equivalent" appears largely justified.

## 10.4 Pipe Excitation

In this section, we apply the non-linear lumped oscillator model in a simulation of a pipe excited with a clarinet reed. The main objective is to investigate the effect of the extra non-linearity on the behaviour of the reed/pipe system.

### 10.4.1 Modelling the Pipe

A 40cm long pipe with a radius of 6.5mm, was modelled in the discrete-time domain using the techniques described in chapter 4. Forward and backward-propagation through the pipe is modelled with a delay-line in cascade with two filters, and the open-end reflectance is approximated with a digital filter (see figure 10.22). The loss-filter and the open-end reflectance filter are fifth-order IIR filters, and model the boundary and radiation losses, respectively. The fractional delay filter (FD) is a third-order FIR Lagrange interpolation filter.

### 10.4.2 Numerical Formulation of the Coupled System

The pipe model computes the response $p^-(t)$ to an in-going pressure wave $p^+(t)$. At time $t$, these waves are related to the pressure and the volume flow by:

$$p(t) = p^+(t) + p^-(t), \tag{10.53a}$$

$$Z_0\, u(t) = p^+(t) - p^-(t), \tag{10.53b}$$

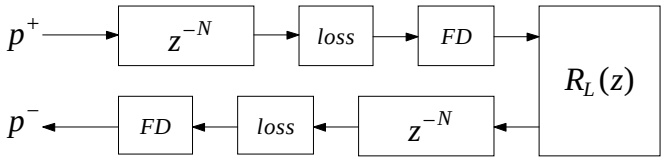


Figure 10.22: Discrete-time model of the cylindrical pipe.

where $Z_0$ is the characteristic impedance of the pipe. These equations couple the pipe system to the reed excitation system. The complete system can be solved at discrete-time instants $t = (nT)$ as follows. Given a pressure difference $\Delta p(n)$, the reed displacement $y(n+1)$ is computed with (10.51). Next, the reed-induced flow is approximated with:

$$u_r(n+1) = S_r \left[\frac{y(n+1) - y(n)}{T}\right]. \tag{10.54}$$

By combining (10.7), (10.53) and (10.2), we obtain a single non-linear equation for the flow $u_f(n+1)$:

$$D_1 \cdot Sgn \cdot u_f^2(n+1) + D_2 \cdot u_f(n+1) + D_3 = 0, \tag{10.55}$$

where at each time instant, $D_1$, $D_2$ and $D_3$ are temporarily considered as constants[11]:

$$D_1 = \frac{\rho}{2\,[w\,h(n+1)]^2}, \tag{10.56a}$$

$$D_1 = Z_0, \tag{10.56b}$$

$$D_3 = 2p^-(n+1) - p_m(n+1) + Z_0\,u_r(n+1), \tag{10.56c}$$

where $h(n+1) = max(H - y(n+1), 0)$ is the reed aperture. The value of the returning wave $p^-(n+1)$ is known because it is simply the next value stored in the delay-line. Equation (10.55) is solved using the Newton-Rhapson method. The function for which the root is solved is monotonic under all circumstances, thus there always is a single, unique solution to (10.55). Using the last solution (i.e., $u_f(n)$) as the initial value for the iteration, it was found that nine iterations is typically sufficient for an accurate solution of the non-linear equation. The new volume flow $u(n+1) = u_f(n+1) + u_r(n+1)$ into the instrument is now known, and is used to calculate the next in-going wave using (10.53):

$$p^+(n+1) = p^-(n+1) + Z_0\,u(n+1). \tag{10.57}$$

[11] For the purpose of solving (10.55), we may temporarily consider $D_1$, $D_2$ and $D_3$ as constants because within the numerical formulation, the variables $p_m(n+1)$, $u_r(n+1)$ and $h(n+1)$ do not depend on $u_f(n+1)$.

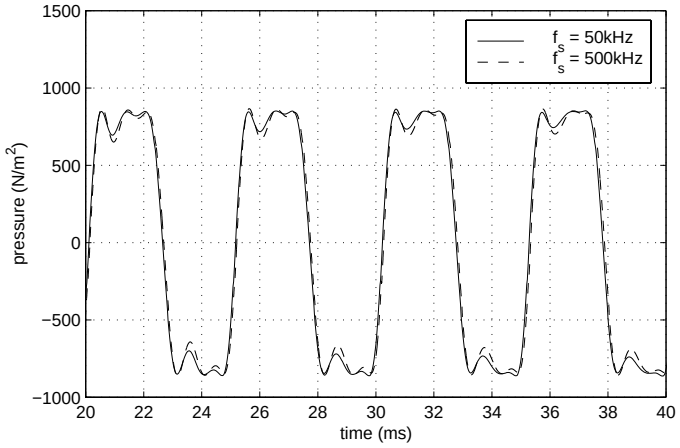


Figure 10.23: Mouthpiece pressure calculated with the reed/pipe simulation. The mouth pressure was constant ($p_m = 1100\ \mathrm{N\,m^{-2}}$).

Finally, the new mouthpiece pressure and pressure difference are computed:

$$p(n+1) = p^+(n+1) + p^-(n+1), \tag{10.58a}$$

$$\Delta p(n+1) = p_0(n+1) - p(n+1). \tag{10.58b}$$

Equations (10.54), (10.55), (10.56), (10.57) and (10.58), in combination with (10.51) and (10.52) form the set of equations from which each variable is solved sample by sample. Note that the system is computable without having added a fictitious delay to the system. As pointed out by Avanzini and Rochesso [13], such a fictitious delay is sometime used in order to avoid a delay-free loop in the system (for example in [124, 54]). The key to avoiding a fictitious delay in this case is the use of a reed oscillator difference equation (equation (10.51)) in which only delayed input-terms are used. This is not the case for all methods for discretisation of the harmonic oscillator (see appendix F). It is for this reason that the finite difference method is preferred above the bilinear transform. As seen in figure 10.18, this leads to a small discretisation error, especially concerning the resonance frequency of the digital reed oscillator. Since sustained oscillations in the reed/pipe system are at frequencies below the reed resonance, it can be argued that this discretisation error is of minor importance to the behaviour of the system. This was tested by comparing the pressure waveforms generated with two different sample rates. In general, the difference between a digital model and its continuous-time counterpart converges towards zero with increasing sample rate. It was found that using a sample rate higher than $f_s = 500\mathrm{kHz}$ hardly leads to any differences in the waveform. Therefore, the waveform produced using $f_s = 500\mathrm{kHz}$ was taken as the "true" result. Figure 10.23 compares this waveform with the waveform produced with using $f_s = 50\mathrm{kHz}$.

A more general solution for avoiding fictitious delays is achieved with the use of the

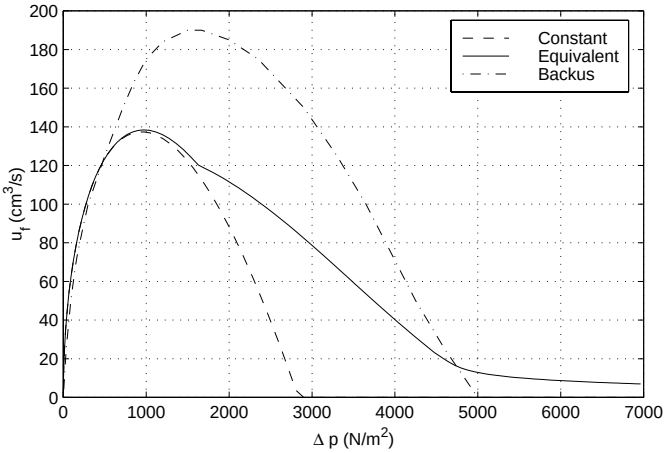


Figure 10.24: Volume flow versus pressure difference, as calculated with the lumped model, using constant parameters (dashed) and equivalent parameters (solid). The third curve (dash-dot) is from Worman [167] based on Backus' experimental results.

so-called "$K$-method" [31], which was applied to a clarinet simulation in [13, 14]. This method is independent of the choice of discretisation method.

### 10.4.3 System Properties

The digital simulation of the reed/pipe system using the non-linear lumped oscillator model allows us to test various of its properties. Here we are particularly interested in two specific features. Firstly, we analyse the flow versus pressure difference behaviour. This gives us some initial clues about the basic properties such as threshold pressure [22]. Secondly, we compute the spectral evolution of the mouthpiece pressure waveform for an increasing mouth pressure. This gives us insight in the influence of the mechanical non-linearity of the reed/mouthpiece system on the timbre of the sound produced by the reed/pipe system.

Flow versus Pressure Difference

The flow versus pressure difference curve is usually obtained by measuring or calculating the amount of flow through the reed channel under static conditions (i.e., there is no reed oscillation), for a range of pressure differences. The relation between pressure difference and flow obtained this way also holds for quasi-static conditions (i.e., when the reed is assumed to move exactly in phase with the pressure difference) [65]. Figure 10.24 compares three different flow vs. pressure difference curves. The shape of the curve depends heavily on the stiffness of the reed employed [140]. This explains why the computed curves are below Backus' experimental curve: Backus used a normal (non-humid) cane reed, which is much stiffer than the plastic-coated reed that was simulated in the lumped model.

It could therefore be argued that the computed curves more realistically indicate the system behaviour under playing conditions. However, the shape of the curves also strongly depends on the interaction with the lip and the mouthpiece. Hence there is by no means a "definitive" curve, but rather a set of curves that depend on the player's embouchure as well as on the mouthpiece lay shape.

Perhaps more interesting is to compare the "constant-parameter" curve (obtained using the parameters set to the values of the equivalent lumped model at equilibrium) with the "equivalent-parameter" curve. The curve maxima are very close, thus it can be expected that the values of the threshold pressure differences (which lie closely near the maxima, on the right side [140]) are very similar. On the other hand, the pressure difference at which the reed fully closes (at $u_f = 0$) is much larger in the case of using equivalent parameters. In other words, with using the equivalent parameters, there is a much wider mouth pressure range for which sustained oscillations are produced with the reed/pipe model.

Spectral Evolution

The inclusion of the effects of reed curling in the reed/pipe model has a strong influence on the spectral evolution of the mouthpiece pressure. Figure 10.25 depicts the spectogram of the mouthpiece pressure computed using equivalent parameters (i.e. displacement-dependent parameters). In this example, the mouth pressure was linearly increased from 1100 to 2000 $\mathrm{N\,m^{-2}}$, after a short period of constant mouth pressure. There is clearly a gradual rise of higher harmonics during the period of increasing mouth pressure, i.e., the spectral content is controlled by the mouth pressure. Because the spectrum of the sound radiated from the instrument is related to the mouthpiece pressure via a simple transfer function [26], this means that the player is able to change the timbre by blowing softer (producing a "mellow" tone) or harder (producing a "bright" tone). We note that apart from the timbre, also the pitch and the overall amplitude of the sound increase with mouth pressure.

If constant parameters are used (i.e. the parameters are held constant at the values they have at equilibrium), the spectral evolution is rather different (see figure 10.26)[12]. The most striking characteristic of the spectogram displayed in figure 10.26 is that it does not show much change after the reed has started beating (at about $t = 0.8$s). That is, before this point in time, the number of harmonics that are involved in the sound generation process is rising, whereas after this point, the harmonic content more or less stays the same. On the other hand, the spectogram in figure 10.25 shows an increasing

[12] In the generation of the spectogram figures, the colours are automatically normalised in order to show the maximum contrast. Thus a particular level of grey in figure 10.25 does not necessarily indicate the same amplitude as the same level of grey in figure 10.26.

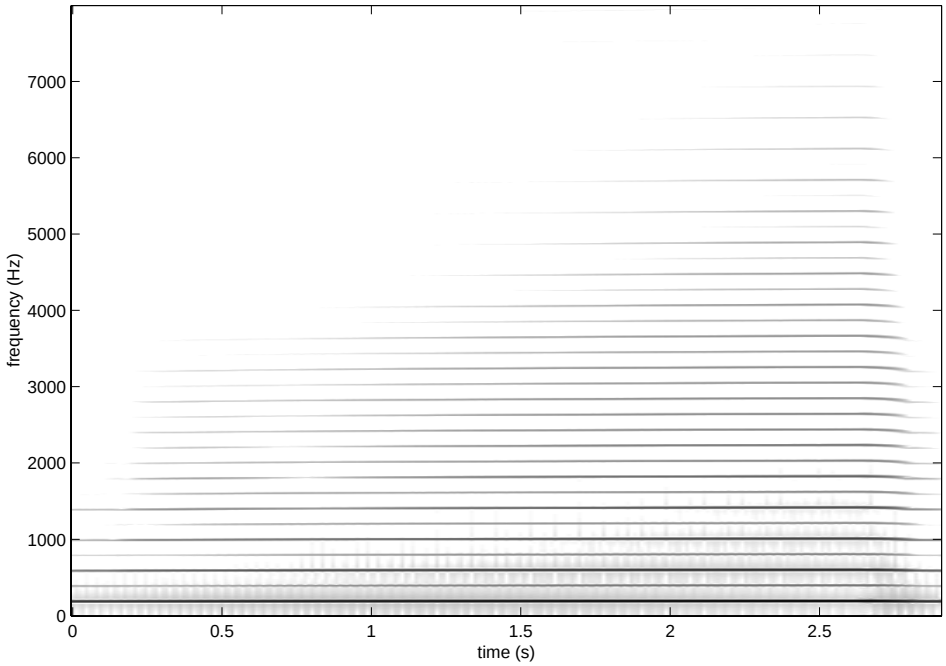


Figure 10.25: Spectogram of the mouthpiece pressure, as computed with the reed/pipe system, using equivalent parameters. The blowing pressure was linearly increased from $1100\mathrm{N\,m^{-2}}$ at $t = 0.2\mathrm{s}$ to $2000\mathrm{N\,m^{-2}}$ at $t = 2.7\mathrm{s}$. The sample rate is 176.4kHz.

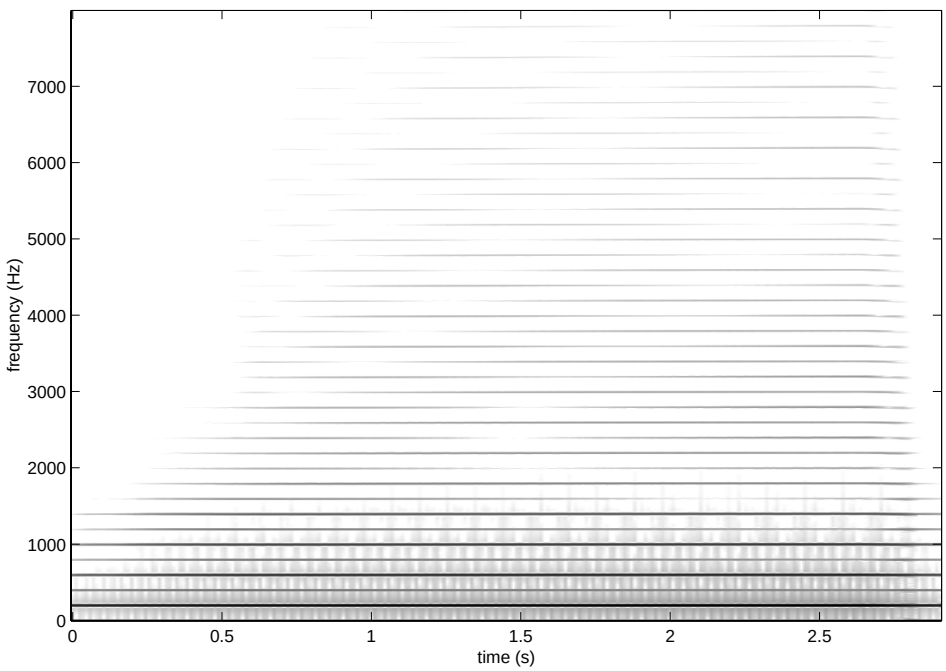


Figure 10.26: Spectogram of the mouthpiece pressure, as computed with the reed/pipe system, using constant parameters. The blowing pressure was varied in the same way as for the example in figure 10.25. The sample rate is 176.4kHz.

number of harmonics over the total time period of increasing mouth pressure. Hence the two cases (using constant or using equivalent parameters) result in significantly different spectral evolutions of the mouth pressure.

Using the method of the radiation filter, which was expained in section 9.2.3, we can obtain an approximate radiation pressure signal from the simulation. The four time-domain signals that were computed with the reed-excited pipe simulation (the mouthpiece pressure signals obtained with constant as well as with equivalent parameters, and the radiation pressure signals obtained with constant as well as with equivalent) can also be judged by ear[13].

## 10.5 Conclusions and Future Work

In this chapter we have discussed single reed excitation, with emphasis on the mechanical behaviour of the reed/mouthpiece system. We have developed a distributed model of the reed/mouthpiece system that is formulated numerically using finite difference methods, and for which the simulation parameters can be determined via experiments. Various improvements were made in comparison with previously developed models, particularly with respect to discretisation issues and methods for modelling the mouthpiece and lip interaction. Simple tests with the simulation have shown that it behaves similarly to what has been (qualitatively) observed in artificial blowing experiments. It is important to note that the properties of the system strongly depend on various parameters, most notably those related to mouthpiece design, reed type and embouchure. Hence the results presented in this chapter by no means form a representative set for all possible cases. Investigating the model for a more wide variety of parameter sets could be the subject of future research. Moreover, further experiments are still required in order to provide a more thorough verification of how well the model describes the behaviour of a real clarinet reed/mouthpiece system. For example, it would be interesting to investigate whether the "separation-point jumps", as discussed in section 10.3.2 can be observed in experiments. We envisage that such experiments will be carried out using a setup in which the reed (clamped to the mouthpiece) is driven by a horn driver, similar to the experiments with the artificial lip setup employed in the brass instrument research by Cullen et al. [40, 41].

In section 10.3, we have seen that an equivalent lumped oscillator model of the reed/mouthpiece system is possible, for which the parameters are determined using the distributed model. Although this parameter determination is based on a quasi-static simulation, the resulting equivalent lumped model closely approximates the dynamic behaviour of the distributed model.

Furthermore, we have shown that an accurate discrete-time simulation of a pipe excited

[13] Sound examples **(ex9)**, **(ex10)**, **(ex11)** and **(ex12)** in appendix K.

by a clarinet reed is possible, without the use of a fictitious delay. Various properties of this system were discussed, and comparisons were made between using a linear (using constant parameters) and a non-linear (using equivalent parameters) lumped model of the reed. The nature of the differences observed are such that Thomson's suggestion that these differences "can be thought of as perturbations" [144] is questionable.

There are interesting implications with respect to musical sound synthesis. It was found that for the non-linear reed model, the mouth pressure range in which sustained oscillations are possible is much wider. Varying the mouth pressure within this range corresponds to changing the amplitude of the higher harmonics in the mouthpiece pressure signal and the radiated sound. This is a feature that is typically aimed for in the context of sound synthesis via physical modelling: it allows for a simple and intuitive, though "natural" control of the sound timbre.

Future work other than that already mentioned is envisaged in two directions. Firstly, it is theoretically possible that also the damping parameter of the lumped model is derived using the distributed model. Our first attempts in this direction indicate that this should be done using a dynamic rather than a quasi-static simulation. Secondly, the distributed model can be extended towards modelling the flow though the reed. Combined with the insights provided by recent research [65, 57, 67, 64, 82] this could lead to an improved understanding of the non-linear oscillations in single reed woodwind instruments. Furthermore, this would allow us to derive all parameters (including those related to the flow) of the elementary valve model presented in section 10.1.2 from simulations with a distributed model.

# Chapter 11

# General Conclusions

Methods for time-domain simulation of brass and reed woodwind instruments have been studied in this work. Acoustic theories were reviewed and used as a basis for the derivation of discrete-time models of the differents parts of an instrument. Simplifications and discretisations have been carried out taking into account a number of criteria that are relevant with regard to application in a musical sound synthesis environment.

Throughout the thesis, newly developed methods are presented next to reviews of previously developed methods and theories. The reader might not always be able to distinguish between new and previous work. In order to give an absolutely clear account on this matter, the exact contributions by the author are summarised below.

## 11.1 Summary of Contributions

In chapter 2, viscothermal losses in a conical bore were formulated by means of the integrand method. This method was shown to be more accurate than the conventional "means-radius method". Further contributions include a piecewise model comparison, which showed that flaring bores can be modelled accurately using a piecewise conical series approximation as long as no large wavefront cross-section mismatch arises at the boundary.

In chapter 3, we have formulated the wave digital modelling approach that combines digital waveguide modelling techniques with wave digital filter techniques. This approach offers distinct advantages over previously developed techniques. In particular, the approach allows for efficient implementation of lumped acoustic elements, which is a subject that was not adequately covered previously in the context travelling-wave based simulation of wind instruments. In addition, we have formulated a new method for modelling the bore response via convolution with the reflection function. This "full reflection method" does not rely on any assumptions about the dimensions of the bore, whereas the conventional

reflection function method assumes a non-tapered bore entry.

In chapter 4, a one-filter formulation of a junction of two conical bore sections was presented. This formulation is more efficient than those given in previous work. A comparison between the various available methods for discretisation of the junction filter showed that the bilinear transform and the continuous-time interpolation method result in extremely similar structures. Furthermore, the chapter includes an investigation into the effects of modelling conical bore systems using a lossless formulation of the propagation constant in the junctions while using a lossy version in the formulation of the propagation in each bore section. It was found that this simplification (1) diminishes the height of the low-frequency input impedance peaks, (2) causes the impulse response to be divergent, and (3) affects the effective length of the bore at low frequencies. The most important part of this chapter is the investigation into the conditions under which a travelling-wave based digital simulation of a conical bore system remains stable. A series of simulations indicate that stability is maintained only in cases where viscothermal losses are excluded. Furthermore, it was found that under certain conditions, the simulation can be run for a considerable amount of time without exhibiting any significant unwanted signal growth. Because most musical wind instrument bore configurations are such that these conditions are fulfilled, this feature allows for the computation of the (truncated) system impulse response. In this part of the work, aim (4) outlined in section 1.3 is fulfilled only in part; future research in this area seems warranted.

In chapter 5, a lumped element model of a partially open tonehole was formulated. This model allows dynamic control of the tonehole state, and closely approximates established tonehole theory at low frequencies. Discretisation was carried out by means of wave digital modelling techniques. A six-hole flute application demonstrated that the errors due to simplifications and discretisation are extremely small at low frequencies. Further contributions include the formulation of an efficient method for discrete-time modelling of the sound radiated from a tonehole. The modelling approach taken here completely fulfils aim (1) outlined in section 1.3.

In chapter 6, the simulation of the wave scattering at a junction of two conical bore sections by means of a junction model that is derived via WDF tecniques was presented. This model is mathematically equivalent to the junction model presented in section 4.3.2, but is more efficient. More importantly, it can be adapted for modelling a conical section in series with a lumped acoustic element; this enables the derivation of realisable structures for discrete-time modelling of conical bore woodwinds. The last part of the chapter consists of a detailed comparison between the wave digital modelling approach and the multi convolution approach. This comparison revealed that, with respect to modelling the open-end reflectance and the inclusion of viscothermal losses, a better balance between accuracy and efficiency can be obtained with the wave digital modelling approach.

In chapter 7, we combined pulse reflectometry measurements with piecewise-modelling based bore reconstruction techniques for the experimental determination of a bell reflectance. Furthermore, minimum-phase reconstruction techniques were used for the calculation of the bell transmittance, which allowed for an effective and numerically robust design of an IIR filter approximation. The main body of this chapter describes the application and design of one-pole TIIR filter elements in a digital approximation of a brass bell reflectance. It was demonstrated that this approach results in an extremely efficient approximation of the growing portion of the bell reflectance, while the decaying tail of the reflection function may be modelled with a lower-order IIR filter. In cases where accuracy is a high priority, it is advisable to model the growing portion of the reflection function with an FIR filter. This part of the work fulfils aim (3) outlined in in section 1.3.

In chapter 8, pulse reflectometry and input impedance measurement techniques were used in experimental determination of the acoustical function of the mouthpiece. These measurements were used for validation of theoretical models of a trumpet and a clarinet mouthpiece. The trumpet mouthpiece was simulated in discrete-time by means of a wave digital volume (that represents the mouthpiece cup) and a conical bore model (that represents the backbore). This model, which is also directly applicable to simulation of various other brass mouthpieces, exhibits the approximately correct acoustical properties. The clarinet mouthpiece was simulated by means of a model consisting of a conical and a cylindrical bore section, discretised with wave digital modelling techniques. It was shown that this model accurately simulates the acoustical function of the clarinet mouthpiece at low frequencies. Aim (2) in section 1.3 is fulfilled in this chapter.

The elements described in the previous chapters were combined in chapter 9 to formulate simulations of the complete air columns of a trumpet and a clarinet. The simulation parameters were determined by acoustical and geometrical measurements on real instruments. It was demonstrated that both models closely approximated the established acoustic theories at low frequencies. In addition, we presented methods that we argue will give perceptually representative radiation pressure signals.

In chapter 10, we have discussed the single reed excitation mechanism. A distributed model of the clarinet reed is formulated using the finite difference approach. Because of various improvements with respect to discretisation, parameter determination and collision modelling, this model captures the interaction of the reed with the mouthpiece and the lip in a much more precise way than previous models. The distributed model is then used for the derivation of an equivalent lumped oscillator model, in which the parameters of this model are formulated as a function of the reed tip deflection. It was demonstrated that the lumped model closely approximates the behaviour of the distributed model. The properties of a simulation of a pipe driven with the lumped oscillator model were investigated. One of the main conclusions of the work on this subject is that using a lumped oscillator

model with deflection-dependent parameters results in a much smoother dependency of the mouthpiece spectrum on the blowing pressure amplitude than if constant parameters are used. The modelling techniques described in this chapter fulfil aim (5) in section 1.3.

## 11.2 What has not been Modelled

It is important to note that this thesis does not cover all aspects of sound production in brass and reed woodwind instruments. While the techniques presented here provide a suitable basis for modelling brass and reed woodwind instruments, other aspects have been left out for various different reasons.

For full simulation of a brass instrument, a model of excitation by the player's lips is required. As explained in section 1.2, Msallam et al. [100] and Vergez et al. [161] have recently developed lip models which excel in capturing the properties of lip excitation that are most relevant in application to musical sound synthesis. Such a model can for example be used in combination with the trumpet bore model presented in section 9.1 in order to simulate the generation of trumpet tones.

Although a reed excitation model was presented in chapter 10, we have not yet coupled it to a full woodwind bore model. This step would be necessary for a deeper and more specific analysis of the simulation techniques developed in this work. For example, it would be interesting to compare the transient behaviour of a full clarinet simulation to that of a real clarinet. Furthermore, such a full simulation is required for the generation of musical output signals.

Aero-acoustic features have not been considered in this work, but cannot be neglected in the context of realistic simulation of wind instrument tones. With respect to brass instruments, this involves modelling the effects of non-linear wave propagation that occurs at high dynamic playing levels. Methods for including such effects in a travelling-wave based simulation have been published recently [100, 160], and can be directly combined with the techniques presented in the present study.

A realistic simulation of a reed woodwind includes the effects of turbulent flow in the mouthpiece. Such turbulent effects result in noise components in the sound of the instrument and also trigger bifurcations in the oscillation [64].

Other aero-acoustical aspects include the effects of vortex shedding and non-linearities at woodwind toneholes. Since various studies indicate that most wind instruments are designed to minimise such effects (see for example, [74]), it is questionable whether it is essential to include them in a sound synthesis model.

What should also be considered is the influence of the player's windway. Studies by Benade [23] and Hoekje [66] have indicated that the player can cause significant changes in the sound production mechanism by altering the shape of the oral cavity. As shown in

a trumpet simulation by Dietz [45], the player's windway can be modelled with methods similar to those employed for modelling the instrument air column.

Finally, we remark that any simulation requires a controller interface. For generation of steady-state tones, it is usually sufficient to simply update the parameters off-line, but in real-time applications the parameters are usually updated in a quasi-continuous fashion, which requires a much more sophisticated and extensive form of interfacing. Such an application offers the type of possibilities for exploration of the sonoric features of the model that are typically desirable from a musical point of view.

## 11.3 Suggestions for Future Work

Numerous suggestions for future work have already been made in sections 5.4, 7.5, 8.3, 9.3 and 10.5. In this section we elaborate on the modelling aspects and improvements that we consider as most urgently needed.

### Tonehole Modelling

As explained in section 5.4, the wave digital tonehole model could possibly be improved by (1) explicitly modelling the negative inertances, and (2) the inclusion of a resistive element in its shunt impedance. The latter of these is vital from the point of view of modelling a register hole, because its acoustical function is partly to provide *damping* at the lowest resonance frequency [22].

Although the inclusion of a resistive element might look straightforward at first sight, there is in fact a serious complication. As can be seen from equation (5.2), the resistance of a side branch is in fact to a first approximation proportional to the square of the frequency. A straightforward approach would be to derive a wave digital tonehole from this impedance expression. Unfortunately, the reflection function associated with this side branch impedance formulation is an exponentially growing function of time. Hence the side branch impedance expression would first have to be adapted such that it becomes suitable for application in the time-domain.

### Radiation Pressure

As explained in section 9.3, the high-frequency inaccuracies of the radiation pressure obtained from a wave digital model can possibly be compensated for by a single filter. Such a compensation filter would have to be designed to approximate the transfer function between the calculated radiation pressure and the actual radiation pressure. The actual radiation pressure can be either measured or predicted by means of a precise and complex model that takes into account the influences of the higher modes and the directivity

effects. Note that in principle such a transfer function would have to be determined for each listening point, although in practice it is probably sufficient to use a finite set of grid-points and interpolate between the corresponding transfer functions.

Aero-Acoustical Aspects in Reed Woodwinds

As explained by Hirschberg et al. [64], realistic simulation of a reed-driven instrument requires taking into account various aero-acoustical aspects of the volume flow through the reed channel. In particular, the turbulent effects associated with the free jet that is formed in the reed channel are important since they cause significant dissipation and supply noise components to the radiated sound of the instrument. Moreover, due to the unstable nature of the free jet it is very difficult to predict how the flow through the channel relates to the mouthpiece pressure, the mouth pressure, and the reed opening. Dynamic measurements have been carried out by Gilbert [57], but this did not result in reliable data for small reed openings. As explained by Hirschberg et al. this lack of data precludes the formulation of a realistic model, since the reed *closure* is essential with regard to the generation of higher harmonics in the radiated spectrum. An interesting direction for future research would therefore be to obtain such data using (1) improved dynamic measurement techniques or (2) simulation with a highly precise numerical fluid dynamical simulation. With respect to the second option, a systematic approach would be to couple such a fluid dynamical model with a distributed model of the reed/mouthpiece system such as the one presented in section 10.2.

Stability of Conical Bore Systems

The discrete-time models presented in the present study can be used for the simulation of musical bores without inclusion of viscothermal losses in any of the conical sections. It was demonstrated in section 9.2 that the conical sections in the main bore of a clarinet may be replaced with cylindrical, while excluding loss-filters from the remaining conical sections in the model, without introducing any significant errors. However, it remains to be seen whether such an approach would lead to accurate simulation of wind instruments that have an essentially conical main bore, such as the saxophone or the oboe. A more satisfactory solution would be to first develop new methods that enable stable simulation of conical bore systems *with* inclusion of propagation losses. The results presented in section 4.4 indicate that an essential requirement for a conical bore system to be stable is that the junctions are modelled using the same formulation of the propagation constant as is used in the modelling of the propagation in tubular sections. Hence a possible appropiate direction for future research on this subject is to develop methods for simulation of wave scattering using a junction model that is formulated using a lossy propagation constant.

# Appendix A

# Thermodynamic Constants

Throughout the thesis, unless mentioned differently, the gas thermodynamic constants that are used in the computations are taken from the consistent set of gas parameters for air at standard pressure, as used by Benade [21] and Keefe [75] (see table A.1). This set is valid for temperatures in the range $290^o$–$310^o$K. Here $\rho$ is the air density, $c$ is the wave velocity, $\eta$ is the viscosity coefficient, $\nu$ is the square root of the Prandtl number, and $\gamma$ is the ratio of specific heats. See [21, 75, 35] for further explanation of these constants. The truncated expansion formulae for the transmission-line parameters of a cylindrical duct with taking into account viscothermal losses, as formulated by Keefe [75] are given

| |
|---|
| $\rho = 1.1769 \cdot (1 - 0.00335\Delta\mathcal{T})\,\mathrm{Kg\ m^{-}3}$ |
| $\eta = 1.846 \cdot 10^{-5}(1 + 0.0025\Delta\mathcal{T})\mathrm{Kg\ s^{-1}\ m^{-1}}$ |
| $\gamma = 1.4017(1 - 0.00002\Delta\mathcal{T})$ |
| $\nu = 0.8410(1 - 0.00002\Delta\mathcal{T})$ |
| $c = 3.4723 \cdot 10^{2}(1 - 0.00166\Delta\mathcal{T})\,\mathrm{m\,s^{-1}}$ |

Table A.1: Thermodynamic constants. All the values are evaluated at $\mathcal{T}_0 = 26.85^o$C $(300^oK)$, and are accurate within $\pm 10^o$C of that temperature. The temperature difference relative to $\mathcal{T}_0$ is $\Delta\mathcal{T}$. After Keefe [75].

in equations (2.57). The coefficients in these expansions are:

$$d_1 = \frac{1}{\sqrt{2}}\left[1-\psi\right], \tag{A.1a}$$

$$d_2 = \left[1-\psi+\frac{\psi}{2\nu}+\frac{3\psi^2}{2}\right], \tag{A.1b}$$

$$d_3 = \frac{1}{\sqrt{2}}\left[\frac{7}{8}-\psi+\frac{\psi}{2\nu}+\frac{\psi}{8\nu^2}+\frac{3\psi^2}{2}-\frac{3\psi^2}{2\nu}-\frac{5\psi^3}{2}\right], \tag{A.1c}$$

and

$$e_1 = \frac{1}{\sqrt{2}}\left[1+\psi\right], \tag{A.2a}$$

$$e_2 = \left[1+\psi-\frac{\psi}{2\nu}-\frac{\psi^2}{2}\right], \tag{A.2b}$$

$$e_3 = \frac{1}{\sqrt{2}}\left[\frac{7}{8}+\psi-\frac{\psi}{2\nu}-\frac{\psi}{8\nu^2}-\frac{\psi^2}{2}+\frac{\psi^2}{2\nu}+\frac{\psi^3}{2}\right], \tag{A.2c}$$

with

$$\psi = \frac{\gamma-1}{\nu}. \tag{A.3}$$

# Appendix B

# Coordinate Systems

In the present study, references are made to different coordinate systems in which to calculate the motion of waves in air. This appendix forms a brief description of the relevant coordinate systems. A more detailed explanation can be found in [84, 98].

## B.1 Cartesian Coordinates

The Laplacian operator for Cartesian coordinates $(x, y, z)$ is:

$$\nabla^2 = \frac{\partial^2}{\partial x^2} + \frac{\partial^2}{\partial y^2} + \frac{\partial^2}{\partial z^2}. \tag{B.1}$$

## B.2 Cylindrical Coordinates

Figure B.2 depicts a cylindrical bore and its associated cylindrical coordinates. The polar cylindrical coordinates $(a, \phi, x)$ are related to the Cartesian coordinates by:

$$x = x, \tag{B.2a}$$

$$y = a\, sin(\phi), \tag{B.2b}$$

$$z = a\, cos(\phi). \tag{B.2c}$$

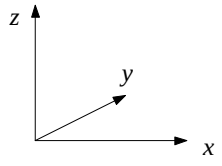


Figure B.1: The Cartesian coordinate system.

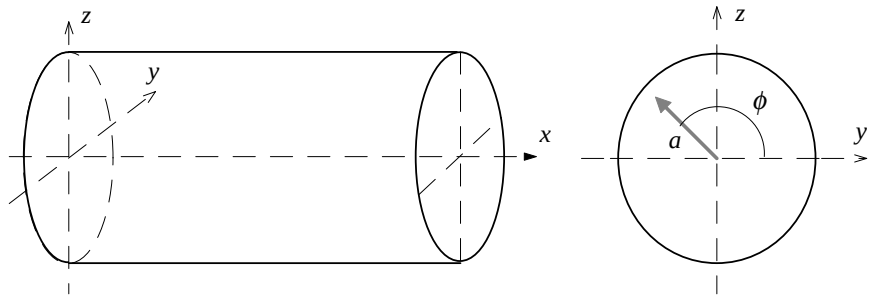


Figure B.2: A cylindrical bore and its associated cylindrical coordinates.

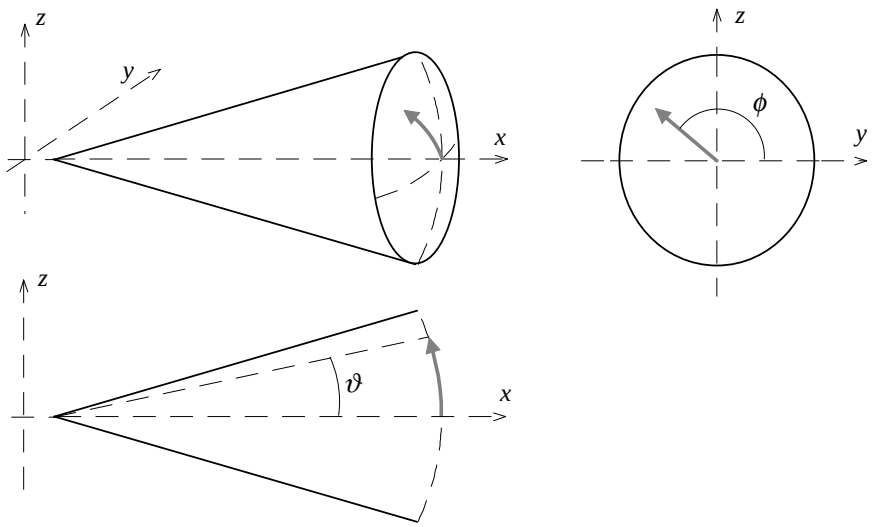


Figure B.3: A conical bore and its associated spherical coordinates.

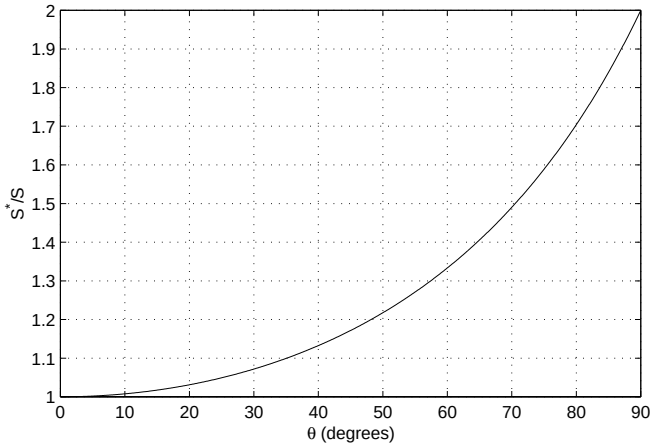


Figure B.4: Ratio of spherical and planar wavefront areas as a function of angle of conicity.

The Laplacian operator for cylindrical coordinates is [98]:

$$\nabla^2 = \frac{1}{a}\frac{\partial}{\partial a}\left(a\,\frac{\partial}{\partial a}\right) + \frac{1}{a^2}\,\frac{\partial^2}{\partial \phi^2} + \frac{\partial^2}{\partial x^2}. \tag{B.3}$$

## B.3 Spherical Coordinates

Figure B.3 depicts a conical tube and its associated spherical coordinates. The spherical coordinates $(r, \phi, \vartheta)$ are related to the Cartesian coordinates by:

$$x = r\,cos(\vartheta), \tag{B.4a}$$

$$y = r\,sin(\vartheta)\,cos(\phi), \tag{B.4b}$$

$$z = a\,sin(\vartheta)\,sin(\phi). \tag{B.4c}$$

The Laplacian operator for spherical coordinates is [98]:

$$\nabla^2 = \frac{1}{r^2}\frac{\partial}{\partial r}\left(r^2\,\frac{\partial}{\partial r}\right) + \frac{1}{r^2\,sin(\vartheta)}\,\frac{\partial}{\partial \vartheta}\left(sin\vartheta\,\frac{\partial}{\partial \vartheta}\right) + \frac{1}{r^2\,sin^2(\vartheta)}\frac{\partial^2}{\partial \phi^2}. \tag{B.5}$$

The surface area of a spherical wavefront in a cone, located a distance $r$ from the cone apex, is [25, 119];

$$\begin{aligned} S^*(r) &= 2\,\pi\,r^2\,(1 - cos(\theta)) \\ &= 2\,\pi a^2\,\left(\frac{1 - cos(\theta)}{sin^2\theta}\right), \end{aligned} \tag{B.6}$$

where $\theta$ is the angle of conicity. Figure B.4 shows the ratio $S^*/S$ as function of $\theta$, where $S = \pi a^2$.

# Appendix C

# The Effective Length of an Acoustic System

The bell and mouthpiece of a brass instrument are frequency-dispersive devices [90]. The effect of dispersion in tubes is classically expressed in terms of *effective length*, which is defined by Long [90] as:

> *"the physical length that would be required to account for the transit time if the wave velocity were assumed standard velocity"*

This length was determined at resonance frequencies, following a procedure to find the closed-end cylinder that resonates at exactly the same frequency at the corresponding harmonic, assuming plane wavefronts and lossless wave propagation. With this procedure, the effective length is only defined at maxima of the input impedance.

Pyle [110] generalised the concept of effective length to all frequencies by defining it in terms of the reflectance rather than input impedance. Losses due to viscothermal damping and open-end radiation are not taken into account by Pyle, which ensures that the effective length is real-valued.

More recently, the concept of effective length was further generalised by Ayers [15], who defined two versions of "complex effective length" as the complex-valued length of the cylinder (either with open or closed end) having the same reflectance as the object of which we are defining the effective length. The "closed-end" effective length of a certain acoustical object (e.g., a horn or a mouthpiece) is found by equating the object reflectance $R(\omega)$ to the reflectance of a closed-end cylinder:

$$R(\omega) = e^{-2\Gamma L_c}, \tag{C.1}$$

where $\Gamma$ is the propagation constant. The closed-end effective length thus is:

$$L_c(\omega) = -\frac{1}{2\Gamma} ln\left[R(\omega)\right]. \tag{C.2}$$

In the same way, but starting from $R(\omega) = -e^{-2\Gamma L_c}$, we can derive the "open-end effective length":

$$L_o(\omega) = -\frac{1}{2\Gamma} ln\left[-R(\omega)\right]. \tag{C.3}$$

These effective lengths are complex-valued, and therefore we can not directly compare them with the real physical length of the object. Ayers suggests to plot the real part of these expressions against frequency in order to gain a more intuitive understanding.

We can further simplify the concept if we ignore the effects of viscothermal damping, thus setting $\Gamma = j\omega/c$. Let $\phi(\omega)$ be the phase of $R(\omega)$, then we find:

$$L_c(\omega) = \frac{c}{2\omega}\left[j\, ln\left|R(\omega)\right| - \phi(\omega)\right], \tag{C.4a}$$

$$L_o(\omega) = \frac{c}{2\omega}\left[j\, ln\left|R(\omega)\right| + \pi - \phi(\omega)\right]. \tag{C.4b}$$

The real part of the closed-end formula corresponds to the effective length as defined by Pyle. The closed-end formula is more intuitive when the object in fact indeed has a closed end. For example, this is the case for computing the effective length of a mouthpiece (that is closed at its end under playing conditions). For open-ended horns or bells, the open-end formulation is more practical. Finally, it can be seen easily that the real part of the open- and closed-end formulae are closely related to the *phase delay* of the object reflectance:

$$\Re e\{L_c(\omega)\} = \left(\frac{c}{2}\right)\frac{-\phi(\omega)}{\omega} = \frac{c}{2}\,\tau_p(\omega), \tag{C.5a}$$

$$\Re e\{L_o(\omega)\} = \left(\frac{c}{2}\right)\frac{\pi - \phi(\omega)}{\omega} = \frac{c}{2}\left[\frac{\pi}{\omega} + \tau_p(\omega)\right]. \tag{C.5b}$$

Throughout the thesis, equations (C.5) are used for calculation of the open-end and closed-end effective length.

# Appendix D

# Two-Port Representations of Acoustical Systems

This appendix describes the basic $2 \times 2$ matrix types that are used in the present study to represent acoustic systems as *two-port systems*. The general graphical representation of a two-port system is shown in figure D.1. Any linear acoustic system can be mathematically formulated in this way. We note that the travelling-wave decomposition used here corresponds to assuming plane waves. However, the resulting wave variables do not necessarily correspond to plane waves in a physical sense. For example, pressure waves in conical bores are spherical, but the cone itself may still be mathematically described with a cascade of two-port matrices which are derived using decomposition of the acoustical variables into decomposition into wave variables that are defined in the same way as plane waves (see section 2.3.4). In the frequency-domain, the relation between the variables on one side of the system can be expressed through different type of matrices, which are discussed below.

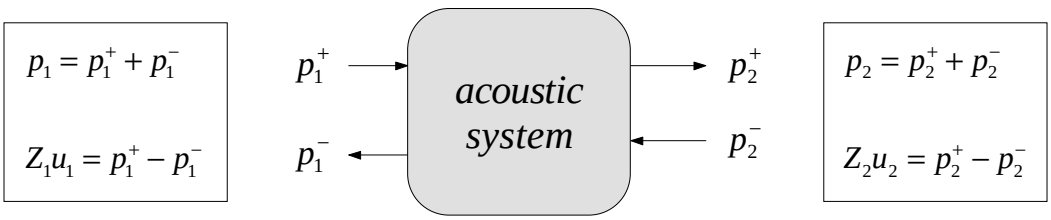


Figure D.1: Generalised representation of a plane wave two-port acoustic system.

## D.1 Matrix Representations

### D.1.1 Transmission-Line Matrix

The transmission-line matrix relates the pressure and volume velocity $(P_1, U_1)$ on the left of the side of the system to the pressure and volume velocity $(P_2, U_2)$ on the right side of the system:

$$\begin{bmatrix} P_1 \\ U_1 \end{bmatrix} = \begin{bmatrix} A & B \\ C & D \end{bmatrix} \begin{bmatrix} P_2 \\ U_2 \end{bmatrix}, \tag{D.1}$$

where $A, B, C, D$ are complex-valued, and frequency-dependent.

### D.1.2 Waveguide Matrix

The waveguide matrix relates the pressure waves $(P_1^+, P_1^-)$ on the left of the side of the system to the pressure waves $(P_2^+, P_2^-)$ on the right side of the system:

$$\begin{bmatrix} P_1^+ \\ P_1^- \end{bmatrix} = \begin{bmatrix} E & F \\ G & H \end{bmatrix} \begin{bmatrix} P_2^+ \\ P_2^- \end{bmatrix}, \tag{D.2}$$

where $E, F, G, H$ are complex-valued, and frequency-dependent.

### D.1.3 Scattering Matrix

The general scattering matrix relates the out-going waves $(P_2^+, P_1^-)$ to the in-coming waves $(P_1^+, P_2^-)$:

$$\begin{bmatrix} P_2^+ \\ P_1^- \end{bmatrix} = \begin{bmatrix} T^+ & R^+ \\ R^- & T^- \end{bmatrix} \begin{bmatrix} P_1^+ \\ P_2^- \end{bmatrix}, \tag{D.3}$$

where $T^+, T^-$ are the transmittances in positive and negative $x$-direction, respectively, and $R^+, R^-$ are the reflectances back into positive and negative $x$-direction, respectively. As in the case of *ABCD*- and *EFGH*-matrices, the elements of the scattering matrix are complex-valued, and a function of frequency.

## D.2 Matrix Transformations

The different matrix types described above all hold exactly the same acoustical information. In many cases, it is desirable to be able to compute one type of matrix from another. In other words, we need to be able to *transform* between the different matrix types. These linear transformations can be worked out using the definition of the plane input- and

output-waves on both sides of the system:

$$P_1 = P_1^+ + P_1^-, \tag{D.4a}$$
$$P_2 = P_2^+ + P_2^-, \tag{D.4b}$$
$$Z_1 U_1 = P_1^+ - P_1^-, \tag{D.4c}$$
$$Z_2 U_2 = P_2^+ - P_2^-. \tag{D.4d}$$

### D.2.1 Transmission-Line Matrix $\leftrightarrow$ Waveguide Matrix

Given a transmission-line matrix with elements $A, B, C, D$, the corresponding waveguide matrix elements are found by substituting (D.4) into (D.1), and solving for $P_1^+, P_1^-$:

$$\begin{aligned} E &= \frac{1}{2}\left(A + \frac{1}{Z_2}B + Z_1 C + \frac{Z_1}{Z_2}D\right), \\ F &= \frac{1}{2}\left(A - \frac{1}{Z_2}B + Z_1 C - \frac{Z_1}{Z_2}D\right), \\ G &= \frac{1}{2}\left(A + \frac{1}{Z_2}B - Z_1 C - \frac{Z_1}{Z_2}D\right), \end{aligned} \tag{D.5}$$
$$H = \frac{1}{2}\left(A - \frac{1}{Z_2}B - Z_1 C + \frac{Z_1}{Z_2}D\right). \tag{D.6}$$

The inverse transformation can be found by combining (D.4) and (D.2), and solving for $P_1, U_1$:

$$\begin{aligned} A &= \frac{1}{2}(E + F + G + H), \\ B &= \frac{1}{2}Z_2(E - F + G - H), \\ C &= \frac{1}{2}\frac{1}{Z_1}(E + F - G - H), \end{aligned} \tag{D.7}$$
$$D = \frac{1}{2}\frac{Z_2}{Z_1}(E - F - G + H). \tag{D.8}$$

### D.2.2 Waveguide Matrix $\leftrightarrow$ Scattering Matrix

Given a waveguide matrix with elements $E, F, G, H$, the corresponding scattering matrix elements are found by simply solving (D.2) for $P_2^+, P_1^-$:

$$\begin{aligned} T^+ &= \frac{1}{E}, \\ R^+ &= -\frac{F}{E}, \qquad \text{(D.9)} \\ R^- &= \frac{G}{E}, \\ T^- &= H - \frac{FG}{E}. \qquad \text{(D.10)} \end{aligned}$$

Vice versa, given a scattering matrix with elements $T^+, R^+, R^-, T^+$, the corresponding waveguide matrix elements are found by solving (D.3) for $P_1^+, P_1^-$:

$$\begin{aligned} E &= \frac{1}{T^+}, \\ F &= -\frac{R^+}{T^+}, \qquad \text{(D.11)} \\ G &= \frac{R^-}{T^+}, \\ H &= T^- - \frac{R^+R^-}{T^+}. \qquad \text{(D.12)} \end{aligned}$$

# Appendix E

# Three-Port Scattering Equations

## E.1 General Three-Port Scattering Junction

Figure E.1a depicts a junction of three acoustic channels, and figure E.1b shows the wave digital modelling scheme for this junction. In the frequency-domain, each pair of wave variables $(P_x^+, P_x^-)$ is related to the acoustical variables $(P_x, U_x)$ as:

$$P_x = P_x^+ + P_x^-, \tag{E.1a}$$

$$R_x U_x = P_x^+ - P_x^-. \tag{E.1b}$$

for $x = a, b, c$, where $(R_a, R_b, R_c)$ are the port-resistances. In the wave digital modelling approach, the port-resistance $R_x$ is set equal to the characteristic impedance $Z_x$ if the acoustic channel $x$ communicates to a distributed system.

According to Kirchoff's laws, the pressure at the junction must be continuous and the

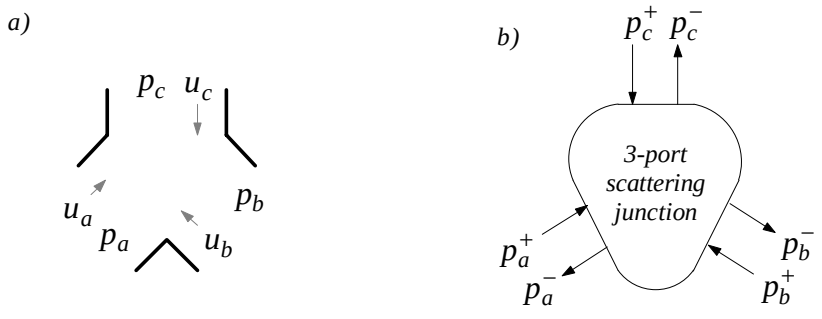


Figure E.1: A junction of three acoustical channels (a), and its three-port wave digital modelling scheme (b). The direction of the flow $U_k$ of each channel $k = a, b, c$ is chosen positive here for a flow going *into* the junction, and negative for a flow going *out of* the junction.

total net flow *into* the junction must be zero:

$$P_a = P_b = P_c, \tag{E.2a}$$

$$U_a + U_b + U_c = 0. \tag{E.2b}$$

If we substitute (E.1), the following set of scattering equations are found:

$$P_a^- = k_a\, P_a^+ + (1 + k_b)\, P_b^+ + (1 + k_c)\, P_c^+, \tag{E.3a}$$

$$P_b^- = (1 + k_a)\, P_a^+ + k_b\, P_b^+ + (1 + k_c)\, P_c^+, \tag{E.3b}$$

$$P_c^- = (1 + k_a)\, P_a^+ + (1 + k_b)\, P_b^+ + k_c\, P_c^+, \tag{E.3c}$$

where the junction reflection coefficients are:

$$k_a = \frac{G_a - G_b - G_c}{G_a + G_b + G_c}, \tag{E.4a}$$

$$k_b = \frac{G_b - G_a - G_c}{G_a + G_b + G_c}, \tag{E.4b}$$

$$k_c = \frac{G_c - G_a - G_b}{G_a + G_b + G_c}, \tag{E.4c}$$

and $G_x = 1/R_x$ is the port-admittance of channel $x$.

## E.2 Branching Junction

In wind instrument modelling, the specific junction in figure E.2a is often encountered, in which an acoustical channel (1) splits up into two branching (channel 2 and 3). In this case, it is convenient to choose the direction of the flow as in figure E.2a. This means that, in comparison with the general three-port junction (figure E.1), the flows for channels 2 and 3 are defined as positive in opposite directions. The corresponding three-port scattering junction is depicted in figure E.2b. The frequency-domain scattering equations for this system are found by substituting:

$$\begin{aligned}
P_a^+ &= P_1^+, \quad P_a^- = P_1^-, \quad G_1 = G_a, \\
P_b^+ &= P_2^-, \quad P_b^- = P_2^+, \quad G_2 = G_b, \\
P_c^+ &= P_3^-, \quad P_c^- = P_3^+, \quad G_3 = G_c.
\end{aligned}$$

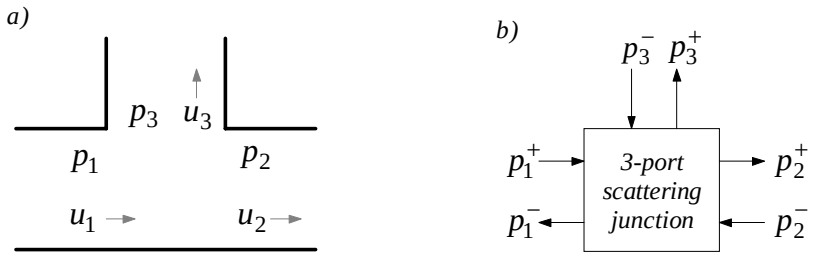


Figure E.2: An acoustical branching junction (a), and its three-port wave digital modelling scheme (b). The direction of flow $u_1$ are chosen positive here when going *into* the junction, and negative when going *out of* the junction. The direction of the flows $u_2$ and and $u_3$ are chosen the other way around, thus positive when going *out* of the junction, and negative when going *into* the junction. This is done for convenience in the context of wave digital modelling of wind instruments.

into (E.3), which yields:

$$P_1^- = k_1 P_1^+ + (1+k_2) P_2^- + (1+k_3) P_3^-, \tag{E.5a}$$
$$P_2^+ = (1+k_1) P_1^+ + k_2 P_2^- + (1+k_3) P_3^-, \tag{E.5b}$$
$$P_3^+ = (1+k_1) P_1^+ + (1+k_2) P_2^- + k_3 P_3^-, \tag{E.5c}$$

where the junction scattering coefficients are defined in the same way as in (E.4):

$$k_1 = \frac{G_1 - G_2 - G_3}{G_1 + G_2 + G_3}, \tag{E.6a}$$
$$k_2 = \frac{G_2 - G_1 - G_3}{G_1 + G_2 + G_3}, \tag{E.6b}$$
$$k_3 = \frac{G_3 - G_1 - G_2}{G_1 + G_2 + G_3}. \tag{E.6c}$$

Often it is convenient to write $k_3$ in terms of $k_1$ and $k_2$:

$$k_3 = -(1 + k_1 + k_2), \tag{E.7}$$

so that the scattering can be computed using only two multiplications:

$$P_1^- = P_2^- + W, \tag{E.8a}$$
$$P_2^+ = P_1^+ + W, \tag{E.8b}$$
$$P_3^+ = P_1^+ + P_2^- + P_3^- + W, \tag{E.8c}$$

with

$$W = k_1 \left[ P_1^+ - P_3^- \right] + k_2 \left[ P_2^- - P_3^- \right] . \tag{E.9}$$

# Appendix F

# Discretisation of the Driven Harmonic Oscillator

Harmonic oscillation can be described as the motion of a mass that is connected to a fixed point, through a spring with damping, and driven by an external force (see figure F.1). In this model, the spring is assumed be massless and linear (with stiffness $K$), and the damping of the spring is entirely represented by a separate element $R$ (resistance). Thus the equation of motion of the mass $M$ is:

$$M\frac{d^2x}{dt^2} + R\frac{dx}{dt} + Kx = f_d, \tag{F.1}$$

where $f_d$ is the driving force and $x$ is the deflection of the mass from its equilibrium position. This is a second-order system, which can be simulated in the discrete-time domain using the difference equation:

$$x(n) = b_0 f(n) + b_1 f(n-1) + b_2 f(n-2) - a_1 x(n-1) - a_2 x(n-2). \tag{F.2}$$

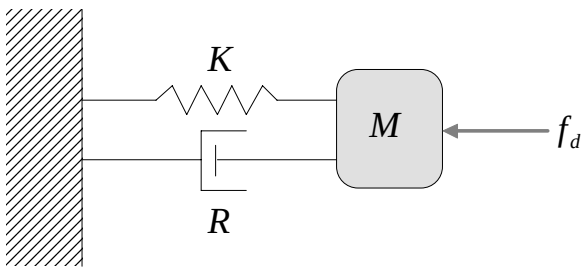


Figure F.1: A harmonic oscillator in the form of a mechanical mass-spring-damper system.

This difference equation corresponds to the second-order digital filter transfer function

$$H(z) = \frac{b_0 + b_1 z^{-1} + b_2 z^{-2}}{1 + a_1 z^{-1} + a_2 z^{-2}}. \tag{F.3}$$

There are several methods for obtaining the filter coefficients $(b_0, b_1, b_2, a_1, a_2)$ available in the literature, each of which has its own discretisation effects. Here we will discuss and compare three different methods of discretisation.

## F.1 Analytic Solutions to the Equation of Motion

### F.1.1 General Time-Domain Solution

The general solution of (F.1) can be found by first solving the equation for $f_d = 0$:

$$\frac{\partial^2 x}{\partial t^2} + \left(\frac{R}{M}\right)\frac{\partial x}{\partial t} + \left(\frac{K}{M}\right)x = \frac{f_d}{M} = 0. \tag{F.4}$$

The characteristic equation of (F.4) is:

$$\lambda^2 + \frac{R}{M}\lambda + \frac{K}{M} = 0. \tag{F.5}$$

with the roots

$$\lambda = \frac{-\frac{R}{M} \pm \sqrt{\left(\frac{R}{M}\right)^2 - \frac{4K}{M}}}{2}. \tag{F.6}$$

In the case where the damping is sufficiently small in relation to the mass and stiffness

$$\left(\frac{R}{2M}\right)^2 < \frac{K}{M}, \tag{F.7}$$

the roots are complex-valued:

$$\lambda = -\alpha \pm j\omega_r, \tag{F.8}$$

where we introduced some new variables:

$$\omega_r = \sqrt{\omega_0^2 - \alpha^2} \quad \text{(angular resonance frequency)}, \tag{F.9a}$$

$$\alpha = \frac{R}{2M} \quad \text{(damping factor)}, \tag{F.9b}$$

$$\omega_0 = \sqrt{\frac{K}{M}} \quad \text{(angular resonance frequency for } R = 0). \tag{F.9c}$$

We can express the complete mathematical solution of (F.4) as:

$$x(t) = C_1 e^{(-\alpha + j\omega_r)t} + C_2 e^{(-\alpha - j\omega_r)t}, \tag{F.10}$$

where $C_1$ and $C_2$ are complex-valued. If we substitute:

$$C_1 = A_1 + jB_1, \tag{F.11a}$$
$$C_2 = A_2 + jB_2, \tag{F.11b}$$

into (F.10), then the complete solution can be written:

$$\begin{aligned} x(t) &= e^{-\alpha t}\left[(A_1 + A_2)cos(\omega_r t) - (B_1 - B_2)sin(\omega_r t)\right] \\ &\quad + je^{-\alpha t}\left[(A_1 - A_2)sin(\omega_r t) - (B_1 + B_2)cos(\omega_r t)\right]. \end{aligned} \tag{F.12}$$

Only the real part of this solution has a physical meaning. We can re-formulate (F.10) such that it represents only all possible real-valued solutions, by setting:

$$A_1 = A_2, \tag{F.13a}$$
$$B_1 = -B_2. \tag{F.13b}$$

It can be shown that the real-valued solution is always a sinusoidal wave, since we can write the real part of (F.10) as:

$$x(t) = C\, e^{-\alpha t} cos(\omega_r t - \phi), \tag{F.14}$$

where

$$C = \sqrt{(A_1 + A_2)^2 + (B_2 - B_1)^2}, \tag{F.15a}$$
$$\phi = tan^{-1}\left(\frac{B_2 - B_1}{A_1 + A_2}\right). \tag{F.15b}$$

The full solution of (F.1) is the sum of the solution of the reduced equation and the specific solution that depends on the driving force. For a driving force with angular frequency $\omega_d$ and amplitude $A_d$, it can be found that the specific solution is:

$$x(t) = D\, cos(\omega t - \psi), \tag{F.16}$$

with

$$D = \frac{A_d}{\sqrt{M^2(\omega_0^2 - \omega^2)^2 + R^2\omega^2}}, \tag{F.17a}$$

$$\psi = tan^{-1}\left(\frac{R\omega}{M(\omega_0^2 - \omega^2)}\right). \tag{F.17b}$$

Hence the full solution of (F.1) for a driving force $f_d(t) = A_d\, cos(\omega t)$ is:

$$x(t) = C\, e^{-\alpha t} cos(\omega_r t - \phi) + D\, cos(\omega t - \psi). \tag{F.18}$$

### F.1.2 Mechanical Impedance

The Laplace transform of (F.1) is:

$$X(s) \cdot \left[s^2 + 2\alpha s + \omega_0^2\right] = \frac{F(s)}{M}. \tag{F.19}$$

Multiplication with $s$ corresponds to differentiation in the time-domain, thus $V(s) = s \cdot X(s)$ represents the velocity of the mass $M$. Hence we can compute the mechanical impedance (the ratio between the force and the velocity):

$$Z(\omega) = \frac{F(s)}{V(s)} = \frac{M}{s}\left(s^2 + 2\alpha s + \omega_0^2\right) = R + j\left(M\omega - \frac{K}{\omega}\right). \tag{F.20}$$

### F.1.3 Filter Interpretation

We can also interpret the harmonic oscillator as an analogue filter with the driving force $f_d$ as the input signal. The transfer function of this filter expresses the ratio between input and output:

$$H(s) = \frac{X(s)}{F(s)} = \frac{1}{s \cdot Z(s)} = \frac{M^{-1}}{s^2 + 2\alpha s + \omega_0^2}. \tag{F.21}$$

We can compute the continuous-time impulse response of the filter by using the inverse Laplace transform:

$$h(t) = \mathcal{L}^{-1}.\left\{\frac{M^{-1}}{s^2 + 2\alpha s + \omega_0^2}\right\} = \left(\frac{e^{-\alpha t}}{M\omega_r}\right) sin(\omega_r t). \tag{F.22}$$

## F.2 Discretisation

### F.2.1 The Impulse-Invariance Method

The impulse invariance method (IIM) is based on *sampling* the filter impulse response. First we write the real-valued continuous-time impulse response in the form of (F.10):

$$h(t) = \left(\frac{e^{-\alpha t}}{M\omega_r}\right) sin(\omega_r t), \tag{F.23a}$$

$$= \frac{-je^{-\alpha t}}{2M\omega_r}\left[cos(\omega_r t) + jsin(\omega_r t) - cos(-\omega_r t) - jsin(-\omega_r t)\right], \tag{F.23b}$$

$$= C_1 e^{(-\alpha+j\omega_r)t} + C_2 e^{(-\alpha-j\omega_r)t}, \tag{F.23c}$$

with

$$C_1 = -C_2 = -\frac{j}{2M\omega_r}. \tag{F.24}$$

Now we sample the response by setting $t = nT$, where $f_s = 1/T$ is the sample rate:

$$h(n) = C_1 e^{(-\alpha+j\omega_r)nT} + C_2 e^{(-\alpha-j\omega_r)nT}. \tag{F.25}$$

The digital transfer function is obtained through the $Z$-transform of (F.25):

$$H(z) = \sum_{n=0}^{\infty}\left[C_1 e^{(-\alpha+j\omega_r)nT} + C_2 e^{(-\alpha-j\omega_r)nT}\right] z^{-n}, \tag{F.26a}$$

$$= C_1 \sum_{n=0}^{\infty}\left(e^{(-\alpha+j\omega_r)T} z^{-1}\right)^n + C_2 \sum_{n=0}^{\infty}\left(e^{(-\alpha-j\omega_r)T} z^{-1}\right)^n. \tag{F.26b}$$

The inner sums in (F.26) convert to a finite value because for $|a| < 1$:

$$\sum_{n=0}^{\infty} a^{-n} = \frac{1}{1-a}. \tag{F.27}$$

So now we can write the response as a parallel combination of two first-order filters:

$$H(z) = \frac{C_1}{1 - \left[e^{(-\alpha+j\omega_r)T}\right] z^{-1}} + \frac{C_2}{1 - \left[e^{(-\alpha-j\omega_r)T}\right] z^{-1}}. \tag{F.28}$$

If we substitute the values for $C_1$ and $C_2$ (equation (F.24)), and put the complete expression under one denominator, the digital transfer function becomes:

$$H(z) = \frac{\left[\left(\frac{e^{-\alpha T}}{M\omega_r}\right) sin(\omega_r T)\right] z^{-1}}{1 - \left[2e^{-\alpha T} cos(\omega_r T)\right] z^{-1} + \left[e^{-2\alpha T}\right] z^{-2}}. \tag{F.29}$$

Since we used the Laplace transform to derive the continuous-time impulse response, and then applied the $Z$-transform to obtain the digital frequency-response, a scaling error has been introduced in the process of discretisation. In order to make sure that we have the proper scaling, it must be taken into account that the $Z$-transform $H(z)$ of the discrete-time signal $h(n) = h_a(nT)$ is related to the Laplace transform ($H_a(s)$) by [109]:

$$H(z) = \frac{1}{T} \sum_{k=-\infty}^{\infty} H_a\left(s - j\frac{2\pi k}{T}\right). \tag{F.30}$$

Thus in order to have a digital filter that approximates the analogue filter frequency response in the range $0 < f < f_s$, the digital filter response must be multiplied by $T$. Hence the final filter transfer function, that describes the harmonic oscillator, is

$$H(z) = \frac{\left[\left(\frac{Te^{-\alpha T}}{M\omega_r}\right) sin(\omega_r T)\right] z^{-1}}{1 - \left[2e^{-\alpha T} cos(\omega_r T)\right] z^{-1} + \left[e^{-2\alpha T}\right] z^{-2}}. \tag{F.31}$$

### F.2.2 Finite Differences

Another method of discretisation is to approximate the derivatives in (F.1) with finite differences. For example we can use the following finite difference scheme:

$$\begin{aligned} \frac{dx}{dt} &\approx \frac{x(n) - x(n-1)}{T}, \\ \frac{d^2x}{dt^2} &\approx \frac{x(n+1) - 2x(n) + x(n-1)}{T^2}, \end{aligned} \tag{F.32}$$

in which the velocity is approximated using the backward-difference formula, and the acceleration is approximated using the centered-difference formula. Applying this scheme to (F.1) yields the difference equation:

$$x(n+1) = \left[2 - 2\alpha T - \omega_0^2 T^2\right] x(n) + \left[2\alpha T - 1\right] x(n-1) + \left[\frac{T^2}{M}\right] f(n). \tag{F.33}$$

The corresponding filter transfer function is:

$$H(z) = \frac{\left[\frac{T^2}{M}\right] z^{-1}}{1 + \left[\omega_0^2 T^2 + 2\alpha T - 2\right] z^{-1} + \left[1 - 2\alpha T\right] z^{-2}}. \tag{F.34}$$

### F.2.3 The Bilinear Transform

The bilinear transform (BT) maps the continuous-frequency variable $s$ to the discrete-frequency variable $z$:

$$s = \beta \left( \frac{1 - z^{-1}}{1 + z^{-1}} \right), \tag{F.35}$$

where $\beta = 2/T$ is the bilinear operator. Applying the BT to the transfer function of the harmonic oscillator (equation (F.21)) gives:

$$H(z) = \frac{\left[ \frac{M^{-1}}{\beta^2 + 2\alpha\beta + \omega_0^2} \right] \left(1 + 2z^{-1} + z^{-2}\right)}{1 + \left[ \frac{2(\omega_0^2 - \beta^2)}{\beta^2 + 2\alpha\beta + \omega_0^2} \right] z^{-1} + \left[ \frac{\beta^2 - 2\alpha\beta + \omega_0^2}{\beta^2 + 2\alpha\beta + \omega_0^2} \right] z^{-2}}. \tag{F.36}$$

| | Impulse Invariance Method | Finite Differences | Bilinear Transform |
|---|---|---|---|
| $b0$ | $0$ | $0$ | $\frac{M^{-1}}{\beta^2 + 2\alpha\beta + \omega_0^2}$ |
| $b1$ | $\left( \frac{Te^{-\alpha T}}{M\omega_r} \right) sin(\omega_r T)$ | $\frac{T^2}{M}$ | $\frac{2M^{-1}}{\beta^2 + 2\alpha\beta + \omega_0^2}$ |
| $b2$ | $0$ | $0$ | $\frac{M^{-1}}{\beta^2 + 2\alpha\beta + \omega_0^2}$ |
| $a1$ | $-2e^{-\alpha T} cos(\omega_r T)$ | $\omega_0^2 T^2 + 2\alpha T - 2$ | $\frac{2(\omega_0^2 - \beta^2)}{\beta^2 + 2\alpha\beta + \omega_0^2}$ |
| $a2$ | $e^{-2\alpha T}$ | $1 - 2\alpha T$ | $\frac{\beta^2 - 2\alpha\beta + \omega_0^2}{\beta^2 + 2\alpha\beta + \omega_0^2}$ |

Table F.1: Coefficients of the digital filter approximation of the driven harmonic oscillator. $\beta = 2/T$ is the bilinear operator.

### F.2.4 Comparison

The effect of discretisation of each of the three methods can be seen by comparing the digital filter response with the analogue filter response. This was done for a series of different filters, in which the stiffness was varied such that the resonance frequency $\omega_0$ takes on the values $\omega = i\sqrt{K_0/M}$, for $i = 1, 2, 3$, where $K_0 = 10000\text{N/m}$, $M = 2\times10^{-5}\text{kg}$, and $R = 0.07\text{kg/s}$. Figure F.2 compares the responses. Apparently, the impulse invariance method (IIM) is accurate at and around the location of the resonance frequency. This makes sense, since the IIM can be thought of as a method in which the poles of the analogue filters (the positions of which are related to the resonance frequency) are directly *mapped* from the $s$-plane to the $z$-plane [109]. The fit of the IIM response gets worse as we move away from the resonance frequency, which is due to the effect of aliasing [109]. Both the other methods are not as accurate around the resonance frequency, but instead have an exact fit at $\omega = 0$. For both the method of finite differences (FDM) and the bilinear transform (BT), the discrepancy between the "ideal" analogue response and the digital response gets larger with frequency. The resonance frequency and the amplitude tend to be over-estimated by the FDM and under-estimated by the BT.

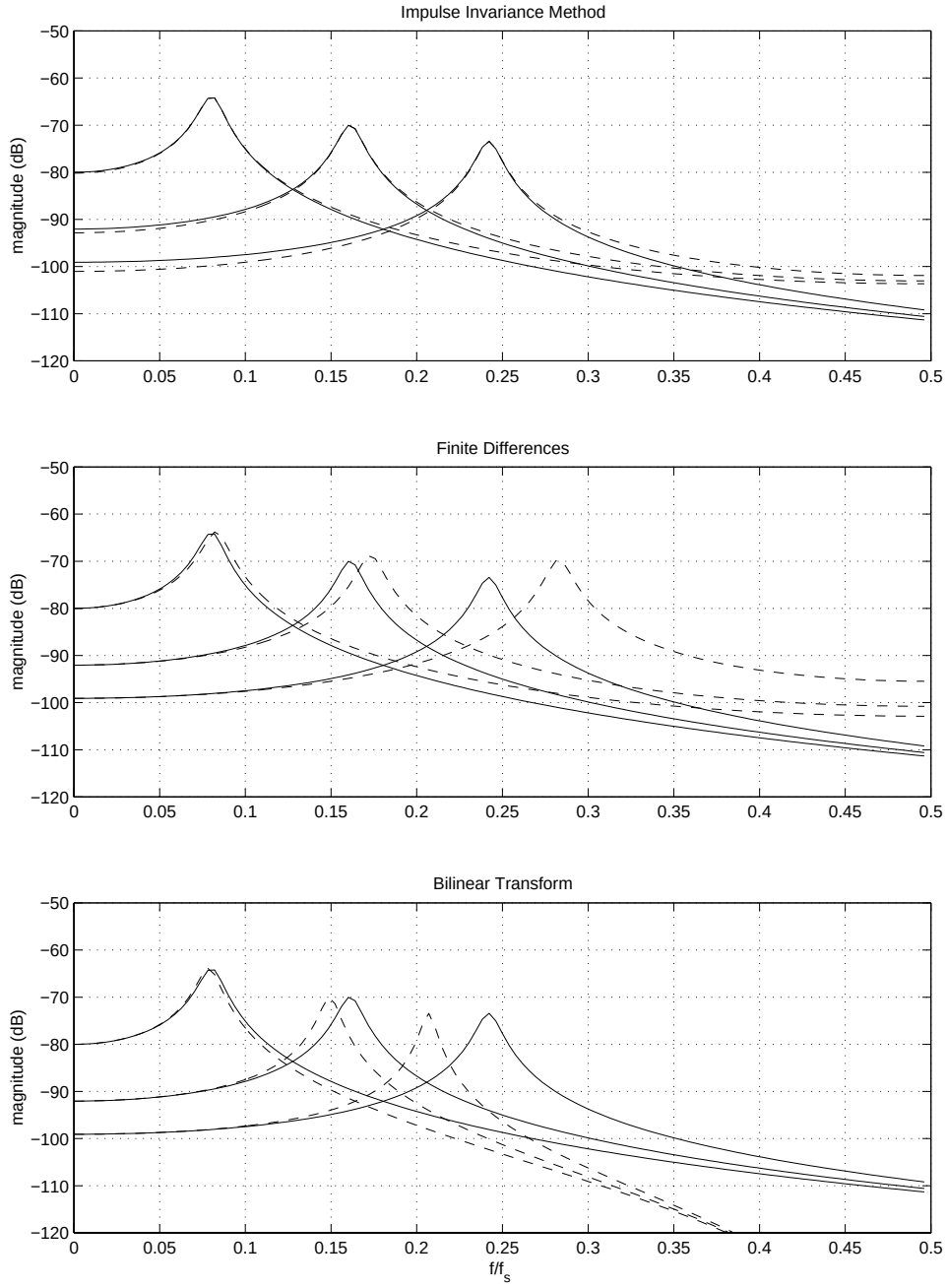


Figure F.2: Magnitude response of the harmonic oscillator, computed for three different resonance frequencies. The solid lines indicates the analogue filter responses, and the dashed lines indicate the digital filter responses.

# Appendix G

# Discretisation of a One-Pole Filter Element

Consider the analogue one-pole system

$$H(s) = g\left(\frac{\alpha}{s+\alpha}\right). \tag{G.1}$$

This is a lowpass filter with a pole at $s = -\alpha$ and gain $g$. We can approximate $H(s)$ in discrete-time with the digital one-pole filter:

$$H(z) = \frac{b_0 + b_1 z^{-1}}{1 + a_1 z^{-1}}. \tag{G.2}$$

There are several methods for obtaining the filter coefficients $(b_0, b_1, a_1)$. In this appendix we will discuss and compare three of such methods. Because we intend to apply these methods to modelling wave scattering at conical junctions, the filter is not a priori assumed to be stable (i.e., $\alpha$ can become negative).

## G.1 The Impulse Invariance Method

As seen in appendix F, the impulse invariance method (IIM) is based on sampling the continuous-time output of the filter. For a one-pole system with a pole at $s = -\alpha$, this results in a digital filter that has a pole at $z = e^{-\alpha T}$ [109], thus we have:

$$a_1 = -e^{-\alpha T}. \tag{G.3}$$

The gain of the digital filter is usually taken equal to $T$ times the gain of the analogue filter, which is realised by with

$$b_0 = gT, \tag{G.4}$$

while the second zero-coefficient $b_1$ is set to zero. However, in digital waveguide and wave digital modelling applications, the magnitude response at $\omega = 0$ needs to be preserved. This can be achieved by setting:

$$b_0 = g\left(1 - e^{bT}\right). \tag{G.5}$$

## G.2 The Bilinear Transform

In appendix F, we have seen that the bilinear transform (BT) is carried out via an $s$ to $z$ mapping (equation (3.40)). Applying the BT to the filter $H(s)$ gives the following filter coefficients:

$$b_0 = b_1 = \frac{g\,\alpha}{\alpha + \beta}, \tag{G.6a}$$

$$a_1 = \frac{\alpha - \beta}{\alpha + \beta}, \tag{G.6b}$$

where $\beta = 2/T$ is the bilinear operator.

## G.3 The Time-Interpolated Convolution Method

The general concept of time-interpolated convolution is briefly explained in section 6.3.1. To apply this method to the problem of discretising a first-order filter element, we need to first formulate the impulse response of the filter. The impulse response $h(t)$ can be obtained via an inverse Laplace transform of equation (G.1). Depending on how we define the region of convergence (ROC) of the system [109], one may obtain either a non-causal or a causal response. For $\alpha > 0$, the causal response is stable and the non-causal response is unstable, whereas for $\alpha < 0$, the non-causal response is stable and the causal response is unstable. In the current context, $h(t)$ represents a physical response, therefore the ROC is always chosen here such that a causal response results. Thus for $t \geq 0$, we have:

$$h(t) = g\,e^{-\alpha\,t}. \tag{G.7}$$

Given an input-signal $x(t)$, the output-signal $y(t)$ can then be computed by means of a recursive formulation of the convolution product $y(t) = h(t) * x(t)$ [94]:

$$y(t+T) = e^{-\alpha T} x(t) + \int_{\tau=0}^{T} h(\tau)\, x(t+T-\tau)\, d\tau. \tag{G.8}$$

Within this formulation, a linear evolution of the input-signal between the discrete-time instants $\tau = t$ and $\tau = t+T$ is assumed:

$$x(t+T-\tau) = c_1 \cdot \tau + c_2, \tag{G.9}$$

where

$$c_1 = \frac{x(t+T) - x(t)}{T}, \tag{G.10a}$$

$$c_2 = x(t). \tag{G.10b}$$

We can analytically determine the convolution product in (G.8):

$$\begin{aligned} \int_{\tau=0}^{T} h(\tau)\, x(t+T-\tau)\, d\tau &= \int_{\tau=0}^{T} g\, e^{-\alpha\tau}\, (c_1\,\tau + c_2)\, d\tau \\ &= g \left\{ c_1 \left[ T e^{-\alpha T} + \frac{e^{-\alpha T} - 1}{\alpha} \right] + c_2 \left[ e^{-\alpha T} - 1 \right] \right\}. \end{aligned} \tag{G.11}$$

After substituting (G.10) into (G.11), and combining with (G.8), we obtain the difference equation

$$y(t+T) = b_0\, x(t+T) + b_1\, x(t) - a_1\, y(t), \tag{G.12}$$

with the coefficients:

$$b_0 = -g \left[ 1 + \frac{e^{-\alpha T} - 1}{\alpha T} \right], \tag{G.13a}$$

$$b_1 = g \left[ e^{-\alpha T} + \frac{e^{-\alpha T} - 1}{\alpha T} \right], \tag{G.13b}$$

$$a_1 = e^{-\alpha T}. \tag{G.13c}$$

Equation (G.12) implements the first-order digital filter in (G.2). Thus, if a linear evolution of the incident wave between discrete-time instants is assumed, the time-interpolated convolution method (TICM) may be interpreted as an alternative way of filter discretisation.

## G.4 Filter Comparison

In order to compare the different methods for obtaining the coefficients, we computed the filter response for a range of $\alpha$-values, and using a unity gain ($g = 1$). In figure G.1, the digital responses are compared to the analogue responses. Apparently, all three methods are exact at $\omega = 0$. For all other frequencies, the IIM overestimates and the TICM as well as the BT underestimate the magnitude response. Furthermore, it can be seen that the responses obtained using the TICM and using the BT are remarkably similar.

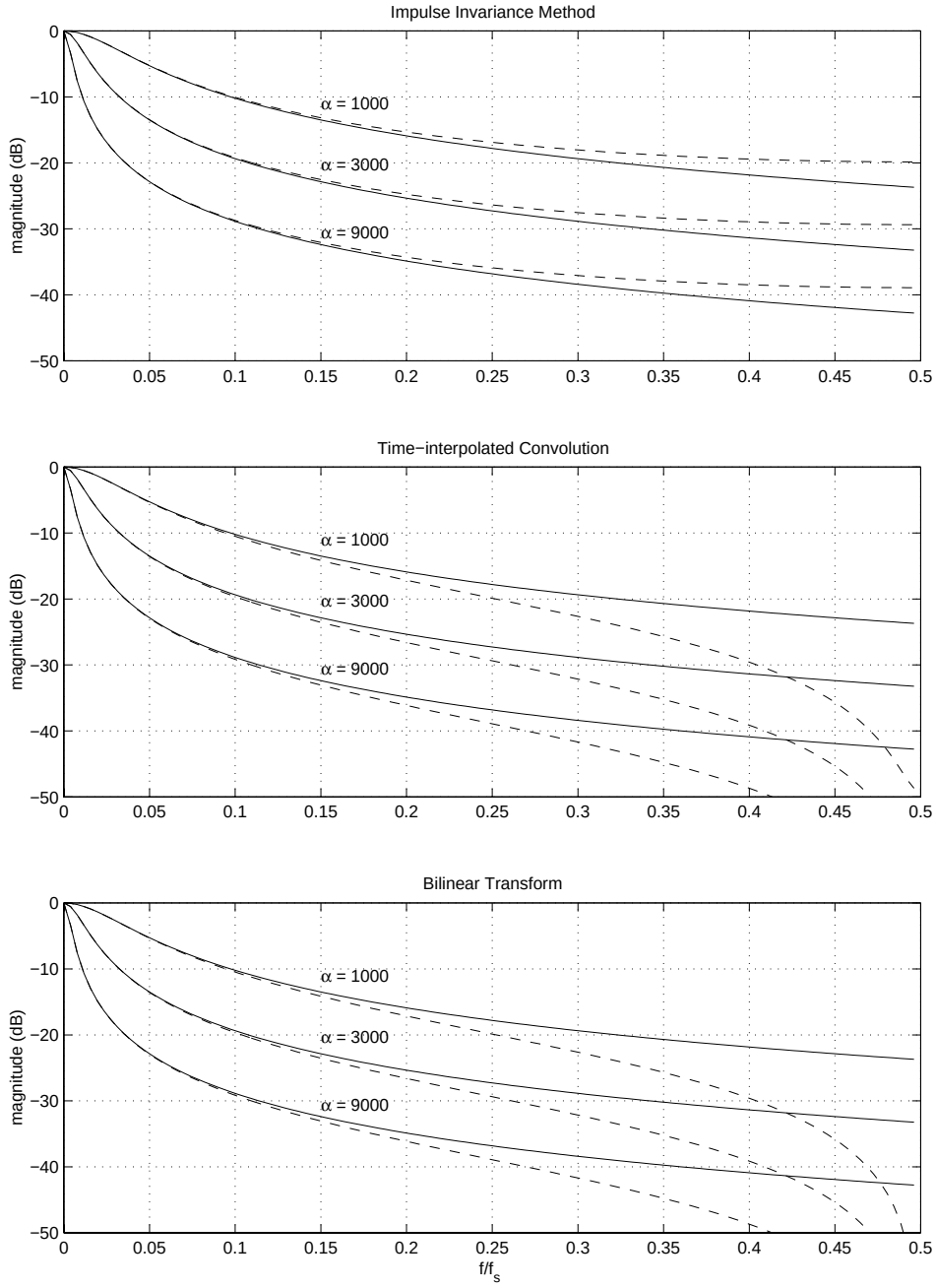


Figure G.1: Magnitude response of the one-pole filter element, computed for $\alpha = 1000$, $\alpha = 3000$, and $\alpha = 9000$, and with $g = 1$. The solid lines indicates the analogue filter responses, and the dashed lines indicate the digital filter responses.

# Appendix H

# Finite Difference Approximations of the Bar Equation

The bar equation (10.11) can be written:

$$\begin{aligned}\frac{F(x_i,t_n)}{Y} &= \frac{\rho\,A(x)}{Y}\left[\frac{\partial^2 y}{\partial t^2}(x_i,t_n)+\gamma_B\,\frac{\partial y}{\partial t}(x_i,t_n)\right]+\frac{\partial^2}{\partial x^2}\left[I(x)\,\frac{\partial^2 y}{\partial x^2}(x_i,t_n)\right]\cdots\\ &\quad+\frac{\partial^2}{\partial x^2}\left[\eta\,I(x)\,\frac{\delta^3 y}{\delta x^2\delta t}(x_i,t_n)\right].\end{aligned}\tag{H.1}$$

The first- and second-order partial derivative with respect to time in (H.1) are approximated using the central difference schemes:

$$\delta y/\delta t(x_i,t_n) \approx \frac{y_i^{n+1}-y_i^{n-1}}{2T},\tag{H.2}$$

$$\delta^2 y/\delta t^2(x_i,t_n) \approx \frac{y_i^{n+1}-2y_i^n+y_i^{n-1}}{T^2}.\tag{H.3}$$

Following the approach used in [36], the fourth-order spatial derivative (the second term on the right-hand side of (H.1))is approximated using a $\theta$-scheme:

$$\frac{\partial^2}{\partial x^2}\left[I(x)\frac{\partial^2 y}{\partial x^2}(x_i,t_n)\right]\approx\theta\left[\delta_x^2[I_i(\delta_x^2 y)_i]^{n+1}+\delta_x^2[I_i(\delta_x^2 y)_i]^{n-1}\right]+(1-2\theta)\,\delta_x^2[I_i(\delta_x^2 y)_i]^n,\tag{H.4}$$

where $\delta_x^2[I_i(\delta_x^2 y)_i]^n$ is given by (10.13). The derivative $\delta^3 y/\delta x^2\delta t$ in (H.1) is approximated with

$$\frac{(\delta_x^2 y)_i^{n+1}-(\delta_x^2 y)_i^{n+1}}{2T},\tag{H.5}$$

where we do not yet explicitly evaluate the second-order spatial derivative terms. Substituting (H.5) into the third term on the righthand-side of (H.1), and again applying the $\theta$-scheme to approximate the resulting fourth-order terms yields:

$$\frac{\partial^2}{\partial x^2}\left[\eta\, I(x)\,\frac{\delta y^3}{\delta x^2 \delta t}(x_i,t_n)\right] \approx \theta\beta\left[\delta_x^2[I_i(\delta_x^2 y)_i]^{n+1} - \delta_x^2[I_i(\delta_x^2 y)_i]^{n-1}\right]. \tag{H.6}$$

Substituting equations (H.2), (H.4), and (H.6) into (H.1) yields the numerical formulation of the system presented in (10.14). If we set $\lambda = Y\,T^2\,(\Delta x)^{-4}$, the bar difference equation can be written:

$$\begin{aligned}
T^2 F_i^n \;=\;& \lambda\,\theta\,(1+\beta)\,I_{i-1}\,y_{i-2}^{n+1},\\
&-2\lambda\,\theta\,(1+\beta)(I_i + I_{i-1})\,y_{i-1}^{n+1},\\
&+\left[\lambda\,\theta\,(1+\beta)(I_{i+1}+4I_i+I_{i-1}) + \rho\,A_i\,(\gamma+1)\right]\,y_i^{n+1},\\
&-2\lambda\,\theta\,(1+\beta)(I_{i+1}+I_i)\,y_{i+1}^{n+1},\\
&+\lambda\,\theta\,(1+\beta)\,I_{i+1}\,y_{i+2}^{n+1},\\
&+\lambda\,(1-2\theta)\,I_{i-1}\,y_{i-2}^{n},\\
&-2\lambda\,(1-2\theta)\,(I_i+I_{i-1})\,y_{i-1}^{n},\\
&+\left[\lambda\,(1-2\theta)(I_{i+1}+4I_i+I_{i-1}) - 2\rho A_i\right]\,y_i^{n},\\
&-2\lambda\,(1-2\theta)(I_{i+1}+I_i)\,y_{i+1}^{n},\\
&+\lambda\,(1-2\theta)I_{i+1}\,y_{i-2}^{n},\\
&+\lambda\,\theta\,(1-\beta)\,I_{i-1}\,y_{i-2}^{n-1},\\
&-2\lambda\,\theta\,(1-\beta)\,(I_i+I_{i-1})\,y_{i-1}^{n-1},\\
&+\left[\lambda\,\theta(1-\beta)\,(I_{i+1}+4I_i+I_{i-1}) + \rho\,A_i\,(\gamma-1)\right]\,y_i^{n-1},\\
&-2\lambda\,\theta\,(1-\beta)(I_{i+1}+I_i)\,y_{i+1}^{n-1},\\
&+\lambda\,\theta\,(1-\beta)\,I_{i+1}\,y_{i+2}^{n-1}.
\end{aligned}$$

The boundary conditions in (10.10) are expressed in discrete-time form as:

$$y_0^n = 0, \tag{H.7a}$$

$$y_{-1}^n = y_1^n, \tag{H.7b}$$

$$y_{N+1}^n = 2y_N^n - y_{N-1}^n, \tag{H.7c}$$

$$y_{N+2}^n = 4y_N^n - 4y_{N-1}^n + y_{N-2}^n. \tag{H.7d}$$

The above difference equation and boundary equations form a set of $(N+4)$ simultaneous equations that can be expressed in matrix form:

$$\mathbf{M}_{n+1} \cdot \mathbf{y}(n+1) = \mathbf{M}_n \cdot \mathbf{y}(n) + \mathbf{M}_{n-1} \cdot \mathbf{y}(n-1) + \mathbf{M}_F \cdot \mathbf{F}(n), \tag{H.8}$$

where $\mathbf{y}(n)$, $\mathbf{y}(n-1)$ and $\mathbf{y}(n-2)$ are the displacement vectors at successive time instants, $\mathbf{F}(n)$ is the force per unit length vector, and $\mathbf{M}_n$ is a $(N+4)$ by $(N+4)$ matrix. Solving for $\mathbf{y}(n+1)$ gives the final matricial formulation in equation (10.15).

# Appendix I

# Reflection Functions of the Exponential Type

In this appendix we discuss localised bore discontinuities that may be characterised by reflection and transmission functions of the exponential type:

$$r(t) = a_0\delta(t) + a_1\, e^{b_1 t} + a_2\, e^{b_2 t}. \tag{I.1}$$

For this type of discontinuity, the pressure and flow are continuous across the discontinuity, in which case the transmission and reflection functions are related through the Dirac distribution $\delta(t)$ [19]. Hence it is sufficient to limit ourselves to the analysis of the reflection functions. In the multi convolution approach, these functions are calculated explicitly, and convolutions of pressure waves with these functions are realised by means of the time-interpolated convolution method. In the wave digital approach, the reflection and transmission functions are not calculated explicitly. Instead, discontinuities associated with bore units such as toneholes are discretised individually. In order to be able to compare the underlying continuous-time models of the two approaches, we derive the reflection functions that are *effectively* implemented with the wave digital approach by means of network theory.

## I.1 Diameter and Taper Discontinuities

In the wave digital approach, a junction of two conical sections is modelled with a WD junction model (see section 6.1). This model is based on a simple parallel inertance network (see figure 6.1), in which the junction is characterised by the inertance $L_j$. For calculating the effective spherical wave reflectance of the junction as seen from the input-end of the bore, we must assume an anechoic termination directly after the junction. This

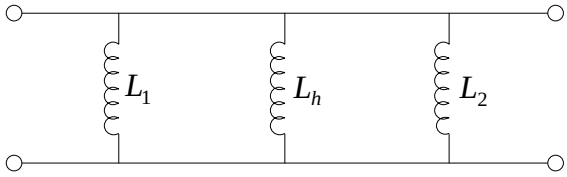


Figure I.1: Equivalent network of an open tonehole discontinuity in a woodwind bore. $L_h = (\rho t_e)/(S_b)$ is the open hole inertance, $L_1 = (\rho r_1)/S$ is the conicity inertance on the input-end, and $L_2 = (\rho r_2)/S$ is the conicity inertance on the output-end, where $r_1$ and $r_2$ indicate the cone apex distances.

reflectance can thus be calculated from the net impedance of an inertance $L_j$ in parallel with the characteristic impedance $Z_2 = (\rho c)/S_2$ at the output-end:

$$R(\omega) = \frac{Z(\omega) - Z_1}{Z(\omega) + Z_1}, \tag{I.2}$$

where

$$\frac{1}{Z(\omega)} = \frac{1}{L_j} + \frac{1}{Z_2}, \tag{I.3}$$

and $Z_1 = (\rho c)/S_1$ is the characteristic impedance a the input-end. Through substitution of equation (6.1), we find equation (4.31b). The reflection function, that is obtained by taking the inverse Fourier transform of (4.31) is:

$$r(t) = \frac{B-1}{B+1}\delta(t) - \left(\frac{2B}{B+1}\right)\epsilon(t)\,\alpha\, e^{-\alpha\, t}, \tag{I.4}$$

which is equivalent to the reflection function given by Martínez and Agulló in [93].

## I.2 Open Hole

In the wave digital approach, an open hole discontinuity is modelled as a parallel network of inertances (see figure I.1), in which each individual inertance is discretised using the BT. For an anechoical termination at the output-end, the reflectance as seen from the input-end is[1]:

$$R(\omega) = \frac{-(\alpha_t + \alpha_h)}{j\omega + (\alpha_t + \alpha_h)}, \tag{I.5}$$

[1]It is assumed that there is no diameter discontinuity at the hole location.

with

$$\alpha_h = \frac{c\, S_b}{2\, S_a\, t_e}, \tag{I.6a}$$

$$\alpha_t = \frac{c}{2}\left[\frac{1}{r_2} - \frac{1}{r_1}\right], \tag{I.6b}$$

where $S_a$ and $S_b$ are the cross-sections of the main bore and the hole, respectievly, and $t_e$ is the effective tonehole length. The open-hole reflection function is:

$$r(t) = -(\alpha_t + \alpha_h)\, e^{-(\alpha_t+\alpha_h)t}\, \epsilon(t). \tag{I.7}$$

which is equivalent to the reflection function given by Barjau et al. in [19].

## I.3 Closed Hole

For a closed hole, we may replace the inertance $L_h$ in figure I.1 with the compliance $C_h = (S_b\, t)/(\rho c^2)$, where $t$ is the tonehole height. The reflectance as seen from the input-end, assuming an anechoic termination at the output-end, then becomes:

$$R(\omega) = -1 + \frac{1}{\Delta}\left[\frac{\alpha^-}{j\omega + \alpha^-} - \frac{\alpha^+}{j\omega + \alpha^+}\right]. \tag{I.8}$$

with

$$\alpha^+ = \frac{\alpha_c}{2}\,(1 - \Delta)\,, \tag{I.9a}$$

$$\alpha^- = \frac{\alpha_c}{2}\,(1 + \Delta)\,, \tag{I.9b}$$

and where

$$\Delta = \sqrt{1 - 4\alpha_t/\alpha_c}, \tag{I.10}$$

with the closed-hole attenuation coefficient

$$\alpha_c = \frac{2\, S_a\, c}{S_b\, t_e^{(c)}}, \tag{I.11}$$

where $t_e^{(c)}$ is the closed-hole effective length. The closed-hole reflection function is

$$r(t) = -\delta(t) + \frac{1}{\Delta}\{\alpha^-\, e^{-\alpha^-\, t} - \alpha^-\, e^{-\alpha^+\, t}\}. \tag{I.12}$$

This is the same result as given by Barjau et al. in [19].

## I.4 Closed End

For a closed end, we have a conicity inertance in parallel with an infinite radiation load, hence the closed-end reflectance is:

$$R(\omega) = \frac{j\omega L - Z_0}{j\omega L + Z_0} = \frac{c/r - j\omega}{c/r + j\omega}, \tag{I.13}$$

where $Z_0$ is the characteristic impedance, $L = -(\rho r)/S_a$ is the conicity inertance, and $r$ is the apex distance at the closed end. The reflection function is:

$$r(t) = \delta(t) - \epsilon(t)\,(2c/r)\,e^{-c\,t/r}, \tag{I.14}$$

which is equivalent to the closed-end reflection function given by Martínez and Agulló in [93].

# Appendix J

# Acoustic Measurements

The techniques used in in this work for measuring the acoustic response of a tubular object are described in detail in [126]. This appendix gives a brief description of these techniques.

## J.1 Input Impedance Measurements

The input impedance is measured for a finite set of frequencies by exciting the air column of an instrument with a sine wave while recording the pressure at the entry with a microphone. The procedure is controlled with a digital computer. Figure J.1 shows a schematic diagram of the the experimental apparatus.

The computer is used to select a frequency, and a sine wave of this frequency is generated electrically with a sine generator. The exact frequency of this signal is measured with an inbuilt frequency meter and sent back to the computer in binary coded form. The sine wave signal is amplified and send to a loud speaker, which results in a sinusoidal pressure variation in the cavity. A feedback loop is employed in order to ensure that there is a constant pressure amplitude in the cavity. The amplitude of the volume flow into the instrument may then also be assumed to be constant, because the resistance of the capillary is independent of frequency and much higher than the impedance of the instrument air column. As a result, the pressure measured at the instrument entry by the microphone is directly proportional to the input impedance of the instrument. This pressure signal is first passed through a highpass filter in order to remove low-frequency noise, and then amplified and sampled by means of an A/D converter. If the volume velocity $U$ amplitude is known, the input impedance amplitude can be computed from a measured pressure amplitude $P$ as $Z_{in} = P/U$. In order to obtain the volume velocity for each frequency, the procedure is first carried out with a tubular object of known impedance $Z_{cal}(\omega)$. The calibration volume velocity curve is then $U_{cal}(\omega) = P_{cal}(\omega)/Z_{cal}(\omega)$.

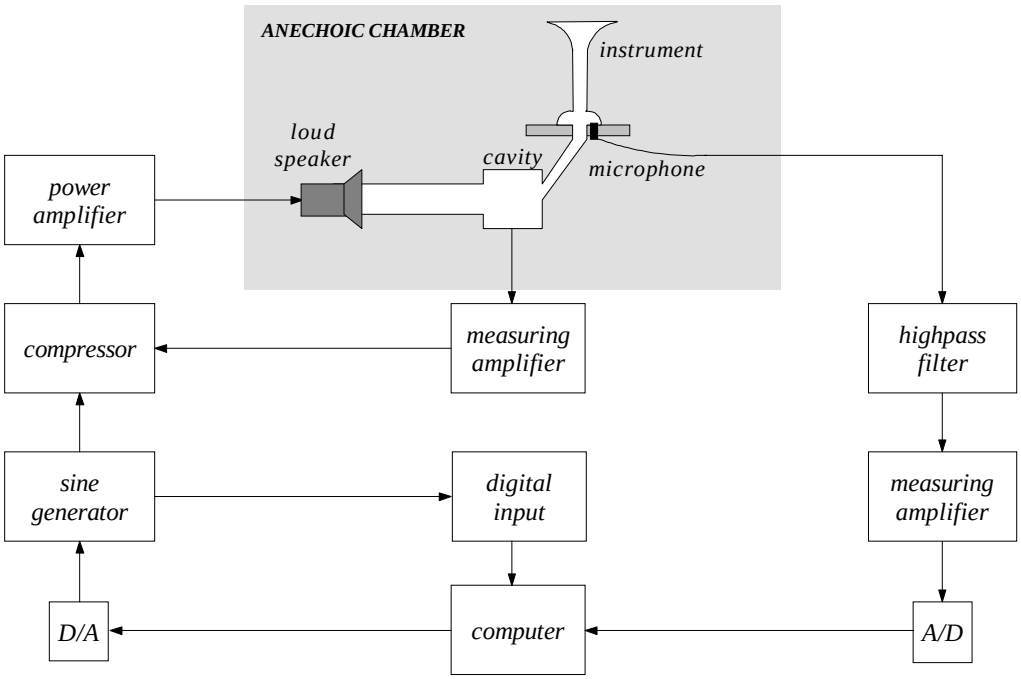


Figure J.1: Schematic diagram of the impedance measurement apparatus (after Sharp [126])).

## J.2 Pulse Reflectometry Measurements

The response of a tubular object may also be measured directly in the time domain. One such a method is by means of sending a pulse into the object and recording the reflections. This procedure is referred to as *pulse reflectometry*. Figure J.2 shows a schematic diagram of the pulse reflectometer used in this study. A computer-generated pulse is amplified and used to drive a loudspeaker. As a result, a pressure wave is released into the source tube and travels into the instrument under test. The signal that reflects from the instrument is recorded with a microphone that is embedded in the source tube wall, and the microphone output signal is sampled with an A/D converter. The computer is programmed to send a sequence of 1000 pulses, and the resulting reflection signals are averaged in order to improve the signal-to-noise ratio. This procedure is first carried out with the source tube blocked off at the end, and then again but with the instrument fitted at the end. The reflection function of the instrument is then obtained by deconvolving the two obtained reflection signals.

The lengths $l_1$ and $l_2$ of the source tube have to be chosen large enough to ensure that the object reflection signal is separated in time from the initial input pulse as well as from any further reflections from the loudspeaker.

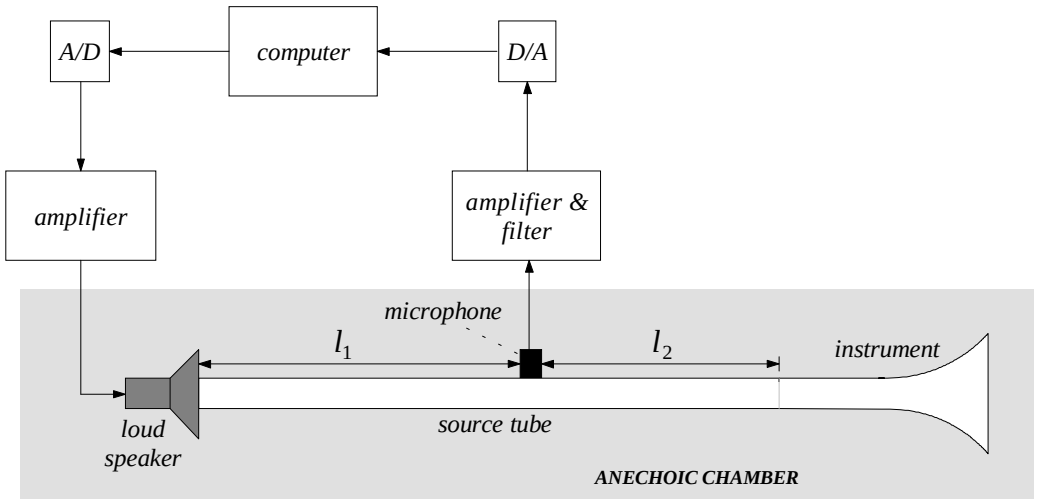


Figure J.2: Schematic diagram of the pulse reflectometer (after Sharp [126])).

# Appendix K

# Sound Examples

This appendix gives a short description of some sound examples. These can be downloaded from `http://www.music.ed.ac.uk/student/pages/pg/maarten/thesissounds.html`. All sound examples are either generated at 44.1kHz, except those marked with *, which are generated at 176.4kHz and downsampled (after lowpass filtering) by a factor four.

**(ex1)** impulse response (Green's function) of the bore depicted in figure 6.7a, as computed with the transmission-line model.

**(ex2)** same as **(ex1)**, but computed with the wave digital model depicted in figure 6.8.

**(ex3)** impulse response (Green's function) of the bore depicted in figure 6.7b, as computed with the transmission-line model.

**(ex4)** same as **(ex3)**, but computed with the wave digital model depicted in figure 6.10.

**(ex5)** impulse response (Green's function) of the Boosey and Hawkes trumpet, as computed with the wave digital model depicted in figure 9.2.

**(ex6)** radiation pressure signal that results when inserting a volume flow input pulse into the wave digital model of the Boosey and Hawkes trumpet depicted in figure 9.2.

**(ex7*)** impulse response (Green's function) of the Selmer clarinet, as computed with the wave digital model of the Selmer clarinet described in section 9.2.2.

**(ex8*)** radiation pressure signal that results when inserting a volume flow input pulse into the wave digital model of the Selmer clarinet describeded in section 9.2.2.

**(ex9*)** mouthpiece pressure signal, as computed with the digital simulation of the reed-excited pipe system described in section 10.4, using displacement-dependent reed parameters. The spectogram of this signal is depicted in figure 10.25.

(**ex10***) same as (**ex9**), but computed using constant reed parameters. The spectogram of this signal is depicted in figure 10.26.

(**ex11***) radiation pressure signal, as computed with the digital simulation of the reed-excited pipe system described in section 10.4, using displacement-dependent reed parameters.

(**ex12***) same as (**ex11**), but computed using constant reed parameters.

# Bibliography


[1] S. Adachi and M. Sato. Time-domain simulation of sound production in the brass instrument. *Journal of the Acoustical Society of America*, 97(6):3850–3861, 1995.

[2] S. Adachi and M. Sato. Trumpet sound simulation using a two-dimensional lip vibration model. *Journal of the Acoustical Society of America*, 99(2):1200–1209, 1996.

[3] J. M. Adrien. *Etude de structures complexes vibrantes, application à la synthèse par modèles physiques*. PhD thesis, Paris: Université de Paris VI, 1988.

[4] J. M. Adrien, R. Caussé, and E. Ducasse. Dynamic modeling of stringed and wind instruments, sound synthesis by physical models. In *Proceedings of the 1988 International Computer Music Conference*, pages 265–276, Köln, 1988. Computer Music Association.

[5] J. Agulló, A. Barjau, and J. Martínez. Alternatives to the impulse response *h(t)* to describe the acoustical behavior of conical ducts. *Journal of the Acoustical Society of America*, 84(5):1606–1612, 1988.

[6] J. Agulló, A. Barjau, and J. Martínez. On the time-domain description of conical bores. *Journal of the Acoustical Society of America*, 91(2):1099–1105, 1992.

[7] R. J. Alfredson. The propagation of sound in a circular duct of continuously varying cross-sectional area. *Journal of Sound and Vibration*, 23(4):433–442, 1972.

[8] N. Amir, V. Pagneux, and J. Kergomard. A study of wave propagation in varying cross-section waveguides by modal decomposition. Part II. Results. *Journal of the Acoustical Society of America*, 101(5):2504–2517, 1997.

[9] N. Amir, U. Shimony, and G. Rosenhouse. Input impedance of musical horns and the 'horn function'. *Applied Acoustics*, 38:15–35, 1993.

[10] N. Amir, U. Shimony, and G. Rosenhouse. Discrete model for tubular acoustic systems with varying cross section - the direct and inverse problems. Part I: Theory. *Acustica*, 81:450–462, 1995.

[11] N. Amir, U. Shimony, and G. Rosenhouse. Losses in tubular acoustic systems - theory and experiment. *Acustica*, 82:1–8, 1996.

[12] F. Avanzini, 2000. Private communication.

[13] F. Avanzini. On the use of weighted sample methods in digitizing the clarinet equations. In *Proceedings of the 2000 International Computer Music Conference*, pages 46–49, Berlin, Germany, 2000. Computer Music Association.

[14] F. Avanzini. *Computational Issues in Physically-based Sound Models.* PhD thesis, University of Padova, Dept. of Electronics and Informatics, 2002. Downloadable from http://www.dei.unipd.it/ avanzini/.

[15] D. R. Ayers. Two complex effective lengths for musical wind instruments. *Journal of the Acoustical Society of America*, 98(1):81–87, 1995.

[16] J. Backus. Vibrations of the reed and air column in the clarinet. *Journal of the Acoustical Society of America*, 33(6):806–809, 1961.

[17] J. Backus. Small-vibration theory of the clarinet. *Journal of the Acoustical Society of America*, 35(3):305–313, 1963.

[18] J. Backus. Input impedance curves for the brass instruments. *Journal of the Acoustical Society of America*, 60(2):470–480, 1976.

[19] A. Barjau, D. H. Keefe, and S. Cardona. Time-domain simulation of acoustical waveguides with arbitrarily spaced discontinuities. *Journal of the Acoustical Society of America*, 105(5):1951–1964, 1999.

[20] A. H. Benade. On the mathematical theory of woodwind finger holes. *Journal of the Acoustical Society of America*, 32(12):1591–1608, 1960.

[21] A. H. Benade. On the propagation of sound waves in a cylindrical conduit. *Journal of the Acoustical Society of America*, 44(2):616–623, 1968.

[22] A. H. Benade. *Fundamentals of Musical Acoustics.* Oxford University Press, New York, 1976.

[23] A. H. Benade. Air column, reed, and player's windway interaction in musical instruments. In I. R. Titze and R. C. Scherer, editors, *Vocal Fold Physiology, Biomechanics, Acoustics, and Phonatory Control*, chapter 35, pages 425–452. Denver Center for the Performing Arts, 1985.

[24] A. H. Benade. Equivalent circuits for conical waveguides. *Journal of the Acoustical Society of America*, 83(5):1764–1769, 1988.

[25] A. H. Benade and E. V. Jansson. On plane and spherical waves in horns with nonuniform flare. Part I: Theory of radiation, resonance frequencies, and mode conversion. *Acustica*, 31(2):80–98, 1974.

[26] A. H. Benade and S. N. Kouzoupis. The clarinet spectrum. *Journal of the Acoustical Society of America*, 83(1):292–304, 1988.

[27] D. Berners. *Acoustics and Signal Processing Techniques for Physical Modelling of Brass Instruments*. PhD thesis, Elec. Engineering Dept., Stanford University, 1999.

[28] D. P. Berners, 2002. Personal communication.

[29] R. W. Berry. Experiments in computer controlled acoustic modelling (A step backwards?). In *Proceedings of the 1988 International Computer Music Conference*, pages 333–348, Köln, Germany, 1988. Computer Music Association.

[30] D. Bilbao. *Wave scattering methods for the numerical integration of partial differential equations*. PhD thesis, Elec. Engineering Dept., Stanford University, 2001.

[31] G. Borin, G. De Poli, and D. Rocchesso. Elimination of delay-free loops in discrete-time models of nonlinear acoustic systems. *IEEE Trans. on Speech and Audio Process.*, 8(5), 2000.

[32] H. Bouasse. *Instruments à vent*, volume 1. Librairie Delagrave, Paris, 1929. Second Edition Blanchard (1986), Paris.

[33] D. M. Campbell and C. Greated. *The musician's guide to acoustics*. J. M. Dent & Sons, London, 1987.

[34] D. M. Campbell, A. Meyers, M. O van Walstijn, and H. Wright. Devices for musical acoustics learning in a museum environment. In *Proceedings of the Fifth French Conference on Acoustics*, pages 257–259, Lausanne, Switzerland, 2000.

[35] R. Caussé, J. Kergomard, and X. Lurton. Input impedance of brass musical instruments-comparison between experiment and numerical models. *Journal of the Acoustical Society of America*, 75(1):241–254, 1984.

[36] A. Chaigne and V. Doutaut. Numerical simulations of xylophones: I. Time-domain modeling of the vibrating bars. *Journal of the Acoustical Society of America*, 101(1):539–57, 1997.

[37] R. E. Collin. *Foundations for microwave engineering*. McGraw-Hill, New York, 1966.

[38] P. R. Cook. Implementation of single reed instruments with arbitrary bore shapes using digital waveguide filters. Technical report, CCRMA, Dept. of Music, Stanford University, Stanford, California, Report no. STAN-M-50, 1988.

[39] P. R. Cook. *Identification of Control Parameters in an Articulatory Vocal Tract Model, With Applications to the Synthesis of Singing*. PhD thesis, Elec. Engineering Dept., Stanford University, 1990.

[40] J. S. Cullen. *A Study of Brass Instrument Acoustics using an Artificial Lip Reed Mechanism, Laser Doppler Anemometry and Other Techniques*. PhD thesis, Department of Physics and Astronomy, University of Edinburgh, 2000.

[41] J. S. Cullen, J. Gilbert, and D. M. Campbell. Brass instruments: Linear stability analysis and experiments with an artificial mouth. *Acustica - Acta Acustica*, 86(4):704–724, 2000. Special Issue on Musical Wind Instrument Acoustics.

[42] J. L. d'Alembert. Investigation of the curve formed by a vibrating string, 1747. In R. B. Lindsay, editor, *Acoustics: Historical and Philosophical Development*, pages 119–123. Dowden, Hutchinson, and Ross, 1973.

[43] G. De Bruin and M. O. Van Walstijn. Physical models of wind instruments. a generalized excitation coupled with a modular tube simulation platform. *Journal of New Music Research*, 24(2), 1995. Special Issue: Selected Papers from the Colloquium of New Music Research, Ghent 1994.

[44] R. Di Federico and G. Borin. Synthesis of the trumpet tone based on physical models. In *Proceedings of the 1997 International Computer Music Conference*, pages 410–413, Thessaloniki, Greece, 1997. Computer Music Association.

[45] P. H. Dietz. Simulation of trumpet tones via physical modeling. Master's thesis, Dept. of Electrical and Computer Engineering, Carnegie Mellon University, Pittsburgh, 1989.

[46] P. H. Dietz and N. Amir. Synthesis of trumpet tones by physical modeling. In *Proceedings of the 1995 International Symposium on Musical Acoustics*, pages 472–477, Dourdan, France, 1995. Société Française d'Acoustique.

[47] V. Dubos, J. Kergomard, A. Khettabi, J.-P. Dalmont, D. H. Keefe, and C. J. Nederveen. Theory of sound propagation in a duct with a branched tube using modal decomposition. *Acustica - Acta Acustica*, 85:153–169, 1999.

[48] E. Ducasse. Modélisation d'instruments de musique pour la synthèse sonore: application aux instruments à vent. In *Colloque de Physique*, Supplément au Journal de Physique II, pages 873–876, Lyon, France, 1990. First French Conference on Acoustics.

[49] J. D. Dudley and W. J. Strong. Computer simulation of a trumpet with mechanical "lips". In *Proceedings of the Stockholm Musical Acoustics Conference*, pages 486–489, 1993.

[50] DSP Committee Editors. Programs for digital signal processing. IEEE Press, John Wiley and Sons, 1979.

[51] A. Fettweis. Wave digital filters: Theory and practice. In *Proceedings of the IEEE*, pages 270–327, 1986.

[52] N. H. Fletcher and T. D Rossing. *The Physics of Musical Instruments*. Springer-Verlag, New York, 1991. Second Edition: 1998.

[53] F. Fontana and D. Rocchesso. Physical modeling of membranes for percussion instruments. *Acustica - Acta Acustica*, 83(1):529–542, 1998.

[54] B. Gazengel, J. Gilbert, and N. Amir. Time domain simulation of single reed wind instrument. From the measured input impedance to the synthesis signal. Where are the traps? *Acta Acustica*, 3:445–472, 1995.

[55] Bruno Gazengel. *Caractérisation objective de la qualité de justesse, de timbre et d'émission des instruments à vent à anche simple.* PhD thesis, Université du Maine, Le Mans, France, 1994.

[56] J. Gilbert. Rapport de stage de D.E.A d'Acoustique appliquée de l'université du Maine. Technical report, Académie de Nantes, Université du Maine, Faculté des Sciences, 1986.

[57] J. Gilbert. *Etude des instruments de musique à anche simple: Extension de la méthode d'équilibrage harmonique, rôle de l'inharmonicité des résonances, mesure des grandeurs d'entrée.* PhD thesis, L'université du Maine, 1991.

[58] J. Gilbert, 1999. Private communication.

[59] J. Gilbert, J. Kergomard, and E. Ngoya. Calculation of the steady state oscillations of a clarinet using the harmonic balance technique. *Journal of the Acoustical Society of America*, 86:35–41, 1989.

[60] J. Gilbert, J. Kergomard, and J. D. Polack. On the reflection functions associated with discontinuities in conical bores. *Journal of the Acoustical Society of America*, 87(4):1773–1780, 1990.

[61] J. Grand, J. Gilbert, and F. Laloë. Oscillation threshold of woodwind instruments. *Acustica - Acta Acustica*, 1:137–151, 1997.

[62] H. Helmholtz. *On the Sensations of Tone as a Physiological Basis for the Theory of Music.* Dover Publications, Inc., New York, 1954. Translated by Alexander J. Ellis from the 4th German Edition of 1877.

[63] S. E. Hirschman. Digital waveguide modeling and simulation of reed woodwind instruments, 1991. Eng. Thesis, Electrical Engineering Dept., Stanford University. Available as CCRMA Technical Report STAN-M-72,Music Dept., Stanford University, July 1991.

[64] A. Hirschberg, J. Gilbert, A. P. J. Wijnands, and A. M. C. Valkering. Musical aero-acoustics of the clarinet. In *Journal de Physique IV*, Supplément au Journal de Physique III, n°5, pages 559–568, Toulouse, France, 1994. Third French Conference on Acoustics.

[65] A. Hirschberg, R. W. A. van de Laar, J. P. Marrou-Maurières, A. P. J. Wijnands, H. J. Dane, S. G. Kruijswijk, and A. J. M. Houtsma. A Quasi-stationary Model of Air Flow in the Reed Channel of Single-reed Woodwind Instruments. *Acustica*, 70(2):146–154, 1990.

[66] P. L. Hoekje. *Intercomponent Energy Exchange and Upstream/Downstream Symmetry in Nonlinear Self-Sustained Oscillations of Reed Instruments.* PhD thesis, Case Western Reserve University, 1986.

[67] T. Idowaga, T. Kobota, K. Komuro, and I. Masakazu. Nonlinear vibrations in the air column of a clarinet. *Journal of the Acoustical Society of America*, 93(1):540–551, 1993.

[68] D. A. Jaffe. Ten criteria for evaluating synthesis techniques. *Computer Music Journal*, 19(1):76–87, 1995.

[69] D. A. Jaffe and J. O. Smith. Extensions of the Karplus-Strong plucked string algorithm. *Computer Music Journal*, 7(2):56–69, 1983. Reprinted in C. Roads (ed.) 1989. *The Music Machine.* Cambridge, Massachusetts, MIT Press, pp. 481–494.

[70] D. A. Jaffe and J. O. Smith. Performance expression in commuted waveguide synthesis of bowed strings. In *Proceedings of the 1995 International Computer Music Conference*, pages 343–346, Banff, Canada, 1995. Computer Music Association.

[71] K. Karplus and A. Strong. Digital synthesis of plucked string and drum timbres. *Computer Music Journal*, 7(2):43–55, 1983.

[72] D. H. Keefe. Experiments on the single woodwind tone hole. *Journal of the Acoustical Society of America*, 72(3):688–699, 1982.

[73] D. H. Keefe. Theory of the single woodwind tone hole. *Journal of the Acoustical Society of America*, 72(3):676–687, 1982.

[74] D. H. Keefe. Acoustic streaming, dimensional analysis of nonlinearities, and tone hole mutual interactions in woodwinds. *Journal of the Acoustical Society of America*, 73(5):1804–1820, 1983.

[75] D. H. Keefe. Acoustical wave propagation in cylindrical ducts: Transmission line parameter approximations for isothermal and nonisothermal boundary conditions. *Journal of the Acoustical Society of America*, 75(1):58–62, 1984.

[76] D. H. Keefe. Woodwind air column models. *Journal of the Acoustical Society of America*, 88(1):35–51, 1990.

[77] D. H. Keefe. Physical modeling of wind instruments. *Computer Music Journal*, 16:57–73, 1992.

[78] J. L. Kelly, Jr. and C. C. Lochbaum. Speech synthesis. In *Proceedings of the Fourth International Congress on Acoustics*, pages 1–4, Copenhagen, Denmark, 1962. Paper G42.

[79] J. A. Kemp, N. Amir, and D. M. Campbell. Calculation of input impedance including higher modes. In *Proceedings of the 5th French Congress on Acoustics*, pages 314–317, Lausanne, Switzerland, 2000.

[80] J. A. Kemp, D. M. Campbell, and M. van Walstijn. Multimodal propagation in acoustic horns. In *Proceedings of the 2001 International Symposium on Musical Acoustics*, pages 521–524, Perugia, Italy, 2001.

[81] J. Kergomard. Elementary considerations on reed-instrument oscillations. In A. Hirschberg, J. Kergomard, and G. Weinreich, editors, *The Mechanics of Musical Instruments*, number 355 in CISM Courses and Lectures. Springer-Verlag, New York, 1995.

[82] J. Kergomard and J. Gilbert. Analyse de quelques aspects du rôle de l'anche d'un instrument à vent cylindrique. In *Proceedings of the Fifth French Conference on Acoustics*, pages 294–297, Lausanne, Switzerland, 2000.

[83] J. Kergomard, S. Ollivier, and J. Gilbert. Calculation of the spectrum of self-sustained oscillators using a variable truncation method: Application to cylindrical reed instruments. *Acustica - Acta Acustica*, 86(4):685–703, 2000. Special Issue on Musical Wind Instrument Acoustics.

[84] L. E. Kinsler, R. F. Frey, A. B. Coppens, and J. A. Sanders, editors. *Fundamentals of Acoustics*. John Wiley & Sons, New York, 1982.

[85] T. I. Laakso, V. Välimäki, M. Karjalainen, and U.K. Laine. Real-time implementation techniques for a continously variable digital delay in modeling musical instruments. In *Proceedings of the 1992 International Computer Music Conference*, pages 14–18, San Jose, California, 1992. Computer Music Association.

[86] T. I. Laakso, V. Välimäki, M. Karjalainen, and U.K. Laine. Crushing the delay – Tools for fractional delay filter design. Technical report, Helsinki University of Technology, Faculty of Electrical Engineering, Laboratory of Acoustics and Audio Signal Processing, Espoo, Finland, Report no. 35, 1994.

[87] S. Lawson and A. Mirzai. *Wave Digital Filters*. Ellis Horwood, New York, 1990.

[88] H. Levine and J. Schwinger. On the radiation of sound from an unflanged circular pipe. *Physics Review*, 73(4):383–406, 1948.

[89] L. Ljung and T. L. Soderstrom. *Theory and Practice of Recursive Identification*. MIT Press, Cambridge MA, 1983.

[90] T. H. Long. The performance of cup-mouthpiece instruments. In E. L. Kent, editor, *Musical Acoustics: Piano and Wind Instruments*, volume 9 of *Benchmark Papers in Acoustics*, pages 180–189. Dowden, Hutchinson, and Ross, 1977. Reprint of the original article in the Journal of the Acoustical Society of America (1947).

[91] X. Lurton. Etude analytique de l'impédance d'entrée des instruments à embouchure. *Acustica*, 49:142–151, 1981.

[92] J. D. Markel and A. H. Gray. *Linear Prediction of Speech*. Springer-Verlag, New York, 1976.

[93] J. Martínez and J. Agulló. Conical bores. Part I: Reflection functions associated with discontinuities. *Journal of the Acoustical Society of America*, 84(5):1613–1619, 1988.

[94] J. Martínez, J. Agulló, and S. Cardona. Conical bores. Part II: Multiconvolution. *Journal of the Acoustical Society of America*, 84(5):1620–1627, 1988.

[95] M. E. McIntyre, R. T. Schumacher, and J. Woodhouse. On the oscillations of musical instruments. *Journal of the Acoustical Society of America*, 74(5):1325–1345, 1983.

[96] X. Meynial. *Systèmes micro-intervalles pour instruments à vents a trous latéraux, oscillation d'une anche simple couplée à un résonateur de forme simple.* PhD thesis, L'université du Maine, Le Mans, 1987.

[97] P. M. Morse. *Vibration and Sound.* American Institute of Physics, for the Acoustical Society of America, 1981. (1st ed. 1936, 2nd ed. 1948).

[98] P. M. Morse and K. U. Ingard. *Theoretical Acoustics.* Princeton University Press, Princeton, New Jersey, 1968.

[99] R. Msallam. *Modèle et simulations numériques de l'acoustique non-linéaire dans les conduits. Application à l'étude des effets non-linéaires dans le trombone.* PhD thesis, L'université Paris VI, 1998.

[100] R. Msallam, S. Dequidt, R. Caussé, and S. Tassart. Physical model of the trombone including nonlinear effects. Application to the sound synthesis of loud tones. *Acustica - Acta Acustica*, 86(4):725–736, 2000. Special Issue on Musical Wind Instrument Acoustics.

[101] C. J. Nederveen. *Acoustical Aspects of Woodwind Instruments.* Frits Knuf, Amsterdam, The Netherlands, 1969. Revised 1998 Nortern Illinois University Press DeKalb.

[102] C. J. Nederveen, K. M. Jansen, and R. R. van Hassel. Corrections for woodwind tone-hole calculations. *Acustica - Acta Acustica*, 84:957–966, 1998.

[103] H. F. Olson. *Acoustical Engineering.* D. Van Nostrand Company, Inc., Princeton, New Jersey, 1957.

[104] Alan V. Oppenheim and Ronald W. Schafer. *Discrete-Time Signal Processing.* Prentice Hall, Inc., Englewood Cliffs, New Jersey, 1989.

[105] V. Pagneux, N. Amir, and J. Kergomard. A study of wave propagation in varying cross-section waveguides by modal decomposition. Part I: Theory and validation. *Journal of the Acoustical Society of America*, 100(4):2034–2048, 1996.

[106] T. Parks and C. S. Burrus. *Digital Filter Design.* John Wiley & Sons, New York, 1987.

[107] G. R. Plitnik and W. J. Strong. Numerical method for calculating input impedances of the oboe. *Journal of the Acoustical Society of America*, 65(3):816–825, 1979.

[108] R. Plomp. *Aspects of Tone Sensation.* Academic Press, New York, 1976.

[109] J. Proakis and D. Manolakis. *Digital Signal Processing. Principles, Algorithms, and Applications.* MacMillan Publishing Company, New York, 1992.

[110] R. W. Pyle, Jr. Effective length of horns. *Journal of the Acoustical Society of America*, 57(6):1309–1317, 1975.

[111] J. W. S. Rayleigh. *The Theory of Sound.* The Macmillan Company, London, 2nd edition, 1896. Reprinted 1945, New York: Dover Publications.

[112] S. Regalia, K. Mitra, and P. P. Vaidyanthan. The digital all-pass filter: A versatile signal processing building block. In *Proceedings of the IEEE*, pages 19–37, 1988.

[113] D. Rocchesso. *Strutture ed Algoritmi per l'Elaborazione del Suono basati su Reti di Ritardo Interconesse.* PhD thesis, Università degli Studi di Padova, Dipartimento di Ellettronica e Informatica, 1996.

[114] D. Rocchesso and J. O. Smith. Circulant feedback delay networks for sound synthesis and processing. In *Proceedings of the 1994 International Computer Music Conference*, pages 378–382, Århus, Denmark, 1994. Computer Music Association.

[115] D. Rocchesso and F. Turra. A generalized excitator for real-time sound synthesis by physical model. In *Proceedings of the Stockholm Musical Acoustics Conference*, pages 584–588, 1993.

[116] M. Roseau. *Vibrations in mechanical systems : analytical methods and applications.* Springer-Verlag, Berlin, 1987.

[117] V. Salmon. Generalized plane wave theory of horns. *Journal of the Acoustical Society of America*, 17:199–211, 1946.

[118] V. Salmon. A new family of horns. *Journal of the Acoustical Society of America*, 17:212–218, 1946.

[119] G. P. Scavone. *An Acoustic Analysis of Single-Reed Woodwind Instruments with an Emphasis on Design and Performance Issues and Digital Waveguide Modeling Techniques.* PhD thesis, Music Dept., Stanford University, 1997.

[120] G. P. Scavone, 2000. Personal communication.

[121] G. P. Scavone and P. R. Cook. Real-time computer modeling of woodwind instruments. In *Proceedings of the 1998 International Symposium on Musical Acoustics*, pages 197–202, Leavenworth, Washington, 1998. The Acoustical Society of America.

[122] G. P. Scavone and J. O. Smith. Digital waveguide modeling of woodwind toneholes. In *Proceedings of the 1997 International Computer Music Conference*, Thessaloniki, Greece, 1997. Computer Music Association.

[123] R. T. Schumacher. Self-sustained oscillations of the clarinet: An Integral Equation Approach. *Acustica*, 40:298–309, 1978.

[124] R. T. Schumacher. *Ab Initio* calculations of the oscillations of a clarinet. *Acustica*, 48(2):71–85, 1981.

[125] J. Schwinger and D. Daxon. *Discontinuities in Waveguides.* Gordon and Breach, New York, 1968.

[126] D. B. Sharp. *Acoustic pulse reflectometry for the measurement of musical wind instruments.* PhD thesis, Department of Physics and Astronomy, University of Edinburgh, 1996.

[127] J. O. Smith. *Techniques for Digital Filter Design and System Identification with Application to the Violin.* PhD thesis, Elec. Engineering Dept., Stanford University, 1983.

[128] J. O. Smith. A new approach to digital reverberation using closed waveguide networks. In *Proceedings of the 1985 International Computer Music Conference*, pages 47–53, Vancouver, Canada, 1985. Computer Music Association.

[129] J. O. Smith. Efficient simulation of the reed-bore and bow-string mechanisms. In *Proceedings of the 1986 International Computer Music Conference*, pages 275–280, The Hague, Netherlands, 1986. Computer Music Association.

[130] J. O. Smith. Music applications of digital waveguides. Technical Report STAN–M–39, CCRMA, Music Department, Stanford University, 1987. A compendium containing four related papers and presentation overheads on digital waveguide reverberation, synthesis, and filtering.

[131] J. O. Smith. Physical modeling using digital waveguides. *Computer Music Journal*, 16(4):74–91, 1992. Special issue: Physical Modeling of Musical Instruments, Part I.

[132] J. O. Smith. Discrete-time modeling of acoustic systems with applications to sound synthesis of musical instruments. In *Proceedings of the Nordic Acoustical Meeting, Helsinki*, pages 21–32, 1996. Plenary paper.

[133] J. O. Smith, 1998. Personal communication.

[134] J. O. Smith and D. Rocchesso. Connections between feedback delay networks and waveguide networks for digital reverberation. In *Proceedings of the 1994 International Computer Music Conference*, pages 376–377, Århus, Denmark, 1994. Computer Music Association.

[135] J. O. Smith and D. Rocchesso. Aspects of digital waveguide networks for acoustic modeling applications. *Web publication downloadable from http://www-ccrma.stanford.edu/ jos/wgj/wgj.html*, 1997.

[136] J. O. Smith and G. P. Scavone. The one-filter keefe clarinet tonehole. In *Proceedings of the IEEE Workshop on Applications of Signal Processing to Audio and Acoustics, New Paltz, NY*, New York, 1997. IEEE Press.

[137] S. D. Sommerfeldt and W. J. Strong. Simulation of a player-clarinet system. *Journal of the Acoustical Society of America*, 83(5):1908–1918, 1988.

[138] K. Steiglitz and L. E. McBride. A technique for the identification of linear systems. *IEEE Trans. Automatic Control*, AAC-10:461–464, 1965.

[139] G. W. Stewart and R. B. Lindsay. *Acoustics.* D. Van Nostrand Company, Inc., New York, 1930.

[140] S. E. Stewart and W. J. Strong. Functional model of a simplified clarinet. *Journal of the Acoustical Society of America*, 68(1):109–120, 1980.

[141] W. J. Strong. Computer simulation of a trumpet. *Journal of the Acoustical Society of America*, 87(1):A138, 1990.

[142] W. J. Strong and J. D. Dudley. Simulation of a player-trumpet system. In *Proceedings of the Stockholm Musical Acoustics Conference*, pages 520–524, 1993.

[143] R. Stuifmeel. Vibration modes of a metal reed of a reed organ pipe: Theory and experiment. Technical report, Eindhoven University of Technology, 1989.

[144] S. C. Thompson. The effect of the reed resonance on woodwind tone production. *Journal of the Acoustical Society of America*, 66(5):1299–1307, 1979.

[145] T. Tolonen. Model-based analysis and resynthesis of acoustic guitar tones. Master's thesis, Helsinki University of Technology, Faculty of Electrical Engineering, Laboratory of Acoustic and Audio Signal Processing, Espoo, Finland, Report no. 46, 1998.

[146] R. Väänänen, V. Välimäki, J. Huopaniemi, and M. Karjalainen. Efficient and parametric reverberator for room acoustics modeling. In *Proceedings of the 1997 International Computer Music Conference*, pages 200–203, Thessaloniki, Greece, 1997. Computer Music Association.

[147] V. Välimäki. Fractional delay waveguide modeling of acoustic tubes. Technical report, Helsinki University of Technology, Faculty of Electrical Engineering, Laboratory of Acoustic and Audio Signal Processing, Espoo, Finland, Report no. 34, 1994.

[148] V. Välimäki. *Discrete-Time Modeling of Acoustic Tubes Using Fractional Delay Filters*. PhD thesis, Helsinki University of Technology, Faculty of Electrical Engineering, Laboratory of Acoustic and Audio Signal Processing, Espoo, Finland, Report no. 37, 1995.

[149] V. Välimäki, J. Huopaniemi, M. Karjalainen, and Z. Jánosy. Physical modeling of plucked string instruments with application to real-time sound synthesis. *Journal of the Audio Engineering Society*, 44(5):331–353, 1996.

[150] V. Välimäki and M. Karjalainen. Digital waveguide modeling of wind instrument bores constructed of truncated cones. In *Proceedings of the 1994 International Computer Music Conference*, pages 423–430, Århus, Denmark, 1994. Computer Music Association.

[151] V. Välimäki, M. Karjalainen, and T. I. Laakso. Modeling of woodwind bores with finger holes. In *Proceedings of the 1993 International Computer Music Conference*, pages 32–39, Tokyo, Japan, 1993. Computer Music Association.

[152] V. Välimäki, T. I. Laakso, and J. Mackenzie. Elimination of transients in time-varying allpass fractional delay filters with application to digital waveguide modelling. In *Proceedings of the 1995 International Computer Music Conference*, pages 327–334, Banff, Canada, 1995. Computer Music Association.

[153] S. Van Duyne and J. O. Smith. Physical modeling with the 2-D digital waveguide mesh. In *Proceedings of the 1993 International Computer Music Conference*, pages 40–47, Tokyo, Japan, 1993. Computer Music Association.

[154] S. Van Duyne and J. O. Smith. Developments for the commuted piano. In *Proceedings of the 1995 International Computer Music Conference*, pages 319–326, Banff, Canada, 1995. Computer Music Association.

[155] M. O. Van Walstijn, J. S. Cullen, and D. M. Campbell. Modeling viscothermal wave propagation in wind instrument air columns. In *Proceedings of the 1997 International Symposium on Musical Acoustics*, pages 413–418, Edinburgh, Scotland, 1997. Institute of Acoustics.

[156] M. O. van Walstijn and G. de Bruin. Conical waveguide filters. In *Proceedings of the Second International Conference On Acoustics and Music Research*, pages 47–54, Ferrara, Italy, 1995.

[157] M. O. van Walstijn and J. O. Smith. Use of truncated infinite impulse response (TIIR) filters in implementing efficient digital waveguide models of flared horns and piecewise conical bores with unstable one-pole filter elements. In *Proceedings of the 1998 International Symposium on Musical Acoustics*, pages 309–314, Leavenworth, Washington, 1998. The Acoustical Society of America.

[158] M. O. Van Walstijn and V. Välimäki. Digital waveguide modeling of flared acoustical tubes. In *Proceedings of the 1997 International Computer Music Conference*, pages 196–199, Thessaloniki, Greece, 1997. Computer Music Association.

[159] M.-P. Verge. *Aeroacoustics of Confined Jets*. PhD thesis, Technische Universiteit Eindhoven, 1995.

[160] C. Vergez. *Trompette et Trompettiste: Un Système Dynamique Non Linéaire à Analyser, Modèliser et Simuler dans un Contexte Musical*. PhD thesis, L'université Paris VI, 2000.

[161] C. Vergez and X. Rodet. Air flow related improvements for basic physical models of brass instruments. In *Proceedings of the 2000 International Computer Music Conference*, pages 62–65, Berlin, Germany, 2000. Computer Music Association.

[162] A. L. Wang and J. O. Smith. On fast FIR filters implemented as tail-canceling IIR filters. *IEEE Trans. Signal Processing*, 45(6):1415–1427, 1997.

[163] J. A. Ware and K. Aki. Continuous and discrete inverse scattering problems in a stratified elastic medium. Part I: Planes at normal incidence. *Journal of the Acoustical Society of America*, 45(4):911–921, 1969.

[164] A. G. Webster. Acoustical impedance and the theory of horns and of the phonograph. *Proc. Nat. Acad. Sci. (US)*, 5:275–282, 1919.

[165] R. T. Weidner and R. L. Sells. *Elementary Modern Physics*. Allyn and Bacon, Boston, 1980. 3rd edition.

[166] T. A. Wilson and G. S. Beavers. Operating modes of the clarinet. *Journal of the Acoustical Society of America*, 56(2):653–658, 1974.

[167] W. E. Worman. *Self-Sustained Nonlinear Oscillations of Medium Amplitude in Clarinet-Like Systems*. PhD thesis, Case Western Reserve University, 1971.

[168] H. A. K. Wright and D. M. Campbell. The influence of the mouthpiece on the timbre of cup-mouthpiece wind instruments. In *Proceedings of the 1998 International Symposium on Musical Acoustics*, pages 159–164, Leavenworth, Washington, 1998. The Acoustical Society of America.

[169] W. E. Zorumski. Generalized radiation impedances and reflection coefficients of circular and annular ducts. *Journal of the Acoustical Society of America*, 54(6):1667–1673, 1973.

# Publications

M. O. Van Walstijn, J. S. Cullen, and D. M. Campbell. Modeling viscothermal wave propagation in wind instrument air columns. In *Proceedings of the 1997 International Symposium on Musical Acoustics*, pages 413–418, Edinburgh, Scotland, 1997. Institute of Acoustics.

M. O. Van Walstijn and V. Välimäki. Digital waveguide modeling of flared acoustical tubes. In *Proceedings of the 1997 International Computer Music Conference*, pages 196–199, Thessaloniki, Greece, 1997. Computer Music Association.

M. O. van Walstijn and J. O. Smith. Use of truncated infinite impulse response (TIIR) filters in implementing efficient digital waveguide models of flared horns and piecewise conical bores with unstable one-pole filter elements. In *Proceedings of the 1998 International Symposium on Musical Acoustics*, pages 309–314, Leavenworth, Washington, 1998. The Acoustical Society of America.

M. O. van Walstijn and D. M. Campbell. The wave digital filter brass mouthpiece model. In *Proceedings of the Forum Acusticum Meeting*, page S77, Berlin, Germany. Acustica - Acta Acustica, 1999. Poster presentation.

M. O. van Walstijn and G. P. Scavone. The wave digital tonehole model. In *Proceedings of the 2000 International Computer Music Conference*, pages 465–468, Berlin, Germany, 2000. Computer Music Association.

M. O. van Walstijn and F. Avanzini. Determination of the Lumped Parameters of a Non-Linear Clarinet Reed Oscillator using a Finite Difference Approach. In *Proceedings of the 2001 International Symposium on Musical Acoustics*, Perugia, Italy, 2001.

F. Avanzini and M. van Walstijn. Modelling the mechanical response of the reed-mouthpiece-lip system of a clarinet. Part I. the finite difference approach. *Acustica - Acta Acustica*, 2002. Submitted for publication.

M. van Walstijn and F. Avanzini. Modelling the mechanical response of the reed-mouthpiece-lip system of a clarinet. Part II. A lumped model approximation. *Acustica - Acta Acustica*, 2002. Submitted for publication.

M. O. van Walstijn and D.M. Campbell. Discrete-time modelling of woodwind instrument bores using wave variables. *Journal of the Acoustical Society of America* , 2002. Submitted for publication.